

DOCTOR OF PHILOSOPHY

A multi-disciplinary approach to fuel cell vehicle modelling and simulation – a study to investigate and optimise overall electric vehicle and hydrogen fuel cell electric vehicle efficiency

Apicella, Michael

Award date:
2019

Awarding institution:
Coventry University

[Link to publication](#)

General rights

Copyright and moral rights for the publications made accessible in the public portal are retained by the authors and/or other copyright owners and it is a condition of accessing publications that users recognise and abide by the legal requirements associated with these rights.

- Users may download and print one copy of this thesis for personal non-commercial research or study
- This thesis cannot be reproduced or quoted extensively from without first obtaining permission from the copyright holder(s)
- You may not further distribute the material or use it for any profit-making activity or commercial gain
- You may freely distribute the URL identifying the publication in the public portal

Take down policy

If you believe that this document breaches copyright please contact us providing details, and we will remove access to the work immediately and investigate your claim.

**A Multi-Disciplinary Approach to
Fuel Cell Vehicle Modelling and
Simulation – A Study to Investigate
and Optimise Overall Electric
Vehicle and Hydrogen Fuel Cell
Electric Vehicle Efficiency**

**By
Michael Apicella**

PhD

June 2018



**A Multi-Disciplinary Approach to
Fuel Cell Vehicle Modelling and
Simulation – A Study to Investigate
and Optimise Overall Electric
Vehicle and Hydrogen Fuel Cell
Electric Vehicle Efficiency**

By

Michael Apicella

**A thesis submitted in partial fulfilment of the University's
requirements for the Degree of Doctor of Philosophy**

June 2018



Some materials have been removed from this thesis due to Third Party Copyright or confidentiality issues. Pages where material has been removed are clearly marked in the electronic version. The unabridged version of the thesis can be viewed at the Lanchester Library, Coventry University

Some materials have been removed from this thesis due to Third Party Copyright or confidentiality issues. Pages where material has been removed are clearly marked in the electronic version. The unabridged version of the thesis can be viewed at the Lanchester Library, Coventry University

Abstract

The focus of this thesis is to determine if a novel multi-disciplinary fuel cell electric vehicle model can accurately predict energy consumption for electric vehicles and hydrogen fuel cell electric vehicles. This is important in order for fuel cell electric vehicle development to take place within the virtual environment and to speed up the route to market for new vehicle technologies.

The thesis has met this research aim through an extensive study of relevant literature, the implementation of state-of-the-art modelling methodologies using the software tool Dymola, the validation of each model using test data, by comparing test results for type approval methods against real-world test data, and by showing the capabilities of the developed model.

The research produced several key findings: There are no multi-disciplinary fuel cell electric vehicle models within the public domain; The electric vehicle version of the developed model can represent vehicle energy consumption on both the New European Drive Cycle and the Coventry University Drive Cycle to 1.3%; The fuel cell electric vehicle model can represent the vehicle energy consumption on the Coventry University Drive Cycle to 8%; The difference in energy consumption between a real-world practical drive cycle and the typical type approval practical test is 36%, where the real-world drive cycle requires 36% more energy per kilometre; The difference in energy consumption estimation between conventional type approval methods and the proposed method is 40%, where the conventional method under predicts energy consumption for real-world driving conditions.

The main outcome from this research is that the current approaches to estimate energy consumption in the simulation environment fails to provide accurate results against real world data, because they do not embrace the varying loads associated with driving on a real road. This work has resulted in a novel multi-disciplinary model that can represent electric vehicles and fuel cell electric vehicles to accurately predict energy consumption for real-world driving conditions.

Abstract

Contents

CHAPTER 1 - Introduction	1
1.1 Background.....	1
1.2 Microcab Background	3
1.2.1 Coventry University Microcab H2EV System Description	5
1.3 Aim and Objectives	8
1.4 Structure of the Thesis	9
CHAPTER 2 - Literature Review	11
2.1 The History of the Fuel Cell Vehicle	12
2.2 Review of Modelling and Simulation tools for Automotive Applications.....	16
2.2.1 <i>Advanced Vehicle Simulator</i>	16
2.2.2 <i>AVL Cruise</i>	16
2.2.3 <i>Modelica</i>	17
2.2.4 <i>Modelica and Automotive</i>	17
2.2.5 <i>Object Orientated Modelling</i>	18
2.2.6 <i>Dymola</i>	18
2.2.7 <i>Summary of Modelling and Simulation Tools</i>	19
2.3 Vehicle Dynamic Modelling	22
2.3.1 <i>Multibody Systems Modelling</i>	22
2.3.2 <i>Tyre Modelling</i>	24
2.3.3 <i>Summary of Tyre Modelling Techniques</i>	27
2.4 Battery Modelling	29
2.4.1 <i>Summary of Battery Modelling Techniques</i>	40
2.5 Fuel Cell Modelling.....	41
2.5.1 <i>Summary of Fuel Cell Modeling Techniques</i>	53
2.6 Drive Cycle Characteristics	55
2.6.1 <i>Summary of Drive Cycles</i>	60
2.7 Summary of Literature.....	61

Contents

CHAPTER 3 - Modelling.....	63
3.1 Modelica and Dymola Connectors.....	64
3.2 Vehicle Model Structure	68
3.3 Chassis Model	71
3.4 Braking Model	78
3.5 Aerodynamics Model.....	81
3.6 Tyre Model.....	84
3.7 Transmission Model	86
3.8 Battery Model.....	88
3.9 Battery Management System Model.....	96
3.10 Motor Model.....	101
3.11 Control Model.....	106
3.12 Fuel Cell Model	112
3.13 Fuel Cell Controller Model.....	119
3.14 Buck-Boost DCDC Model.....	121
3.15 Driver Model.....	123
3.16 Road Models.....	125
3.17 Summary of Modelling	127
CHAPTER 4 - Data Collection, Experiments and Testing.....	129
4.1 Component Mass and Positioning Collection	130
4.2 Battery Testing.....	133
4.2.1 Battery Pack Discharge Testing	133
4.2.2 Battery Pack Charge Testing	136
4.2.3 Individual Cell Discharge Test.....	140
4.2.4 Individual Cell Direct Current Internal Resistance Testing.....	144
4.3 Fuel Cell Testing	147
4.3.1 Fuel Cell Fracture Testing.....	147
4.3.2 Fuel Cell, Battery & Hydrogen Consumption Testing.....	149
4.4 Road Data Acquisition.....	158

4.4.1	NEDC Rolling Road Test.....	158
4.4.2	Coventry University Drive Cycle	161
4.5	Summary of Tests	166
	CHAPTER 5 – Simulation Results, Correlation and Validation	167
5.1	Sub-System Validation	168
5.1.1	Battery Pack Steady State Discharge Validation	168
5.1.2	Battery Pack Goodwolfe Charge Simulation.....	172
5.1.3	Single Cell Model Validation.....	176
5.1.4	Fuel Cell Model Validation.....	181
5.1.5	DCDC System Model Validation.....	185
5.1.6	Motor Model Validation	188
5.2	NEDC Vehicle Validation.....	192
5.2.1	NEDC Electric Vehicle Simulation	192
5.2.2	NEDC Fuel Cell Electric Vehicle Simulation	197
5.3	CUDC Vehicle Validation	198
5.3.1	CUDC Straight Line Electric Vehicle Simulation	198
5.3.2	CUDC 3D Road Electric Vehicle Simulation	200
5.3.3	CUDC 3D Road Fuel Cell Vehicle Simulation.....	203
5.4	Throttle Controller Simulation Results	205
5.4.1	CUDC EV SOC Throttle Controller Simulation	205
5.4.2	CUDC EV Speed Throttle Controller Simulation.....	208
5.4.3	CUDC EV Dual Throttle Controller Simulation.....	210
5.5	Continuous CUDC Fuel Cell Electric Vehicle Simulation Results	211
5.6	Summary of Results.....	218
	CONCLUSIONS & RECOMMENDATIONS FOR FURTHER WORK.....	221
6.1	Conclusions	221
6.2	Discussion and Future Work	223
	References.....	224
	APPENDICES	236

List of Figures

List of Figures

Figure 1-1 - Coventry University Microcab H2EV (Microcab Industries Ltd 2016)	5
Figure 1-2 - Coventry University Microcab H2EV Powertrain.....	7
Figure 2-1 - Harry Karl Ihrig's Fuel Cell Vehicle (Kantola 2004).....	13
Figure 2-2 - ISO-W tyre axis system modified (Blundell, and Harty 2004)	25
Figure 2-3 - Magic Tyre Formula Curve (Blundell, and Harty 2004).....	25
Figure 2-4 - Thevenin Equivalent Circuit Battery Model by (Barreras et al. 2012)....	30
Figure 2-5 - Extended Thevenin Equivalent Circuit Battery Model by (Barreras et al. 2012).....	30
Figure 2-6 - Second Extended Thevenin Equivalent Circuit Battery Model by (Barreras et al. 2012)	31
Figure 2-7 - Randles' Lead-Acid Equivalent Circuit Battery Model by (Gould et al. 2009)	33
Figure 2-8 - Equivalent Circuit Battery Model by (Zhang, and Chow 2010).....	34
Figure 2-9 - FreedomCAR Battery Model by (Verbugge et al. 2009)	35
Figure 2-10 - Proposed Modified Randles' Lead-Acid Battery Model (Gould et al. 2009)	36
Figure 2-11 - Proposed Runtime and I-V Performance Battery Model (Chen, and Rincón-Mora 2006)	37
Figure 2-12 - Black-Box Fuel Cell Model By (Raga et al. 2014).....	41
Figure 2-13 - Large Signal Fuel Cell Model by (Ural, and Gencoglu 2010)	46
Figure 2-14 - Small-Signal Fuel Cell Model by (Ural, and Gencoglu 2010)	47
Figure 2-15 - Simplified MATLAB/Simulink Fuel Cell Model by (Ural, and Gencoglu 2010).....	47
Figure 2-16 - Detailed Fuel Cell Model by (Ural, and Gencoglu 2010)	48
Figure 2-17 - DCDC Convertor Configurations by (Forsyth, and Mollov 1998)	51
Figure 2-18 - DCDC Converter Schematic	52
Figure 2-19 - Fuel Cell Modelling VI Comparison	54
Figure 2-20 - NEDC Drive Cycle Velocity Profile (Barlow et al. 2009).....	56
Figure 2-21 - ARTEMIS Urban Drive Cycle (ECOpaint 2011).....	57
Figure 2-22 - ARTEMIS Rural Drive Cycle (ECOpaint 2011).....	57
Figure 2-23 - ARTEMIS Motorway Drive Cycle (ECOpaint 2011)	58
Figure 2-24 - Coventry University Drive Cycle Map (Ryan et al. 2014)	59
Figure 2-25 - Coventry University Drive Cycle Velocity Profile (Ryan et al. 2014)....	59
Figure 3-1 - Dymola Simulation Setup.....	68

Figure 3-2 - Dymola Road Generator Function..... 69

Figure 3-3 - Dymola Standard Vehicle Model 70

Figure 3-4 - Developed Fuel Cell Vehicle Model..... 71

Figure 3-5 - Dymola Chassis Model 72

Figure 3-6 - Mass Model Parameter Modification 73

Figure 3-7 - Front Suspension Model, Mc Pherson Strut 76

Figure 3-8 - Rear Suspension Model, Rear Twisted Beam 77

Figure 3-9 - Brake System Model 78

Figure 3-10 - Vehicle Side Profile Comparison 82

Figure 3-11 - Tyre Model Overview 84

Figure 3-12 - Transmission Model 86

Figure 3-13 - Gearbox Model 87

Figure 3-14 - Battery Model Package 88

Figure 3-15 - Battery Model Overview 89

Figure 3-16 - Battery Management System Model 96

Figure 3-17 – Simplified Buck-Boost DCDC Schematic..... 98

Figure 3-18 - Motor Model Overview 101

Figure 3-19 - SOC Throttle Restrictive Control Result 107

Figure 3-20 - Vehicle Speed Throttle Restrictive Control Results 109

Figure 3-21 - SOC & Vehicle Speed Restrictive Control Results 111

Figure 3-22 - Hydrogen System Model..... 117

Figure 3-23 - Fuel Cell Controller Model..... 119

Figure 3-24 - Driver Model Overview..... 123

Figure 3-25 - Dymola Road Generator Function..... 126

Figure 4-1 - Coventry University Microcab H2EV CAD 130

Figure 4-2 - Battery Discharge Test Setup 133

Figure 4-3 - Battery Discharge Test Schematic 133

Figure 4-4 – 50 A Constant Current Battery Discharge Voltage vs SOC..... 134

Figure 4-5 – 50 A Constant Current Battery Discharge Voltage vs Time 135

Figure 4-6 – 72 V Zivan NG1 Charger 136

Figure 4-7 - Battery Charge Test Schematic 136

Figure 4-8 - Goodwolfe Charge Curve..... 137

Figure 4-9 - Battery Charge Test, Voltage vs SOC..... 138

Figure 4-10 - Battery Charge Test, Voltage vs Time..... 138

Figure 4-11 - Goodwolfe 72v 4kWh Battery Pack Layout 140

Figure 4-12 - Goodwolfe 72v 4 kWh Battery Pack, Cell Configuration 140

Figure 4-13 - Battery Cell Discharge Test Schematic 142

List of Figures

Figure 4-14 – 3 C Discharge Cell Characteristics	142
Figure 4-15 - Battery Pack, Cell Capacity Results	143
Figure 4-16 - Battery Cell DCIR Test Setup.....	145
Figure 4-17 - Battery Pack, Cell DCIR Results	145
Figure 4-18 - Cell Internal Resistance vs Cell Capacity	146
Figure 4-19 - Fuel Cell Fracture Test Rig	147
Figure 4-20 - Programmed Motohawk VCU and Wiring Loom for Data Acquisition Purpose.....	150
Figure 4-21 - Vehicle Test Schematic.....	151
Figure 4-22 - Fuel Cell Voltage at Each Test Increment	151
Figure 4-23 - Fuel Cell Current at Each Test Increment	152
Figure 4-24 - Fuel Cell Temperature at Each Test Increment	153
Figure 4-25 - Battery Pack Voltage at Each Test Increment	154
Figure 4-26 - Battery Pack Current at Each Test Increment	154
Figure 4-27 - Battery Pack SOC at Each Test Increment	155
Figure 4-28 - Hydrogen Tank Pressure at Each Test Increment.....	156
Figure 4-29 - Hydrogen Volume Flow Rate at Each Test Increment	156
Figure 4-30 - 3kW Fuel Cell Hydrogen Flow Rate during Shutdown	157
Figure 4-31 - NEDC Velocity Procedure	158
Figure 4-32 - NEDC Distance Driven.....	159
Figure 4-33 - NEDC Battery Consumption.....	159
Figure 4-34 - NEDC Vehicle Consumption	160
Figure 4-35 - Coventry University Drive Cycle Map	161
Figure 4-36 - Coventry University Drive Cycle Velocity Profile.....	162
Figure 4-37 - Coventry University Drive Cycle - Battery Voltage Results	163
Figure 4-38 - Coventry University Drive Cycle - Battery Current Results	163
Figure 4-39 - Coventry University Drive Cycle - Battery SOC Results	164
Figure 4-40 - Coventry University Drive Cycle, Altitude Profile	164
Figure 4-41 - Coventry University Drive Cycle, X, Y GPS Positioning.....	165
Figure 5-1 - Steady State Battery Discharge, Simulation Setup.....	168
Figure 5-2 - Steady State Battery Discharge Current Simulation Results	169
Figure 5-3 - Steady State Battery Discharge Voltage Simulation Results	169
Figure 5-4 - Steady State Battery Discharge SOC.....	170
Figure 5-5 - Steady State Battery Discharge Simulation Results	170
Figure 5-6 - Goodwolfe Battery Charge, Simulation Setup	172
Figure 5-7 - Battery Charge Current Simulation Results	173
Figure 5-8 - Battery Charge Voltage Simulation Results.....	173

Figure 5-9 - Battery Charge SOC Simulation Results 174

Figure 5-10 - Battery Charge Simulation Results..... 174

Figure 5-11 - Single Cell Test Simulation Layout..... 176

Figure 5-12 - Cell Discharge Voltage Simulation Results 177

Figure 5-13 - Cell Discharge Voltage Simulation Errors..... 177

Figure 5-14 - Cell Charge Currents 178

Figure 5-15 - Cell Charge Voltage Simulation Results..... 179

Figure 5-16 - Cell Discharge Voltage Simulation Errors..... 179

Figure 5-17 - Single Cell Validation Error Analysis 180

Figure 5-18 - Fuel Cell Voltage Validation, Simulation Layout 181

Figure 5-19 - Fuel Cell Voltage Simulation Results at Each Power Output 182

Figure 5-20 - Fuel Cell Validation, RMS Voltage Error..... 182

Figure 5-21 - Fuel Cell Hydrogen Consumption Validation, Simulation Layout 183

Figure 5-22 - Hydrogen Tank Pressure Results 1..... 183

Figure 5-23 - Hydrogen Tank Pressure Results 2..... 184

Figure 5-24 - Fuel Cell Validation, Hydrogen Consumption Error 184

Figure 5-25 - Fuel Cell System Validation, Simulation Layout 185

Figure 5-26 - DCDC Power Loss Error Results 186

Figure 5-27 - DCDC Validation, RMS Power Error 186

Figure 5-28 - DCDC Efficiency Validation..... 187

Figure 5-29 - Motor Model Validation, Simulation Layout 188

Figure 5-30 – Motor Validation, Efficiency Error 189

Figure 5-31 – Motor Validation, Speed & Back Voltage Error 189

Figure 5-32 – Motor Validation, Current Error..... 190

Figure 5-33 - Motor Validation, Output Power Error..... 190

Figure 5-34 - Motor Validation, Torque Error 191

Figure 5-35 - Motor Validation, RMS Percentage Errors..... 191

Figure 5-36 - NEDC Simulation Layout..... 193

Figure 5-37 - NEDC Vehicle Speed Validation 194

Figure 5-38 - NEDC Energy Consumption Validation 194

Figure 5-39 - NEDC Fuel Cell Energy Consumption Estimation 197

Figure 5-40 – Flat & Straight CUDC EV Simulation, Battery Energy Consumption Estimation Results 198

Figure 5-41 – 3-Dimensional CUDC EV Simulation, Battery Energy Consumption Estimation Results 200

Figure 5-42 - CUDC EV Battery Range Prediction Results..... 202

List of Figures

Figure 5-43 – 3-Dimensional CUDC FCEV Simulation, Battery Energy Consumption Estimation Results	203
Figure 5-44 - 3-Dimensional CUDC FCEV 3kW FC Simulation, Battery Consumption Estimation and Hydrogen Consumption Estimation	204
Figure 5-45 - CUDC EV SOC Dynamic Throttle Controller Results	206
Figure 5-46 - CUDC EV SOC 60% Throttle Limit Controller Results.....	207
Figure 5-47 - CUDC EV Speed Throttle Controller Results.....	208
Figure 5-48 - CUDC EV Speed and SOC Throttle Controller Results	210
Figure 5-49 - Continuous CUDC FCEV 3kW FC Simulation, Battery Consumption Estimation and Hydrogen Consumption Estimation	211
Figure 5-50 - Continuous CUDC FCEV 3kW FC Simulation, Battery Consumption Estimation and Hydrogen Consumption Estimation, Throttle Controller Comparison Results.....	212
Figure 5-51 - CUDC FCEV Battery Power and Fuel Cell Power, Simulation Results	213
Figure 5-52 - CUDC FCEV Battery Energy Consumption Estimation and Hydrogen Consumption Estimation, Simulation Results at FC Outputs Power of 5.55kW and 6.1kW.....	214
Figure 5-53 - CUDC FCEV 5.55kW Battery Energy Consumption Estimation and Hydrogen Consumption Estimation	215
Figure 5-54 - CUDC FCEV 8kW Battery Energy Consumption Estimation and Hydrogen Consumption Estimation	216
Figure 8-1 - Suspension Nomenclature (Dassult Systems 2002-2013).....	237
Figure 8-2 - Battery Pack Cell Variation.....	246
Figure 8-3 - Battery Layout.....	246
Figure 8-4 - Cell Testing - Capacity Comparison	248
Figure 8-5 - Cell Testing - Voltage Comparison.....	248
Figure 8-6 - Fuel Cell Ambient Temperature Test.....	250
Figure 8-7 - Chassis Mounted Accelerometers.....	251
Figure 8-8 - MTS Shaker Rig Procedure 1	252
Figure 8-9 - 0.25hz - 11.25hz Frequency Sweep, 5mm In-Phase Displacement, 0.25hz/s, FC Mounts Installed	252
Figure 8-10 - 0.25hz - 11.25hz Frequency Sweep, 5mm In-Phase Displacement, 0.25hz/s – No FC Mounts Installed.....	253
Figure 8-11 - Difference Between Figure 8-9 and Figure 8-10 Results	253
Figure 8-12 - MTS Shaker Rig Procedure 2	254

List of Figures

Figure 8-13 - 0.25hz - 11.25hz Frequency Sweep, 5mm, 180 Degrees Out-Of-Phase Displacement, 0.25hz/s, FC Mounts Installed.....	254
Figure 8-14 - 0.25hz - 2hz Frequency Sweep, 5mm, 180 Degrees Out-Of-Phase Displacement, 0.25hz/s, FC Mounts Installed.....	255
Figure 8-15 - 2hz - 4hz Frequency Sweep, 5mm, 180 Degrees Out-Of-Phase Displacement, 0.25hz/s, FC Mounts Installed.....	255
Figure 8-16 - 4hz - 6hz Frequency Sweep, 5mm, 180 Degrees Out-Of-Phase Displacement, 0.25hz/s, FC Mounts Installed.....	256
Figure 8-17 - 6hz - 8hz Frequency Sweep, 5mm, 180 Degrees Out-Of-Phase Displacement, 0.25hz/s, FC Mounts Installed.....	257
Figure 8-18 - 8hz - 10hz Frequency Sweep, 5mm, 180 Degrees Out-Of-Phase Displacement, 0.25hz/s, FC Mounts Installed.....	257
Figure 8-19 - 8hz - 10hz Frequency Sweep, 5mm, 180 Degrees Out-Of-Phase Displacement, 0.25hz/s, FC Mounts Installed.....	258
Figure 8-20 - 0.25hz - 11.25hz Frequency Sweep, 5mm, 180 Degrees Out-Of-Phase Displacement, 0.25hz/s, No FC Mounts Installed	258
Figure 8-21 - Difference Between Figure 8-13 and Figure 8-20.....	259
Figure 8-22 - Ethical Approval Certificate	263

List of Tables

List of Tables

Table 1-1- Coventry University and Microcab UK and European Funded Project list.	4
Table 1-2 - Coventry University Microcab H2EV Specification History	6
Table 2-1 - Multibody System Simulation Tool List	22
Table 3-1 - Modelica Elementary Connectors (Modelica 2013)	64
Table 3-2 - Aerodynamic Drag Coefficient Examples	81
Table 4-1 - Vehicle Component Database Example	131
Table 4-2 - Component Positions in Relation to the Centre of Mass	131
Table 4-3 - Vehicle Component Inertia Example	131
Table 4-4 - Vehicle Mass Calculations	132
Table 4-5 - Vehicle Measurements	132
Table 4-6 - Logged Battery Test Variables	134
Table 4-7 - Presented Cells Internal Resistance and Capacity	146
Table 5-1 - Lynch Data Vs Simulation Results	188
Table 8-1 - Model Data, Steering Geometry	236
Table 8-2 - Model Data, Front Suspension Geometry	236
Table 8-3 - Model Data, Rear Suspension Geometry	237
Table 8-4 - Model Data, Component Centre of Mass	238
Table 8-5 - Battery Cell Capacity and DCIR Results	247
Table 8-6 - Test Equipment	249
Table 8-7 - Model Validation	260

Supervisory Team

Mike Blundell, Bernard Porter, Jinlei Shang and John Jostins.

Acknowledgements

I would like to thank;

Mike Blundell – provided guidance with simulations to ensure the models reacted as expected along a baseline setting.

Bernard Porter – for continuous moral support and guidance throughout the project.

Jinlei Shang – for assistance with specific fuel cell knowledge.

John Castell – for providing lunches when I forgot to eat and for being a great friend.

Peter Jostins – for detailed electrical knowledge.

John Jostins, everyone within the Coventry University Research team and at Microcab Industries – for making the Coventry University Microcab H2EV vehicles available for testing and providing thought-provoking discussions about fuel cell electric vehicles in general.

And finally, a special thank you to both of my parents and my sister for all of their support throughout my studies. Without them, none of the work presented would be possible and I would not be the person I am today.

Glossary of Terms

Glossary of Terms

3D	Three Dimensional
ADVISOR	Advanced Vehicle Simulator
AFC	Alkaline Fuel Cell
APU	Auxiliary Power Unit
ARTEMIS	Assessment and Reliability of Transport Emissions Models and Inventory Systems
BMM	Battery Management Module
BMS	Battery Management System
C	Capacity Based Test Rate
CAD	Computer Aided Design
CAN	Controller Area Network
CC	Constant Current
CFD	Computational Fluid Dynamics
CM	Centre of Mass
CUDC	Coventry University Drive Cycle
CV	Constant Voltage
DC	Direct Current
DCDC	Direct Current to Direct Current convertor
DCIR	Direct Current Internal Resistance
DMFC	Direct Methanol Fuel Cell
DOD	Depth of Discharge
DOE	Department of Energy
DTI	Department of Trade and Industry
EMF	Electromotive Force
EV	Electric Vehicle
EV	Electric Vehicle
FAFC	Phosphoric Acid Fuel Cell
FC	Fuel Cell
FCEV	Fuel Cell Electric Vehicle
FCEV	Fuel Cell Electric Vehicle
FCV	Fuel Cell Vehicle
FEA	Finite Element Analysis
GMT	Greenheart Millennium Transport Ltd
GPS	Global Positioning System
H ₂	Hydrogen
HFC	Hydrogen Fuel Cell
IC	Internal Combustion
I-V	Current versus Voltage
Li-Ion	Lithium-Ion
LVP	Low Voltage Protection
MBS	Multi-body Systems
MF-Swift	Magic Formula-Swift
MF-Tyre	Magic Formula-Tyre
NASA	National Aeronautics and Space Administration
NECAR	New Electric Car
NEDC	New European Drive Cycle
NiCd	Nickel-Cadmium
NiMH	Nickel Metal Hydride
NREL	National Renewable Energy Laboratory

OEM	Original Equipment Manufacturer
Open	
Source	Non-Commercial
OTP	Over Temperature Protection
OVP	Over Voltage Protection
PEM	Proton Exchange Membrane
PEMFC	Proton Exchange Membrane Fuel Cell
PID	Proportional-Integral-Derivative Controller
RC	Resistor and Capacitor
RMS	Root Mean Square
RPM	Revolutions per Minute
SAM	Systems Advisor Model
slpm	Standard Litres per Minute
SME	Small and Medium-sized Enterprise
SOC	State of Charge
SOH	State of Health
TNO	The Netherlands Organisation for Applied Scientific Research
TRL	Transport Research Laboratory
U.S.	United States of America
VCU	Vehicle Control Unit
VI	Voltage versus Current Graph
x	Longitudinal Geographical Position
y	Lateral Geographical Position
z	Altitudinal Geographical Position

Units

%	Percent	kW	Kilowatt
°C	Degrees Celsius	kWh	Kilowatt hour
μHz	Microhertz	kWh/km	Kilowatt-hours per kilometre
A	Amperes	m	Metres
Ah	Ampere hours	m ²	Metres squared
Ah/Purge	Ampere hours per purge	mA	Milliampere
e		mm	Millimetres
As	Ampere seconds	m/s	Metres per second
As/Purge	Ampere seconds per purge	m/s ²	Metres per second squared
bar	Unit of gas pressure	MHz	Megahertz
bar/km	Bar per kilometre	mOhm	Milliohm
barg	Unit of gas pressure, gauge	mΩ	Milliohm
g	Gravity	mph	Miles per hour
h	Hour	mV	Millivolt
Hz	Hertz	N	Newton
J	Joules	Nm	Newton metres
J/mol	Joules per moles	Ω	Ohm
k	Kilo	rad/s ²	Radians per second squared
kg	Kilogram	RPM	Revolutions per minute
kg/km	Kilogram per kilometre	s	Seconds
Kg m ²	Kilogram metre squared	s/km	Seconds per kilometre
kg/m ²	Kilogram per metre squared	slpm	Standard litres per minute
kJ	Kilojoules	V	Volts
km	Kilometres	W	Watt
km/h	Kilometres per hour		

Nomenclature

Wh/km Watthour per kilometre |

Nomenclature

The following symbols are used generally in the thesis. Alternative usages are identified for specific models that follow.

Greek Symbols

α = Alpha, Typically used for angular acceleration in rad/s^2 and coefficients
 Δ = Delta, Typically used to denote the change in a variable
 ε = Epsilon, Used to denote efficiency
 η = Eta, Typically used to denote a loss in a model
 γ = Gamma, Used for the Longitudinal Slip in the Pacejka Magic Formula
 μ = Mu, Typically used to represent a coefficient of friction
 ω = Omega, Typically used to denote angular velocity in rad/s
 φ = Phi, Typically used to denote the absolute rotation angle in radians
 ψ = Psi, Typically used as a correctional factor
 ρ = Rho, Typically used to denote density
 τ = Tau, Typically used to denote torque
 ζ = Zeta, Used to denote coefficients in the fuel cell model

Pacejka Tyre Model – Section 2.3.2 – Page 26

B = Stiffness Factor
 C = Shape Factor
 E = Peak Factor
 F_x = Brake Force
 F_y = Side Force
 M_y = Self Aligning Torque
 S_H = Horizontal Shift
 S_V = Vertical Shift
 X = Slip Angle (α) or Longitudinal Slip (γ)
 Y = Either Side Force (F_y), Self Aligning Torque (M_y) or Brake Force (F_x)

Greek Symbols

α = Slip Angle
 γ = Longitudinal Slip

Barreras et al. (2012) Thevenin Equivalent Circuit Battery Model – Section 2.4 – Pages 30 - 32

I = The battery current
 I_{1C} = The current used to discharge at 1C
 I_{equiv} = The equivalent current drawn from the battery due to Peukert number
 I_x = The current used to discharge the battery during test Q_x
 k = The Peukert number
 Q_{1C} = The capacity when discharged at 1C
 Q_x = The capacity when discharged at a defined current
 $R_{int,cha}$ = The internal resistance during charge
 $R_{int,dis}$ = The internal resistance during discharge
 R_{int} = The internal resistance of the battery

R_{sd}	= The resistance which characterises the self discharge rate
$V_{OCV(DoD)1}$	= The open circuit voltage of the voltage source
V_{OCV}	= The open circuit voltage of the battery
V_{cha}	= The voltage of the battery when fully charged
V_{dis}	= The voltage of the battery when fully discharged
$v_{t,x1}$	= The terminal voltage at the battery at DoD point 1 on the 1C datasheet
$v_{t,x2}$	= The terminal voltage at the battery at DoD point 2 on the 1C datasheet
v_t	= The terminal voltage at the battery for each point on the 1C datasheet
x	= The ratio of the actual available capacity divided by the total capacity
x_1	= The DoD point 1 on the 1C datasheet
x_2	= The DoD point 2 on the 1C datasheet

Greek Symbols

α	= The coefficient for the battery model
$\Delta V_{OCV(T)}$	= The change in open circuit voltage at the battery due to temperature

Shepherd (1965) Battery Model – Section 2.4 – Page 33

B	= A constant parameter
E	= The no load voltage
E_s	= The constant battery voltage
i_t	= The current drawn from the battery in coulombs
K	= The coefficient of polarization
N	= The internal resistance of the battery
Q	= The amount capacity of the battery in coulombs
i	= The battery current

Randles' Equivalent Circuit Battery Model – Section 2.4 – Page 33

C_b	= The capacity of the battery
C_s	= The surface capacitance
I_{in}	= The battery current
R_d	= The self discharge resistance
R_i	= The internal resistance of the battery
R_t	= The charge transfer resistance
V_0	= The battery voltage
V_{Cb}	= The open circuit voltage of the battery
V_{cs}	= The voltage drop due to the surface layer capacitance

Zhang, and Chow (2010) Equivalent Circuit Battery Model – Section 2.4 – Page 34

$C_{capacity}$	= The battery capacity
C_m	= A capacitance to model the battery relaxation effect
C_1	= A capacitance to model the battery relaxation effect
C_2	= A capacitance to model the battery relaxation effect
i_l	= The battery current
R_m	= A resistance to model the battery relaxation effect
R_0	= The internal resistance of the battery
R_1	= A resistance to model the battery relaxation effect
R_2	= A resistance to model the battery relaxation effect

Nomenclature

V_{SoC} = The battery voltage due to change in SOC
 V_{oc} = The battery open circuit voltage

Verbugge et al. (2009) FreedomCAR Battery Model – Section 2.4 – Page 35

C = The shunt capacitance around R_p
 $i_{p(t)}$ = The current through the polarisation resistance
 OCV = The ideal open circuit battery voltage
 OCV' = The capacitance that accounts for the change in OCV with the time integral of current
 R_0 = The internal resistance of the battery
 R_p = The internal polarisation resistance
 V_l = The battery terminal voltage

Gould et al. (2009) Randles Based Battery Model – Section 2.4 – Page 36

C_n = The capacitance to represent the capacity of the battery
 C_p = The capacitance to represent battery impedance
 I_{in} = The battery current
 R_i = The internal resistance of the battery
 R_n = The linear battery resistance due to state of charge
 R_p = The resistance to represent battery impedance
 V_0 = The battery terminal voltage
 V_{Cn} = The battery voltage due to battery state of charge
 V_{Cp} = The impedance based voltage due dynamic battery loads

Chen, and Rinón-Mora (2006) Runtime and I-V Performance Battery Model – Section 2.4 – Page 37

$C_{Transient_L}$ = The capacitance responsible for the long term voltage response during transients
 $C_{Transient_S}$ = The capacitance responsible for the short term voltage response during transients
 $C_{capacity}$ = The capacity of the battery
 $R_{SelfDischarge}$ = The self discharge resistance
 R_{Series} = The varying internal resistance due to state of charge
 $R_{Transient_L}$ = The resistance responsible for the long term voltage response during transients
 $R_{Transient_S}$ = The resistance responsible for the short term voltage response during transients
 SOC = The state of charge of the battery
 $V_{OC(SOC)}$ = The battery open circuit voltage due to battery state of charge

Tremblay, and Dessaint (2009) MATLAB/Simulink Battery Model – Section 2.4 – Page 38

A = The exponential zone amplitude
 B = The exponential zone time constant inverse
 E_0 = The battery constant voltage
 i = The battery current
 i_l = The filtered battery current
 i_t = The remaining battery capacity

K	= The polarisation constant
$NiCD$	= Nickel Cadmium chemitry
$NiMH$	= Nickel Metal Hydride chemistry
Q	= The battery capacity
R	= The internal resistance of the battery
t	= A coefficient for exponential zone voltage
$V_{char,LeadAcid}$	= The battery voltage for lead acid chemistry during charge
$V_{char,LiIon}$	= The battery voltage for lithium ion chemistry during charge
$V_{char,NiMH,NiCD}$	= The battery voltage for NiMH and NiCD chemistry during charge
$V_{dis,LeadAcid}$	= The battery voltage for lead acid chemistry during discharge
$V_{dis,LiIon}$	= The battery voltage for lithium ion chemistry during discharge
$V_{dis,NiMH,NiCD}$	= The battery voltage for NiMH and NiCD chemistry during discharge

Raga et al. (2014) Black-Box Fuel Cell Model – Section 2.5 – Page 41

C_p	= The capacitance for the dynamic voltage curve
E_{OC}	= The fuel cell open circuit voltage
i_{fc}	= The fuel cell current
L	= The inductance for the dynamic voltage curve
$R_L(i_{fc})$	= The variable resistance for the dynamic voltage curve
R_s	= The resistance for the static $I - V$ curve
$R_v(i_{fc})$	= The variable resistance for the static $I - V$ curve

Souleman, Tremblay, and Dessaint (2009) Generic Fuel Cell Model – Section 2.5 – Pages 41 - 42

A	= The tafel slope
E_N	= The nernst voltage
E_{OC}	= The fuel cell open circuit voltage
F	= The Faraday Constant, 96485
h	= The Planck's constant
i_0	= The exchange current
i_{fc}	= The fuel cell current
k	= The Boltzmann's constant
K_c	= The voltage constant at normal condition of operation
N	= The number of cells in series
P_{H_2}	= The partial pressure of hydrogen inside the stack
P_{O_2}	= The partial pressure of oxygen inside the stack
R	= The Universal gas constant, 8.3145
R_{ohm}	= The internal resistance
T	= The temperature of operation
T_d	= The responce time (at 95% if the final value)
V_{fc}	= The fuel cell voltage
z	= The number of moveing electrons ($z = 2$)

Greek Symbols

α	= The charge transfer coefficient
ΔG	= The activation energy barrier

Nomenclature

Boscaino et al. (2013) Fuel Cell Model – Section 2.5 – Page 43

A	= 35.61 V
B	= 4.844 V
C	= 50.3425 A
D	= 821.7721×10^{-9} V
E	= 13.083 A
i_{fc}	= The fuel cell current
V_{FC}	= The fuel cell voltage

Benchouia et al (2013) Fuel Cell Model – Section 2.5 – Pages 43 - 44

A	= The active area of the membrane
B	= The concentration resistance
CO_2	= The concentration of oxygen in the cathode
E_{cell}	= The nernst cell voltage
I	= The fuel cell current
I_{lim}	= The current density of the cell
l	= The thicknes of the membrane
losses	= The activation loss, resistive loss and diffusion losses
N_{cell}	= The number of cells in the fuel cell stack
P_{H_2}	= The partial pressure of hydrogen in atm
P_{O_2}	= The partial pressure of oxygen in atm
R_c	= The proton resistance
R_m	= The equivalent resistance of the electron flow
T	= The temperature in kelvin
V_{cell}	= The cell voltage
V_{stack}	= The fuel cell stack voltage

Greek Symbols

η_{act}	= The activation loss
η_{con}	= The concentration polarization loss
η_{ohm}	= The ohmic polarization loss
ψ	= The temperature correction factor
ρ_m	= The specific resistance of the membrane
ζ_1	= The first parametric coefficient
ζ_2	= The second parametric coefficient
ζ_3	= The third parametric coefficient
ζ_4	= The forth parametric coefficient

Ural, and Gencoglu (2010) Dynamic Fuel Cell Model – Section 2.5 – Page 45

B	= A constant to simulate the activation over voltage
C	= A constant to simulate the activation over voltage
E	= The nernst instantainous voltage
E_0	= The open circuit voltage
F	= The Faraday Constant, 96485
I_{FC}	= The fuel cell stack current
K_r	= A modelling constant
M_{H_2}	= The molar mass of hydrogen
M_{H_2O}	= The molar mass of oxygen
R	= The Universal gas constant, 8.3145
R_{int}	= The sum of electric and protonic resistance
T	= The fuel cell temperature in kelvin
V_{an}	= The volume of the anode

- V_{cell} = The DC output cell voltage of the fuel cell system
 k_{H_2} = The hydrogen valve molar constant
 k_{H_2} = The hydrogen valve molar constant
 k_{an} = The anode valve constant
 p_{H_2} = The hydrogen partial pressure inside the stack
 p_{H_2O} = The oxygen partial pressure inside the stack
 p_{O_2} = The molar flow of oxygen
 $q_{H_2}^{in}$ = The hydrogen input molar flow
 q_{H_2O} = The molar flow of oxygen

Greek Symbols

- η_{act} = The activation over voltage
 η_{ohmic} = The ohmic over voltage
 τ_{H_2} = The hydrogen time constant

Ural, and Gencoglu (2010) Basic Electrochemical Steady State Fuel Cell Model – Section 2.5 – Page 46

- A = The activation polarization constant
 B = The concentration polarization constant
 E_{rev} = The reversible voltage
 I_0 = The exchange current
 I_l = The maximum current production of the fuel cell

Greek Symbols

- α_{H_2} = The charge transfer coefficient of hydrogen
 α_{H_2O} = The charge transfer coefficient of water
 α_{O_2} = The charge transfer coefficient of hydrogen
 ΔG = The size of the activation barrier
 η_{act} = The revised activation over voltage
 η_l = The concentration losses

Ural, and Gencoglu (2010) Basic Electrical Large Signal Fuel Cell Model – Section 2.5 – Page 46

- C_{DL} = The capacitor to represent a charged double layer capacitor response
 E_{FC} = The open circuit voltage of the fuel cell
 I_{FC} = The fuel cell current
 R_P = The parallel resistance accros the capacitor for dynamic response
 R_S = The series resistance for static IV representation
 V_{FC} = The fuel cell voltage

Ural, and Gencoglu (2010) Basic Electrical Small Signal Fuel Cell Model – Section 2.5 – Page 47

- C_{∞} = The capacitor to represent geometrical capacitance
 E_{FC} = The open circuit voltage of the fuel cell
 R_{∞} = The series resistance for static IV representation
 R_{DL} = The parallel resistance accros the capacitor for dynamic response
 Z = An unspecified impedance

Nomenclature

Ural, and Gencoglu (2010) Simplified MATLAB/Simulink Fuel Cell Model – Section 2.5

– Page 47

A	= The activation polarization constant
E	= The nernst instantaneous voltage
E_{OC}	= The open circuit voltage of the fuel cell
i_0	= The exchange current
i_{fc}	= The fuel cell current
N	= The number of cells in the fuel cell stack
R_{int}	= The sum of electric and protonic resistance
T_d	= The time constant for representing the capacitance of the fuel cell
V_{fc}	= The fuel cell stack voltage

Ural, and Gencoglu (2010) Detailed MATLAB/Simulink Fuel Cell Model – Section 2.5 –

Pages 48 - 50

A	= The activation polarization constant
E_n	= The nernst voltage of the fuel cell
E_{OC}	= The open circuit voltage of the fuel cell
E_{n1}	= The nernst voltage of the fuel cell
F	= The Faraday constant
h	= Planck's constant
I_{fc}	= The fuel cell current
I_{nom}	= The nominal stack current
K	= The voltage undershoot constant
K_C	= The voltage constant at the normal operating condition
N	= The number of cells within the fuel cell stack
p_{H_2}	= The hydrogen partial pressure inside the stack
p_{H_2O}	= The partial pressure of water vapour inside the stack
p_{O_2}	= The oxygen partial pressure inside the stack
p_{air}	= The absolute supply pressure of air
p_{fuel}	= The absolute supply pressure of fuel
R	= The universal gas constant
T	= The fuel cell temperature in kelvin
T_{nom}	= The nominal stack temperature
U_{fH_2}	= The rate of hydrogen conversion
U_{fH_2nom}	= The nominal hydrogen utilization
U_{fH_2peak}	= The maximum hydrogen utilization
U_{fO_2nom}	= The nominal oxygen utilization
$V_{lpm(air)}$	= The air flow rate
$V_{lpm(air)nom}$	= The nominal air flow rate of air
$V_{lpm(fuel)}$	= The fuel flow rate
V_{nom}	= The nominal voltage of the fuel cell
V_u	= The voltage undershoot coefficient
W	= The percentage of water vapour in the oxidant
$X_{\%}$	= The percentage of hydrogen in the fuel
$Y_{\%}$	= The percentage of oxygen in the fuel
Z	= The number of moving electrons

Greek Symbols

ΔG	= The size of the activation barrier
$\Delta h^\circ(H_2O_{gas})$	= Gibbs free energy, $241.83_{\times 10^3}$ J/mol

Forsyth, and Mollov (1998) DCDC Model – Section 2.5 – Page 51

C = Is the capacitance of the capacitor
 d = Is the transistor state (0 – 1)
 L = Is the inductance of the inductor
 R = Is the resistance of the resistor
 u = Is either the input voltage or the output current
 x = Is either the inductor current or the capacitor voltage

Modelica (2013) Connector Modelling – Section 3.1 – Page 65

f_a = The flow variable on connector a
 f_b = The flow variable on connector b
 P = The potential variable across the connector
 p_a = The potential variable on connector a
 p_b = The potential variable on connector b

Modelica (2013) Rotational Flange Connector – Section 3.1 – Page 66

Greek Symbols

α = The angular acceleration of the flange in rad/s^2
 τ = Is the flow variable as cut torque in the flange in Nm
 φ = Is the potential variable as the absolute rotation angle of the flange in radians
 ω = The angular velocity of the flange in rad/s

Modelica (2013) Ideal Gear Model – Section 3.1 – Page 66

b = Is the gear ratio that changes both the the torque and the angular rotation angle

Greek Symbols

φ_a = Is the absolute rotation angle of the first flange in radians
 φ_b = Is the absolute rotation angle of the second flange in radians
 τ_a = Is the torque at the first flange in Nm
 τ_b = Is the torque at the second flange in Nm

Modelica (2013) Electrical Pin Connector – Section 3.1 – Page 66

i = Is the flow variable as current flowing into the pin in amperes
 v = Is the potential variable as the voltage of the pin in volts

Modelica (2013) Resistor Model – Section 3.1 – Page 66

i = The current flowing through the resistor model
 i_a = The current flowing through the positive pin
 i_b = The current flowing through the negative pin
 R = The resistive value of the resistor being modeled
 v = The voltage across the electrical pins
 v_a = The voltage at the positive pin
 v_b = The voltage at the negative pin

Nomenclature

Mass Model Parameter Estimation – Section 3.3 – Pages 73 - Error! Bookmark not defined.

CM	= The vehicle's Centre of Mass
$I_{XX,CM}$	= The vehicle's moment of inertia about the longitudinal axis
$I_{XZ,CM}$	= The vehicle's moment of inertia about the vertical axis
$I_{YY,CM}$	= The vehicle's moment of inertia about the lateral axis
$m_{component}$	= The mass of components
m_{total}	= The total mass of the vehicle
X	= The longitudinal distance to the component from the CM of the vehicle
X_{CM}	= The longitudinal distance to the CM from the front of the vehicle
$X_{component}$	= The longitudinal distance to the component from the global coordinate system
Y	= The lateral distance to the component from the CM of the vehicle
Y_{CM}	= The lateral distance to the CM from the centre of the vehicle
$Y_{component}$	= The lateral distance to the component from the global coordinate system
Z	= The vertical distance to the component from the CM of the vehicle
Z_{CM}	= The vertical distance to the CM from the bottom of the tyre
$Z_{component}$	= The vertical distance to the component from the global coordinate system

Dassault Systems (2002-2013) Braking Model – Section 3.4 – Pages 78 - 80

A_{piston}	= The area of the brake piston inside the caliper
B_{ratio}	= The boost ratio for the pedal force
$D_{masterCylinder}$	= Diameter of the master cylinder's internal bore
F_{Runout}	= The pressure at which the booster stops working, input forces larger than this are not amplified
$F_{frontCalliperBF}$	= Bipolar force which acts as a clamping force on the front brake pads
F_{pedal}	= Pressure supplied to the vacuum booster by the drivers pedal
$F_{rearCalliperBF}$	= Bipolar force which acts as a clamping force on the rear brake pads
F_{vacumm}	= Force out of the vacuum booster
F_{vacumm}	= Force supplied to the master cylinder by the vacuum booster
$P_{kneePoint}$	= Pressure threshold to start reducing the brake pressure
$P_{masterCylinder}$	= Pressure out of the master cylinder
$P_{masterCylinder}$	= Pressure supplied to the rear proportional valve by the master cylinder
$P_{masterCylinder}$	= Pressure supplied to the front calipers from the master cylinder
$P_{proportionalValve}$	= Pressure out of the rear proportional valve
$P_{proportionalValve}$	= Pressure supplied to the rear calipers from the rear proportional valve
P_{ratio}	= The pressure reduction ratio to apply after the knee point pressure is reached
$P_{threshold}$	= The minimum pressure to apply a braking force on the brake pads
$r_{frontEffective}$	= The effective radius of the front brake disc
$r_{rearEffective}$	= The effective radius of the rear brake disc

Greek Symbols

$\mu_{frontPad}$	= The coefficient of friction of the front brake pad
$\mu_{rearPad}$	= The coefficient of friction of the front brake pad
$\tau_{frontBrake}$	= Front brake torque applied to the rotational flang

$\tau_{rearBrake}$ = Rear brake torque applied to the rotational flang

Modelon AB (2004-2014) Aerodynamics Model – Section 3.5 – Page 83

F_{front} = Quadratic longitudinal drag force which acts on the vehicle at $r0cp_{front}$

F_{side} = Quadratic lateral drag force which acts on the vehicle at $r0cp_{side}$

v_x = The relative longitudinal velocity of wind and vehicle speed acting at the front of the vehicle

v_y = The relative lateral velocity of wind and vehicle speed acting at the side of the vehicle

Greek Symbols

$\mu_{rearPad}$ = The coefficient of friction of the front brake pad

ρ = Density of air at the location of the vehicle

Battery Model – Section 3.8 – Pages 89 - 94

A_c = Exponential zone amplitude during charging

A_d = Exponential zone amplitude during Discharge

B_c = Resistance which determines the exponetial slope of the baseline voltage due to a change in the battery SOC

B_d = Resistance which determines the exponetial slope of the baseline voltage due to a change in the battery SOC

D = Resistance which determines the slope of the baseline voltage due to a change in the battery SOC

$E0_c$ = The first of three equations that determine the basline voltage of the battery during charging

$E0_d$ = The first of three equations that determine the basline voltage of the battery during discharge of the battery

$E1_c$ = The second of three equations that determine the basline voltage of the battery during charging and due to the filtered current

$E1_d$ = The second of three equations that determine the basline voltage of the battery during disharge of the battery and due to the filtered current

$E2_c$ = The third of three equations that determine the basline voltage of the battery during charging and due to the current

$E2_d$ = The third of three equations that determine the basline voltage of the battery during disharge of the battery and due to the current

$E3_c$ = The first of two equations that determine the dynamic voltage of the battery during charging and due to the filtered current

$E3_d$ = The first of two equations that determine the dynamic voltage of the battery during disharge of the battery and due to the filtered current

$E4_c$ = The second of two equations that determine the dynamic voltage of the battery during charging and due to the current

$E4_d$ = The second of two equations that determine the dynamic voltage of the battery during disharge of the battery and due to the current

i = The current law accross the positive pin and negative pin in the model

i_{batt} = Current at the cell

i_{filt} = Filtered current

i_n = The current at the negative pin in the model

i_p = The current at the positive pin in the model

n_p = Number of cells connected in parallel

n_s = Number of cells connected in series

Q = The actual charge remaining in the battery

Q_{cell} = Maximum capacity of the cell

$Q_{cellstart}$ = Capacity of the cell at the start of the simulation

Nomenclature

Q_{il}	= The filtered charge used from the battery
Q_{it}	= The actual charge used from the battery
R_c	= Direct Current Internal Resistance of the battery during charging
R_d	= Direct Current Internal Resistance of the battery during discharge of the battery
SOC	= State of Charge of the battery
SOC_{start}	= State of Charge start percentage
T_s	= Battery response time
v	= The voltage of the battery pack
V_{baseC}	= A sum of the base line voltage equations for charging
V_{baseD}	= A sum of the base line voltage equations during discharge of the battery
V_{cell}	= Determines which cell voltage characteristics dependant on the flow direction of current
V_{cellC}	= The cell voltage of the battery during charging
V_{cellD}	= The cell voltage of the battery during discharge of the battery
V_{con}	= Typical nominal voltage
V_{dynC}	= A sum of the dynamic voltage equations for charging
V_{dynD}	= A sum of the dynamic voltage equations during discharge of the battery
V_{exp}	= Start of nominal voltage zone
V_{max}	= Maximum charge voltage
v_n	= The voltage at the negative pin in the model
v_p	= The voltage at the positive pin in the model

Greek Symbols

η	= The efficiency on the battery
η_a	= A gain used to parametrise the coulombic efficiency of the battery
η_b	= An offset used to parametrise the coulombic efficiency of the battery
η_{max}	= The maximum coulombic efficiency of the battery
η_{min}	= The minimum coulombic efficiency of the battery
η_{SOCmax}	= The the point of battery SOC where the battery is most efficient
η_{SOCmin}	= The the point of battery SOC where the battery is least efficient

Battery Management System Model – Section 3.9 – Pages 97 - 99

C	= The capacitance of the DCDC capacitor
D	= The transistor state (input value 0 – 1)
ϵ	= A negligible value to prevent divisions by zero
i	= The current flowing through the battery
i_1	= The current at the input of the DCDC
i_2	= The current at the output of the DCDC
i_L	= The current flowing through the inductor
\dot{i}_L	= The current flowing through the inductor
\dot{i}_{loadI}	= The current load to be applied due to the current flowing through the battery
\dot{i}_{loadV}	= The current load to be applied due to the voltage at the battery terminals
$i_{maxDrain}$	= The maximum current to draw from the battery
$i_{maxDrainThres}$	= The current threshold where the maximum load is applied
$i_{minDrain}$	= The minimum current to draw from battery, a negligible amount of current
$i_{minDrainThres}$	= The current threshold which the the BMS starts applying a load
L	= The inductance of the inductor
R_2	= The resistance at the output of the DCDC
R_L	= The resistance at the inductor

R_c	= The voltage at the DCDC capacitor
R_{in}	= The resistance at the input of the DCDC
v_1	= The voltage at the input of the DCDC
v_2	= The voltage at the output of the DCDC
v_c	= The voltage at the capacitor
v_{thres}	= The voltage threshold which the the BMS starts applying a load
y	= The output of the model which is sent to the Buck Boost converter which physically applies the load

Motor Model – Section 3.10 – Pages 102 - 105

<i>Brake</i>	= The braking signal wich is sent to the motor controller
i	= The current law accross the positive pin and negative pin in the model
$i_{driveMotorCurve}$	= The current that the motor can provide based on RPM, the torque constant and the throttle
i_{fan}	= The electrical load induced by turning the mechanical fan
i_{motor}	= The supplied or generated current at the motor in regenerative braking
$i_{motorBrakeMax}$	= Limits the maximum current at the motor to that of the curve and the datasheet during braking
$i_{motorMax}$	= Limits the maximum current at the motor to that of the curve and the datasheet
$i_{motorMaxP}$	= The maximum current supplied to the motor to achieve the max torque, parameter
$i_{motorTotal}$	= Determines the total current which is drawn accross the electrical pin in the model
i_n	= The current at the negative pin in the model
i_p	= The current at the positive pin in the model
$i_{regenMotorControllerLimit}$	= Determines the regen current to apply when braking and infers a braking torque
$i_{regenMotorCurve}$	= The current that the motor can provide based on RPM, the torque constant and the brake signal
k_{speed}	= The characteristic of the back Electromotive Force of the motor (RPM/v)
P_{fan}	= Determines an ideal loss due to turning the mechanical fan, it is a linear relationship with RPM. Where the fan is used to remove heat from the motor, the power is used to determine maximum energy that will be required to turn the fan at the motors maximum rotational speed
P_{fanP}	= Sets the maximum equivalent cooling power of the mechanical fan attached to the rotor
$P_{motorIn}$	= The electrical power at the motor
$P_{motorOut}$	= The mechanical power at the motor
$Regen_{enable}$	= The boolean variable which enables the regenerative braking when above a certain speed
<i>RPM</i>	= The rotational speed of the motor
RPM_{maxP}	= The maximum rotational speed of the motor, parameter
$RPM_{minSpeedP}$	= The minimum speed which the motor can supply regenerative braking
RPM_{ratedP}	= The rated rotational speed of the motor, parameter
<i>Throttle</i>	= The throttle signal which is sent to the motor controller
v	= The voltage between the positive pin and negative pin in the model
v_{motor}	= The back Electromotive Force of the motor
v_n	= The voltage at the negative pin in the model

Nomenclature

$v_{nominalP}$ = The rated working voltage of the motor, parameter
 v_p = The voltage at the positive pin in the model

Greek Symbols

η_{motor} = Calculates the efficiency of the motor
 τ = The torque supplied or generated by the motor
 τ_{const} = The electrical torque constant
 $\tau_{motorMaxP}$ = The maximum rotational torque supplied by the motor, parameter

Throttle Controller 1 – Section 3.11 – Pages 106 - 107

Dyn_{limSOC} = The dynamic limit to be applied to the throttle
 Dyn_{soc} = The result of the scaled and gained throttle limit
 SOC = The State of Charge of the battery
 SOC_{max} = The State of Charge value which T_{max} is applied
 SOC_{min} = The State of Charge value which T_{min} is applied
 T_{In} = The input throttle signal
 T_{max} = The maximum throttle value, typically 100%
 T_{min} = The lower value which the throttle will be limited to
 T_{Out} = The limited throttle signal

Greek Symbols

ΔSOC = The State of Charge range
 ΔT = The throttle range
 $\Delta TSOC$ = The gain of the throttle limit

Throttle Controller 2 – Section 3.11 – Page 108

Dyn_v = The result of the scaled and gained throttle limit
 Dyn_{limv} = The dynamic limit to be applied to the throttle
 T_{In} = The input throttle signal
 T_{max} = The maximum throttle value, typically 100%
 T_{min} = The lower value which the throttle will be limited to
 T_{Out} = The limited throttle signal
 V = The velocity of the vehicle
 V_{max} = The velocity of the vehicle which T_{max} is applied
 V_{min} = The velocity of the vehicle which T_{min} is applied

Greek Symbols

ΔTV = The gain of the throttle limit
 ΔV = The velocity range

Throttle Controller 3 – Section 3.11 – Pages 109 - 110

Dyn_v = The result of the scaled and gained throttle limit
 Dyn_{lim3} = The dynamic limit to be applied to the throttle based on both
 Dyn_{limv} and Dyn_{limsoc}
 Dyn_{limSOC} = The dynamic limit to be applied to the throttle
 Dyn_{limv} = The dynamic limit to be applied to the throttle
 Dyn_{soc} = The result of the scaled and gained throttle limit
 SOC = The State of Charge of the battery
 SOC_{max} = The State of Charge value which T_{max} is applied
 SOC_{min} = The State of Charge value which T_{min} is applied
 T_{In} = The input throttle signal
 T_{Out} = The limited throttle signal
 T_{max} = The maximum throttle value, typically 100%
 T_{min} = The lower value which the throttle will be limited to

V	= The velocity of the vehicle
V_{max}	= The velocity of the vehicle which T_{max} is applied
V_{min}	= The velocity of the vehicle which T_{min} is applied

Greek Symbols

ΔSOC	= The State of Charge range
ΔT	= The throttle range
$\Delta TSOC$	= The gain of the throttle limit
ΔTV	= The gain of the throttle limit
ΔV	= The velocity range

Fuel Cell Model – Section 3.12 – Pages 112 - 118

A	= The active area of the membrane
B	= A parametric coefficient, -1.022
C_{O_2}	= The concentration of oxygen dissolved in water
E_{nerst}	= The thermodynamic potential of the cell
I_{FC}	= The current produced by the fuel cell
I_{max}	= The maximum current that the fuel cell can produce
J	= The active current density of the cell
J_{max}	= The maximum current density of the fuel cell
m	= The mass of hydrogen in the tank
\dot{m}	= The mass flow rate of hydrogen due to current production of the fuel cell
\dot{m}_{tank}	= The mass flow rate at the tank
m_{used}	= The hydrogen used since the start of the simulation
N_{act}	= The activation voltage loss
N_{con}	= The concentration voltage loss
N_{diff}	= The gas diffusion voltage loss
N_{ohm}	= The ohmic voltage loss
n_s	= The number of cells in series within the fuel cell
P_{H^2}	= The partial pressure of hydrogen at the anode
P_{O_2}	= The partial pressure of oxygen at the cathode
P_{anode}	= The pressure at the anode
P_{cath}	= The pressure at the cathode
P_{fan}	= The power of the fuel cell cooling fan
$P_{initial}$	= The start pressure of the hydrogen tank for the simulation, parameter
$Q_{created}$	= The heat produced by fuel cell
Q_{fan}	= The heat removed by fuel cell's cooling fan
Q_{loss}	= The heat lost at the thermal connector of the fuel cell
R	= The specific gas constant of hydrogen
R_C	= The resistance to the transfer of protons through the membrane
r_m	= The specific resistivity of the membrane for electron flow
R_m	= The equivalent resistance of the membrane for electron flow
S_1	= A parametric coefficient, 1.215
S_2	= A parametric coefficient, 0.044
S_3	= A parametric coefficient, -0.003
S_4	= A parametric coefficient, 0.012
t	= The thickness of the membrane
T	= The temperature of the fuel cell in Kelvin
$T_{environment}$	= The ambient temperature of the environment in Kelvin
V	= The physical volume of the hydrogen tank
v_{cell}	= The voltage of a single cell within the fuel cell
V_{fan}	= The velocity of the cooling fan as a percentage from max
v_{fc}	= The voltage of the whole fuel cell
V_{slpm}	= The volume flow rate at the tank

Nomenclature

X = The water content in the membrane

Greek Symbols

η_{fan} = The efficiency of the fuel cell cooling fan

ρ_{H^2} = The density of hydrogen

Fuel Cell Controller Model – Section 3.13 – Page 120

f = The value to set the purge valve condition, 1 is open, 0 is closed

i = The current produced by the fuel cell

Purge = The signal sent to the purge valve

t = The time counter

y = The Integral of current

$y_{duration}$ = The duration in which the purge valve is open, parameter

$y_{interval}$ = The interval in which the purge valve is closed, parameter

Buck-Boost DCDC Model – Section 3.14 – Pages 121 - 122

C = The capacitance of the DCDC capacitor

D = The averaged transistor state (input value range 0 – 1)

ϵ = A negligible value to prevent divisions by zero

i_L = The current flowing through the inductor

i_1 = The current at the input of the DCDC

i_2 = The current at the output of the DCDC

L = The inductance of the inductor

P_{in} = The power at the input of the DCDC

P_{out} = The power at the output of the DCDC

R_L = The resistance at the inductor

R_{out} = The resistance at the output of the DCDC

R_c = The voltage at the DCDC capacitor

R_{in} = The resistance at the input of the DCDC

v_c = The voltage at the capacitor

v_1 = The voltage at the input of the DCDC

v_2 = The voltage at the output of the DCDC

Battery Cell Capacity Estimation – Section 4.2.3 – Page 141

3600 = The amount of seconds within an hour

C = The Coulombic electrical charge

Current = The current during the integration

time(0) = The start point of time for the integration

time(end) = The end point of time for the integration

Greek Symbols

Δ time = The change in time during the integration

BS EN 61960:2011 (2011) DCIR Testing – Section 4.2.4 – Page 144

DCIR = The Direct Current Internal Resistance of the battery in mOhms

I_1 = The load current, $I_2 * 0.2$ in A

I_2 = The maximum load current in A

V_1 = The voltage at I_1 in V

V_2 = The voltage at I_2 in V

Energy Consumption Estimation – Section 5.2.1 – Page 192

$i_{battery}$	= The instantaneous battery current in A
$P_{battery}$	= The instantaneous power at the battery in kW
$Q_{battery}$	= The energy used from the battery in kJ
$Q_{consumption}$	= The amount of energy per kilometer provided by the battery in kWh/km
$Q_{usedbattery}$	= The energy used from the battery in kWh
$S_{travelled}$	= The distance travelled over the simulation in km
$v_{battery}$	= The instantaneous battery voltage in V
$V_{vehicle}$	= The speed of the vehicle in m/s
t	= Time in s

Range Estimation – Section 5.2.1 – Page 195

S	= The distance travelled over the simulation in km
S_{range}	= The estimated range of the vehicle based on the battery capacity and simulation in km
Q	= The energy used from the battery over the simulation in kWh
$Q_{batterynominal}$	= The nominal battery capacity in Wh
$Q_{consumption}$	= The amount of energy per kilometer provided by the battery in kWh/km

Fuel Cell Power Requirement Estimation – Section 5.2.1 – Page 195

$Q_{consumption}$	= The amount of energy per kilometer provided by the battery in kWh/km
Q_{FC}	= The estimated energy requirement for continuous driving in Wh
t	= The time taken to complete the simulation in s
P_{FC}	= The estimated continuous power requirement from the fuel cell in W
Greek Symbols	
ε_{DCDC}	= The efficiency of the DCDC at the given power.

CHAPTER 1 - INTRODUCTION

1.1 Background

Although Fuel Cell (FC) vehicles exist, mostly as research demonstration vehicles, they have yet to become established in the market place. This is due to the complex nature of fuel cells, the challenges associated with their integration into automotive applications and a lack of hydrogen refuelling infrastructures. A collaboration between Coventry University and Microcab has identified several key issues for fuel cells within an automotive application which include reliability, a strategy for their use, longevity and their efficiency gains.

Over recent years there have been significant improvements with battery technology and this is increasingly making the switch to electric vehicles easier for the general public. However, in general, vehicle examples from large manufacturers cannot obtain range whilst maintaining efficiency without increasing battery capacity. The result is a substantial increase in vehicle weight. This is currently the solution for limited Electric Vehicle (EV) range to compete with Internal Combustion (IC) engine vehicles. This can be seen when analysing the battery sizes in terms of power, as the Nissan Leaf is sold with a 24 kWh battery which is capable of providing 124 miles on the NEDC Drive cycle (Nissan 2015) with an average kerb weight of 1507 kg, and the BMW i3 with a 18.8 kWh battery which is capable of providing 118 miles on the ECE driving cycle (93/116/EC) with a curb weight of 1195 kg (BMW 2015). The Coventry University Microcab H2EV Fuel Cell Electric Vehicle (FCEV) has a 4 kWh battery, 3 kW fuel cell and a 350 bar 1.65 kg hydrogen tank and is theoretically capable of a similar range to that of the Nissan and the BMW on the New European Driving Cycle (NEDC), due to its hydrogen storage. However, the curb weight of the Coventry University Microcab H2EV at 800 kg is approximately 53% of the Nissan and 66% of the BMW (Nissan 2015) and (BMW 2015). Therefore, the development and integration of a hydrogen powered fuel cell system is critical to increase EV range without a drastic compromise in both weight and performance.

One of the most important requirements for any electrically propelled vehicle is the definition of its use. This will differ between, for example, a city vehicle, a motorway vehicle, a delivery vehicle, an agricultural vehicle or a recreational vehicle.

This definition of the vehicle's use is critical to define the way in which the power is either delivered or conserved dependent on the situation. Once this definition of use is established an industry standard drive cycle is usually assigned to a computational model of the intended vehicle to determine its behaviour. However, the current and

typical industry standard drive cycles which are used are extremely limited and do not realistically represent true operating conditions as they only consider speed against time (Barlow et al. 2009).

Current simulation tools such as Multibody Systems (MBS), Finite Element Analysis (FEA), and Computational Fluid Dynamics (CFD) are all separately used to model and analyse the integrity of a vehicle prior to manufacturing. This is done to reduce costs in the physical testing and development stage of a vehicle, and is part of a current drive in the automotive sector to move towards total vehicle sign-off using virtual prototypes. However, for a complex and slow developing technology, such as Hydrogen Fuel Cells (HFC) in automotive vehicles, a broader approach to modelling is required so that a more accurate virtual representation of the vehicle's efficiency and performance can be established prior to manufacturing. Therefore, a more mathematical forward looking multi-disciplinary approach is required where the vehicle dynamics can interact with the electronics, the drive cycle, the heat dissipation and the driver.

To meet this challenge, a flexible mathematical simulation tool, Dymola (Dassult Systems 2002-2013), has been used to model a FCEV in this work. Dymola can be used to simulate the dynamic behaviour and complex interactions between systems representing many engineering fields, such as mechanical, electrical, thermodynamics, hydraulic, pneumatic, thermal and control systems.

Each of the systems within a FCEV requires the modelling of other sub-systems or components. To represent the vehicle dynamics behaviour and losses. The model must include a representation of the suspension springs, suspension damping, tyre models, chassis, suspension configuration, steering geometry, mass locations, aerodynamics, motors and motor controllers.

The vehicle battery is a major system, and battery modelling and simulation is a relatively new area in automotive applications. This part of the model requires a detailed parametric model of a lithium ion battery. The model must also include a detailed parametric Proton Exchange Membrane (PEM) fuel cell model and a representation of the Vehicle Control Unit (VCU).

Drive cycles are used to establish an energy consumption for a vehicle, however, a forward looking multi-disciplinary model, which is capable of simulating vehicle dynamic behaviour, would require additional characterisation. Therefore, the drive cycle can be modelled as a road profile which requires the representation of vehicle speed, longitude, latitude and altitude positioning, so that a realistic representation of the road can be created from real driving test data. A predictive driver model is also required which can use a closed loop approach to follow the path and road profile whilst computing the commands to steer, accelerate and brake the vehicle. With this

approach to modelling it is intended that a closer representation of a FCEV can be established in the virtual prototype phase. This allows for more rigorous investigation of efficiency and performance prior to the manufacturing of a FCEV and will therefore result in the physical testing phase of a prototype being shortened.

With the use of the proposed model questions such as range, charge independence, predictability, and overall energy consumption can be answered within the simulation environment rather than through physical testing. Optimisation of control and power management strategies can be implemented and tested to determine their effectiveness. Typically, a manufacturer will want to know if their proposed vehicle will be able to function in a meaningful way and will want to know what their proposed vehicle can achieve and what are its limits. These questions are typically not answered with confidence until the prototype testing phase has been completed. However, with a high fidelity representative FCEV model these questions can be addressed with more certainty within the virtual simulation environment, saving the manufacturer time and money.

This project will be conducted in collaboration with the Small and Medium-sized Enterprise (SME) company Microcab Ltd. The Microcab company is a spinout company of Coventry University, which physically builds and runs the Coventry University Microcab H2EVs on a day to day basis. They have agreed to supply vehicles to allow for sub-system and full vehicle testing so that model validation can be accomplished for the purposes of this thesis.

The next section of the thesis 'Microcab Background' shows the history of the Coventry University Microcab H2EV's specification and provides a clear summary of the modelling requirements.

1.2 Microcab Background

Early work on environmentally-friendly vehicle design was undertaken by Greenheart Millennium Transport Ltd. (GMT), a company registered in 1998. The trade mark 'Microcab' was first used in 1999 by GMT. Their interest in zero tailpipe emission vehicles started with a three-wheeled, pedal assisted electric vehicle and a prototype was demonstrated in 1999 at Interlaken, Switzerland (Microcab H1), (Jostins 1999). With Department of Trade and Industry (DTI) funding, GMT went on to develop this platform to carry a passive hydrogen fuel cell (600 W) and removable steel hydrogen cylinder. This vehicle was named the Microcab H3. In 2004 Microcab Industries Ltd was founded and began to work in collaboration with Coventry University, effectively as a spinout company. Microcab and Coventry University jointly developed a new design and manufactured a small four-wheeled vehicle prototype, the Microcab H4,

which made use of a 1.2 kW hydrogen fuel cell and lead acid battery system. A fleet of 5 H4 vehicles were built for government funded trials on the University of Birmingham campus from 2006 to 2008. Data from these trials allowed for the specification of a new vehicle design, the H2EV. With further grant funding and partners including Delta Motorsport, Penso and Lotus, the new vehicle design and engineering work was undertaken, and the first prototype was built in 2010 (Jostins 2017). The vehicle was then launched at the Low Carbon Vehicle Event 2011 after a few system design changes. Since Coventry University and Microcab Industries joined forces the collaboration has been part of multiple UK and European funded projects, as shown in Table 1-1 (Microcab Industries Ltd 2016).

Table 1-1- Coventry University and Microcab UK and European Funded Project list

ECOBULK	New Horizon 2020 project Partner in the pan-European project 'ECOBULK' to 'close the loop' on product design and promote the re-use of products, parts and materials. The project aims at adopting a whole life cycle approach, with the innovative design of long-lasting eco-products.
CABLED	Zero-tailpipe emission demonstration project, testing and data collection in 3 sites in the UK
SWARM	Hydrogen fuel cell vehicle demonstration project, testing and data collection in 3 sites across Europe
SED	Smart Electric Drivetrain, brings together low carbon powertrain technology and connected car technology creating "smart" powertrain technology, giving significant efficiency improvements and vehicle autonomy risk reductions.
DISCUSS	Drivetrain Integration, Supply Chain Upscaling and Streamlining
NVN	Demountable fuel cell design, failure modes relating to vibration on the stack
LREV	Experimental onboard solid-state hydrogen storage and generation on the H2EV

The involvement of the Coventry University Microcab H2EV in these projects has helped in the development and adoption of fuel cell electric vehicles in the public domain by either showing supply chain routes, through the demonstration of functioning vehicles and new technology, or through the life cycle of the given vehicle type. The Coventry University Microcab H2EV is shown in Figure 1-1.



Figure 1-1 - Coventry University Microcab H2EV (Microcab Industries Ltd 2016)

Figure 1-1 shows the Coventry University Microcab H2EV at the 2016 Hydrogen London Transport Fair. This is the vehicle which will be used for the purpose of this thesis.

1.2.1 Coventry University Microcab H2EV System Description

One of the key aspects of the Coventry University Microcab H2EV is that the vehicle is specifically designed to be a modular system so that the vehicle could be used as a developmental platform for research applications. The modular vehicle design can accommodate various fuel cells and battery systems, with its intended use as a city vehicle. However, the Microcab company concept is slightly different to that of most Original Equipment Manufacturers (OEM). The company believes that the vehicle should only have the equipment on board capable of driving to its intended use, and minimal redundancy built into the system. Therefore, there 'powertrain concept' leads to small batteries and small fuel cells, so that they can maintain a lightweight vehicle system to achieve better overall efficiency. The result of this idea is that the company specified the vehicle to have a 4 kWh Lithium Ion-Phosphate battery pack, a 3 kW proton exchange membrane fuel cell and a 1.65 kg (Usable) hydrogen tank. As the stored electrical energy on board is low, only 4 kW, and the fuel cell is small, in terms of continuous power output, control of the vehicle system requires finesse to ensure that the vehicle can perform as expected without running out of available electrical energy. The vehicle has a top speed of 55 mph, a wheel torque of 119 Nm and a dry mass of approximately 800 kg (average mass has been taken across 8 prototypes) (Jostins 2017). The Coventry University Microcab H2EV has had continuous development since the launch in 2011 and has undergone various design changes

which can be seen in Table 1-2, thus, demonstrating its ability to accommodate a variety of different powertrains through its modular vehicle design.

Table 1-2 - Coventry University Microcab H2EV Specification History

System Area	2009-2011	2011-2013	2013-2016	2016+
Battery Pack	72 V 60 A generation 1 lithium ion phosphate battery pack produced by Goodwolfe Energy	72 V 60 A generation 2 lithium ion phosphate battery pack produced by Goodwolfe Energy	72 V 60 A generation 2 lithium ion phosphate battery pack produced by Goodwolfe Energy	72 V 60 A lithium ion phosphate battery pack designed and manufactured by Coventry University
	24 cells connected in series then connected to three other groups of 24 cells in parallel	24 cells connected in series then connected to three other groups of 24 cells in parallel	24 cells connected in series then connected to three other groups of 24 cells in parallel	Four cells connected in parallel then connected in series 24 times.
Hydrogen Fuel Cell System	3 kW Serenergy high temperature fuel cell	3 kW Horizon low temperature fuel cell	3 kW Ballard low temperature fuel cell	3.3 kW Ballard low temperature fuel cell.
	Fuel cell system supplied by Serenergy	Fuel cell system supplied by Arcola Energy	Fuel cell system supplied by Arcola Energy	Fuel cell system developed by Coventry University
	350 bar 1.65 kg hydrogen tank			
Vehicle Control System	Vehicle Control Unit system supplied by Potenza Energy Ltd	Vehicle Control Unit system supplied by Potenza Energy Ltd	Vehicle Control Unit system supplied by Potenza Energy Ltd	Vehicle Control Unit System developed by Coventry University
Electric Motors	2x 25 kW Lynch LEM-200 D127 brushed DC motors	2x 25 kW Lynch LEM-200 D127 brushed DC motors	2x 25 kW Lynch LEM-200 D127 brushed DC motors	2x 25 kW Lynch LEM-200 D127 brushed DC motors
Chassis	Mc Pherson strut front suspension			
	No Anti-Roll bar	No Anti-Roll bar	No Anti-Roll bar	19 mm Front Anti-Roll bar
	H Beam rear suspension			
	Mechanical spring dampers, front and rear			
	165/70R13 tyres, front and rear			
	800 kg curb mass			

Table 1-2 shows that the fuel cell system is the main area of development which the Coventry University Microcab H2EV has undertaken across the revisions. Figure 1-2 shows a Computer Aided Design (CAD) render of the latest Coventry University Microcab H2EV powertrain (2016+). This has been generated by the author of this thesis.

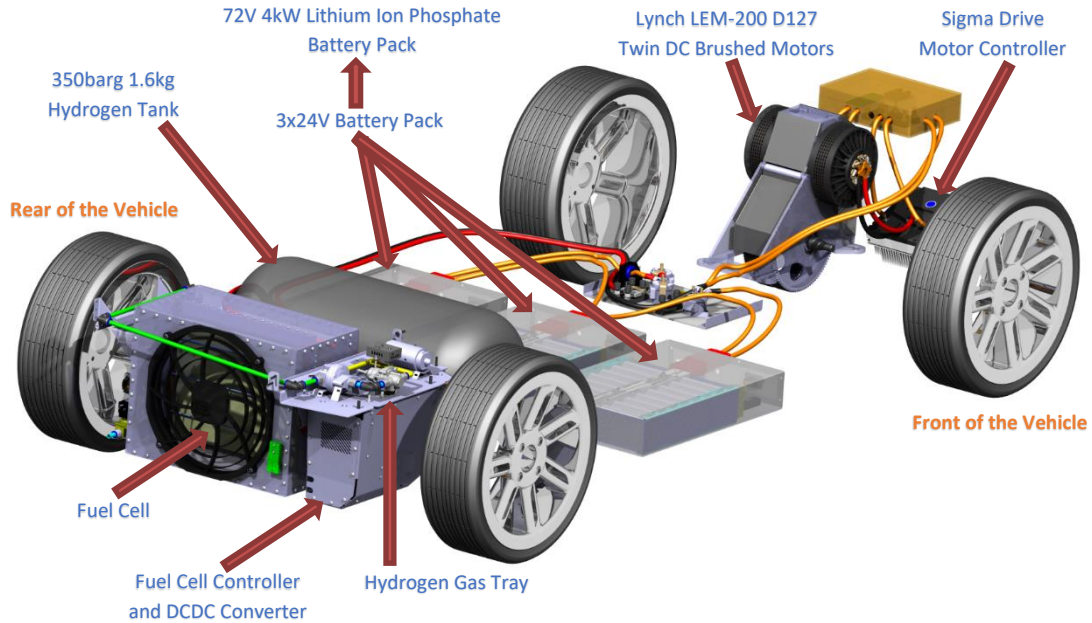


Figure 1-2 - Coventry University Microcab H2EV Powertrain

Figure 1-2 shows the motors and motor controller at the front of the vehicle, the battery packs in the centre of the vehicle, the hydrogen tank and the fuel cell system at the rear of the vehicle. From Table 1-2 and Figure 1-2 a clear description of the modelling requirements is provided to meet the aims and objectives set out in the following section.

The Coventry University Microcab H2EV is a prototype vehicle with only 10 in production, and the vehicle has undergone specification upgrades typically due to difficulties with fuel cell reliability, battery pack reliability and the usability of the vehicle systems. However, the usability of the vehicle systems is more procedural and outside of the scope of propulsion and powertrain. For example, the control and logic routines between driving the vehicle and charging the vehicle via plug in charge, along with driver information displays are not to be addressed within this thesis. Due to issues regarding reliability of the subsystems discussed, it has been difficult to identify the true capabilities of the vehicle through physical prototyping. By using a comprehensive vehicle model, the true capability of the vehicle could be identified (Jostins 2017). Therefore, within this project it is important to focus on modelling the powertrain components of the vehicle such as the lithium ion phosphate battery, air cooled PEM fuel cell and power delivery control strategies which operate between the driver and the motor controllers to change the vehicle's performance and efficiency. Initially the FCEV was modelled using typical energy consumption estimation methods, where the vehicle's weight, and other parasitic losses were the main factor for the energy consumption of the vehicle. The approach used was a backwards modelling technique

where the energy consumption was derived, using typical losses of a vehicle, from the vehicle speed over the NEDC. This initial process influenced the design specification of the Coventry University Microcab H2EV powertrain and fuel cell requirements (Jostins 2017).

1.3 Aim and Objectives

The research question addressed in this project is to determine if a novel multi-disciplinary fuel cell vehicle model can accurately predict energy consumption for EV and FCEV. To address this problem an investigation of the novel FCEV model must be completed to determine if it can be used in automotive design to predict energy consumption. In order to meet this aim following project objectives must be met:

- Create a multi-disciplinary FCEV model with the following complex subsystems:
 - Chassis System
 - Battery
 - Fuel Cell
 - Motor
 - Vehicle Control Unit
 - Road Profiles (Drive Cycles)
 - Closed-loop Driver
- Provide parametric modelling capability for versatility of vehicle design and simulation
- Carry out a validation exercise at both:
 - Sub-system validation
 - Whole vehicle level validation
- Provide predictive energy consumption capability
- Compare real world driving data and energy consumption against current type approval method

By meeting these objectives this work will aim to deliver a novel multi-disciplinary model of a FCEV that can be used in an improved design process for integrated vehicle systems. This will allow FCEV manufacturers to optimise system performance and improve the operational efficiency of the vehicle. The provisions of this new model will contribute to the drive towards virtual prototypes in the automotive industry and the associated cost reductions in vehicle development.

1.4 Structure of the Thesis

This thesis consists of six main bodies of work, not including the appendices and references. Chapter 1 provides an introduction where the key issues surrounding the topic are presented with the aim and objectives.

Chapter 2 presents a descriptive overview of current literature relating specifically to fuel cells, electric vehicles, drive cycles and modelling tools, whilst the review pays close attention to model usability and the aims and objectives of the project throughout the discussion of the literature.

A comprehensive sub-system modelling description is provided within Chapter 3 and demonstrates how the use of parameters can modify the vehicle platform.

Chapter 4 presents various test results which have been conducted over the project and explains how the specific tests can be used to validate the vehicle model.

Simulation and validation results are provided within Chapter 5, where each major area of the vehicle model is validated and comparisons are made against the test data.

Chapter 6 summarises this thesis and clearly presents the contributions to both the research area and the automotive industry. Additionally, the future work that can follow this project is presented.

CHAPTER 2 - LITERATURE REVIEW

To address the overall aim of this study a literature review has been carried out to identify the gap in current knowledge that has been investigated and also to inform the methodology and modelling techniques that will be used. As such, this literature review covers current modelling techniques and simulation tools, vehicle and tyre modelling, battery modelling, fuel cell modelling and the drive cycles that are used to evaluate energy consumption. An initial section covers the history of the fuel cell with references that can be traced back to the 18th century. The main body of the literature review focuses on the transitional period in the late 20th and early 21st century where electric vehicle technologies, as an alternative to the traditional internal combustion engine, gathered momentum. The main impetus for this has been the capability of electric drive and fuel cell systems to offer a cleaner and more environmentally-friendly option in automotive propulsion.

Published material relating to many of these developments is extensive and a selective approach was required to assess the literature for relevance. Therefore, whilst some attention has been given to the full range of technical literature relating to vehicle design, emphasis has duly been given to more recent technical developments. This is particularly so in relation to proton exchange membrane fuel cell systems and lithium ion battery systems, as these are most relevant to the vehicle used as the basis of the modelling and experimental work in the project. In terms of modelling and simulation techniques, practical software options have been covered in addition to generic approaches used in other applications and investigations. These have typically emphasised methods widely used in automotive applications. Therefore, in the initial stage of the investigation, several areas were explored and fundamental knowledge on battery modelling, fuel cell modelling, and vehicle system integration modelling was required to develop testing criteria and appropriate simulation analyses. The detail of the battery modelling processes and analyses will be discussed throughout the thesis in the relevant chapters. The aim of this chapter is to provide a summary of the given areas to determine the best route of modelling methodology for the project.

This section presents summaries of the key information found during the investigation, and demonstrates what methods are currently being used, and are relevant to this project. A summary of each review will be given to determine its usefulness to the project and the project objectives.

2.1 The History of the Fuel Cell Vehicle

This section demonstrates the order in which researchers have developed both fuel cells and fuel cell vehicles, showing a background into the quantity of research which has previously been accomplished and the current state of FCEV's.

In 1766 Cavendish applied a spark to hydrogen and produced water. He did this in a demonstration to the Royal Society of London, by doing this the discovery led to his later finding that water consists of hydrogen and oxygen. In 1788 Lavoiser, who was building on Cavendish's work, gave hydrogen its name. The name hydrogen has been derived from the Greek words "hydro" and "genes" which means "water" and "born of", respectively (New York State Energy Research and Development Authority 2005).

In 1838 Schoenbein discovered the fuel cell effect, combining hydrogen and oxygen to produce water and electric current (New York State Energy Research and Development Authority 2005).

In 1837 Grove created his first scientific paper. This paper consisted of the first novel constructions for fuel cells. The young Welsh scientist created this paper during his honeymoon, where Grove and his wife travelled the continent and investigated their scientific interests (Morus 2004). In 1839 Grove produced a rather novel form of electric fuel cell. The fuel cell used zinc and platinum electrodes exposed to two acids and were separated by a porous ceramic pot (Rendus 1839). It wasn't until 1845 where Grove demonstrated a combination of his and Schoenbein's discovery, in the form of a "gas battery", that he earned the title "Father of the Fuel Cell" (New York State Energy Research and Development Authority 2005).

Langer and Mond were the first two researchers to present the term 'Fuel Cell' in 1889 whilst these two scientists were attempting to develop an air and coal fuel cell. In 1932 a Cambridge engineering professor, Francis Bacon, modified Langer and Mond's equipment to develop the first Alkaline Fuel Cell (AFC), (Johnson Matthey Plc 2013). In the 1950's General Electric invented the Proton Exchange Membrane Fuel Cell (PEMFC). The researcher Grubb was credited with this invention and then Niedrach continued Grubb's work by using platinum as the catalyst on the membranes. Following this development the National Aeronautics and Space Administration (NASA) continued to develop, in collaboration with the two inventors, the PEMFC which was then used in the Gemini Space program in the 1960's (New York State Energy Research and Development Authority 2005) and (Johnson Matthey Plc 2013). In 1959 Bacon built the first practical 5 kW hydrogen-air fuel cell, Bacon used this machine to power a welding machine and named the design the 'Bacon Cell'. Following this, Harry Karl Ihrig demonstrated the first fuel cell vehicle (New York State

Energy Research and Development Authority 2005) and (Johnson Matthey Plc 2013). Ihrig's fuel cell vehicle is shown in Figure 2-1.



Figure 2-1 - Harry Karl Ihrig's Fuel Cell Vehicle (Kantola 2004)

Figure 2-1 shows the first fuel cell vehicle, which is a tractor, that Ihrig designed using the 'Bacon Cell' to power the vehicle (New York State Energy Research and Development Authority 2005). Due to the significant worry about the availability of oil across the world in the 1970's, this sparked the need to embrace the concept of energy efficiency. Due to the clean air and efficiency drive by multiple governments, research into fuel cells and fuel cell vehicles increased. This led to a multitude of one-off demonstration vehicles to determine the possibility of implementing fuel cells into vehicles. Shell developed a Direct Methanol Fuel Cell (DMFC), where liquid fuel was suggested to be more suitable for vehicle applications. During the 1970's many German, Japanese and US major vehicle manufactures experimented with the FCEV concept. In 1974 the first ever 'Hydrogen Economy Miami Energy Conference' took place; this being the first international conference which was solely based around hydrogen energy (New York State Energy Research and Development Authority 2005).

During the 1980's the US Navy utilised fuel cells in submarines due to their high efficiency, almost silent running and zero emissions benefits. In 1983, Ballard started researching fuel cells, with the intention to become a major player in the fuel cell industry. The Canadian company were predominantly working with NASA and were regarded as leading in the fuel cell industry. Also within this decade, substantial technical and commercial development was accomplished in the area of the Phosphoric Acid Fuel Cells (PAFC) (Johnson Matthey Plc 2013).

In 1990 GM (General Motors), Dow Chemical Company and Ballard Power Systems worked on a 10kW PEM (Proton Exchange Membrane) fuel cell due to the Matsunaga

CHAPTER 2 - Literature Review

Act which ensured consultation on and coordination of hydrogen research (New York State Energy Research and Development Authority 2005).

In 1992 Toyota started development on a fuel cell vehicle which took four years to develop to their first FCEV (Toyota Motor Corporation 2016).

In 1994 Daimler Benz demonstrated its first "NECAR 1" (New Electric CAR) fuel cell vehicle in Germany and in 1998 Iceland presented a plan to create the first hydrogen economy by 2030 with Daimler Benz and Ballard Power Systems.

In 1998 Hyundai started to establish their own fuel cell system (Hyundai Motor UK 2016).

In 1999, a consortium of Icelandic institutions partnered with Shell, DaimlerChrysler and Norsk Hydro to create the Icelandic Hydrogen and Fuel Cell Company Ltd. to further develop the hydrogen economy within Iceland (New York State Energy Research and Development Authority 2005). In 1999, Honda unveiled their first attempt at a Fuel Cell Electric Vehicle, named "FCX-V1" & "FCX-V2" (Honda 2008).

In the year 2000, Ballard attended and presented, at the Detroit Auto Show, the first PEM fuel cell which was production ready for automotive applications (New York State Energy Research and Development Authority 2005). "FCX-V3 development goes on at Honda and begins service as the official pace car of L.A. Marathon" (Honda 2008) and Hyundai present their FCV based on their Santa Fe vehicle (Hyundai Motor UK 2016).

In 2001 Microcab (UK) implemented a small fuel cell into its EV platform with the DTI funding whilst Toyota announced their "FCHV-3" FCV and improvements to their hydrogen tank design (Toyota Motor Corporation 2016).

In 2003 Honda showed development to their stacks which give operational temperatures as low as -20°C and becomes the world's first company to supply a fuel cell vehicle to a private corporation (Honda 2008).

In 2004 the German Navy implemented the world's first Fuel Cell powered Submarine and put the submarine through deep water trials (New York State Energy Research and Development Authority 2005).

In 2007 Fuel cells began to become commercial and PEM Fuel cells were sold, fitted as Auxiliary Power Units (APU) and stationary power units. Microcab continued its work into FCEV's and produced a fleet of 5 FCEV's at the University of Birmingham for a two-year trial within the university's campus.

Then in 2008, both Honda and Toyota came to lead the race in FCV's and began limited leasing for consumer use, with the "FCX Clarity" FCV (Honda 2008) and the "FCHV-adv" (Toyota Motor Corporation 2016).

In the 2010 a few demonstrator projects arose in which multiple small companies acquired government funding to manufacture, develop and demonstrate the implementation of fuel cells into vehicles. Many of these projects found difficulty in producing reliable FCEV's with a common problem of fuel cell reliability.

In 2013 Toyota released their concept vehicle the Mirai at the 2013 Tokyo Motor show prior to going on sale at the end of 2015 and Hyundai put their ix35 on sale as first hydrogen fuel cell vehicle. However, to date there are still government funded projects such as "SWARM" which is a European funded project consisting of H2o E-mobile, Riversimple and Microcab as fuel cell vehicle manufacturers (PLANET GbR 2013). The goal of projects like SWARM is to demonstrate fleets of vehicles with fuel cells fitted to help the movement towards hydrogen vehicle reliability and sustainability.

2.2 Review of Modelling and Simulation tools for Automotive Applications

This section looks at the most commonly used simulation tools for modelling both vehicle dynamics and EV's, to determine the most appropriate use of software to meet the objectives set out within section 1.3.

2.2.1 Advanced Vehicle Simulator

Advanced Vehicle Simulator (ADVISOR) has been developed by the National Renewable Energy Laboratory (NREL) since 1994 where the simulation tool was used by the U.S. Department of Energy (DOE) to help develop and understand Hybrid Electric Vehicles through the use of hybrid vehicle propulsion (Wipke et al. 1999). In 1999 NREL made the ADVISOR 2.0 tool available on the internet with a new graphical user interface, an exhaust after treatment model and with browser-based documentation. Since then Advisor has been updated a few times to include better electrical models and a fuel cell model. The tool uses the MATLAB/Simulink platform for its backward-facing calculation modelling approach. The drive cycle affects the vehicle, which in turn affects the wheel, the transmission and then the engine, all via transfer functions. ADVISOR, renamed, Systems Advisor Model (SAM) in 2010, uses a combination of differential equations and lookup tables based on test data to create the vehicle model, and using drop down boxes the user can select different components from existing vehicles from a database to create their own model and vehicle layout (NREL 2010). However, the addition of new components would require a large quantity of test data in order to achieve a high level of accuracy when comparing a vehicle or component which isn't in the database (Brooker et al. 2013).

2.2.2 AVL Cruise

AVL Cruise is defined as a real-time multi-disciplinary vehicle system simulation tool which uses a holistic modelling approach where the concept is that the whole model is defined more than merely the sum of the components (AVL LIST GmbH 2013). The simulation tool is typically used for powertrain and engine development. The tool uses test data of individual components to build up a systems model and can prove very accurate in the simulating of real vehicle scenarios. Although there is a large library supplied with the simulation tool, to implement a new component a large quantity of test data is required to gain the same level of accuracy within the simulations. AVL Cruise uses a gearbox as an example, and the following would be needed to create a component based model of the gearbox; transmission loss map at different speeds, loads and temperatures, requiring a large quantity of test data per component model.

The data is required for their matrix calculation method to be used. Therefore, due to the nature of the proposed full vehicle model it could prove difficult to acquire all the required test data to complete the model to the desired accuracy and within the scope of the project.

2.2.3 *Modelica*

“Modelica is a non-proprietary, object-oriented, equation based language to conveniently model complex physical systems.” (Modelica 2000-2013). Modelica consists of multiple pre-defined Libraries. Therefore, the software can prove extremely useful when investigating areas which are not the operator’s expertise as a base modelling approach can be established through investigating the given models. The software is also ‘Open Source’. This excludes the necessity of licences and reduces the overall cost of the project. The software is multi-domain and therefore, allows the interaction between different types of physics and, allowing the influence of heat on electrical circuits as well as heat on mechanical systems. Therefore, due to the nature of this project where a fuel cell will be simulated in a vehicle then, gas flow, electricity, heat and vibration, will all be required in the model and it is necessary to have a tool which is capable of this multi-physics environment. However, due to the nature of ‘Open Source’ programs it is unlikely that the software is validated for all modelling applications and technical support may not be readily available which could result in an unstable model.

2.2.4 *Modelica and Automotive*

Modelica’s standard library section consists of the following named sub-libraries; ‘Modelica’, ‘Vehicle Interfaces’, ‘Modelica Device Drivers’ and ‘Modelica Synchronous’ (Modelica 2000-2013). However, there are many other libraries which can be downloaded from their web site. Modelica provides details for many of their consultants with their areas of speciality, and Modelica can be used for; simulation of electric drives, prototype and testing, thermal, fluid, mechanics, electronics, power generation, robotics, control, electromagnetic, real-time modelling, vehicle dynamics, hardware-in-the-loop and battery modelling. (Modelica 2000-2013)

From the given list, it is possible to create almost any physical system within Modelica. However, research into each area would be necessary to create reliable models so that full integration of the pre-defined library models and their different domains could be validated. Furthermore, concerns stated in section 2.2.3 are still present with the use of Modelica as an option for the software tool.

2.2.5 *Object Orientated Modelling*

“Tools like Modelica and Dymola can be used to gain the accuracy of bond graph modelling” (Zupančič, and Sodja 2013), where a bond graph is a visual representation of a physical dynamic system. The benefit to using object orientated modelling tools, is that the approach does not require the same amount of in-depth knowledge of each individual sub-component, to that of a bond graph, this is due to the “truly reusable components” within object-orientated modelling tools like Modelica and Dymola. This provides the user with the ability to create a powerful model-based performance simulation tool by just defining the relationships as equations in the components, and then to connect those components in an identical manner to which the system is assembled. Therefore, the development of component based modelling for a complex system model can be carried out with ease, and can provide exceptional model versatility, allowing the model to be used for a variety of different test conditions (Hirano, Inoue, and Ota 2015).

2.2.6 *Dymola*

“The unique systems engineering capabilities of Dymola present new and revolutionary solutions for modelling and simulation as it is possible to simulate the dynamic behaviour and complex interactions between systems of many engineering fields, such as mechanical, electrical, thermodynamic, hydraulic, pneumatic, thermal and control systems.” (Dassult Systems 2002-2013). Dymola is built upon the Modelica platform. Therefore, Dymola can accomplish all that Modelica can and potentially more as the software package provides pre-validated models which can be used and built upon. The main benefit of Dymola over Modelica is that it consists of pre-defined and validated libraries. The software also allows for 3D representation modelling and, allowing the visual representation of what is being modelled can be extremely useful when simulating vehicle dynamics. Also, the general user interface is more user friendly, allowing for more key-board shortcuts and duplication of models is simply achieved as this can be rather strenuous in Modelica. This enables the user to create more complex models quicker and with fewer errors.

Areas of relevance in which Dymola have been used are shown below;

- Ceres Power use Dymola for fuel cell modelling
- Saab use Dymola for aircraft design and simulation
- Volvo use Dymola for model-based active safety systems

(Modelon 2012-2013)

- Lyonnaise des Eaux use Dymola for control build validation for dynamic testing

- PSA Peugeot Citroen use Dymola with Reqtify in support of embedded systems development
- Alstom use Dymola with Reqtify used to deliver a model driven engineering process
- Airbus use Dymola with Reqtify across all the software and hardware projects
- Formula one teams use Dymola to model the energy recovery systems used in 2012.

(Claytex 2010-2013)

2.2.7 Summary of Modelling and Simulation Tools

ADVISOR uses MATLAB/Simulink to simulate vehicle emissions and vehicle energy consumption. It achieves this using both lookup tables, and equation-based models to hold the characteristics of different sub-systems. The tool provides multiple models of different vehicle types, sub system models, and through using the provided sub-system models the ability to create your own vehicle model. The simulation uses a backwards modelling approach where the vehicle speed, in the time domain, is used to calculate the effect that is had on the vehicle (Markel et al. 2002). When simulating a vehicle model provided by ADVISOR, it can predict energy consumption to within 10% and fuel economy to within 19% of measured data on a standard drive cycle (Senger 1997) and (Markel et al. 2002). As previously stated in section 2.2.1, the ability to create your own sub-system is not present, so the user is limited by the sub-system models which come with the software to generate a vehicle model. Another limitation of the modelling tool is that deviations from a straight line, altitude and weather conditions are not taken into consideration in the simulation environment.

AVL Cruise uses MATLAB/Simulink to simulate vehicle emissions and vehicle energy consumption using complex lookup tables to characterise each vehicle component based on test data. The tool provides a large library of sub-system models and the ability to create your own sub-system model through using lookup tables. The simulation of the vehicle model uses the same approach as ADVISOR (Vock et al. 2014). When simulating a vehicle model provided by the tool, it can predict fuel consumption to within 9% of measured data on both a standard drive cycle and a specific real-world driving route (Vock et al. 2014). The route chosen to demonstrate the level of accuracy that this tool can provide was relatively 'straight and flat', so that similar conditions to dynamometer testing could be achieved (Vock et al. 2014). A limitation of the modelling tool is that deviations from a straight line, altitude and weather conditions are not taken into consideration in the simulation environment and

creating your own sub-system model is heavily dependent on test data to populate the lookup table approach.

Modelica is a custom open source modelling and simulation tool. There is no vehicle model provided by the software, but library models can be purchased. Models are generated through using an object-oriented approach that allows for multi-disciplinary systems to be modelled (Modelica 2000-2013). Where validated library models are not provided with the software, each component of the model would have to be fully analysed, developed and validated to create a representable vehicle model. Drogies, and Bauer (2000), show that good correlation of vehicle dynamic tests, such as double lane changes can be achieved using Modelica as a tool. Simic et al. (2014) show that the energy consumption of a vehicle can be predicted to within 1% of measured data on a standard drive cycle (Simic et al. 2014). A limitation of Modelica is where no vehicle simulation examples are provided, the generation of a forward-looking vehicle model would have to be created from the ground up (Drogies, and Bauer 2000) and each area of the model which is created would need to be validated against test data. Dymola is a commercial software package which is built on the Modelica programming language. There are many pre-defined validated library models supplied within the software ranging across multiple disciplines. The tool has a vehicle dynamics package where vehicles can be simulated in the 3-dimensional environment using virtual visualization of moving components. It has been established as “state of the art” in modelling for simulation vehicle dynamics and powertrain models (Thanheiser, Kohler, and Herzog 2012) and (Deuring, Gerl, and Wilhelm 2010). Dymola uses the same approach to simulating a vehicle as Modelica. Therefore, the accuracy which Dymola can achieve is equal to that of Modelica. However, the ability to create and develop a high-fidelity model is made easier by using the supplied pre-defined validated models. The ability to use the 3-dimensional virtual visualisation allows for more complex drive cycles that can incorporate deviations from a straight line and altitude to be simulated. This will allow for better prediction of energy consumption for real-world driving data (Bogosyan, Gokasan, and Goering 20017). The tool provides a solution to the limitations of the alternative tools and achieves this by providing validated models and the ability to simulate ground test manoeuvres in a multi-disciplinary environment, so that evaluation of both energy consumption and vehicle handling performance can be accomplished.

Dymola shows where it has been used within the automotive sector and how it could benefit this type of project. Dymola and Modelica have both been presented as valid software tools which could be utilised to create a working multi-disciplinary model. With full technical support being available for Dymola through a local agency, and the

availability of a comprehensive vehicle dynamics library, it was decided that the Dymola Software tool should be used for the project.

2.3 Vehicle Dynamic Modelling

2.3.1 Multibody Systems Modelling

MBS are used to solve problems related to MBS Analysis and have increasingly been used to analyse the ride and performance of all types of vehicles. MBS modelling is also frequently being used to identify highly non-linear systems such as large amplitude vibrational studies into powertrain components. For MBS tools, such as MSC ADAMS the model consists of code which defines force and joint relationships between points and, by defining the component the point belongs to, a shape can be generated for three-dimensional representation. From the assembly of components via joints and material properties it is possible to generate extremely versatile and complex vehicle systems models which can be used for a multitude of vehicle handling and performance scenarios. A typical model will consist of rigid parts, connecting joints, motion generators, forces and compliances. Each rigid part also requires the centre of gravity, component mass and the component's mass moments of inertia. The internal, external and joint relationships can be made so that components move only in respect to their constraints (Blundell, and Harty 2004). Currently there are 31 main simulation tools solely dedicated to multibody systems simulation which are listed in Table 2-1.

Table 2-1 - Multibody System Simulation Tool List

Software Name	Developer
ADAMS	MSC Software
Alaska	Technical University of Chemnitz
Autolev	OnLine Dynamics Inc
AutoSim	Mechanical Simulation Corp.
ALV Excite	AVL
CAMeL-View	IXtronics GmbH
Compamm	CEIT
Dynawiz	Concurrent Dynamics International
Hotint	Linz Center of Mechatronics
Hyperview	Altair Engineering
Motionview	Altair Engineering
Virtual Lab Motion	LMS
MapleSim	Maplesoft
Mecano	Samtech
MechDesigner	PSMotion

MBDyn	Politecnico do Milano
MBSOft	Universite Catholique de Louvain
Neweul	University of Stuttgart
RecurDyn	Function Bay In.
ReDySim	Indian Institute of Technology
RoboAnalyser	Indian Institute of Technology
Robotran	Uniersite Catholique de Louvain
SAM	Artas Engineering Software
SD/FAST	PTC
Simbody	Simbios
SimCreator	Realtime Technologies
SimMechanics	The Mathworks
SimPack	INTEC GmbH
Spacar	University of Twente
TRUE	True-World
Universal Mechanism	Bryansk State Technical University
Working Model	Knowledge Revolution

In Table 2-1, MSC ADAMS is the most widely used amongst the list of MBS simulation tools (McPhee 2014). Although, typically mathematical vehicle models have been used to determine ride and handling, MBS has taken over as it is the most common approach due to simplicity in building a model based on realistic connections and components. Another reason is that MBS simulation tools prove more versatile in adapting simulation scenarios so that the same model can be used to simulate a variety of different driving conditions. Another aspect which is very important in the software packages, is the implementation of tyre models. Many of the packages claim to provide some basic tyre models or at least the capability of computing the complex set differential equations to solve the highly nonlinear reaction of the tyre. Software packages such as MATLAB/Simulink, Modelica and Dymola have been left out of this list as their sole purpose is not to be used for MBS. However, since Modelica and Dymola are object-oriented based modelling they have the capability of acting as a MBS simulation tool due to their connector classes and modelling approach. This supports the decision made in Section 2.2.7 to use Dymola as the modelling software tool for this project.

2.3.2 Tyre Modelling

Due to the complex nature of vehicle systems dynamics it is deemed necessary to investigate tyre modelling, so that the appropriate choice of tyre model can be made.

The Fiala tyre model is a well-known tyre model which can be provided by MBS simulation tools such as MSC Adams, and it only requires 10 parameters to characterise the tyre (Fiala 1954). The mathematical approach to the model is well described by (Blundell, and Harty 2004). The main advantage to the Fiala model is the low number of parameters. However, the model is unable to represent combined braking and cornering forces, negative aligning moments, ignores the influence of camber and has a lack of lateral force offsets (Blundell 2004).

Due to the limitations of the Fiala model an empirical tyre model was developed, the “Harty tyre model” (Blundell 2004). The main features of the model are presented below (Blundell, and Harty 2007):

- Use of an empirical representation of tyre properties
- A simpler implementation than the Magic Formula
- Produces a more complete implementation than the Fiala tyre model
- Provides robustness for prolonged wheel spin and low grip conditions
- Can model comprehensive slip for combined cornering and braking
- Models the dependence of cornering stiffness on tyre load
- Includes camber thrust.

The given features of the Harty tyre model address the limitations of the Fiala model and claim to provide a rounded set of equations which is less complicated than the Magic Formula, in regard to tyre coefficients, and more robust than the Fiala model (Blundell, and Harty 2007).

The Pacejka tyre model is highly regarded for most automotive simulation applications and has been deemed state-of-the-art (Tsinias 2014). As such a more detailed treatment will now follow.

Between 1991 and to date there have been multiple publications produced showing the development of the renowned ‘Magic Tyre Formula’. However, it was in 1987 where a publication showed the efforts of a collaboration project involving Hans Pacejka, Egbert Bakker, Volvo Car Corp. and Delft University of Technology. This resulted in the Magic Tyre Formula where together they proposed a set of equations which accurately represented their measured data of steady state pure cornering and braking scenarios (Bakker et al. 1987). It was then in 1989 that the same group published a second paper in which they accomplished their goals set in their previous publication, where they incorporated the interaction between side and brake force to

extend to camber angle and positive longitudinal slip (Bakker, Pacejka, and Lidner 1989). The authors presented the first appearance of the Magic Tyre Formula, initially named 'The Tyre Formulae', as the given formulae in equations (1),(2) and (3). The representation of each equation and its relationship to a tyre can be seen by analysing Figure 2-2;

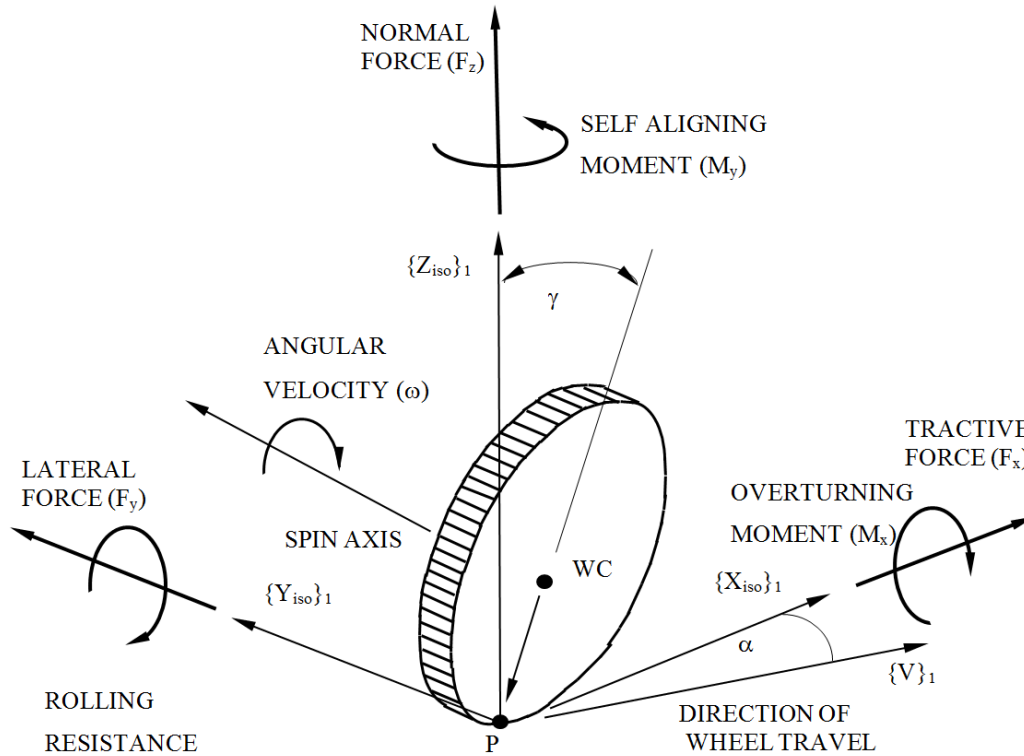


Figure 2-2 - ISO-W tyre axis system modified (Blundell, and Harty 2004)

When analysing Figure 2-2 of the ISO-W tyre axis system with the annotated Pacejka tyre force curve in Figure 2-3 and the definitions to equations (1)-(4), the way that the Magic Tyre Formula is used can be understood.

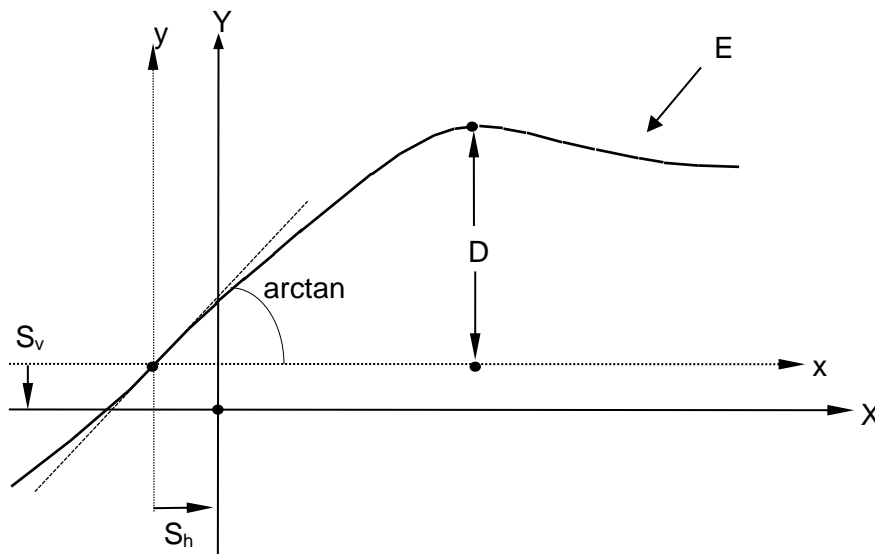


Figure 2-3 - Magic Tyre Formula Curve (Blundell, and Harty 2004)

CHAPTER 2 - Literature Review

$$Y(x) = D * \sin \left(C * \arctan * \left(Bx - E * \left(Bx * \left(\arctan(Bx) \right) \right) \right) \right) \quad (1)$$

$$Y(X) = y(x) + S_v \quad (2)$$

$$x = X + S_H \quad (3)$$

$$E = \frac{B * x - \tan \left(\frac{\pi}{2 * C} \right)}{B * x - \arctan(B * x)} \quad (4)$$

(Bakker, Pacejka, and Lidner 1989)

Where:

Y = *Either Side Force (F_y), Self Aligning Torque (M_y) or Brake Force (F_x)*

X = *Slip Angle (α) or Longitudinal Slip (γ)*

B = *Stiffness Factor*

C = *Shape Factor*

E = *Peak Factor*

S_v = *Vertical Shift*

S_H = *Horizontal Shift*

In 1991 Pacejka and Sharp published a review on the use of tyre models for vehicle dynamicists and tyre designers. The authors divide the report into sections regarding physically founded models, physically based models, analytic solutions and formula based models and empirical models. The authors state the importance of how each technique aids each other by either using correctional factors obtained from analytic solution to aid the empirical model or formula based models to create mechanical principles for physically based models (Pacejka, and Sharp 1991).

In 1992 Pacejka and Bakker continued their work and published a third paper presented "version 3" of the Magic Tyre Formula. It was here that the authors developed the model to contain a physically based formulation to avoid correction factors to the model (Pacejka, and Bakker 1992).

In 1997 Pacejka and Besselink presented the 'Delft Tyre 97' which was designed to simulate transient manoeuvres, when cornering on undulating road surfaces and for the analysis of oscillatory braking and steering. Within the 'Delft Tyre 97' model, the Magic Tyre Formula is used for steady-state pure slip and combined slip conditions, and presents another set of equations to determine relaxation lengths in respect to the wheel rim to represent the lag in the response to lateral and longitudinal slip (Pacejka, and Besselink 1997).

In 2002 which Pacejka wrote a comprehensive book called 'Tire and Vehicle Dynamics' providing in-depth knowledge of the tyre model (Pacejka 2002). The creation of this book enabled other researchers to continue in the development of the Magic Tyre Formula by providing researchers with a base understanding of how to develop a similar model. The book has since then been revised in 2006 (Pacejka 2006) and 2012 (Pacejka 2012). Between book publications Pacejka and other researchers continued

their work on tyre modelling and multiple publications were made in this time. However, a fairly large improvement to the model came in 2010 where Besselink, Schmeitz and Pacejka published a paper on another developed model called the MF-Swift (Magic Formula-Swift). The reason for this development is that the authors felt that The Netherlands Organisation for Applied Scientific Research (TNO) MF-Tyre 5.2 tyre model, based on the Delft tyre model (TNO Automotive 2008), had “reached its maturity” and required the implementation of tyre inflation pressure changes, tyre dynamics consistent between the MF-Swift and MF-Tyre and to improve the camber stiffness formulation to have better capabilities at large camber angles (Besselink, Schmeitz, and Pacejka 2010).

When analysing sources of literature in the public domain, in reference to vehicle dynamic studies, a clear pattern arises, stating the importance of tyre modelling and most vehicle dynamics books typically dedicate a chapter of the book to the modelling of tyre behaviour (Blundell, and Harty 2004) (Gillespie 1992).

2.3.3 Summary of Tyre Modelling Techniques

The Fiala model is a useful model where a low number of parameters are required to characteristic the tyre. However, there are limitations presented that would restrict the vehicle model’s ability to perform a range of simulations.

The Harty model also requires a low number of parameters to simulate the tyre characteristics and the latest version of the model requires only 13 parameters (Blundell, and Harty 2007). The model overcomes the limitations of the Fiala model and compares well to the Magic Formula regarding test data presented by (Blundell, and Harty 2007).

The Pacejka Magic Formula is the most established and is the most refined. However, over the years the development of the formula has resulted in a large increase of parameters and coefficients. The 1989 Magic formula has at least 50 parameters to represent the different tyre forces (Blundell, and Harty 2007) (Pacejka 2012).

If a pre-defined tyre model is not available within the software simulation choice, then Harty model proves to be the most appropriate tyre model method to use, due to its low parameter count and ability to represent a wide range of tyre forces. However, if Dymola provide a pre-defined validated Magic Formula tyre model which is of similar size and profile to that of the vehicle’s tyre which is being modelled, then the Magic Formula will be used. This is because a tyre testing facility is not presently available, so testing and curve fitting tyre test data to a model cannot be done within this project.

CHAPTER 2 - Literature Review

Due to these reasons and the availability of a tyre model dataset, the Magic Formula tyre model has been used in this study.

2.4 Battery Modelling

Over the past twenty-five years, several types of mathematical models have been developed by researchers and developers in order to predict the behaviour of batteries, dependant on a combination of external and internal conditions. It is also a well-known fact that the performance of batteries varies significantly from that of an ideal power source and that the manufacturing of batteries is yet to be perfected. Manufacturers state there can be a variation in battery internal resistance of up to 5% (Goodwolfe 2014). This can result in the requirement to measure the internal resistance of each cell prior to building any battery pack. Batteries are a highly non-linear electrochemical system and conditions which affect battery behaviour are shown below;

- **Internal conditions:** depth of discharge, state of health, impedance, chemistry, geometry, electrolyte concentration and electrode thickness
- **External conditions:** temperature, C-rate, short and long term history. (Barreras et al. 2012)

The purpose of this section is to determine the most appropriate method of modelling a battery to represent the main traction battery in the proposed vehicle model. Where this is a lithium ion phosphate battery, papers regarding this particular chemistry will be prioritised in the investigation.

Barreras, et al. (2012) present a datasheet-based modelling approach to lithium ion batteries and, from first appearance, this approach to modelling a cell seems most appealing as it does not require expensive and time consuming tests which require specialist equipment (Barreras et al. 2012). The model results show that it can create discharging resistance, charging resistance and open circuit voltage graphs which are validated against the author's models. However, when comparing the authors data with the Goodwolfe Energy LifePO4 'X2E 15Ah 40166' Cell data (Goodwolfe Energy 2012) the graphs clearly show that there is a difference in cell chemistry.

The first model proposed by Barreras et al. (2012) is a Thevenin equivalent circuit model, which is the simplest of three and can be seen in Figure 2-4.

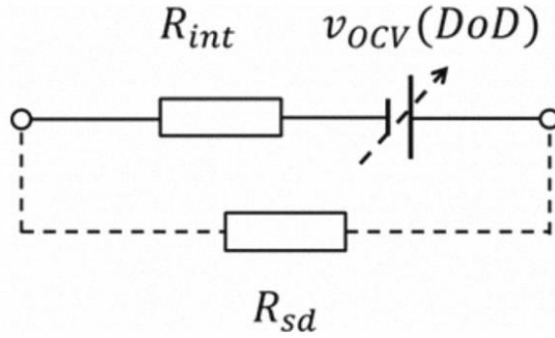


Figure 2-4 - Thevenin Equivalent Circuit Battery Model by (Barreras et al. 2012)

It uses a controlled voltage source and a series resistor to represent the internal resistance of the battery. The authors have suggested that a resistor could be put across the model to represent self discharge but that there would be difficulty establishing the value of that resistor as manufacturers do not usually disclose that information (Barreras et al. 2012). The mathematics which make the equivalent circuit model shown in Figure 2-4 are presented below:

$$V_{OCV(DoD)1} = V_{cha} * \left[1 - \frac{V_{cha} - V_{dis}}{V_{cha}} * \frac{\alpha * (1 - x)}{1 - (1 - \alpha) * (1 - x)} \right] \quad (5)$$

Where:

- $V_{OCV(DoD)1}$ = The open circuit voltage of the voltage source
- V_{cha} = The voltage of the battery when fully charged
- V_{dis} = The voltage of the battery when fully discharged
- α = The coefficient for the battery model
- x = The ratio of the actual available capacity divided by the total capacity
- R_{int} = The internal resistance of the battery
- R_{sd} = The resistance which characterises the self discharge rate

The given model accounts for the voltage drop at high depth of discharges only.

The authors then present an extended Thevenin equivalent circuit battery model which is shown in Figure 2-5.

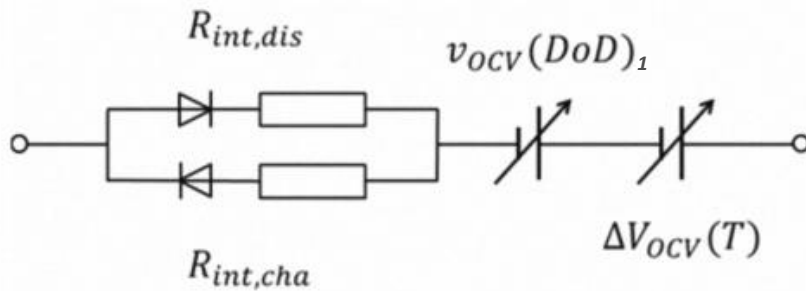


Figure 2-5 - Extended Thevenin Equivalent Circuit Battery Model by (Barreras et al. 2012)

The model uses a different internal resistance for discharge and charging of the battery and diodes have been added by the authors with a symbolic meaning to represent an IF statement which switches between the charge and discharge internal resistors. The authors have added an additional voltage source to represent a correctional voltage which changes based on temperature. However, the authors do not provide the

mathematics for the correctional voltage and states that the charge and discharge resistor values are a constant. The terminology used for Figure 2-5 is shown below:

Where:

- $V_{OCV(DoD)1}$ = The open circuit voltage of the voltage source
- $\Delta V_{OCV(T)}$ = The change in voltage at the battery due to temperature
- $R_{int,dis}$ = The internal resistance during discharge
- $R_{int,cha}$ = The internal resistance during charge

The model shows an interesting approach to how temperature could be considered, but where the mathematics are not provided it will not be useful to the project.

The last model which the authors present uses a further extended Thevenin equivalent circuit battery model, which considers the Peukert effect and Depth of Discharge (DOD) to create the internal charge/discharge resistance graphs. The authors used the same approach as their previous model. The authors have made the charge and discharge resistance variable dependant on depth of discharge and have removed the temperature correction voltage as seen in Figure 2-6 (Barreras et al. 2012).

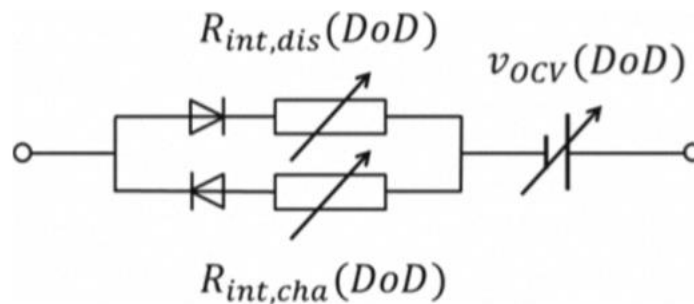


Figure 2-6 - Second Extended Thevenin Equivalent Circuit Battery Model by (Barreras et al. 2012)

The published model formulation is given below where;

$$k = \frac{\log(Q_x) - \log(Q_{1C})}{\log(I_{1C}) - \log(I_x)} + 1 \tag{6}$$

Where:

- k = The Peukert number
- Q_x = The capacity when discharged at a defined current
- Q_{1C} = The capacity when discharged at 1C
- I_{1C} = The current used to discharge at 1C
- I_x = The current used to discharge the battery during test Q_x

$$I_{equiv} = I_{1C} * \left(\frac{I}{I_{1C}}\right)^k \tag{7}$$

Where:

- I_{equiv} = The equivalent current drawn from the battery due to Peukert number
- I = The battery current

$$R_{int,dis} = \frac{v_{t,x1}}{(x_2 - x_1) * I_{1C}} - \frac{v_{t,x2}}{(x_2 - x_1) * I_{1C}} \tag{8}$$

Where:

- $R_{int,dis}$ = The internal discharge resistance of the battery
- $v_{t,x1}$ = The terminal voltage at the battery at DoD point 1 on the 1C datasheet
- $v_{t,x2}$ = The terminal voltage at the battery at DoD point 2 on the 1C datasheet

CHAPTER 2 - Literature Review

x_1 = The DoD point 1 on the 1C datasheet
 x_2 = The DoD point 2 on the 1C datasheet

This provides a fixed average internal resistance for battery discharge.

$$R_{int,cha} = \frac{V_{OCV} - v_t}{I} \quad (9)$$

Where:

$R_{int,cha}$ = The internal charge resistance of the battery for each point on the 1C datasheet
 V_{OCV} = The open circuit voltage of the battery
 v_t = The terminal voltage at the battery for each point on the 1C datasheet

$$v_{OCV(DoD)} = \begin{cases} v_{OCV(DoD)1} + R_{int,dis} * I_{equiv} & \left[\text{for } I_{equiv} \geq 0 \right] \\ v_{OCV(DoD)1} + R_{int,cha} * I_{equiv} & \left[\text{for } I_{equiv} < 0 \right] \end{cases} \quad (10)$$

Where:

$v_{OCV(DoD)}$ = The open circuit voltage of the battery

Here the authors have used the same $V_{OCV(DoD)}$ equation as the previous models but has modified the current due to the Peukert number. They suggest using a variable resistance which changes based on DOD but do not provide the equations that determine this. The authors suggest that by using equation (8)-(9) and datasheets from manufacturers that a variable resistance could be tabulated. When using equation (6) and the values provided by the author to calculate the Peukert number, the number generated is very small and is almost negligible. Where; $k = 0.996$, this changes the equivalent current by maximum 0.5% over the data provided by the authors, additionally if was $k = 1$ then it would have no effect on the equivalent current (Barreras et al. 2012).

Omar et al. (2013) state that lithium ion phosphate batteries typically have a low Peukert number of 1 and that the reduction of available capacity is only at the high DOD's and this is because at high DOD's the voltage falls away rapidly. However, It is still possible to access the capacity but not at the higher current values (Omar et al. 2013).

Jossen (2005) uses sets of differential equations to determine the dynamic response of batteries (Jossen 2005). The report focuses mostly on Nickel Metal Hydride (NiMH) batteries but it does briefly mention Li-ion polymer cells. The report uses differential equations to determine the State of Health (SOH) and State of Charge (SOC) of a battery cell. It does this by studying the physical effects of the battery such as, mass transport, electrochemical double layer and simple electrical effects. The report concludes that the dynamic response of batteries covers a wide frequency range from μHz to MHz and that the typical frequency range depends on the battery technology and the battery design. However, the report does not provide any equations to characterise the voltage of a battery.

Spotnitz (2005) highlights some major applications of battery modelling in the areas of performance and design in his paper 'Battery Modelling'. The authors describe

recent developments aimed at making modelling more accessible to battery developers and users (Spotnitz 2005). However, the paper does not consist of any physical equations or modelling techniques, rather it demonstrates the issues around battery modelling.

Zhang, and Chow (2010) initially present Shepherd's model which is the primary basis of the MATLAB/Simulink SimPowerSystems generic battery model. Shepherd's battery model is presented below (Shepherd 1965):

$$E = E_s - K * \left(\frac{Q}{Q - i_t} \right) * i + A * \exp(-B * Q^{-1} * i_t) - N * i \quad (11)$$

Where:

- E = The no load voltage
- E_s = The constant battery voltage
- K = The coefficient of polarization
- Q = The amount capacity of the battery in coulombs
- i_t = The current drawn from the battery in coulombs
- i = The battery current
- B = A constant parameter
- N = The internal resistance of the battery

The above equation shows the fundamentals of the MATLAB Simulink generic battery model created by Shepherd in 1965 (Shepherd 1965).

Zhang, and Chow (2010) state that the original Shepherd's model is too simple to determine dynamic battery behaviour and therefore, recommends impedance-based modelling which uses an equivalent circuit to represent the results of the battery impedance through the results of an electrochemical impedance spectroscopy test (Zhang, and Chow 2010). The fundamentals of this model are based on Randle's circuit model (Gould et al. 2009) shown in Figure 2-7.

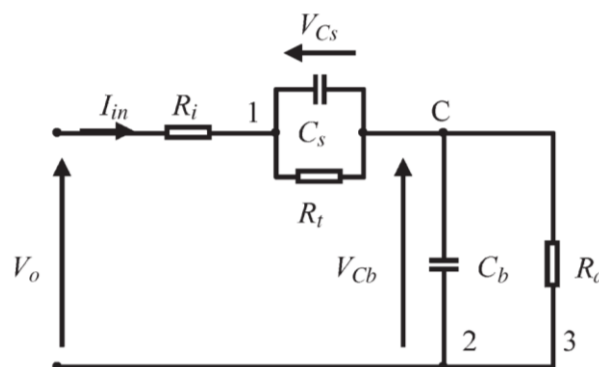


Figure 2-7 - Randles' Lead-Acid Equivalent Circuit Battery Model by (Gould et al. 2009)

Where:

- V_0 = The battery voltage
- I_{in} = The battery current
- R_i = The internal resistance of the battery
- V_{Cs} = The voltage drop due to the surface layer capacitance
- C_s = The surface capacitance
- R_t = The charge transfer resistance
- C_b = The capacity of the battery
- V_{Cb} = The open circuit voltage of the battery

R_d = The self discharge resistance

Zhang, and Chow (2010) improve upon this model, shown in Figure 2-7, and provide an image of their developed Randle's equivalent circuit battery model consisting of a variety of capacitors, resistors, power source and loads as shown in Figure 2-8 (Zhang, and Chow 2010). The rest of the report focuses on the error in the equations and the validation of his model.

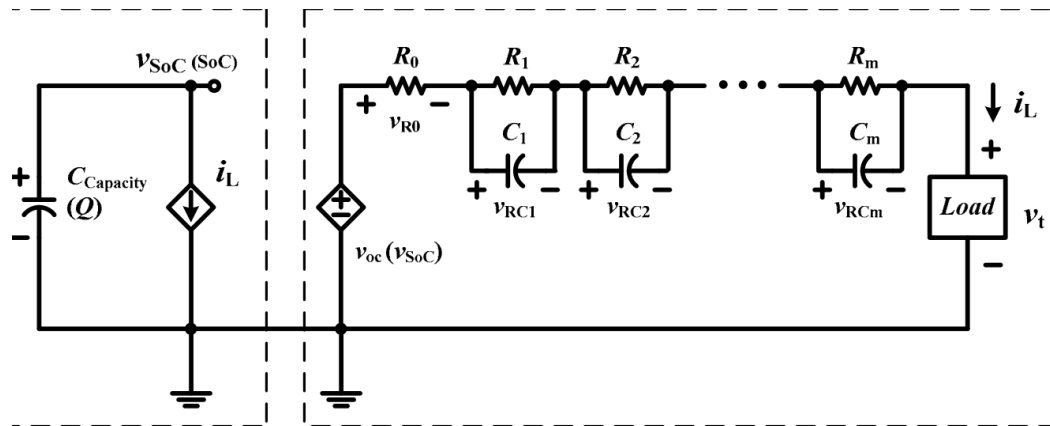


Figure 2-8 - Equivalent Circuit Battery Model by (Zhang, and Chow 2010)

Where:

- $C_{capacity}$ = The battery capacity
- V_{SoC} = The battery voltage due to change in SOC, the equation is not given
- i_l = The battery current
- V_{oc} = The battery open circuit voltage
- R_0 = The internal resistance of the battery
- R_1 = A resistance to model the battery relaxation effect
- C_1 = A capacitance to model the battery relaxation effect
- R_2 = A resistance to model the battery relaxation effect
- C_2 = A capacitance to model the battery relaxation effect
- R_m = A resistance to model the battery relaxation effect
- C_m = A capacitance to model the battery relaxation effect

The paper shows how some values from the parallel resistor and capacitor circuits can be estimated based on experimental results, typically pulse current tests. The authors adjust the values of the parallel resistor and capacitor circuits until the relaxation voltage error is reduced. The authors show that more parallel resistor circuits added to the equivalent circuit model provide better correlation to the test results, where 5 sets of circuits can reduce the error to 0.03% (Zhang, and Chow 2010).

Verbugge et al. (2009) presents the development of the FreedomCAR battery model through the process of testing a battery cell using the NREL test method within their paper, 'Modelling the RESS: Describing Electrical Parameters of Batteries and Electric Double-Layer Capacitors through Measurements' (Verbugge et al. 2009). The proposed FreedomCAR battery model is shown in Figure 2-9.

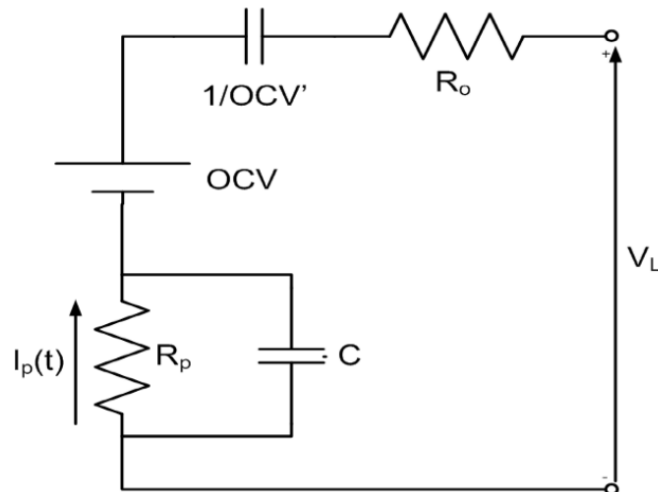


Figure 2-9 - FreedomCAR Battery Model by (Verbugge et al. 2009)

Where:

OCV = The ideal open circuit battery voltage

$1/OCV'$ = The capacitance that accounts for the change in OCV with the time integral of current

R_o = The internal resistance of the battery

R_p = The internal polarisation resistance

C = The shunt capacitance around R_p

$i_p(t)$ = The current through the polarisation resistance

V_L = The battery terminal voltage

This battery model shown in Figure 2-9 is based on the Thevenin battery model which has been discussed and shown in Figure 2-4. However, it incorporates a capacitance that accounts for the variation in open circuit voltage with the time integral of load current. It demonstrates how the combination of the Digatron test-facility and the Excels LINEST function can be used to estimate the parameters for the model to fit the test results (Verbugge et al. 2009).

The paper presented by (Gould et al. 2009) describes a novel battery model based on the previously described Randles' lead acid battery model in order to estimate SOH and SOC. The paper uses a similar method to that of the previously mentioned paper by (Verbugge et al. 2009), where the authors use expensive testing equipment so that subspace estimation can be accomplished to enable the model to converge. The difference between the proposed model and Randles' model is that the inductance effect of the double layered capacitor and resistor, is removed and put in series and then in parallel between the internal resistance and the negative of the battery. This difference can be seen between Figure 2-7 and Figure 2-10.

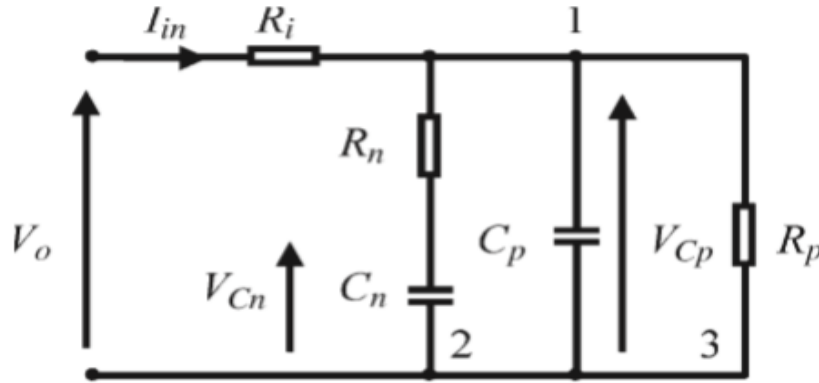


Figure 2-10 - Proposed Modified Randles' Lead-Acid Battery Model (Gould et al. 2009)

$$V_{C_n} = -\frac{V_{C_n}}{R_n * C_n} + \frac{V_{C_p}}{R_n * C_n} \quad (12)$$

$$V_{C_p} = \frac{V_{C_n}}{R_n * C_p} - \frac{V_{C_p}}{R_n * C_p} + \frac{I_{in}}{C_p} \quad (13)$$

$$V_0 = V_{C_p} + I_{in} * R_i \quad (14)$$

Where:

- V_{C_n} = The battery voltage due to battery state of charge
- V_{C_p} = The impedance based voltage due dynamic battery loads
- R_n = The linear battery resistance due to state of charge
- C_n = The capacitance to represent the capacity of the battery
- C_p = The capacitance to represent battery impedance
- R_p = The resistance to represent battery impedance
- I_{in} = The battery current
- V_0 = The battery terminal voltage
- R_i = The internal resistance of the battery

The proposed model is only suitable for lead acid batteries (Gould et al. 2009).

Chen, and Ricón- Mora (2006) present three typical types of battery models, these are; the Thevenin based model, An impedance based electrical model and a runtime based electrical model. Stating their accuracy and capabilities, the paper then proposes its own “accurate, intuitive and comprehensive model” (Chen, and Rincón-Mora 2006). The authors propose a model which consists of the Resistor and Capacitor (RC) configuration, similar to that of the Thevenin Model, to simulate the transient responses and then a capacitor and current-controlled current source is used from the runtime based models in order to simulate SOC and capacity. The paper concludes that the model supplies a 0.12% error for Lithium ion Phosphate batteries and that it is capable of capturing the entire dynamic characteristics of a battery, from nonlinear open-circuit voltage, current-temperature, cycle number and storage time-dependant capacity to transient response. The authors proposed model can be seen in Figure 2-11.

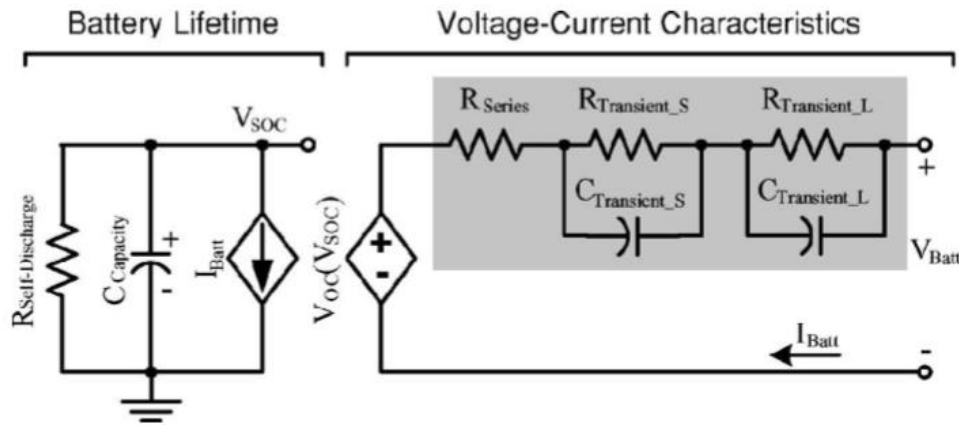


Figure 2-11 - Proposed Runtime and I-V Performance Battery Model (Chen, and Rincón-Mora 2006)

$$V_{OC(SOC)} = -1.031 * e^{-35 * SOC} + 3.685 + 0.2156 * SOC - 0.1178 * SOC^2 + 0.3201 * SOC^2 \quad (15)$$

$$R_{Series} = 0.1562 * e^{-24.37 * SOC} + 0.07446 \quad (16)$$

$$R_{Transient_S} = 0.3208 * e^{-29.14 * SOC} + 0.04669 \quad (17)$$

$$C_{Transient_S} = -752.9 * e^{-13.51 * SOC} + 703.6 \quad (18)$$

$$R_{Transient_L} = 6.603 * e^{-155.2 * SOC} + 0.04984 \quad (19)$$

$$C_{Transient_L} = -6056 * e^{-27.12 * SOC} + 4475 \quad (20)$$

Where:

- $V_{OC(SOC)}$ = The battery open circuit voltage due to battery state of charge
- SOC = The state of charge of the battery
- $C_{capacity}$ = The capacity of the battery
- R_{Series} = The varying internal resistance due to state of charge
- $R_{SelfDischarge}$ = The self discharge resistance
- $R_{Transient_S}$ = The resistance responsible for the short term voltage response during transients
- $C_{Transient_S}$ = The capacitance responsible for the short term voltage response during transients
- $R_{Transient_L}$ = The resistance responsible for the long term voltage response during transients
- $C_{Transient_L}$ = The capacitance responsible for the long term voltage response during transients

The values used in the proposed model by (Chen, and Rincón-Mora 2006) have been obtained through either the fitting of multi-variable functions or multi-dimensional lookup tables and hundreds of battery cycle tests at different temperatures. Therefore, although the model proves capable of representing lithium ion batteries to a high level of accuracy (0.4%), the requirement of extensive test data makes the model inappropriate for use within this project (Chen, and Rincón-Mora 2006). If the model was parametric and achievable through manufacturer datasheet parameters, then this would be a very useful model for automotive vehicle simulation.

Tremblay, Dessaint, and Dekkiche (2007) present the MATLAB/Simulink SimPowerSystems generic battery model. The paper goes through the process in which it creates the model and shows how it has developed the Shepherd's battery

model, by using it as the controlled voltage source and implements the given model into a full vehicle model to simulate battery SOC, Current, Voltage, Direct Current to Direct Current (DCDC) convertor duty cycle of the vehicle and Direct Current (DC) bus voltage. The model uses only three parameters to fit the equation and the paper validates the model for the following battery types; Lead-Acid, Lithium-Ion (Li-Ion), NiMH and Nickel-Cadmium (NiCd). Tremblay and Dessaint (2009) presented a developed version of their model, in a paper named 'Experimental Validation of a Battery Dynamic Model for Electric Vehicles', and they give a well-presented set of equations for creating discharge and charge models. It also provides the equations for Lead-Acid, Li-Ion, NiMH and NiCd batteries, therefore, the paper is very useful for making an EV model versatile so that the battery chemistry can be changed to see the total vehicle efficiency dependant on battery type (Tremblay, and Dessaint 2009). The authors present the assumptions that they have made to develop the model and they state that the internal resistance of the battery does not vary between charge and discharge. They state that the parameters for charging and discharging are equal, the capacity of the battery does not change with the amplitude of the current (No Peukert Effect, 100% columbic efficiency), the temperature does not affect the model, self-discharge is not included and the battery has no memory effect. The paper validates the model, stating the fact that the model can represent battery voltage to $\pm 5\%$ between 100% & 30% SOC and $\pm 10\%$ between 30% & 0% SOC for dynamic battery behaviour. This model is the latest, to date, MATLAB/Simulink SimPowerSystems battery model. The mathematics which are used for this model are presented below (Tremblay, and Dessaint 2009):

$$V_{dis,LeadAcid} = E_0 - R * i - K * \frac{Q}{Q - i_t} * (i_t + i_l) + \exp(t) \quad (21)$$

$$V_{char,LeadAcid} = E_0 - R * i - K * \frac{Q}{i_t - 0.1 * Q} * i_l + \exp(t) \quad (22)$$

$$V_{dis,LiIon} = E_0 - R * i - K * \frac{Q}{Q - i_t} * (i_t + i_l) + A * \exp(-B * i_t) \quad (23)$$

$$V_{char,LiIon} = E_0 - R * i - K * \frac{Q}{i_t - 0.1 * Q} * i_l - K * \frac{Q}{Q - i_t} * i_t + A * \exp(-B * i_t) \quad (24)$$

$$V_{dis,NiMH,NiCD} = E_0 - R * i - K * \frac{Q}{Q - i_t} * (i_t + i_l) + \exp(t) \quad (25)$$

$$V_{cha,NiMH,NiCD} = E_0 - R * i - K * \frac{Q}{|i_t| - 0.1 * Q} * i_l - K * \frac{Q}{Q - i_t} * i_t + \exp(t) \quad (26)$$

Where:

$V_{dis,LeadAcid}$ = The battery voltage for lead acid chemistry during discharge
 $V_{char,LeadAcid}$ = The battery voltage for lead acid chemistry during charge

$V_{dis,LiIon}$	= The battery voltage for lithium ion chemistry during discharge
$V_{char,LiIon}$	= The battery voltage for lithium ion chemistry during charge
$V_{dis,NiMH,NiCD}$	= The battery voltage for NiMH and NiCD chemistry during discharge
$V_{char,NiMH,NiCD}$	= The battery voltage for NiMH and NiCD chemistry during charge
NiMH	= Nickel Metal Hydride chemistry
NiCD	= Nickel Cadmium chemistry
E_0	= The battery constant voltage
R	= The internal resistance of the battery
i	= The battery current
K	= The polarisation constant
Q	= The battery capacity
i_f	= The filtered battery current
i_t	= The remaining battery capacity
t	= A coefficient for exponential zone voltage
A	= The exponential zone amplitude
B	= The exponential zone time constant inverse

When analysing the proposed model by (Tremblay, and Dessaint 2009) it is clear how the model is a developed Shepherd's battery model, except that, the authors have identified a clear set of equations to represent different cell chemistries via parameters. They have also managed to incorporate the exponential zone voltage dynamics at high state of charges for lithium ion battery chemistry, which is usually overlooked by other battery models.

The battery model presented by (Tremblay, and Dessaint 2009), shown as equations (21)-(26), which is a developed Shepherd's battery model has been released as the standard battery model for MATLAB/Simulink within the SimPowerSystems library and is the only model found which is capable of representing both the high and low exponential zone voltage dynamics.

The paper, 'Single Switched Capacitor Battery Balancing System Enhancements' by (Daowd et al. 2013), goes through the different types of battery balancing system which are available on the market with consumer batteries. It goes through the effectiveness of each balancing system respectively, providing balancing durations for cell variations of up to 11% and explains the problems with balancing specific cells such as Lithium ion phosphate where the voltage difference between 10% and 90% SOC is very low. It concludes that cell balancing is the key to prolonging battery life, safety and capacity of the battery pack. The paper demonstrates a novel control strategy for 'Single Switched Capacitor' battery balancing system which solves the 'flat voltage' problem described. It does this by maximising the energy transfer between the cells and the capacitor, and also manages to reduce the balancing time by 30% along with supplying a minimal voltage difference of 1 millivolt (mV). Although this paper is useful for a novel battery management system design, it is not useful in representing a typical battery management system for the type of battery models which have been discussed. As battery models tend to treat a battery as ideal, all cells within a battery pack have the same characteristics. Because of this, a simple load which is attached to a battery model which is characterised based on test data would be more useful.

2.4.1 Summary of Battery Modelling Techniques

From the review it is clear that most models are based on either Thevenin's circuit, Randle's circuit or Shepherd's model. Typically, Thevenin and Randle circuit models are equivalent circuit models using an open circuit voltage, resistors and capacitors to characterise a battery. Barreras, et al. (2012) shows an equivalent circuit model based on Thevenin's model which required both time consuming and expensive testing in order to achieve the parameters for characterising the battery model. The model shows the use of the Peukert effect to change the amount of capacity available from the battery but is not capable of representing the high exponential voltage zone dynamics. Omar et al. (2013) shows that the Peukert number for lithium ion phosphate batteries is typically 1. Zhang, and Chow (2010) present a Randle's based model which is capable of representing the relaxation voltage of a battery due to step current loads. The authors only validate to this step change in current and recommend electrochemical spectroscopy testing to determine the best parameters to use for the model. Verbugge et al. (2009) present a Randle's based model and the authors validate the model through the representation of battery voltage during step current loads. Characterisation of the voltage over the state of charge of the battery is not given. Gould et al. (2009) only provides equations for a lead-acid battery although they talk about lithium ion. Chen, and Rincón-Mora (2006) present a Thevenin circuit model which can achieve very good results at characterising a battery model. However, to gain the level of accuracy that the authors discuss requires performing "hundreds of battery cycle tests at different temperatures" (Chen, and Rincón-Mora 2006). Tremblay, and Dessaint (2009) present a refined Shepherd's battery model which can represent a battery's characteristics well, without the use of expensive or time-consuming testing. The model is capable of both high and low exponential voltage dynamics. The authors provide equations for a range of cell chemistries and validate the model's battery voltage to both step current load changes and continuous discharge curves. The model presented by Tremblay, and Dessaint (2009) is the 'Generic Battery Model' supplied by MATLAB/Simulink and does not consider the coulombic efficiency of the battery or the Peukert effect. From the review it is clear the (Tremblay, and Dessaint 2009) Shepherd's battery model is the most appropriate for the project, as the model can accurately represent both the high and low exponential zone dynamics of a lithium ion battery, and the limitation of not considering the coulombic efficiency of a battery cell is addressed in section 3.8.

2.5 Fuel Cell Modelling

This section will analyse the state-of-the-art fuel cell models to determine the most appropriate type for automotive application. It will analyse the usefulness of the papers and discuss the advantages and disadvantages of each type of modelling process.

Raga et al. (2014) discuss “a simple and precise PEM fuel cell black-box model” and develop on the model presented by (Raga et al. 2012). The authors model is shown in Figure 2-12.

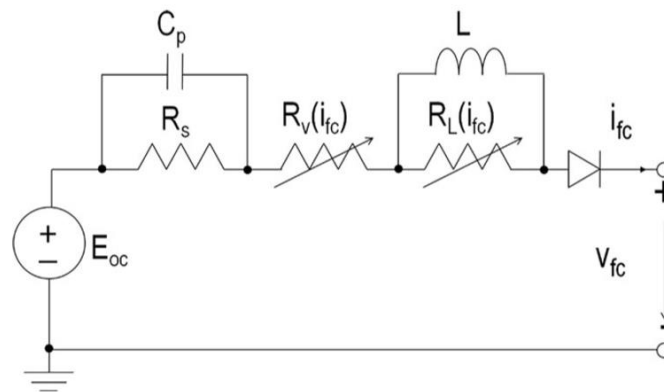


Figure 2-12 - Black-Box Fuel Cell Model By (Raga et al. 2014)

Where:

- E_{oc} = The fuel cell open circuit voltage
- R_s = The resistance for the static I – V curve
- $R_v(i_{fc})$ = The variable resistance for the static I – V curve
- $R_L(i_{fc})$ = The variable resistance for the dynamic voltage curve
- L = The inductance for the dynamic voltage curve
- C_p = The capacitance for the dynamic voltage curve

The electrical based model shown in Figure 2-12 consists of an open circuit voltage, three resistors, a capacitor and an inductor, along with a diode to model unidirectional power flow of the fuel cell. The author claims that their proposed “simplified model” is capable of providing an accurate V-I graph to an average of $\pm 2\%$ (Raga et al. 2014).

Souleman, Tremblay, and Dessaint (2009) present a generic fuel cell model which requires parameters solely available from the manufacturer’s datasheets. The paper makes use of combining chemical and electrical models to formulate the generic model. The model has been presented via MATLAB/Simulink and the authors provide a list of equations to enable the reader to formulate the model easily rather than having to refer to other papers. These equations are shown below: (Souleman, Tremblay, and Dessaint 2009).

$$E = E_{oc} - N * A * \ln\left(\frac{i_{fc}}{i_0}\right) * \frac{1}{sT_d/3 + 1} \quad (27)$$

$$V_{fc} = E - R_{ohm} * i_{fc} \quad (28)$$

CHAPTER 2 - Literature Review

Where:

- E_{oc} = The fuel cell open circuit voltage
- N = The number of cells in series
- A = The tafel slope
- i_0 = The exchange current
- T_d = The response time (at 95% of the final value)
- R_{ohm} = The internal resistance
- i_{fc} = The fuel cell current
- V_{fc} = The fuel cell voltage

The authors describe equation (27) and (28) as the “Simplified Fuel Cell Model” which can be used to represent fuel cells under ideal operating conditions. The authors then go on to describe the “Detailed Fuel Cell Model” as shown in the equations below (Souleman, Tremblay, and Dessaint 2009).

$$E_{oc} = K_c * E_n \quad (29)$$

$$i_0 = \frac{z * F * K * (P_{H_2} + P_{O_2})}{R * h} * \exp\left(\frac{-\Delta G}{R * T}\right) \quad (30)$$

$$A = \frac{R * T}{z * \alpha * F} \quad (31)$$

Where:

- R = The Universal gas constant, 8.3145
- F = The Faraday constant, 96485
- z = The number of moving electrons ($z = 2$)
- E_n = The nernst voltage
- α = The charge transfer coefficient
- P_{H_2} = The partial pressure of hydrogen inside the stack
- P_{O_2} = The partial pressure of oxygen inside the stack
- k = The Boltzmann's constant
- h = The Planck's constant
- ΔG = The activation energy barrier
- T = The temperature of operation
- K_c = The voltage constant at normal condition of operation

The authors describe the combination of equations (27)-(31) as the “Detailed Fuel Cell Model” which can be used to represent fuel cells under varying operating conditions. Where the main development to their “Simplified Fuel Cell Model” is to include variables rather than parameters. The model is accurate to $\pm 1\%$, however it also states that air pressure and temperature severely decrease the accuracy of the model in relation to voltage representation (Souleman, Tremblay, and Dessaint 2009).

Boscaino et al. (2013) present an empirical fuel cell modelling approach and validate it with the use of their experimental results from a 5 kW Nuvera PowerFlow PEM fuel cell. The author presents the model with a total of 5 parameters, however the parameters are not well described, and the coefficients are not explained to the sensitivity of the model. Therefore, it would be difficult to adjust the parameters to suit that of different fuel cells, although it is stated that the model is capable of providing accuracy to an impressive 0.4 V, which is a $\pm 1.2\%$ error, it could prove difficult to gain this level of accuracy for fuel cells when data for curve fitting the result isn't available (Boscaino et al. 2013). The authors simplify the fuel cell characteristics into one

equation and uses curve fitting to determine the values. The authors equation is shown below. The authors provide some values for the parameters, but do not explain them.

$$V_{FC} = A - B * \ln\left(1 + \frac{i_{fc}}{C}\right) - D * e^{\frac{i_{fc}}{E}} \quad (32)$$

Where:

V_{FC} = The fuel cell voltage
 i_{fc} = The fuel cell current
 A = 35.61 V
 B = 4.844 V
 C = 50.3425 A
 D = 821.7721_{x10⁻⁹} V
 E = 13.083 A

(Boscaino et al. 2013)

Benchouia et al. (2013) present a mathematical model to simulate steady-state and transient phenomena in a PEM fuel cell. The authors present their mathematical approach to solving the PEM fuel cell model, and they provide a written description for each equation. Each parameter is documented and provided with units to ensure fewer errors are made during replication of results. However, the authors do not provide a level of accuracy for their model but do state that the predicted results are in good agreement with their experimental results. The equations used are presented below (Benchouia et al. 2013):

$$E_{cell} = 1.229 - 0.85_{x10^{-3}} * (T - 298.15) + 4.3085_{x10^{-5}} * T \quad (33)$$

$$* (\ln P_{H_2} + 0.5 * \ln P_{O_2})$$

Where:

E_{cell} = The nernst cell voltage
 T = The temperature in kelvin
 P_{H_2} = The partial pressure of hydrogen in atm
 P_{O_2} = The partial pressure of oxygen in atm

$$V_{cell} = E_{cell} - losses \quad (34)$$

Where:

V_{cell} = The cell voltage
 $losses$ = The activation loss, resistive loss and diffusion losses

$$\eta_{act} = \xi_1 + \xi_2 * T + \xi_3 * T * \ln(CO_2) + \xi_4 * T * \ln(I) \quad (35)$$

$$CO_2 = \frac{P_{O_2}}{5.08_{x10^6} * \exp^{(-498/T)}} \quad (36)$$

Where:

η_{act} = The activation loss
 ξ_1 = The first parametric coefficient
 ξ_2 = The second parametric coefficient
 ξ_3 = The third parametric coefficient
 ξ_4 = The fourth parametric coefficient
 I = The fuel cell current
 CO_2 = The concentration of oxygen in the cathode

$$\eta_{ohm} = I * (R_m + R_c) \quad (37)$$

$$R_m = \frac{\rho_m * l}{A} \quad (38)$$

$$\rho_m = \frac{181.6 * [1 + 0.03 * (I/A) + 0.062 * (T/303)^2 * (I/A)^{2.5}]}{[\psi - 0.634 - 3 * (I/A)] * \exp^{4.18*((T-303)/T)}} \quad (39)$$

Where:

- η_{ohm} = *The ohmic polarization loss*
- R_m = *The equivalent resistance of the electron flow*
- R_c = *The proton resistance*
- ρ_m = *The specific resistance of the membrane*
- A = *The active area of the membrane*
- l = *The thicknes of the membrane*
- ψ = *The temperature correction factor*

$$\eta_{con} = -B * \ln(1 - (I/I_{lim})) \quad (40)$$

Where:

- η_{con} = *The concentration polarization loss*
- B = *The concentration resistance*
- I_{lim} = *The current density of the cell*

$$losses = \eta_{act} + \eta_{ohm} + \eta_{con} \quad (41)$$

$$V_{stack} = N_{cell} * V_{cell} \quad (42)$$

Where:

- V_{stack} = *The fuel cell stack voltage*
- N_{cell} = *The number of cells in the fuel cell stack*

(Benchouia et al. 2013)

The authors state that the parameters used for validating the fuel cell model above have been obtained via experimental results and curve fitting. The authors have taken steps to characterise the effects of the molar flow of hydrogen and the pressures in both the anode and cathode (Benchouia et al. 2013).

Feroldi, and Basualdo (2012) provide an overview of fuel cells, thus giving the reader an in-depth knowledge of the assembly of the stack and components within a fuel cell stack. The authors move on to explain the structure of the fuel cell, along with the advantages and disadvantages of the technology, thus giving the user a level of base knowledge about PEM fuel cell chemistry. The paper establishes equations used to build a complete model of a water cooled fuel cell along with equations related to auxiliary equipment within the system all based on a model widely used in literature. However, the main focus of the paper is orientated around the efficiency of the fuel cell and attempt to determine the optimum operational point of the fuel cell which they have modelled (Feroldi, and Basualdo 2012).

Wang, Nehrir, and Shaw (2005) present a dynamic PEM fuel cell model developed for MATLAB/Simulink. The authors have provided a nomenclature to their model. Although there are several subscripts and symbols within the equations which are not defined, and this limits the replication of the model by a reader. However, the authors do provide commentary for each part of the model and the inclusion of a few electrical model parameters. This paper includes equations related to fuel cell temperature rise and models this by “using the net heat generated by the chemical reaction, electrical

potential, sensible and latent heat absorbed, and heat losses transferred by convection” (Wang, Nehrir, and Shaw 2005). The authors state that the model results “agree well with the measured data”, however, an average accuracy of the model over the tests performed is not present (Wang, Nehrir, and Shaw 2005).

Ural, and Gencoglu (2010) show and analyse various mathematical models of PEM fuel cells. The following types of PEM fuel cell models have been discussed by Ural, and Gencoglu, and their equations to the models are presented below:

- The “dynamic model” (Ural, and Gencoglu 2010)

$$\tau_{H_2} = \frac{V_{an}}{k_{H_2} * R * T} \quad (43)$$

$$p_{H_2O} = \frac{\sqrt{M_{H_2O} * q_{H_2O}}}{k_{an}} \quad (44)$$

$$k_{H_2} = \frac{k_{an}}{\sqrt{M_{H_2}}} \quad (45)$$

$$p_{H_2} = \frac{1/k_{H_2}}{1 + \tau_{H_2}} * (q_{H_2}^{in} - 2 * K_r * I_{FC}) \quad (46)$$

Where:

- τ_{H_2} = The hydrogen time constant
- V_{an} = The volume of the anode
- k_{H_2} = The hydrogen valve molar constant
- R = The universal gas constant
- T = The fuel cell temperature in kelvin
- p_{H_2O} = The oxygen partial pressure inside the stack
- M_{H_2O} = The molar mass of oxygen
- q_{H_2O} = The molar flow of oxygen
- k_{an} = The anode valve constant
- k_{H_2} = The hydrogen valve molar constant
- M_{H_2} = The molar mass of hydrogen
- p_{H_2} = The hydrogen partial pressure inside the stack
- $q_{H_2}^{in}$ = The hydrogen input molar flow
- K_r = A modelling constant
- I_{FC} = The fuel cell stack current

$$E = N * \left[E_0 + \frac{R * T}{2 * F} * \log \left(\frac{p_{H_2} * p_{O_2}^{0.5}}{p_{H_2O}} \right) \right] \quad (47)$$

Where:

- E = The nernst instantaneous voltage
- E_0 = The open circuit voltage
- F = The Faraday constant
- p_{O_2} = The molar flow of oxygen

$$\eta_{ohmic} = -R_{int} * I_{FC} \quad (48)$$

$$\eta_{act} = -B * \ln(C * I_{FC}) \quad (49)$$

$$V_{cell} = E + \eta_{ohmic} + \eta_{act} \quad (50)$$

Where:

- η_{ohmic} = The ohmic over voltage
- R_{int} = The sum of electric and protonic resistance
- η_{act} = The activation over voltage
- B = A constant to simulate the activation over voltage
- C = A constant to simulate the activation over voltage
- V_{cell} = The DC output cell voltage of the fuel cell system

The given dynamic model assumes constant temperature and oxygen concentration but it does incorporate the relationship between hydrogen flow and fuel cell stack current.

- Basic Electrochemical and Electrical models
 - The “steady state model” (Ural, and Gencoglu 2010)

$$E_{rev} = \frac{-\Delta G}{2 * F} + \frac{R * T}{2 * F} * \ln \left(\frac{\alpha_{H_2} * \sqrt{\alpha_{O_2}}}{\alpha_{H_2O}} \right) \quad (51)$$

Where:

- E_{rev} = The reversible voltage
- ΔG = The size of the activation barrier
- α_{H_2} = The charge transfer coefficient of hydrogen
- α_{O_2} = The charge transfer coefficient of hydrogen
- α_{H_2O} = The charge transfer coefficient of water

$$\eta_{act} = -A * \ln \left(\frac{I_{FC}}{I_0} \right) \quad (52)$$

$$\eta_l = B * \ln \left(\frac{I_{FC}}{I_l} \right) \quad (53)$$

Where:

- η_{act} = The revised activation over voltage
- A = The activation polarization constant
- I_0 = The exchange current
- η_l = The concentration losses
- B = The concentration polarization constant
- I_l = The maximum current production of the fuel cell

$$V_{FC} = E_{rev} + \eta_{act} + \eta_{ohmic} + \eta_l \quad (54)$$

Where:

- V_{FC} = The fuel cell voltage

The “steady state model” uses the same η_{ohmic} as the previously described dynamic model but includes characterisation of the concentration losses by adding η_l and modifying effectively what was the Nernst voltage (Ural, and Gencoglu 2010).

- The “large-signal model” is shown in Figure 2-13 (Ural, and Gencoglu 2010)

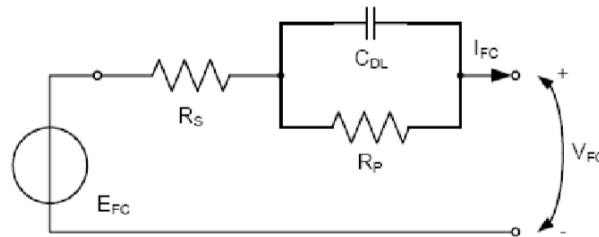


Figure 2-13 - Large Signal Fuel Cell Model by (Ural, and Gencoglu 2010)

Where:

- E_{FC} = The open circuit voltage of the fuel cell
- R_S = The series resistance for static IV representation
- R_P = The parallel resistance across the capacitor for dynamic response
- C_{DL} = The capacitor to represent a charged double layer capacitor response

The “large signal model” by Ural, and Gencoglu use two resistors and a capacitor to represent the fuel cell dynamics based on current drawn from the fuel cell stack, the majority of the dynamics are caused by the double layer capacitor which represents the capacitance of the anode and cathode which is separated by the membrane (Ural, and Gencoglu 2010).

- The “small-signal model” is shown in Figure 2-14 (Ural, and Gencoglu 2010)

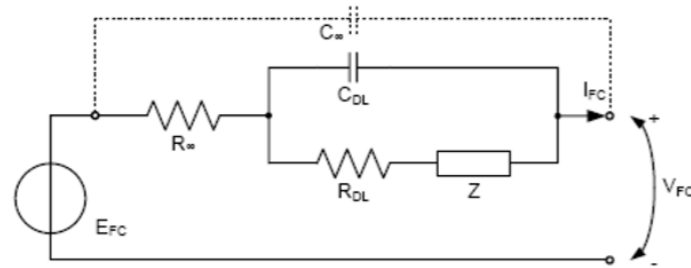


Figure 2-14 - Small-Signal Fuel Cell Model by (Ural, and Gencoglu 2010)

Where:

- E_{FC} = The open circuit voltage of the fuel cell
- R_{∞} = The series resistance for static IV representation
- R_{DL} = The parallel resistance across the capacitor for dynamic response
- C_{∞} = The capacitor to represent geometrical capacitance
- Z = An unspecified impedance

The “small-signal” model by Ural, and Gencoglu has built on their “large-signal model” to include fuel cell impedance characterisation and they have added geometrical capacitance to improve representation of the fuel cell (Ural, and Gencoglu 2010).

- MATLAB/Simulink
 - The “simplified model” is shown in Figure 2-15 (Ural, and Gencoglu 2010)

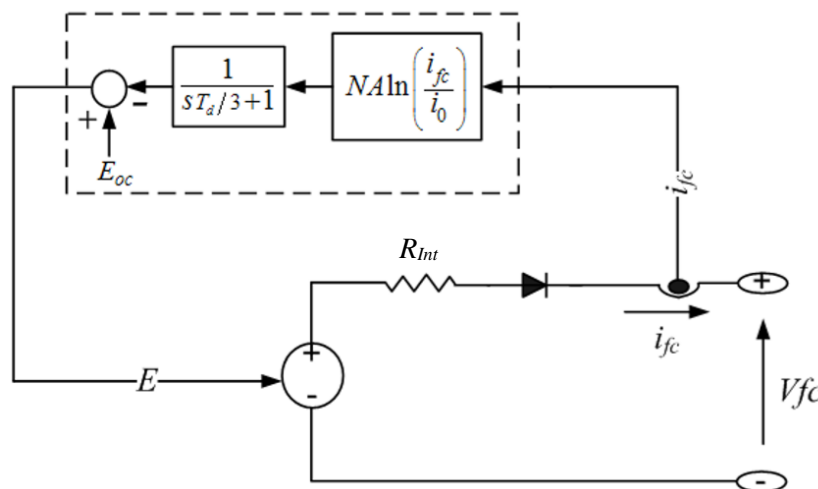


Figure 2-15 - Simplified MATLAB/Simulink Fuel Cell Model by (Ural, and Gencoglu 2010)

Where:

- E_{oc} = The open circuit voltage of the fuel cell
- E = The nernst instantaneous voltage
- T_d = The time constant for representing the capacitance of the fuel cell
- N = The number of cells in the fuel cell stack
- A = The activation polarization constant
- i_{fc} = The fuel cell current
- i_0 = The exchange current
- R_{int} = The sum of electric and protonic resistance
- V_{fc} = The fuel cell stack voltage

The “simplified model” by Ural and Gencoglu shown in Figure 2-15 represents a fuel cell running under ideal operating conditions. It uses a transfer function and an equivalent feedback circuit to represent the fuel cell stack voltage (Ural, and Gencoglu 2010).

- The “detailed model” shown in Figure 2-16 (Ural, and Gencoglu 2010)

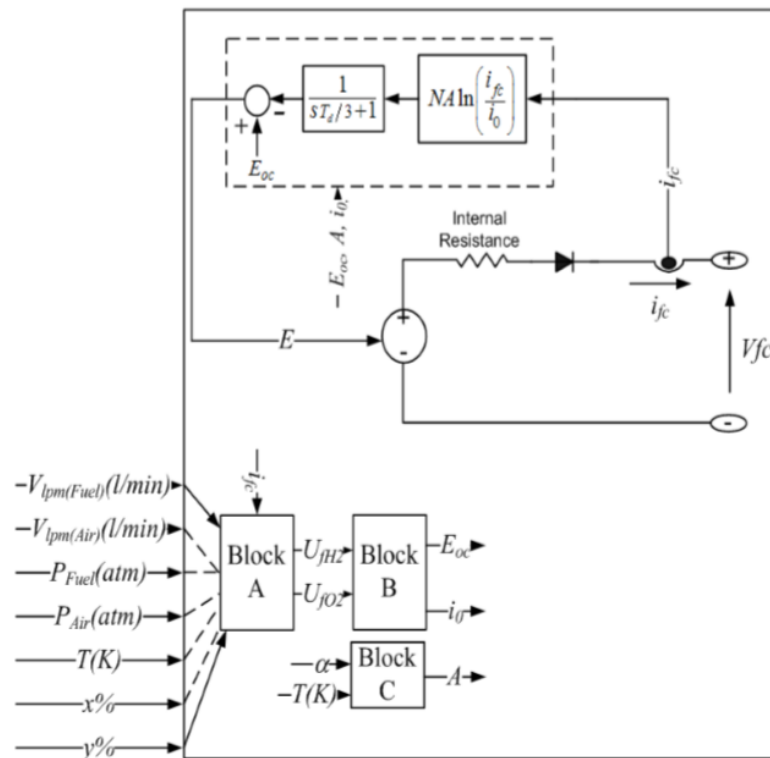


Figure 2-16 - Detailed Fuel Cell Model by (Ural, and Gencoglu 2010)

The “detailed model” consists of 14 equations which develop the “simplified fuel cell model” so that pressure, temperature, composition and flow rate of the fuel and air can vary. This ensures better representation of the fuel cell can be made whilst running under wider operating conditions (Ural, and Gencoglu 2010). The equations that constitute the “detailed model” are shown below:

$$U_{fH_2} = \frac{60000 * R * T * N * I_{fc}}{Z * F * p_{fuel} * V_{lpm(fuel)} * X_{\%}} \quad (55)$$

$$U_{fO_2} = \frac{60000 * R * T * N * I_{fc}}{Z * F * p_{air} * V_{lpm(air)} * Y_{\%}} \quad (56)$$

Where:

- U_{fH_2} = The rate of hydrogen conversion
- R = The universal gas constant
- T = The fuel cell temperature in kelvin
- N = The number of cells within the fuel cell stack
- I_{fc} = The fuel cell current
- Z = The number of moving electrons
- F = The Faraday constant
- p_{fuel} = The absolute supply pressure of fuel
- $V_{lpm(fuel)}$ = The fuel flow rate
- $X_{\%}$ = The percentage of hydrogen in the fuel
- p_{air} = The absolute supply pressure of air
- $V_{lpm(air)}$ = The air flow rate
- $Y_{\%}$ = The percentage of hydrogen in the fuel

$$p_{H_2} = (1 - U_{fH_2}) * X_{\%} * p_{fuel} \quad (57)$$

$$p_{O_2} = (1 - U_{fO_2}) * Y_{\%} * p_{air} \quad (58)$$

$$p_{H_2O} = (W + 2 * Y_{\%} * U_{fO_2}) * p_{air} \quad (59)$$

Where:

- p_{H_2} = The hydrogen partial pressure inside the stack
- p_{O_2} = The oxygen partial pressure inside the stack
- p_{H_2O} = The partial pressure of water vapour inside the stack
- W = The percentage of water vapour in the oxidant

$$E_{n1} = \begin{cases} 1.229 + (T - 298) * \frac{-44.43}{Z * F} * \frac{R * T}{Z * F} * \ln(p_{H_2} * p_{O_2}^{0.5}) & \left[\begin{array}{l} \text{for } T \leq 100 \\ \text{for } T > 100 \end{array} \right] \\ 1.229 + (T - 298) * \frac{-44.43}{Z * F} * \frac{R * T}{Z * F} * \ln\left(\frac{p_{H_2} * p_{O_2}^{0.5}}{p_{H_2O}}\right) \end{cases} \quad (60)$$

Where:

- E_{n1} = The nernst voltage of the fuel cell

$$V_{lpm(air)nom} = \frac{60000 * R * T_{nom} * N * I_{nom}}{2 * Z * F * p_{air} * 0.5 * 0.21} \quad (61)$$

$$U_{fH_2nom} = \frac{\eta_{nom} * \Delta h^{\circ}(H_2O_{gas}) * N}{Z * F * V_{nom}} \quad (62)$$

$$U_{fO_2nom} = \frac{60000 * R * T_{nom} * N * I_{nom}}{2 * Z * F * p_{air} * V_{lpm(air)nom} * 0.21 * X_{\%}} \quad (63)$$

Where:

- $V_{lpm(air)nom}$ = The nominal air flow rate of air
- T_{nom} = The nominal stack temperature
- I_{nom} = The nominal stack current
- U_{fH_2nom} = The nominal hydrogen utilization
- $\Delta h^{\circ}(H_2O_{gas})$ = Gibbs free energy, 241.83_{x10^3} J/mol
- V_{nom} = The nominal voltage of the fuel cell
- U_{fO_2nom} = The nominal oxygen utilization

$$K = \frac{V_u}{K_c * (U_{fO_2peak} - U_{fO_2nom})} \quad (64)$$

$$E_n = \begin{cases} E_{n1} - K * (U_{fO_2} - U_{fO_2nom}) & \left[\begin{array}{l} \text{for } U_{fO_2} > U_{fO_2nom} \\ \text{for } U_{fO_2} \leq U_{fO_2nom} \end{array} \right] \\ E_{n1} \end{cases} \quad (65)$$

$$E_{OC} = K_c * E_n \quad (66)$$

Where:

- K = *The voltage undershoot constant*
- V_u = *The voltage undershoot coefficient*
- K_c = *The voltage constant at the normal operating condition*
- U_{fH_2peak} = *The maximum hydrogen utilization*
- E_n = *The nernst voltage of the fuel cell*
- E_{OC} = *The open circuit voltage of the fuel cell*

$$i_0 = \frac{Z * F * k * (p_{H_2} + p_{O_2})}{R * h} * e^{\frac{-\Delta G}{R * T}} \quad (67)$$

$$A = \frac{R * T}{Z * F} \quad (68)$$

Where:

- ΔG = *The size of the activation barrier*
- h = *Planck's constant*
- A = *The activation polarization constant*

The authors present the difficulties they encountered when recreating the models in terms of assumptions, when information was not present and state what causes the dynamics of each model. Therefore, due to the clear assumptions which the authors provide, the paper will assist in the recreation of a fuel cell model when unknown information from other papers may not clearly be explained (Ural, and Gencoglu 2010). Alongside the fuel cell modelling another area of importance is the DCDC modelling. A DCDC convertor is usually used to convert the input voltage to the correct output voltage of a device. Therefore, a DCDC convertor will sit in between a fuel cell and a battery so the fuel cell voltage can be converted to the correct voltage at the battery, this will also provide the ability to control the current from the fuel cell and reduce dynamic current loading of the fuel cell.

'Control Design Techniques in Power Electronic Devices' by Sira-Ramirez and Silva-Ortigoza (2006) show multiple techniques and control theories which prove relevant to the design of switched power electronic convertors. The book shows multiple circuit diagrams, schematics and closed-loop systems. The authors focus the majority of their modelling around first principles from the circuit diagrams they provide. (Sira-Ramirez, and Silva-Ortigoza 2006).

This trend for DCDC convertor modelling methodology was started with a tutorial published by (Forsyth, and Mollov 1998) where they show schematics of DCDC convertors and use first principles to depict an averaging DCDC convertor model. They do this by drawing two circuit diagrams of the DCDC convertor, one where the transistor state is 'on' and the other while the transistor state is 'off' as shown in Figure 2-17.

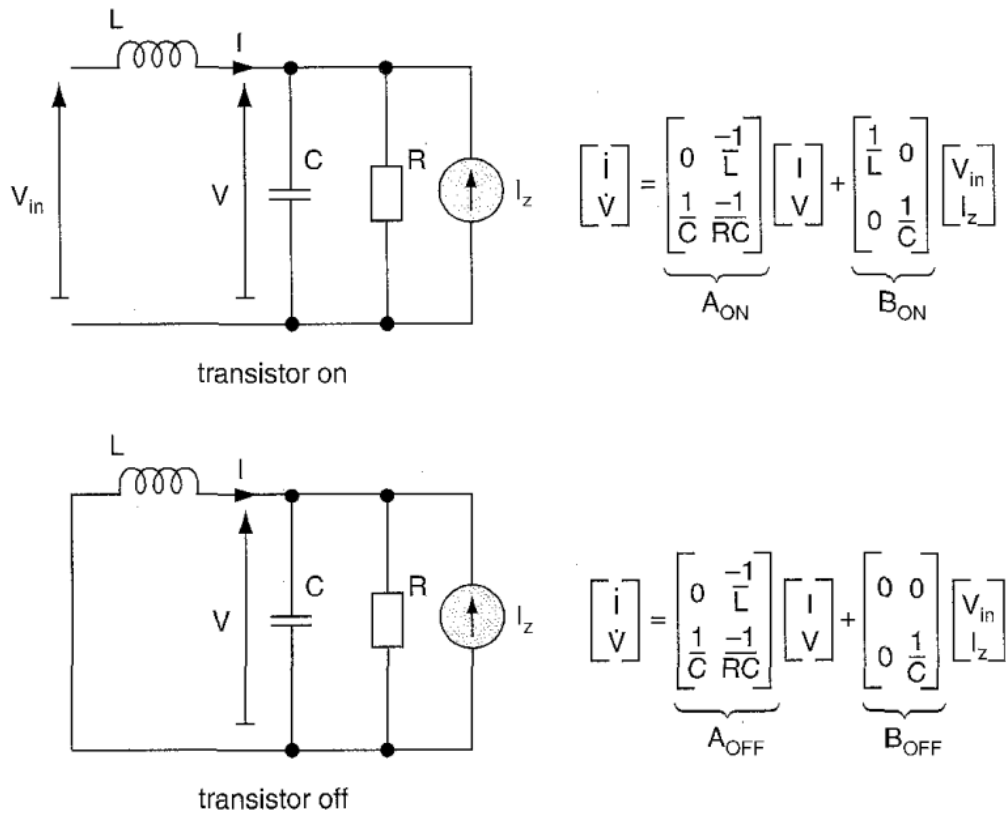


Figure 2-17 - DCDC Converter Configurations by (Forsyth, and Mollov 1998)

Using Figure 2-17 the averaging DCDC Converter model can be formulated: (Forsyth, and Mollov 1998)

$$\dot{x} = Ax + Bu \tag{69}$$

Where:

x = Is either the inductor current or the capacitor voltage
 u = Is either the input voltage or the output current

$$A = d * A_{ON} + (1 - d) * A_{OFF} \tag{70}$$

Where:

d = Is the transistor state (0 – 1)

$$A = \begin{bmatrix} 0 & \frac{-1}{L} \\ \frac{1}{C} & \frac{-1}{R * C} \end{bmatrix} \tag{71}$$

Where:

L = Is the inductance of the inductor
 C = Is the capacitance of the capacitor
 R = Is the resistance of the resistor

$$B = \begin{bmatrix} \frac{d}{L} & 0 \\ 0 & \frac{1}{C} \end{bmatrix} \tag{72}$$

Where:

L = Is the inductance of the inductor
 C = Is the capacitance of the capacitor

R = Is the resistance of the resistor

The above methodology and model formulation by (Forsyth, and Mollov 1998) shows how to create a DCDC Buck Converter model using first principles, which is the same approach used by (Sira-Ramirez, and Silva-Ortigoza 2006), (Dizqah, Busawon, and Fritzon 2012) and (Pop, and Lungu 2010). After contacting the designer of the DCDC converter which is to be modelled, he agreed that the most appropriate modelling methodology to represent the DCDC converter in question is by using first principles, just as (Sira-Ramirez, and Silva-Ortigoza 2006) demonstrated in the publication by Springer and to use the schematic shown in Figure 2-18 (Aston 2015).

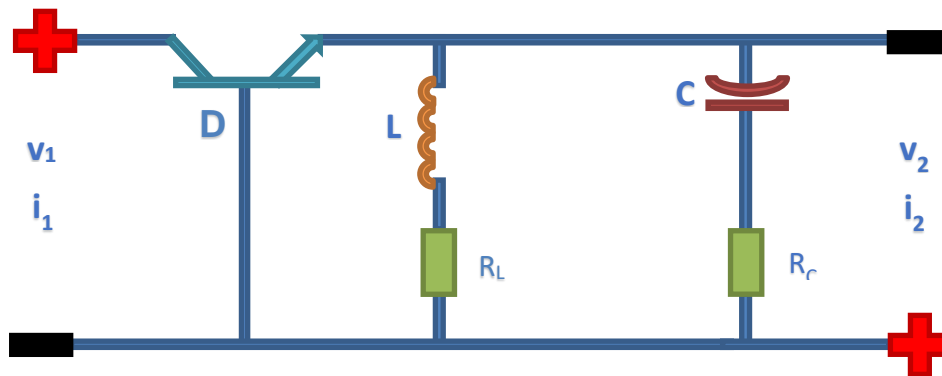


Figure 2-18 - DCDC Converter Schematic

Where:

- v_1 = The input voltage at the fuel cell
- i_1 = The input current at the fuel cell
- v_2 = The output voltage at the battery
- i_2 = The output current at the battery
- D = The transistor state
- L = The inductance at the inductor
- C = The capacitance at the capacitor
- R_L = The resistance at the inductor
- R_c = The resistance at the capacitor

The model formulation derived using the Springer's method by Sira-Ramirez and Silva-Ortigoza (2006) is shown within the modelling section, 3.14.

2.5.1 *Summary of Fuel Cell Modeling Techniques*

From the review its clear that the method used to model fuel cells is similar to that of batteries. However, the more complex models make use of thermodynamic properties and characteristics of gas flow through the fuel cell. It is evident that this is the case where Raga et al. (2014) presents a Randle's based model to represent a fuel cell, although the model they present is only capable of representing fuel cell voltage when operating in ideal conditions. Souleman, Tremblay, and Dessaint (2009) use a similar method to model the fuel cell to the method used to model the battery in Tremblay, and Dessaint (2009). They present the fundamentals of the equations in their model and show it is capable of representing the fuel cell characteristics well. Boscaino et al. (2013) present an empirical based model where they have taken steps to model the molar mass flow of hydrogen and pressure in both the anode and cathode, the model parameters are obtained through curve fitting the simulation with experimental results. Ural, and Gencoglu (2010) show six models from the literature, providing the mathematics for each model and their limitations. The main limitation of the first five models, and the other models presented here is that either temperature or pressure, at either the anode or cathode, has not been taken into consideration. The sixth model presented by Ural, and Gencoglu (2010) and the model presented by Benchouia et al. (2013) are the only fuel cell models to take these into account. A limitation which is present in all of the fuel cell models is that they do not take the hydrogen consumed during production of current and voltage into consideration. The fuel cell model will be used in conjunction with a DCDC model and a battery model. Therefore, the fuel cell model will not experience highly dynamic loads, and will operate relatively slowly within the simulation. This means that the fuel cell model which is used can be a steady-state model and should be able to represent the whole of the fuel cell Voltage versus Current (VI) curve. To determine which steady state model is capable of this, the models have been recreated to establish if they can achieve this. The VI curves for the steady state fuel cell models are shown in Figure 2-19.

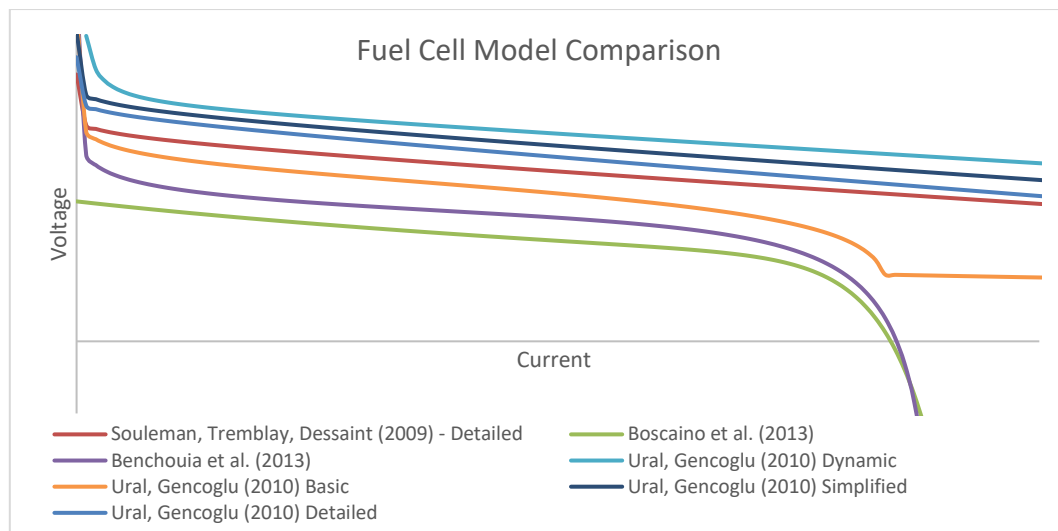


Figure 2-19 - Fuel Cell Modelling VI Comparison

As shown in Figure 2-19 there are only two models which can represent both the high current and low current exponential voltage characteristics. The Benchouia et al. (2013) model is the only one, of the two, which is capable of the low current exponential voltage characteristics as well as representing reverse cell voltages, where the voltage goes below the X-axis on the graph. Each model presented in Figure 2-19 has been given the same cell characteristics given the parameters supplied by the model, however, the offset in voltage has been created by changing the number of cells in series so that better visualisation of the curves can be achieved within the graph. Therefore, it is evident from the work conducted that the model presented by Benchouia et al. (2013) is the most appropriate modelling technique for characterising the fuel cell voltage within this project and the limitation where hydrogen consumption is not taken into consideration is addressed within section 3.12.

2.6 Drive Cycle Characteristics

Drive cycles are primarily a speed versus time graph, representing a controlled schedule of operation for the vehicle's speed. They were created to aid in the benchmarking of vehicle emissions under a laboratory test environment. The test is typically performed by using a chassis dynamometer, where the driven wheels are located on rollers with a variable resistance, so that the correct resistance of the roller can be created to represent the resistance of the road for the tested vehicle. A trained driver is then required to drive the vehicle on the rollers at the indicated speeds so that the vehicle emissions can be monitored throughout the test. Vehicle emissions are typically measured in terms of grams per vehicle kilometre so that environmental agencies can create models to determine air quality estimates. There are currently over 250 drive cycles in existence and attempts have been made to standardise a drive cycle which can universally be used to determine vehicle emissions (Barlow et al. 2009). Within the European Union, type approval emission testing has been created and enforced by law to prevent vehicle manufactures from creating vehicles which perform poorly in regard to emissions (Barlow et al. 2009). Therefore, the necessity of detailed drive cycles is imperative for a full vehicle model. Due to the way drive cycles were created using laboratory tests, it makes it difficult to create a drive cycle which truly represents 'real world driving' and to estimate real world driving conditions. This is because change in altitude and corner forces are not taken into account within the standardised drive cycles. This can considerably affect the parasitic power loss and in turn affect the predicted efficiency of the vehicle (Omami, Pourabedin, and Nekofa 2009). It could be said that drive cycles as they exist have reached their maturity and it is time to develop a more complex type approval method which can incorporate a dynamic resistive force based on the mentioned factors.

Transport Research Laboratory (TRL) Limited stated that the European Union enforced type approved emissions testing by law for all new light-duty vehicle models, and engines which are used in heavy-duty vehicles, above 3.5 tonnes (Barlow et al. 2009). The authors continue to explain that there are three types of drive cycles;

- Highly stylised drive cycle - which bear little representation of real world conditions,
- Real world data collection drive cycle - which has a continuously changing speed where the cycle has been obtained from a vehicle operated on the road,
- Pseudo-steady-state drive cycle - which represents a slightly varying constant speed to simulate free-flowing traffic.

The type approval method for light-vehicle models within the European Union is achieved using New European Drive Cycle (NEDC) (Clean Fleets 2014). The highly stylised NEDC can be seen in Figure 2-20.

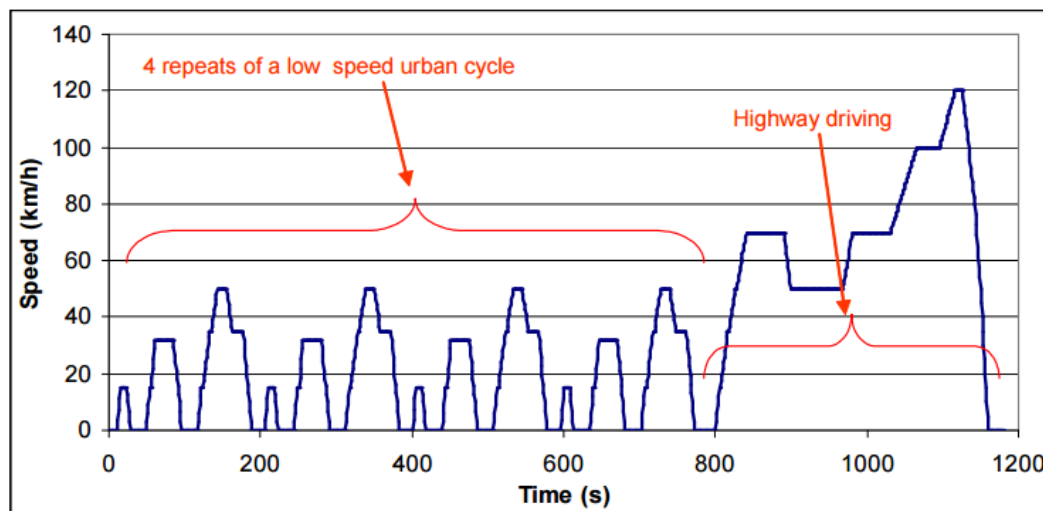


Figure 2-20 - NEDC Drive Cycle Velocity Profile (Barlow et al. 2009)

As shown in Figure 2-20 the NEDC consists of four identical low speed, below 60 km/h, and one high speed, above 60 km/h, procedures which occur over 1200 seconds. The NEDC test has an average speed of 33.6km/h and the distance travelled is 11 km (Barlow et al. 2009).

An alternative drive cycle which uses real world data is the Assessment and Reliability of Transport Emissions Models and Inventory Systems (ARTEMIS) drive cycle (André et al. 2009). The ARTEMIS drive cycle consists of three drive cycles, ARTEMIS Urban Cycle, ARTEMIS Rural Road Cycle and the ARTEMIS Motorway Cycle, and is the result of a European funded project to identify fuel pollutant emissions and fuel consumption (André et al. 2009). Figure 2-21, Figure 2-22 and Figure 2-23 shows the three ARTEMIS Drive Cycles.

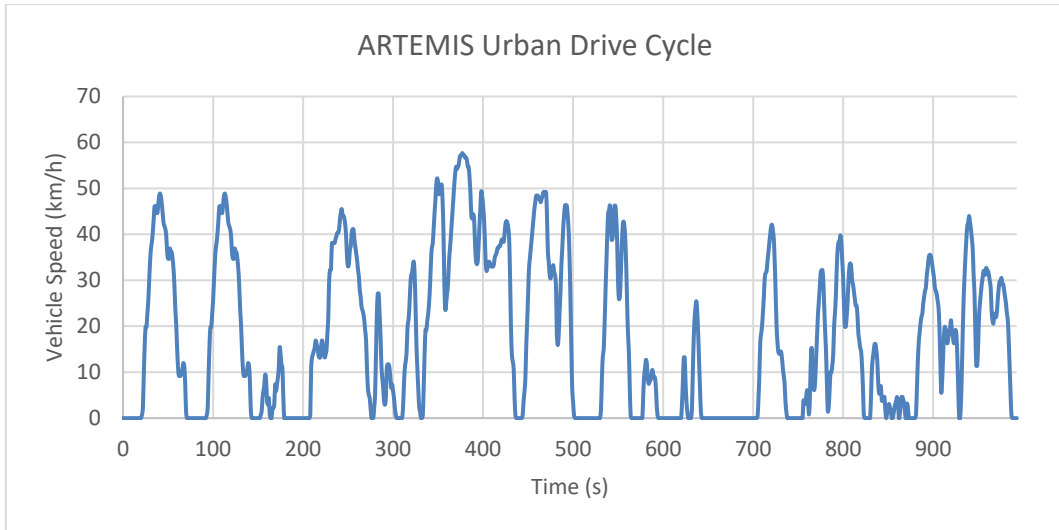


Figure 2-21 - ARTEMIS Urban Drive Cycle (ECOpint 2011)

Figure 2-21 shows the ARTEMIS urban drive cycle where the maximum speed is 57km/h, average speed is 17.6 km/h and the distance travelled is 4.87 km (ECOpint 2011). Figure 2-22 shows the ARTEMIS rural drive cycle.

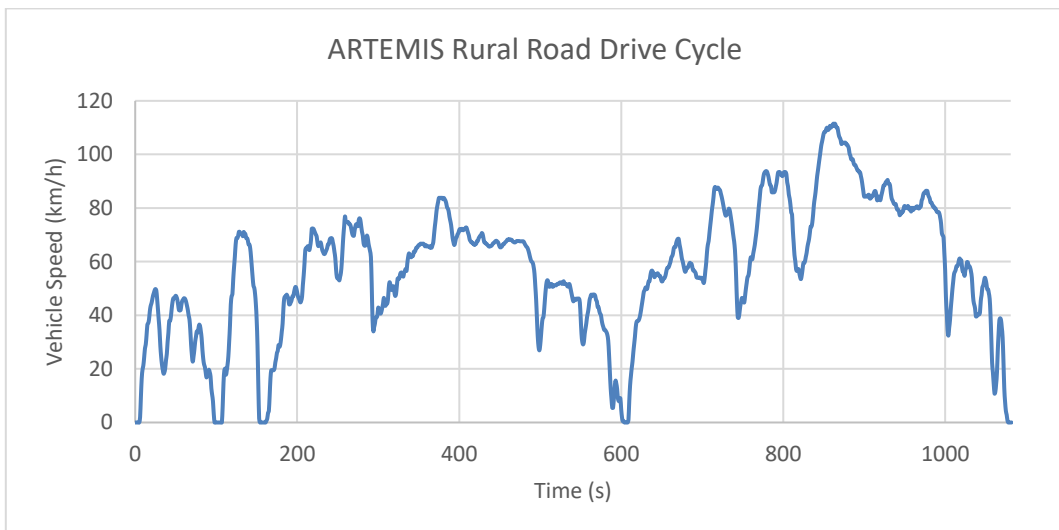


Figure 2-22 - ARTEMIS Rural Drive Cycle (ECOpint 2011)

Figure 2-22 shows that the ARTEMIS rural drive cycle has a maximum speed of 111 km/h. The average speed of this drive cycle is 57.5 km/h and the distance travelled is 17.27 km (ECOpint 2011). Figure 2-23 shows the ARTEMIS motorway drive cycle.

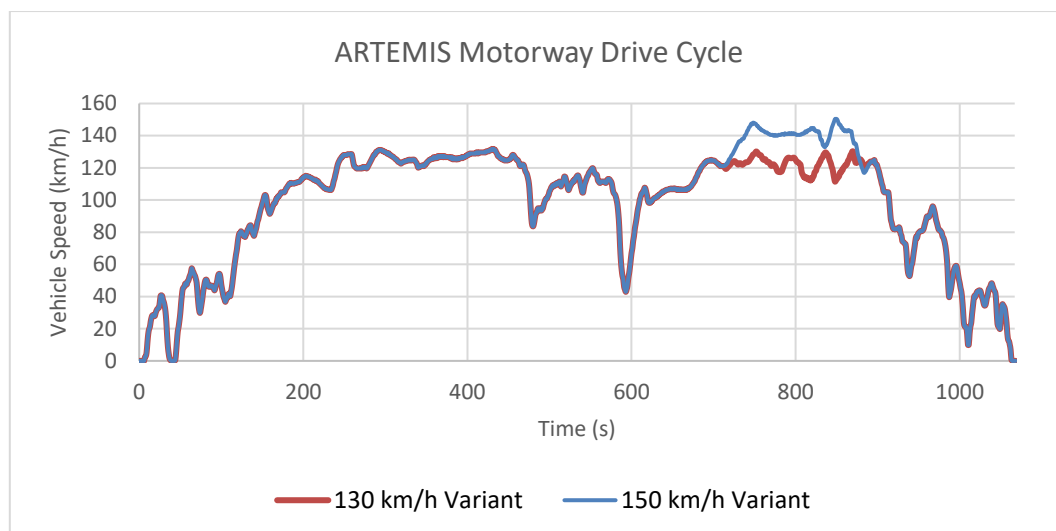


Figure 2-23 - ARTEMIS Motorway Drive Cycle (ECOpint 2011)

Figure 2-23 shows that the ARTEMIS motorway drive cycle has two profiles which can be used, one which is restricted to 130 km/h and one which is restricted to 150 km/h. The 130 km/h drive cycle is used for vehicles which cannot achieve speeds greater than 130 km/h and has an average speed of 96.9 km/h and the distance travelled is 28.74 km. The 150 km/h drive cycle has an average speed of 99.6 km/h and the distance travelled is 29.55 km (ECOpint 2011).

In 2014 a novel approach to drive cycles was taken and presented by (Ryan et al. 2014), where the authors compare energy consumption of an EV on the NEDC to that of a similar speed profile in real conditions. The authors present the Coventry University Drive Cycle (CUDC) to the public for the first time, using Figure 2-24, and shows a difference in energy consumption of 35.9 Wh/km between a NEDC rolling road test and an average of multiple controlled real world CUDC driving tests. The authors present the benefits of the higher energy density of compressed hydrogen over batteries and the comparison of refill times against battery recharge times. This presents a strong argument for FCEVs over EV's especially in relation to vehicle weight and performance.

2.6.1 Summary of Drive Cycles

The NEDC is a highly-stylised drive cycle which is used to type approve a vehicle for sale within the European Union. This drive cycle was created to benchmark vehicle emissions testing and has been used in multiple publications to demonstrate the accuracy of vehicle models (Bogosyan, Gokasan, and Goering 20017), (Deuring, Gerl, and Wilhelm 2010), (Markel et al. 2002) and (Omni, Pourabedin, and Nekofa 2009). The ARTEMIS drive cycle is less popular in the publications, most likely because it is not required in the type approval process of a vehicle, but it is still a valid drive cycle. The ARTEMIS drive cycle provides a larger range of operating conditions compared to the NEDC and is based on real-world speed data. The CUDC is a relatively new drive cycle in the public domain, and was created so that a team of people could represent something similar to that of the urban part of the NEDC test and do real-world testing on a vehicle. As stated at the start of this section, there are over 250 drive cycles in existence and it would be inappropriate to analyse all of them here. Three drive cycles have been presented. All three of the drive cycles presented are defined as speed in the time domain. However, where the CUDC was created in Coventry, United Kingdom, it is possible to recreate the real-world test within this project, and therefore, the CUDC is the best drive cycle for this project as validation tests can be accomplished within the project. The NEDC will also be used in the project as rolling road test data is already available for the Coventry University Microcab H2EV. These two drive cycles and test data will enable the ability to compare energy consumption when either simulating real-world scenarios which have vehicle handling requirements and simplified driving scenarios such as rolling road testing.

2.7 Summary of Literature

The literature review has examined state of the art models in relation to fuel cells and electric vehicles. It has identified that although there are models capable of simulating FCEV sub-systems, there are no validated forward looking multi-disciplinary FCEV models in the public domain. This identifies a gap in the literature and shows that a multi-disciplinary FCEV model is needed to accurately predict energy consumption for EVs and FCEVs. The review has identified key modelling approaches to the sub-systems stated within section 1.3 Aim and Objectives and suggested the appropriate modelling tool required to accomplish the aim and objectives of the project. The literature shows that Dymola is the most suitable modelling and simulation tool for multi-disciplinary systems such as, battery, fuel cell, and vehicle systems modelling. This has done this by showing the capability of Dymola's multi-disciplinary modelling techniques, through areas of relevance, that the software has been previously used for, and through the evidence of pre-validated models which are supplied by the software.

The literature review also covers current state of the art vehicle dynamic simulation methods. This includes a review of the MBS methodology and complex tyre models to represent vehicle dynamics well. The literature has shown that the Pacejka Magic Formula tyre model is the state-of-the-art method of characterising tyre behaviour and should be used if a pre-defined validated model is available. The creation and validation of a tyre model is outside the scope of this project. Therefore, the ability to use a validated tyre model via the software choice is preferable. Dymola provides a MBS Vehicle Dynamics package, with multiple pre-defined tyres and validated tyre models, the choice as the software tool for the project is further supported.

It has identified that a developed Shepherd's model methodology as the most appropriate to represent the battery characteristics and to use a model presented by (Tremblay, and Dessaint 2009), and that the fuel cell model presented by (Benchouia et al. 2013) as the most appropriate to represent fuel cell electrical characteristics.

The review presents three drive cycles which are in the public domain and identifies the CUDC is the most appropriate choice of drive cycles, due to both locational circumstances and the opportunity to perform real world tests so that data can be obtained to validate the new vehicle model.

The literature shows that the concept of a fuel cell vehicle has been around since 1959 and that slow progress has been made. However, the review shows a lack of technical material in the public domain, such as the issues surrounding these components and their integration within vehicles. Section 1.1 clearly shows the current solution to EV

CHAPTER 2 - Literature Review

range within the automotive industry and the problems associated when the vehicles make sole use of batteries. Therefore, the material presented so far shows the necessity for the work presented in this thesis to investigate the development and use of a novel high fidelity multi-disciplinary FCEV model. The work presented in the following chapters will demonstrate the methodology to create the new FCEV model and the use of the new model which can represent various vehicle scenarios, such as conventional vehicle dynamics, handling performance, efficiency predictions, control strategy affects and will compare two different drive cycles. It will go onto show, how such a model would be beneficial to industry to accurately determine and improve upon vehicle specification within the virtual prototype stage, thus showing a contribution to industry and meeting the gap in literature.

CHAPTER 3 - MODELLING

A standardised model, such as the vehicle model in Dymola is made up from sub-models which have been developed for specific applications and validated against relevant criteria. Typically, the models relating to battery electric and fuel cell vehicles are relatively less well developed than those for internal combustion engines and mechanical transmissions systems. Examination of the standard Dymola library models revealed several shortcomings and limitations in relation to the objectives of this investigation, and therefore it was necessary to propose original models to represent certain component systems. An example is the Dymola battery model which is only suitable for representing lead acid batteries. The Dymola electric motor model is also too simple to represent the losses of the motor. There is an existing fuel cell model in Dymola but this is not fully developed, the main problem being that there are many undocumented parameters and variables. As such, after initial attempts to utilise it the model was deemed unusable in this project. However, in some cases it was possible to modify or adapt a Dymola library model. In this study, the electric motor model will be developed using the same fundamental approach to that of the Dymola electric motor model. The objectives of this project were primarily to address prediction methods for overall vehicle energy efficiency and dynamic performance, and to test these methods using factual information obtained from vehicle testing. In the modelling phase of the work, reference will be made to two groups representing the “client”; the Low Carbon Vehicle research team at Coventry University, who participate in several related areas of research, and Microcab Industries Ltd, who designed the base vehicle used for experiment work. Both groups hold an interest in achieving improved designs and specifications. Throughout the project, frequent discussions with and presentations to members of these groups were conducted and informed the modelling approach throughout. This provided an initial identification of the model objectives.

3.1 Modelica and Dymola Connectors

Where Dymola uses the Modelica language it is necessary to define the way in which models are generated using this tool. The modelling method which is adopted by Dymola is through a hierarchical modelling technique and uses models which are assembled from “locally balanced” submodels. These submodels use the properties of the physical domains involved. Where all of the submodel equations are balanced locally, the larger models which are built from these are automatically balanced. Where the total number of unknowns is equal to the total number of equations. The physical properties of the domains are incorporated into the Modelica language by using basic laws of physics. A physical property is the physical quantity and the physical domain of a variable (Modelica Association 2000). In the example of an electrical pin these consist of voltage and current. The law that is assigned to an electrical pin is Kirchhoff’s current law, and this is done by defining the current as a flow variable and the voltage as a potential variable. A flow variable is a real variable that should be summed to zero across a model. A connector is then formed by first, stating the relevant balance equation and boundary condition for the particular physical domain and then assigning the variables needed for the balance equation and boundary condition using the Modelica SI Units library (Modelica 2013). The elementary connectors shown in Table 3-1, are defined by domain, potential variables, flow variables and the connector definitions:

Table 3-1 - Modelica Elementary Connectors (Modelica 2013)

Domain	Potential Variable	Flow Variable	Connector Definition	Icons
Electrical Analog	Electrical Potential	Electrical Current	Pin, PositivePin, NegativePin	
Electrical Space Phasor	2 Electrical Potentials	2 Electrical Currents	Plug, PositivePlug, NegativePlug	
Quasi Stationary Single Phase	Complex Electrical Potential	Complex Electrical Current	Pin, PositivePin, NegativePin	
Electrical Digital	Integer(1...9)		DigitalSignal, DigitalInput, DigitalOutput	
Magnetic Flux Tubes	Magnetic Potential	Magnetic Flux	MagneticPort, PositiveMagneticPort, NegativeMagneticPort	
Magnetic Fundamental Wave	Complex Magnetic Potential	Complex Magnetic Flux	MagneticPort, PositiveMagneticPort, NegativeMagneticPort	
Translational	Distance	Cut-Force	Flange_a, Flange_b	
Rotational	Angle	Cut-Torque	Flange_a, Flange_b	

3-Dimensional Mechanics	Position Vector, Object Orientation	Cut-Force Vector, Cut-Torque Vector	Frame, Frame_a, Frame_b, Frame_Resolve	
Simple Fluid Flow	Pressure, Specific Enthalpy	Mass Flow Rate, Enthalpy Flow Rate	FlowPort, FlowPort_a, FlowPort_b	
Heat Transfer	Temperature	Heat Flow Rate	HeatPort, HeatPort_a, HeatPort_b	
Hydraulic	Pressure	Volume Flow Rate	Port_A, Port_B	
Pneumatic	Pressure	Mass Flow Rate	Port_1, Port_2	
Blocks	Real Variable, Integer Variable, Boolean Variable		RealSignal, ReallInput, Real Output, IntegerSignal, IntegerInput, IntegerOutput, BooleanSignal, BooleanInput, BooleanOutput	
Complex Blocks	Complex Variable		ComplexSignal, ComplexInput, ComplexOutput	
State Machine	Boolean Variables, (Occupied, Set, Available, Reset)		Step_In, Step_Out, Transition_In, Transition_Out	

Using the information from Table 3-1, any model can be formulated using a connector by applying the following mathematical expressions within the model (Modelica 2013):

$$p_a = p_b \quad (73)$$

$$0 = f_a + f_b \quad (74)$$

Where:

- p_a = The potential variable on connector a
- p_b = The potential variable on connector b
- f_a = The flow variable on connector a
- f_b = The flow variable on connector b

In equation (73) we state that the potential variables must be equal to each other, and in equation (74) we state that the sum of the flow variables must be equal to zero. This is the law which is typically associated to a connector within Modelica. As each variable must be assigned an SI unit, the equations must balance, otherwise Modelica or Dymola will not allow the simulation to take place (Modelica 2013).

$$P = p_a - p_b \quad (75)$$

Where:

- P = The potential variable across the connector

In equation (75) we have declared the equation for a new variable (P), this variable must be of the same units as p_a and p_b , and we are essentially measuring the potential across a connector, the same way that you would measure voltage across a battery (Modelica 2013).

CHAPTER 3 - Modelling

Within this chapter reference to both the rotational Flange and the electrical Pin is made frequently. Because of this, the models which determine these connectors are presented below:

- Rotational Flange (Modelica 2013)

$$\frac{d}{dt}\varphi = \omega \quad (76)$$

$$\frac{d}{dt}\omega = \alpha \quad (77)$$

$$\varphi = SI \text{ Unit} = rad \quad (78)$$

$$\tau = flow = SI \text{ Unit} = Nm \quad (79)$$

Where:

- φ = Is the potential variable as the absolute rotation angle of the flange in radians
- ω = The angular velocity of the flange in rad/s
- α = The angular acceleration of the flange in rad/s²
- τ = Is the flow variable as cut torque in the flange in Nm

The rotational flange provides the derivative of the rotational angle as standard within the model, usually a connector only consists of the potential and flow variable definitions which are shown in equations (78) and (79).

The example of an ideal gear in the Modelica standard library can be used to show how two rotational flange connectors are used create a model:

- Ideal gear (Modelica 2013)

$$\varphi_a = \varphi_b * b \quad (80)$$

$$0 = b * \tau_a + \tau_b \quad (81)$$

Where:

- φ_a = Is the absolute rotation angle of the first flange in radians
- φ_b = Is the absolute rotation angle of the second flange in radians
- τ_a = Is the torque at the first flange in Nm
- τ_b = Is the torque at the second flange in Nm
- b = Is the gear ratio that changes both the torque and the angular rotation angle

As shown by equations (80) and (81), the use of connectors to build a mathematically balanced model can quickly be generated using the basic laws of physics (Modelica 2013).

- Electrical Pin (Modelica 2013)

$$v = potential = SI \text{ Unit} = V \quad (82)$$

$$i = flow = SI \text{ Unit} = A \quad (83)$$

Where:

- v = Is the potential variable as the voltage of the pin in volts
- i = Is the flow variable as current flowing into the pin in amperes

An example of a standard resistor model in Modelica can be used to show how two analog electrical pins are used to create a model:

- Resistor (Modelica 2013)

$$v = v_a - v_b \quad (84)$$

$$0 = i_a - i_b \quad (85)$$

$$i = i_a \quad (86)$$

$$v = i * R \quad (87)$$

Where:

- v* = *The voltage across the electrical pins*
- v_a* = *The voltage at the positive pin*
- v_b* = *The voltage at the negative pin*
- i_a* = *The current flowing through the positive pin*
- i_b* = *The current flowing through the negative pin*
- i* = *The current flowing through the resistor model*
- R* = *The resistive value of the resistor being modeled*

This example shows how the voltage drop across the resistor model is defined by using equation (87). As most electrical models, and all physical devices, consist of a positive and a negative pin, equations (84)-(86) are usually in a separate model defined as a 'one port' model within the standard Modelica library. This 'one port' model can be called upon to create a more complex model which is then classed as reusable due to its common layout (Modelica Association 2000).

3.2 Vehicle Model Structure

The highest level of the model is defined as the simulation setup area of the model. This is shown in Figure 3-1 and is the standard simulation setup provided by the Dymola software. A decision to use this simulation setup has been taken because it provides a standard approach to simulating vehicle dynamics and vehicle models within Dymola (Dassult Systems 2002-2013). This section consists of a closed loop driver, a 3-dimensional road profile, atmospheric conditions, world conditions and a vehicle model. Each model within the simulation is vital to the accuracy of the results.

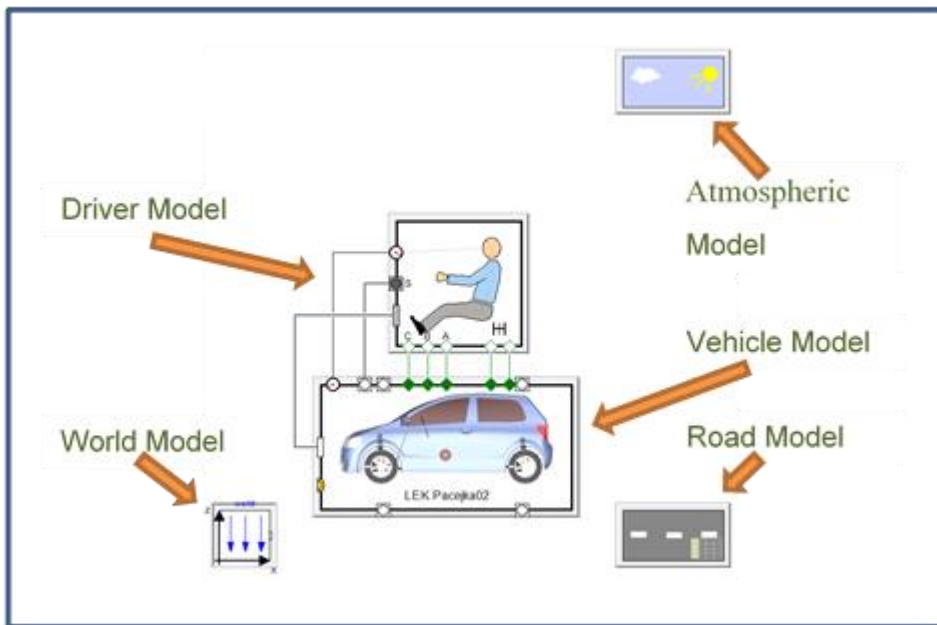


Figure 3-1 - Dymola Simulation Setup

The closed loop driver model supplied with the Dymola software uses the centre line of the road in order to determine steering inputs, which control the vehicle's lateral movements, so that the vehicle can maintain its correct course through the drive cycle profile via using Proportional-Integral-Derivative (PID) controllers. The Dymola road model holds the data regarding vehicle speed and position. This data is sent to the driver model so that the driver model can determine if the vehicle requires more acceleration, or deceleration, and respectively applies a larger value to the accelerator pedal or the brake pedal via parameterised PID controllers, so that the characteristics of the driver can easily be adjusted to represent a range of aggressive driving styles or smoother driving styles. The driver model also consists of a tracking function; this function determines when the driver should use the clutch and change gear based on engine speed as well as the shift durations. Therefore, the adaption of testing different gearboxes for different scenarios can be easily implemented without developing a new driver model.

The atmospheric model provided by the Dymola software includes the ability to define wind velocity and direction, air density, ambient temperature, and atmospheric pressure so that the tests can be conducted under varying ambient conditions.

The Dymola road model is created using the Dymola road generator function as shown in Figure 3-2.

file_name	<input type="text" value="default_road.mat"/>	Road file
Path		
override_velocity	<input type="checkbox"/> false	Overrides the path velocity specified in file
path_velocity	<input type="text" value="30"/> m/s	Constant reference velocity if override_velocity
path_table_velocity	<input type="text" value="[0, 30; 100, 30]"/>	Velocity as function of length along path
override_offset	<input type="checkbox"/> false	Overrides the path offset specified in file
path_offset	<input type="text" value="0.0"/> m	Constant reference path offset
path_table_offset	<input type="text" value="[0, 0; 135, 0; 140, 2; 175, 0; 200, 0]"/>	Path offset as function of length along path
Road condition (see info)		
mu0	<input type="text" value="1"/>	Nominal friction coefficient outside patches
mu_patch	<input type="text" value="ones(0)"/>	Friction coefficient for each patch
x_min_patch	<input type="text" value="ones(0)"/> m	Longitudinal start points for patches
x_max_patch	<input type="text" value="ones(0)"/> m	Longitudinal end points for patches
y_min_patch	<input type="text" value="ones(0)"/> m	Lateral start points for patches
y_max_patch	<input type="text" value="ones(0)"/> m	Lateral end points for patches
x_res_patch	<input type="text" value="0.5*ones(size(mu_patch, 1))"/> m	Longitudinal resolution of grid visualizing the patch
y_res_patch	<input type="text" value="x_res_patch"/> m	Lateral resolution of grid visualizing the patch

Figure 3-2 - Dymola Road Generator Function

The Dymola road model consists of Longitudinal (x), Lateral (y), and Altitudinal (z) coordinates of the road. However, the road is modelled as a smooth surface with a variable friction coefficient, rather than a rough undulated surface. This is preferred as the simulation time will be reduced due to the large driving cycles which are to be simulated. The road velocity is matched to the x, y and z coordinates of the road surface along with the path offset. The combination of these 3 main variables within the road model allow the use of GPS vehicle data to be implemented into the simulation. This allows direct comparison between a real vehicle and a virtual prototype. The variable road surface friction coefficients can be created along the road by adjusting the parameters listed below the 'Road conditions' section, as seen in Figure 3-2.

The world model which is provided by the Dymola software mainly consists of the gravitational forces, along with the ability to enable animation effects to show forces which the vehicle is subjected to, for example, tyre forces can be displayed as a dynamic arrow on the animation of the simulated vehicle's tyres.

The vehicle model is the heart of the simulation and is an area which has been developed from Dymola's 'Vehicle Dynamics' software package. An example of the

standard vehicle model which is provided by Dymola can be seen in Figure 3-3 and is known within the 'Vehicle Dynamics' package as the "CompactLEKPacejka02" Model. The decision to adopt and develop this model has been taken because it is compatible with the standard simulation environment for vehicle dynamics within Dymola, and because the "CompactLEKPacjka02" model is based a similar vehicle architecture to that of the Coventry University Microcab H2EV.

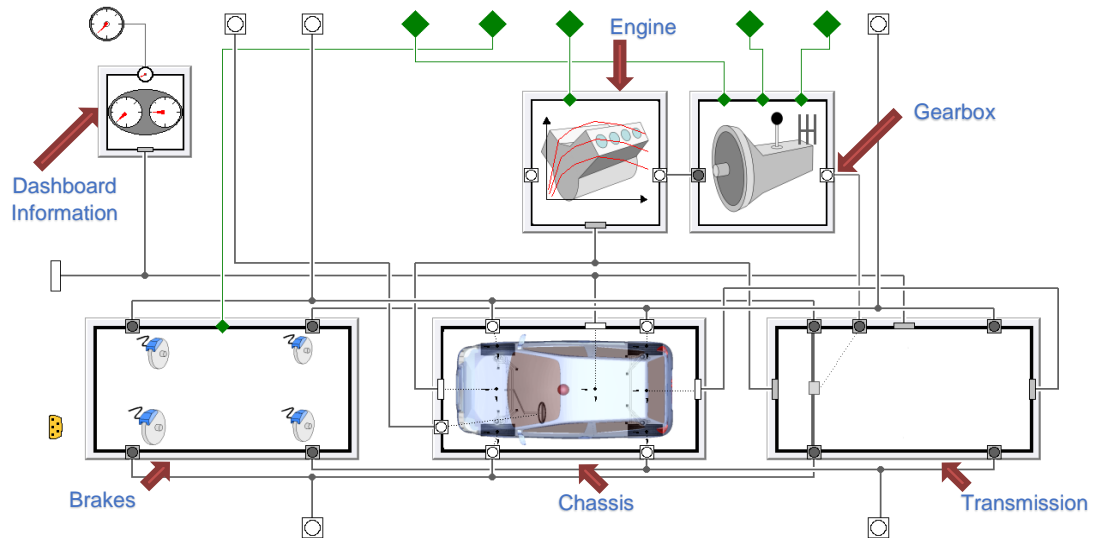


Figure 3-3 - Dymola Standard Vehicle Model

The model shown in Figure 3-3 consists of a dashboard which sends minimal information to the driver, similar to what would be seen on a real vehicle, an engine model, gearbox model, transmission model, brakes model and a chassis model, which will be explained in further detail in the following sections. However, the main development to most of the subsystem models is that they have been made much more parametric, to allow for the modification of components at the highest level rather than having to delve deep into the model. Figure 3-4 shows the developed chassis model.

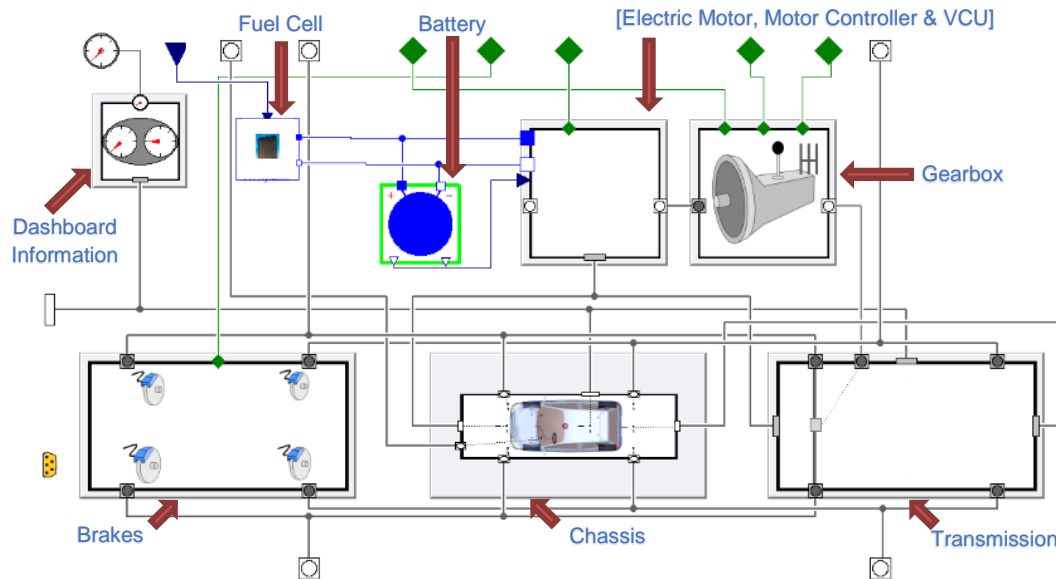


Figure 3-4 - Developed Fuel Cell Vehicle Model

The engine model has been replaced with a motor and motor controller model, along with the addition of a fuel cell, a battery and VCU model as seen in Figure 3-4.

3.3 Chassis Model

The standard chassis model supplied with the Dymola software has been adopted because it has been validated in vehicle dynamic studies and provides the functionality to define all aspects of the chassis via parameters (Deuring, Gerl, and Wilhelm 2010). The standard Dymola chassis model consists of five main areas; Pacejka tyre model, mass model, aerodynamics model, front suspension model and a rear suspension model, as seen in Figure 3-5.

The Pacejka tyre model is provided in the Dymola 'Vehicle Dynamics' package and a predefined 175/70/R13 tyre has been used, as a tyre testing facility is not presently available. This tyre was chosen for the vehicle model as it best represents that of the Coventry University Microcab H2EV, where the radius of the tyre is the main concern. As a different tyre radius, would affect the gear ratios and speed related performance of the vehicle. However, where there are various tyres to choose from so virtual testing of a different tyre for the vehicle can be performed with ease by using the 'Change Class' function within Dymola.

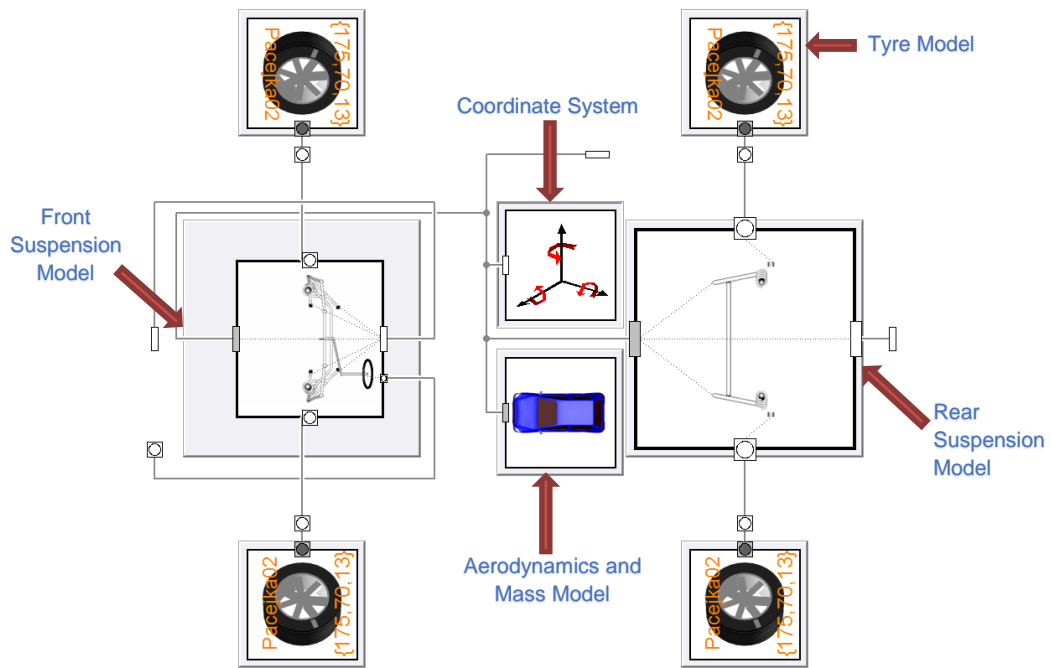


Figure 3-5 - Dymola Chassis Model

The standard mass model provided by Dymola consists of only a mass and a centre of mass with four payload options. The model has been developed using first principles to incorporate each component of the vehicle and their individual locations, with their moments of inertias automatically calculated from this. This makes the mass model more appropriate as a design tool to determine if the design of the vehicle seriously affects the centre of mass, and it can all be generated from a typical vehicle CAD model. However, while it can be rather time consuming to implement all the data, the option to override and use just the centre of mass position and the total sprung mass is also available. Figure 3-6 shows the implementation of the mass model data to the standard Dymola mass model.

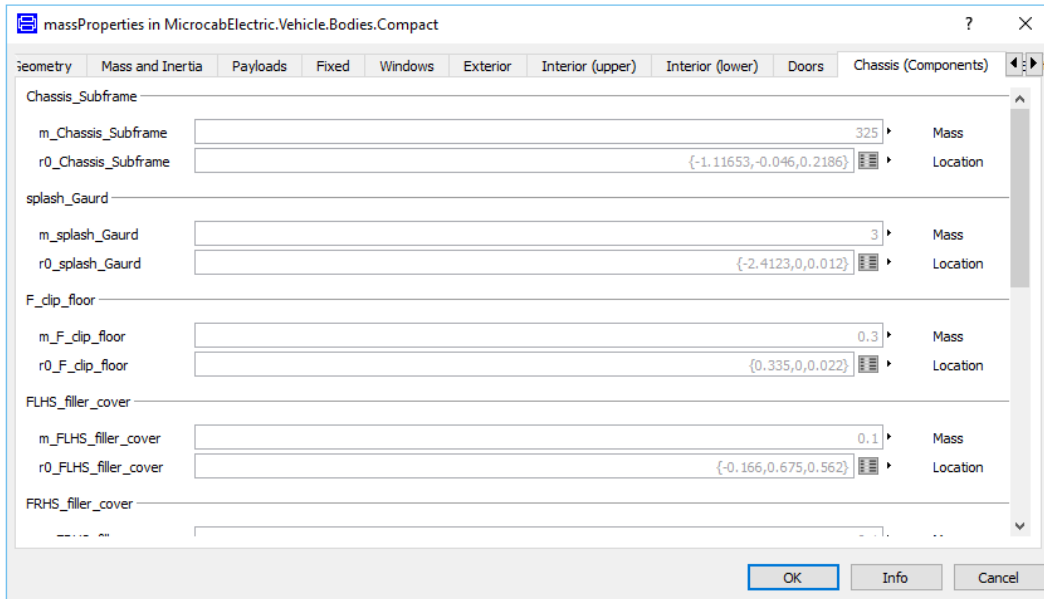


Figure 3-6 - Mass Model Parameter Modification

This mass model shown in Figure 3-6 takes the origin of the coordinate system at the centre of the vehicle's front axle where x points back along the vehicle, z points upwards and y is to the side. When the option for the component data is selected, the mass model uses the following mathematical process to determine the following parameters; total mass of the vehicle, centre of mass for the vehicle and the moments of inertia for the vehicle:

$$m_{total} = \sum m_{component} \quad (88)$$

Where:

m_{total} = The total mass of the vehicle
 $m_{component}$ = The mass of components

Here the total mass has been calculated by summing the mass of all the components. This provides a result for the parameter of the total vehicle mass in the standard Dymola mass model.

$$X_{CM} = \frac{\sum(m_{component} * X_{component})}{m_{total}} \quad (89)$$

$$Y_{CM} = \frac{\sum(m_{component} * Y_{component})}{m_{total}} \quad (90)$$

$$Z_{CM} = \frac{\sum(m_{component} * Z_{component})}{m_{total}} \quad (91)$$

Where:

CM = The vehicle's Centre of Mass
 X_{CM} = The longitudinal distance to the CM from the global coordinate system
 Y_{CM} = The lateral distance to the CM from the global coordinate system
 Z_{CM} = The vertical distance to the CM from the global coordinate system
 $X_{component}$ = The longitudinal distance to the component from the global coordinate system
 $Y_{component}$ = The lateral distance to the component from the global coordinate system

CHAPTER 3 - Modelling

$Z_{component}$ = The vertical distance to the component from the global coordinate system

Here we have calculated the centre of mass position from the origin of the global coordinate system using the same approach as (Blundell, and Harty 2004). This provides a result for the x, y and z center of mass position parameters in the standard Dymola mass model.

$$X = X_{component} - X_{CM} \quad (92)$$

$$Y = Y_{component} - Y_{CM} \quad (93)$$

$$Z = Z_{component} - Z_{CM} \quad (94)$$

Where:

X = The longitudinal distance to the component from the CM of the vehicle

Y = The lateral distance to the component from the CM of the vehicle

Z = The vertical distance to the component from the CM of the vehicle

In order to calculate the vehicles moments of inertia about the centre of mass we must determine the position of the components in relation to the centre of mass rather than the global coordinate system. This is achieved by subtracting the centre of mass position from the components global position. We know that the rotational inertia (moments of inertia) for a mass rotating around an axis can be solved with fundamental principles in classical physics using equation (95).

$$I = m * r^2 \quad (95)$$

Where:

I = The inertia of the mass about the rotational axis that it is moving in $kg\ m^2$

m = The mass of the object in kg

r = The distance between the mass centre and the rotational axis in m

If we treat the component masses as point masses from the vehicle centre, as most of the components which are attached to a vehicle are rigidly mounted, the classical representation of inertia can be used to define the vehicle centre moments of inertia. Thus pitagorous theorem can be used to determine the equivalent distance to the component mass about the axis which the inertia is being taken and the following equations apply;

$$I_{XX,CM} = \sum m_{component} * (Y^2 + Z^2) \quad (96)$$

$$I_{YY,CM} = \sum m_{component} * (X^2 + Z^2) \quad (97)$$

$$I_{ZZ,CM} = \sum m_{component} * (X^2 + Y^2) \quad (98)$$

Where:

$I_{XX,CM}$ = The vehicles moments of inertia about the longitudinal axis in $kg\ m^2$

$I_{YY,CM}$ = The vehicles moments of inertia about the lateral axis in $kg\ m^2$

$I_{ZZ,CM}$ = The vehicles moments of inertia about the vertical axis in $kg\ m^2$

Here the model solves for the vehicle's mass moments of inertia, by summing the component mass moments of inertia about the centre of mass, using the same approach as (Blundell, and Harty 2004). This provides a result for the mass moments of inertia parameters in the standard Dymola mass model.

The aerodynamics model is the same as that of the one provided by the Dymola 'Vehicle Dynamics' package and consists of the following parameters which have been modified to suit the Coventry University Microcab H2EV;

Front Aerodynamic drag coefficient of vehicle body	Dimensionless
Frontal Area of Vehicle body	[m ²]
Centre of Pressure at Front of the vehicle body	X, Y, Z [m]
Side Aerodynamic drag coefficient of vehicle body	Dimensionless
Side Area of Vehicle body	[m ²]
Centre of Pressure at the Side of the vehicle body	X, Y, Z [m]

A more in depth description of the aerodynamic model and the defined parameters can be found in section 3.5 - Aerodynamics Model.

The front suspension model provided by Dymola, shown in Figure 3-7, is fully interchangeable and parametric, meaning that the McPherson Strut suspension model which is either side of the steering rack can be easily replaced with a double wishbone model, and all hard points of the suspension can be set via the parameters page for each sub system model.

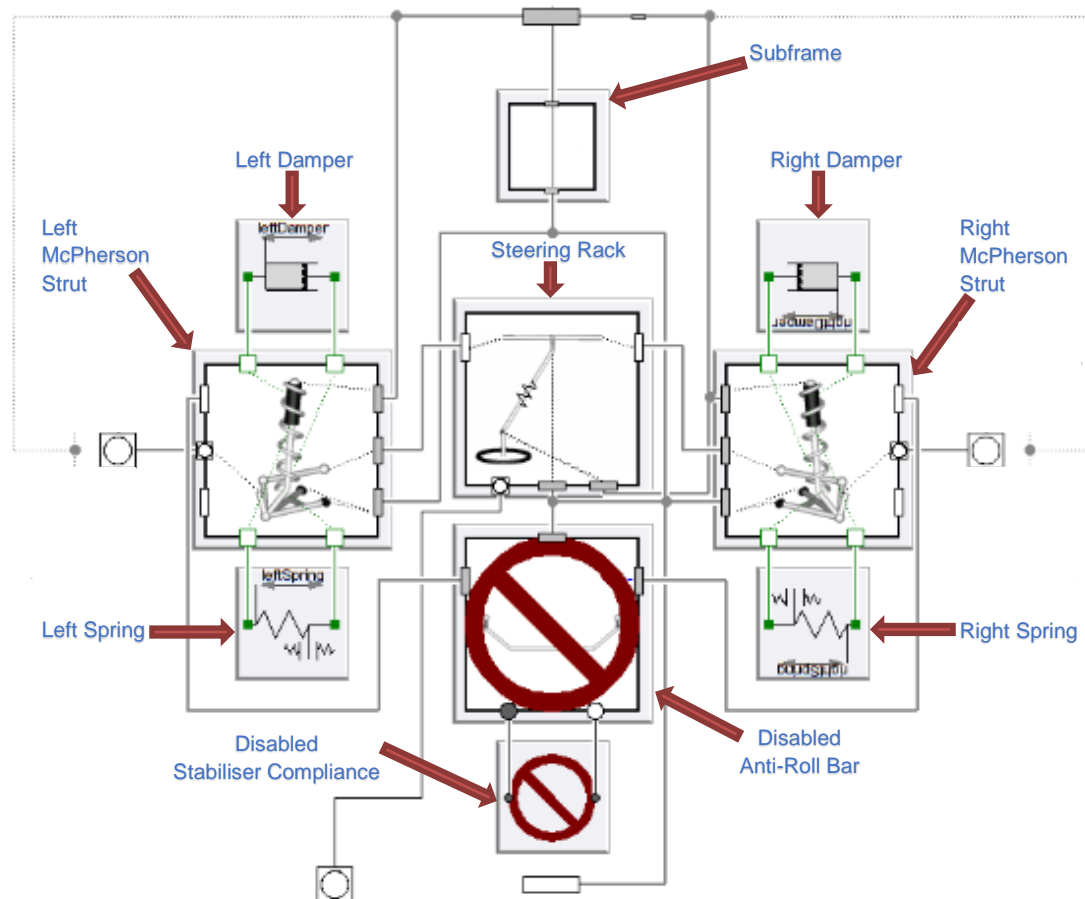


Figure 3-7 - Front Suspension Model, Mc Pherson Strut

The springs in the model can be changed between progressive and linear and the damping can be changed between constant single rate damping, double region damping, quadruple region damping and active damping so that a multitude of different scenarios can be implemented into the vehicle. With the hard points being parametric, scenarios of bump steer, handling and performance issues can be easily checked, and overcome in the design stage. As shown in Figure 3-7 the work conducted within this thesis will not use the anti-roll bar for the simulations. The implementation or removal of an anti-roll bar into the design can be realised with this function, meeting both the need of the client, where vehicle handling was a concern of the Coventry University Microcab H2EV, and the aim and objectives of the project.

The rear suspension model provided by Dymola is shown in Figure 3-8.

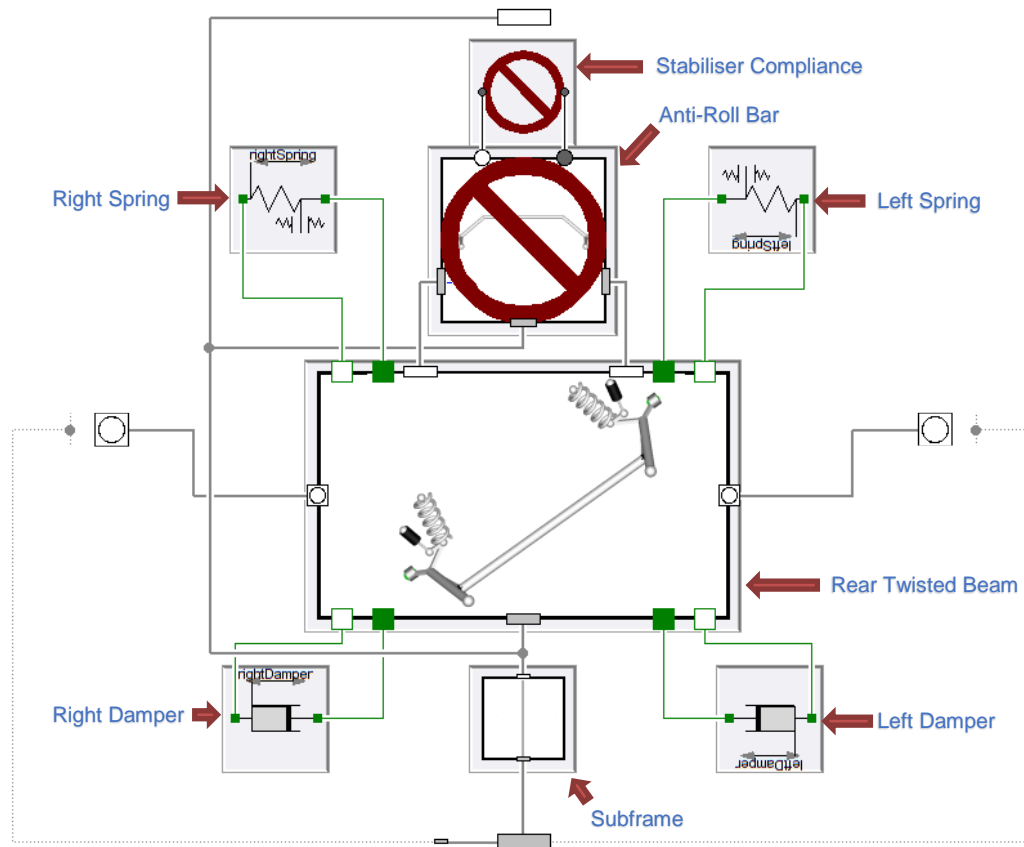


Figure 3-8 - Rear Suspension Model, Rear Twisted Beam

The rear suspension model, shown in Figure 3-8, is also parametric and similar to that of the front suspension model. However, the steering rack is removed and has been modelled with a rear twisted beam. A full list of the parameterised hard point locations can be seen in APPENDIX A – Model Data, Table 8-1, Table 8-2 and Table 8-3.

3.4 Braking Model

The standard braking model provided by Dymola, shown in Figure 3-9 has been adopted because it has the same components as the Coventry University Microcab H2EV's braking system, and since each component is parameterised based on datasheet parameters, it can be used to represent the braking system of the Coventry University Microcab H2EV by only changing the parameters. The Dymola braking model consists of four discs, four calipers, a rear proportioning valve, a master cylinder, a vacuum booster and a brake pedal.

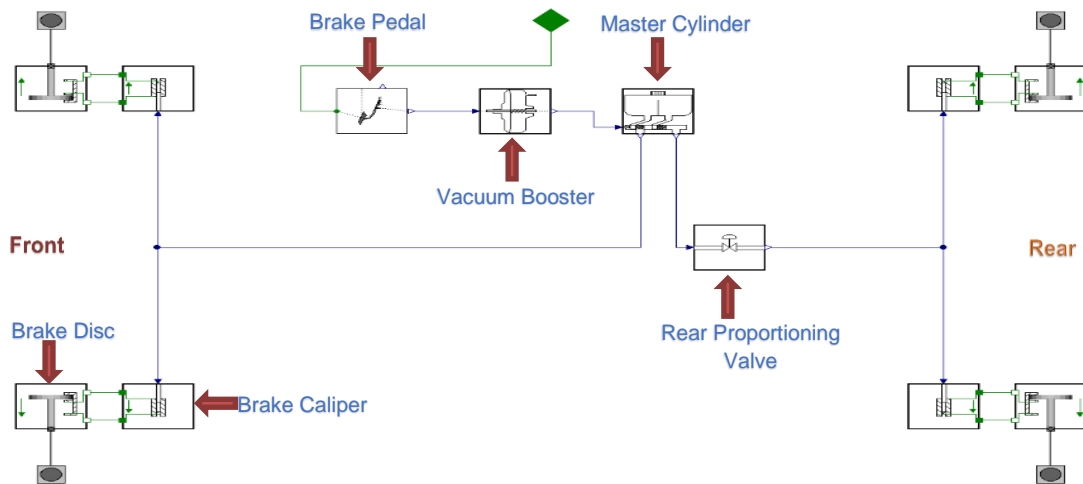


Figure 3-9 - Brake System Model

The brake pedal converts the pedal movement into a force which is then applied to the vacuum booster which boosts the force onto the master cylinder by a ratio and a runout force. The master cylinder then converts the force to a pressure in the brake pipes which is dictated by the master cylinder's diameter. This pressure is then applied to the front two calipers and the rear proportioning valve. The rear proportioning valve provides a threshold and a pressure reduction ratio, which then allows the correct pressure to the rear brake calipers. The brake calipers take the input pressure and, via a piston area and a threshold pressure, output a bipolar force to act on the disc to slow the rotational movement of the rotational output shaft, and apply an inverse torque until the vehicle is stationary (Dassult Systems 2002-2013);

$$F_{vacuum} = \begin{cases} 0 \\ F_{pedal} * B_{ratio} \\ F_{runout} \\ F_{pedal} \end{cases} \left[\begin{array}{l} \text{for } F_{pedal} \leq 0, \\ \text{for } F_{pedal} * B_{ratio} < F_{runout}, \\ \text{for } F_{pedal} * B_{ratio} = F_{runout}, \\ \text{for } F_{pedal} > F_{runout}. \end{array} \right] \quad (99)$$

Where:

F_{vacuum} = Force out of the vacuum booster

F_{pedal} = Pressure supplied to the vacuum booster by the drivers pedal

B_{ratio} = The boost ratio for the pedal force

F_{Runout} = The pressure at which the booster stops working, input forces larger than this are not amplified

Equation (99) applies a set of conditions which determines the assist force of the vacuum booster.

$$P_{masterCylinder} = F_{vacuum} * \left(\frac{1}{\pi * \left(\frac{D_{mastercylinder}}{2} \right)^2} \right) \quad (100)$$

Where:

$P_{masterCylinder}$ = Pressure out of the master cylinder
 F_{vacuum} = Force supplied to the master cylinder by the vacuum booster
 $D_{masterCylinder}$ = Diameter of the master cylinder's internal bore

Equation (100) converts the force from the vacuum booster into a hydraulic pressure in the lines defined by the size of the master cylinders diameter.

$$P_{proportionalValve} = \left\{ \begin{array}{l} 0 \\ P_{masterCylinder} \\ \{(P_{masterCylinder} * P_{ratio}) - (P_{kneePoint} * P_{ratio})\} + P_{kneePoint} \end{array} \right\} \quad (101)$$

$$\left[\begin{array}{l} \text{for } P_{masterCylinder} \leq 0, \\ \text{for } P_{masterCylinder} \leq P_{kneePoint}, \\ \text{for } P_{masterCylinder} \geq P_{kneePoint} * 2. \end{array} \right]$$

Where:

$P_{proportionalValve}$ = Pressure out of the rear proportional valve
 $P_{masterCylinder}$ = Pressure supplied to the rear proportional valve by the master cylinder
 $P_{kneePoint}$ = Pressure threshold to start reducing the brake pressure
 P_{ratio} = The pressure reduction ratio to apply after the knee point pressure is reached

Equation (101) is used to provide less pressure at the rear brake pads and achieves this by using a knee point. Therefore, if the pressure from the master cylinder is less than the knee point it transfers the same pressure to both the rear brakes and the front brakes. Once the pressure from the master cylinder exceeds the knee point threshold, it is then gradually reduced so that in heavy braking conditions more pressure is applied to the front brakes.

$$F_{frontCalliperBF} = \left\{ \begin{array}{l} 0 \\ (P_{masterCylinder} - P_{threshold}) * A_{piston} \end{array} \right\} \left[\begin{array}{l} \text{for } P_{masterCylinder} \leq P_{threshold} \\ \text{for } P_{masterCylinder} > P_{threshold} \end{array} \right] \quad (102)$$

$$F_{rearCalliperBF} = \left\{ \begin{array}{l} 0 \\ (P_{proportionalValve} - P_{threshold}) * A_{piston} \end{array} \right\} \left[\begin{array}{l} \text{for } P_{proportionalValve} \leq P_{threshold} \\ \text{for } P_{proportionalValve} > P_{threshold} \end{array} \right] \quad (103)$$

CHAPTER 3 - Modelling

Where:

$F_{frontCalliperBF}$	= Bipolar force which acts as a clamping force on the front brake pads
$F_{rearCalliperBF}$	= Bipolar force which acts as a clamping force on the rear brake pads
$P_{masterCylinder}$	= Pressure supplied to the front calipers from the master cylinder
$P_{proportionalValve}$	= Pressure supplied to the rear calipers from the rear proportional valve
$P_{threshold}$	= The minimum pressure to apply a braking force on the brake pads
A_{piston}	= The area of the brake piston inside the caliper

Equation (102) and (103) converts the pressure in the brake pipes to a force via the area of the piston in the Calliper.

$$\tau_{frontBrake} = -F_{frontCalliperBF} * r_{frontEffective} * \mu_{frontPad} \quad (104)$$

$$\tau_{rearBrake} = -F_{rearCalliperBF} * r_{rearEffective} * \mu_{rearPad} \quad (105)$$

Where:

$\tau_{frontBrake}$	= Front brake torque applied to the rotational flang
$\tau_{rearBrake}$	= Rear brake torque applied to the rotational flang
$r_{frontEffective}$	= The effective radius of the front brake disc
$r_{rearEffective}$	= The effective radius of the rear brake disc
$\mu_{frontPad}$	= The coefficient of friction of the front brake pad
$\mu_{rearPad}$	= The coefficient of friction of the rear brake pad

Equation (104) and (105) convert the force applied by the calliper into a reverse torque which is applied to a rotational flange to slow the rotational movement of the wheel. The rotational flange is a standard Three Dimensional (3D) mechanical connection in the Modelica, Modelon and Dymola languages.

3.5 Aerodynamics Model

The Aerodynamics model is provided within the Dymola 'Vehicle Dynamics' Package. The standard Dymola model has been used because it has been validated by (Dorling 2005). The vehicle which is being modelled has a relatively low top speed, and as the aerodynamic forces are a product of velocity squared these forces will have less of an effect on the vehicle compared to other dynamic forces such as tyre rolling resistance, change in altitude and cornering forces (Andersson 2012). Dymola defines the model as an uncoupled air resistance model which acts on the body of the vehicle in a longitudinal and lateral direction. The model uses the longitudinal drag coefficient, lateral drag Coefficient, frontal area of the vehicle, side area of the vehicle and the pressure centre location of the front and side of the vehicle to define a quadratic speed dependent drag-force which acts on the centre of the vehicle, via a mechanical flange (Modelon 2012-2013). By using the vehicle model's speed, frontal area of the vehicle, side area of the vehicle and wind speed dictated by the outer world model it is able to dynamically change the aerodynamic resistance acting on the vehicle dependant on the direction in which the vehicle is traveling. Therefore, the investigation of the effect of wind gusts on the vehicles handling and performance could be implemented with ease by modifying the outer world model wind profile similar to the method of modifying the road profile.

The aerodynamic drag coefficient is heavily dependent on the side profile shape of the vehicle and these values are usually obtained via wind tunnel testing or CFD, which are outside the scope of this project. Muthuvel et al. (2013) and Gowtham Raj (2016) show how the frontal shape of a city bus can reduce the frontal drag coefficient by up to 41%, from 0.68 to 0.4, whilst maintaining the same frontal area of the vehicle (Growtham Raj et al. 2016) and (Muthuvel et al. 2013). Thus, where it has been established that the side profile shape of a vehicle is the driving factor for the aerodynamic drag coefficient, typical values based on published data can be used to estimate a value for the aerodynamic drag coefficient of the given vehicle. Heisler (2002) lists the drag coefficient for different vehicle types and Bosch (2007) lists the drag coefficient for different vehicle shapes. Using the data from these publications, Table 3-2 has been populated with relevant data regarding drag coefficients.

Table 3-2 - Aerodynamic Drag Coefficient Examples

Vehicle Definition	Aerodynamic Drag Coefficient	Source
Saloon car	0.22 – 0.40	(Heisler 2002)
Notch-back sedan	0.26 – 0.35	(Bosch 2007)

Sports car	0.28 – 0.40	(Heisler 2002)
Estate / Station-wagon	0.30 – 0.34	(Bosch 2007)
Open convertible	0.33 – 0.50	(Bosch 2007)
Light van	0.35 – 0.50	(Heisler 2002)
Wedge shape body	0.30 – 0.40	(Bosch 2007)
Bus or coach	0.40 – 0.80	(Heisler 2002)
Articulated truck	0.55 – 0.80	(Heisler 2002)
Ridged truck and draw bar trailer	0.70 – 0.90	(Heisler 2002)

Figure 3-10 shows the side profile shape of the Coventry University Microcab H2EV, on the right-hand side, and an example of a light commercial van, on the left-hand side. Figure 3-10 can be used in conjunction with Table 3-2 to estimate an appropriate aerodynamic drag coefficient for the Coventry University Microcab H2EV.

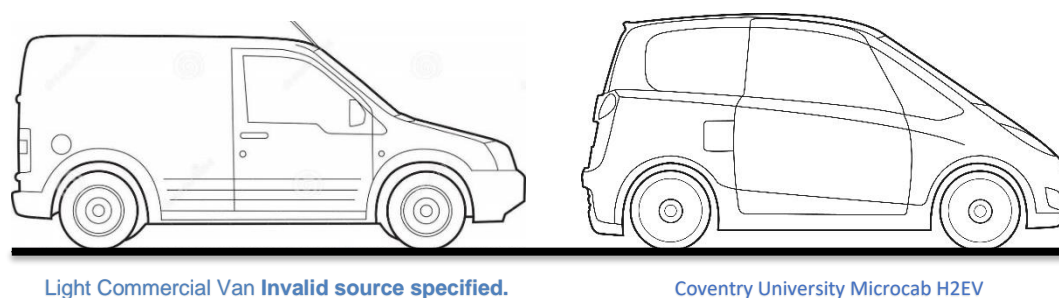


Figure 3-10 - Vehicle Side Profile Comparison

It can be seen from Figure 3-10, that the Coventry University Microcab H2EV has a side profile shape that lies between the profile for a light van and a wedge shaped body. As such, using the range of drag coefficients shown for those vehicle types in Table 3-2, a drag coefficient of 0.35 is used for the Coventry University Microcab H2EV. This conservative estimate of 0.35 also fits with data regarding other 'hatchback' type vehicles which have improved side profile designs, such as the 2012 Nissan Leaf. The Nissan Leaf has a similar frontal area to that of the Coventry University Microcab H2EV but has a more sleek side vehicle profile resulting in an aerodynamic drag coefficient for the Nissan Leaf of 0.32 (Sherman 2014). This supports the use of the conservative value of 0.35 for the Coventry University Microcab H2EV. These values have been used as there is not a direct relationship between the frontal drag coefficient and the frontal area. This supports the use of a conservative value based on a similar vehicle shape. If the vehicle represented by this modelling approach is to achieve high top speeds, then wind tunnel testing should be conducted

so that accurate drag coefficients can be obtained. However, as stated at the beginning of this section, the Coventry University Microcab H2EV can only achieve relatively low top speeds where the aerodynamic loss is not as much of a concern as other forces acting on the vehicle (Andersson 2012).

A list of the parameters used within the aerodynamics model are provided below:

cW_{front}	Aerodynamic frontal drag coefficient of car body	0.35	Coefficient
a_{front}	Frontal Area of Car body	2.94	m ²
$r0cp_{front}$ [3]	Centre of pressure at the front of car body	{0, 0, 0.25}	{x, y, z}
cW_{side}	Aerodynamic side drag coefficient of car body	0.89	Coefficient
a_{side}	Side Area of Car Body	3.51	m ²
$r0cp_{side}$ [3]	Centre of pressure at the side of the car body	{-1.1, 0, 0.5}	{x, y, z}

The equations used within the aerodynamics model are shown below: (Modelon AB 2004-2014)

$$F_{front} = -0.5 * cW_{front} * \rho * a_{front} * v_x^2 \quad (106)$$

$$F_{side} = -0.5 * cW_{side} * \rho * a_{side} * v_y^2 \quad (107)$$

Where:

F_{front} = Quadratic longitudinal drag force which acts on the vehicle at $r0cp_{front}$

F_{side} = Quadratic lateral drag force which acts on the vehicle at $r0cp_{side}$

ρ = Density of air at the location of the vehicle

v_x = The relative longitudinal velocity of wind and vehicle speed acting at the front of the vehicle

v_y = The relative lateral velocity of wind and vehicle speed acting at the front of the vehicle

$\mu_{rearPad}$ = The coefficient of friction of the front brake pad

Here the quadratic longitudinal and quadratic lateral forces which act on the centre of the vehicle are calculated.

3.6 Tyre Model

The tyre model that has been adopted in this project is provided by Dymola and shown in Figure 3-11. The reason to use the tyre provided by Dymola was provided in section 2.3.3. The components within the model are highly inter-dependant and take the vehicle information from the square Flange on the right-hand side.

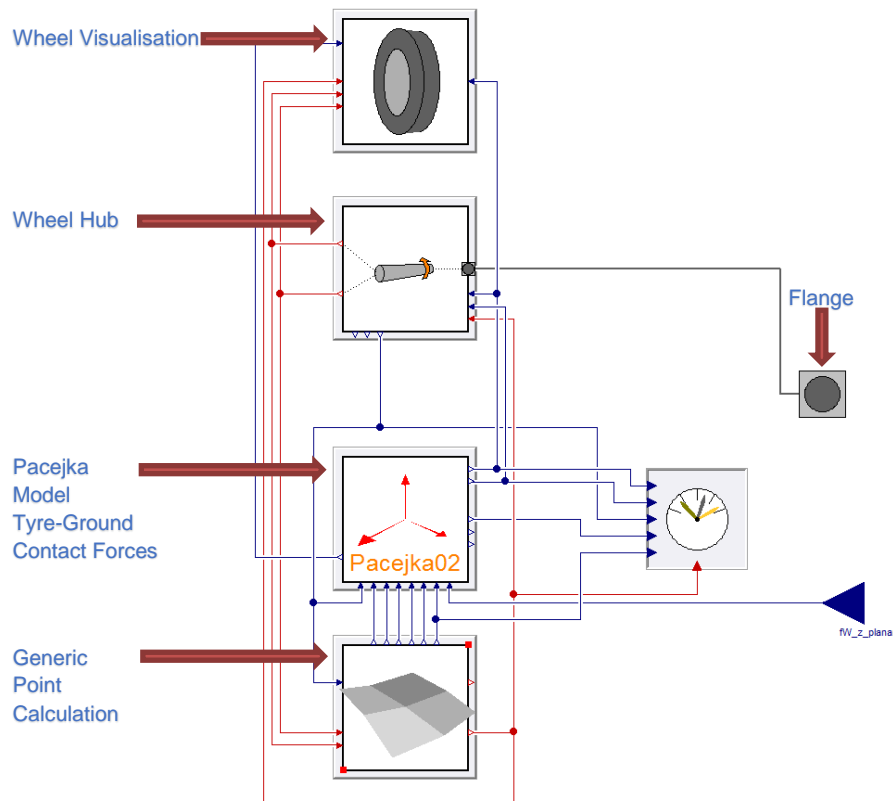


Figure 3-11 - Tyre Model Overview

The flange connector is a standard 3D mechanical connection in the Modelica, Modelon and Dymola language, it consists of a position vector from the world frame, orientation to rotate the world frame, a flowing force, a flowing torque and an absolute rotation of the flange. When a flow variable is used within a model it must ensure that the sum of the flow variables is zero. Therefore, the sum of the force into and out of the model must be zero.

The main area of the tyre model is defined in the sub-model, with the axis and “Pacejka02” text, on the model icon. This part of the model defines the base values for many variables which make up the Pacejka Magic Tyre Formula and can be seen in Figure 3-11. However, the actual Pacejka Magic Tyre Formulation can be found inside the sub-model called ‘Pacejka02’ and is based on the 2002 Pacejka Magic Tyre Formula (Pacejka 2002). Therefore, the model used does not incorporate the variation

in tyre pressure as discussed in section 2.3.2. However, due to the nature of Dymola, if tyre pressure variation was required for the simulation, then the implementation of the SWIFT tyre model as defined in (Besselink, Schmeitz, and Pacejka 2010) could be implemented parametrically within Dymola, and the model could be switched with ease for specific vehicle dynamic handling scenarios. Due to the lack of a tyre testing facility being available, the model has used the predefined Pacejka02 {175/70/13} tyre to represent the Coventry University Microcab H2EV tyre. As stated in section 3.3, the identical tyre is not available within the Dymola library and the rolling radius of the tyre was prioritised when choosing the tyre option to ensure that speed related performance was maintained in the model.

The second main area of the tyre model is the generic point calculation model which determines the turn velocity, contact point, deformed radius, inclination, tyre compression, contact point velocity, centre frame and contact frame. The first six variables feed into The Magic Formula, where the last variable is used to assist in the wheel hub model and the visual representation of the wheel.

and a multiple speed gear box as this would be a thought-provoking feature of the model. The functionality of the transmission model allows for configuration of the gearbox via parameters, thus making it easy to reconfigure to different transmission configurations for testing and development of a vehicle in the virtual environment.

Figure 3-13 shows the internals of the Gearbox Model which consists of a Gear Ratio Table, a Pre-Clutch Inertia, a Clutch, a Gear and Post-Clutch Inertia model.

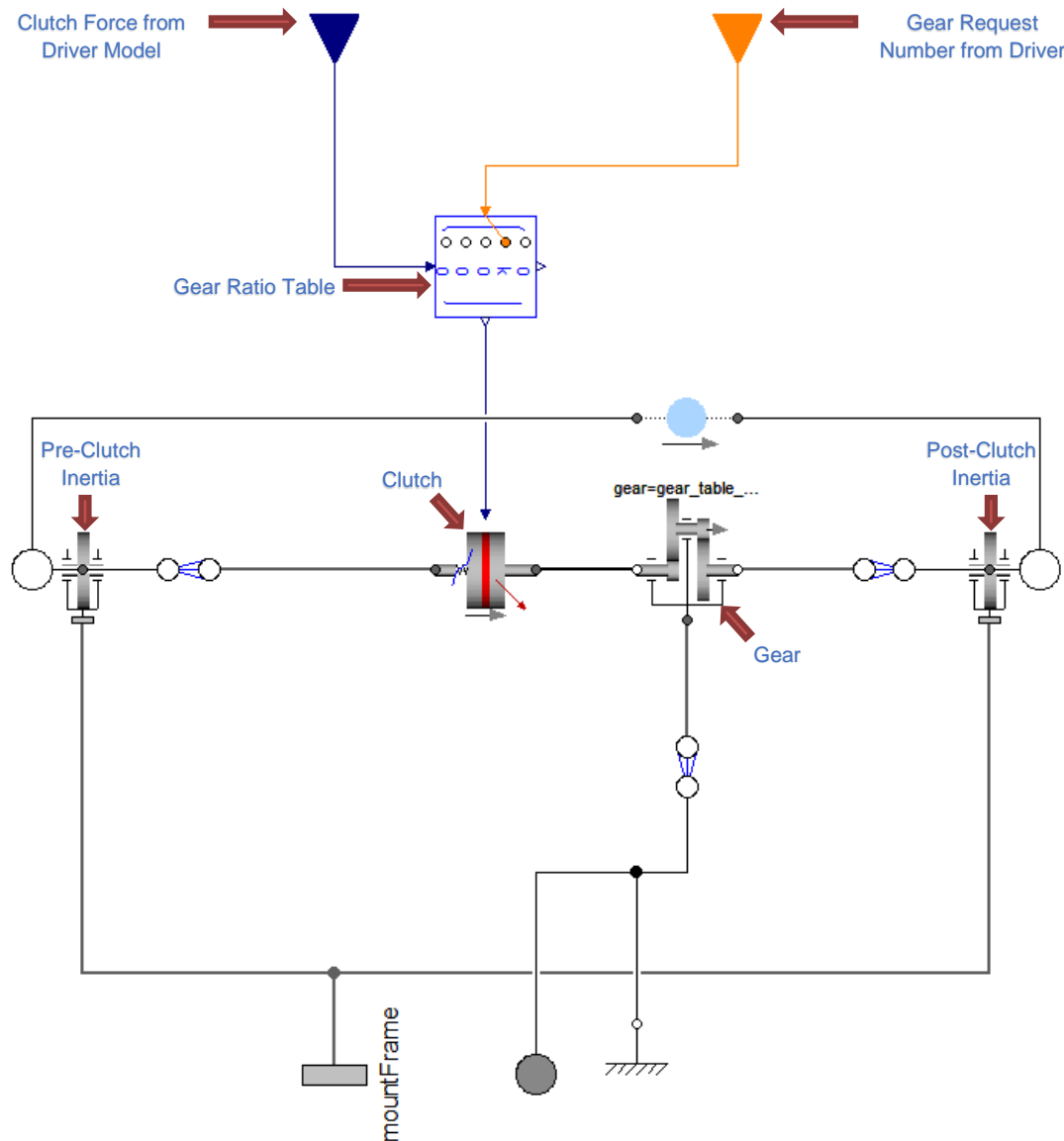


Figure 3-13 - Gearbox Model

The Gear changes its ratio dependant on the Gear Ratio Tables, the ratio is reduced to zero when the clutch is engaged, and this is required in order to change gear. The absolute angle of the output shaft and the flow of torque is transferred to the rest of the vehicle model via the Flange at the bottom of Figure 3-13. The Coventry University

Microcab H2EV does not have a conventional gearbox. The clutch input has been disabled and the gear ratio table has been modified to be a single gear ratio of 3.79 to match the Coventry University Microcab H2EV, via the transmission model parameters. The pre and post clutch engagement inertias are maintained to ensure that there is correct representation of the inertia within the fixed ratio gearbox.

3.8 Battery Model

The battery model has been created in Dymola and is based on a version of the Shepherds model (Tremblay, and Dessaint 2009). The justification to adopt this method of modelling the battery has been given in section 2.4.1 of the literature review and the limitation discussed is addressed by equations (116) - (120). Figure 3-14 shows the created battery model as a reusable model in Dymola.

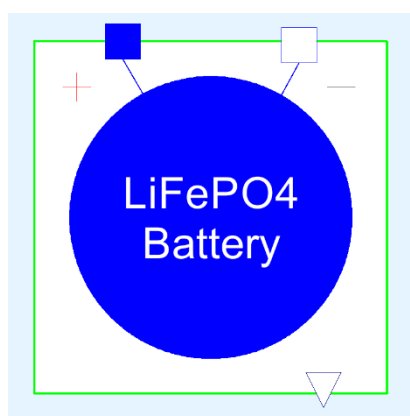


Figure 3-14 - Battery Model Package

As the battery is the main energy source of propulsion for the vehicle it was essential that an appropriate modelling technique was used. The battery model is one of the areas where Dymola fell short, as its electrical battery models were unable to represent the highly nonlinear sections of the battery voltage. Figure 3-14 shows the proposed battery model as a package with the positive and negative terminals at the top and the 'Real' connection at the bottom to export the SOC of the battery. The main consideration for battery modelling was the accuracy of capacity, voltage and speed of simulation. The reason that the voltage of the battery needs to be modelled well when simulating a fuel cell vehicle is because the battery will be dynamically charging and discharging throughout the simulation of the vehicle on a drive cycle. The reason battery capacity needs to be accurate is because of the high-energy density of lithium ion cells which are becoming the most common types of chemistry used for EVs, Hybrid Electric Vehicles and FCEV's. One of the issues with lithium ion chemistry type batteries, is that the voltage can increase exponentially at the high end of the SOC and

decreases exponentially at the low end of the SOC. Therefore, when modelling a vehicle which has a small capacity battery pack, it is vital to ensure that Over Voltage Protection (OVP) scenarios and Low Voltage Protection (LVP) scenarios can be identified and modelled. The benefits of this will allow for correct dynamic control over the charging strategy and better predictions of range on particular drive cycles. This section of the modelling is a key requirement for the both the simulation and the client. It provides the client with confidence as to how their battery system will operate in terms of vehicle usability and reliability.

The overview of the battery model can be seen in Figure 3-15 and consists of three main components: a resistor, battery Internals which create the voltage profile and the Battery Management System (BMS) which manages a max charge voltage.

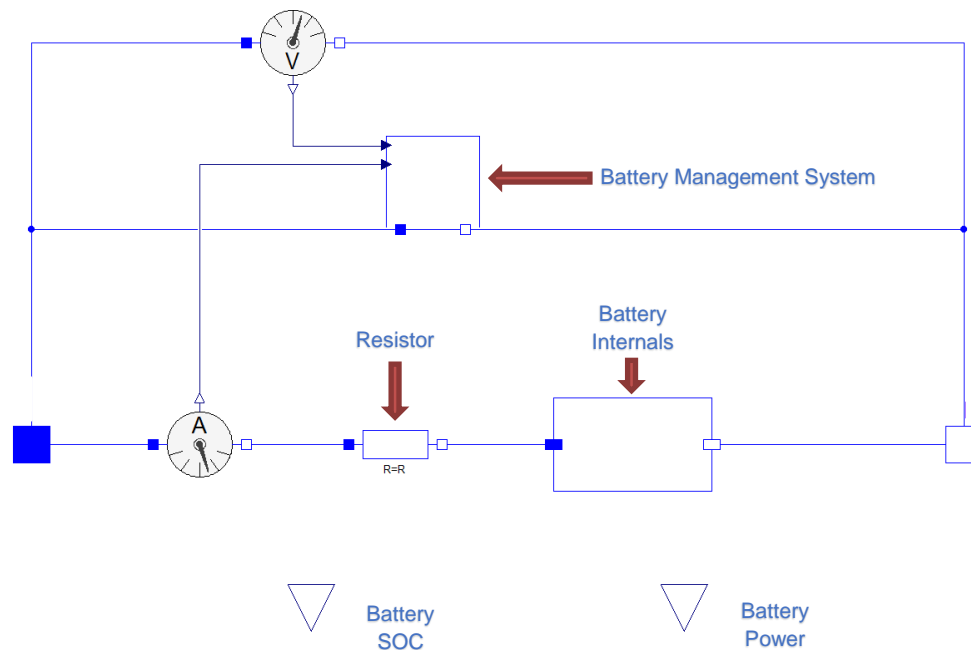


Figure 3-15 - Battery Model Overview

The electrical connectors used allow for the flow of current. Therefore, current cannot be created between two ports nor can it be lost and the following three equations cannot be broken (Modelica 2000-2013).

$$v = v_p - v_n \quad (108)$$

$$0 = i_p + i_n \quad (109)$$

$$i = i_p \quad (110)$$

Where:

v = The voltage between the positive pin and negative pin in the model

v_p = The voltage at the positive pin in the model

v_n = The voltage at the negative pin in the model

CHAPTER 3 - Modelling

- i = The current law accross the positive pin and negative pin in the model
 i_p = The current at the positive pin in the model
 i_n = The current at the negative pin in the model

Due to the importance of the battery model, the main model formulation is presented below within this chapter. However, the full Dymola Code can be found in APPENDIX B – Model Code.

$$A_c = V_{max} - V_{exp} \quad (111)$$

Where:

- A_c = Exponential zone amplitude during charging
 V_{max} = Maximum charge voltage
 V_{exp} = Start of nominal voltage zone

Here the exponential voltage from 100% SOC to normal conditions is calculated during charging of the cell.

$$A_d = V_{max} - V_{con} \quad (112)$$

Where:

- A_d = Exponential zone amplitude during Discharge
 V_{con} = Typical noninal voltage

Here the exponential voltage from 100% SOC to normal conditions is calculated during the discharge of the cell.

$$Q_{cellstart} = Q_{cell} * (1 - SOC_{start}) \quad (113)$$

Where:

- $Q_{cellstart}$ = Capacity of the cell at the start of the simulation
 Q_{cell} = Maximum capacity of the cell
 SOC_{start} = State of Charge start percentage

Here we calculate the capacity of the cell at the start of the simulation based on the start parameters.

$$i_{batt} = -\frac{i}{n_p} \quad (114)$$

Where:

- i_{batt} = Current at the cell
 n_p = Number of cells connected in parallel

Here we calculate the current flowing through a single cell by dividing the current by the number of cells in parallel.

$$\frac{d}{dt} i_{filt} = \left(-1 / \left(\frac{T_s * n_p}{n_s} \right) * i_{filt} \right) + i_{batt} / \left(\frac{T_s * n_p}{n_s} \right) \quad (115)$$

Where:

- i_{filt} = Filtered current
 T_s = Battery response time
 n_s = Number of cells connected in series

Here we filter the current so that the slower voltage responses can be represented later (Tremblay, and Dessaint 2009).

$$\eta_a = \frac{\eta_{min} - \eta_{max}}{\eta_{SOCmax} - \eta_{SOCmin}} \quad (116)$$

Where:

- η_a = A gain used to parametrise the coulombic efficiency of the battery
- η_{min} = The minimum coulombic efficiency of the battery
- η_{max} = The maximum coulombic efficiency of the battery
- η_{SOCmax} = The the point of battery SOC where the battery is most efficient
- η_{SOCmin} = The the point of battery SOC where the battery is least efficient

Here we determine the gain used for setting the coulombic charging efficiency via the use of parameters.

$$\eta_b = \eta_{min} - (\eta_a * \eta_{SOCmax}) \quad (117)$$

Where:

- η_b = An offset used to parametrise the coulombic efficiency of the battery

Here the offset used to parameterise the coulombic efficiency of the battery cell is calculated.

$$\eta = \begin{cases} \eta_{min} \\ SOC * \eta_a + \eta_b \\ \eta_{max} \end{cases} \begin{cases} \text{for } (SOC * \eta_a + \eta_b) \leq \eta_{min} \\ \text{for } (SOC * \eta_a + \eta_b) > \eta_{min} \\ \text{for } (SOC * \eta_a + \eta_b) \geq \eta_{max} \end{cases} \quad (118)$$

Where:

- η = The efficiency on the battery
- SOC = State of Charge of the battery

This now defines efficiency of the cell due to the two thresholds and SOC of the cell.

$$\frac{d}{dt} Q_{it} = \begin{cases} (i_{batt} * \eta) / 3600 \\ i_{batt} / 3600 \end{cases} \begin{cases} \text{for } i_{batt} \leq 0 \\ \text{for } i_{batt} > 0 \end{cases} \quad (119)$$

Where:

- Q_{it} = The actual charge used from the battery

This calculates the actual charge that has gone in or out of the battery and implements the coulombic efficiency whilst the cell is charging during the simulation, addressing a limitation of the (Tremblay, and Dessaint 2009) model discussed in section 2.4.1.

$$\frac{d}{dt} Q_{iu} = \begin{cases} (i_{filt} * \eta) / 3600 \\ i_{filt} / 3600 \end{cases} \begin{cases} \text{for } i_{filt} \leq 0 \\ \text{for } i_{filt} > 0 \end{cases} \quad (120)$$

Where:

- Q_{iu} = The filtered charge used from the battery

This calculates the charge that has gone in or out of the battery when only considering the filtered current during the simulation, addressing a limitation of the (Tremblay, and Dessaint 2009) model discussed in section 2.4.1.

$$Q = Q_{cell} - Q_{it} \quad (121)$$

Where:

- Q = The actual charge remaining in the battery

This calculate the current capacity of the cell due to the charge that has been removed or added during the simulation (Tremblay, and Dessaint 2009).

$$SOC = \frac{Q}{Q_{cell}} \quad (122)$$

Here we calculate the SOC of the battery by using the parameterised capacity and the simulated capacity of the cell.

$$E0_c = V_{exp} \quad (123)$$

Where:

$E0_c$ = *The first of three equations that determine the baseline voltage of the battery during charging*

Here the baseline voltage has been defined for charging using the same approach as (Tremblay, and Dessaint 2009).

$$E1_c = (A_c * \exp((-B_c) * Q_{il})) \quad (124)$$

Where:

$E1_c$ = *The second of three equations that determine the baseline voltage of the battery during charging and due to the filtered current*

B_c = *Resistance which determines the exponential slope of the baseline voltage due to a change in the battery SOC*

Here we define the change in voltage due to the filtered current which has been removed or added to the battery cell using the same approach as (Tremblay, and Dessaint 2009).

$$E2_c = (-D) * \left(\frac{Q_{cell}}{Q} * Q_{it} \right) \quad (125)$$

Where:

$E2_c$ = *The third of three equations that determine the baseline voltage of the battery during charging and due to the current*

D = *Resistance which determines the slope of the baseline voltage due to a change in the battery SOC*

Here we define the change in voltage due to the current which has been removed or added to the battery cell using the same approach as (Tremblay, and Dessaint 2009).

$$E3_c = (-R_c * 0.2) * i_{filt} * \frac{Q_{cell}}{Q + Q_{cell}} \quad (126)$$

Where:

$E3_c$ = *The first of two equations that determine the dynamic voltage of the battery during charging and due to the filtered current*

R_c = *Direct Current Internal Resistance of the battery during charging*

Here we define the dynamic response of the battery due to the filtered current during charging using a similar approach to (Tremblay, and Dessaint 2009).

$$E4_c = (-R_c * 0.8) * i_{batt} * \frac{Q_{cell}}{Q + Q_{cell}} \quad (127)$$

Where:

$E4_c$ = *The second of two equations that determine the dynamic voltage of the battery during charging and due to the current*

Here we define the dynamic response of the battery due to the current during charging using a similar approach to (Tremblay, and Dessaint 2009).

$$V_{baseC} = E0_c + E1_c + E2_c \quad (128)$$

Where:

V_{baseC} = A sum of the base line voltage equations for charging

Here we define the base voltage due to the change in SOC during charging.

$$V_{dynC} = E3_c + E4_c \quad (129)$$

Where:

V_{dynC} = A sum of the dynamic voltage equations for charging

Here we define the dynamic voltage due to current flowing through the cell.

$$V_{cellC} = V_{baseC} + V_{dynC} \quad (130)$$

Where:

V_{cellC} = The cell voltage of the battery during charging

Here we determine the cell voltage during charging.

$$E0_d = V_{exp} \quad (131)$$

Where:

$E0_d$ = The first of three equations that determine the baseline voltage of the battery during discharge of the battery

Here the baseline voltage has been defined for discharge of the cell using the same approach as (Tremblay, and Dessaint 2009).

$$E1_d = (A_d * \exp((-B_d) * Q_{il})) \quad (132)$$

Where:

$E1_d$ = The second of three equations that determine the baseline voltage of the battery during discharge of the battery and due to the filtered current

B_d = Resistance which determines the exponential slope of the baseline voltage due to a change in the battery SOC

Here we define the change in voltage due to the filtered current which has been removed or added to the battery cell using the same approach as (Tremblay, and Dessaint 2009).

$$E2_d = (-D) * \left(\frac{Q_{cell}}{Q} * Q_{it} \right) \quad (133)$$

Where:

$E2_d$ = The third of three equations that determine the baseline voltage of the battery during discharge of the battery and due to the current

Here we define the change in voltage due to the current which has been removed or added to the battery cell using the same approach as (Tremblay, and Dessaint 2009).

$$E3_d = (-R_d * 0.2) * i_{filt} * \frac{Q_{cell}}{Q + Q_{cell}} \quad (134)$$

Where:

$E3_d$ = The first of two equations that determine the dynamic voltage of the battery during discharge of the battery and due to the filtered current

R_d = Direct Current Internal Resistance of the battery during discharge of the battery

CHAPTER 3 - Modelling

Here we define the dynamic response of the battery due to the filtered current flowing through the cell during discharge of the cell using a similar approach to (Tremblay, and Dessaint 2009).

$$E4_d = (-R_d * 0.8) * i_{batt} * \frac{Q_{cell}}{Q + Q_{cell}} \quad (135)$$

Where:

$E4_d$ = *The second of two equations that determine the dynamic voltage of the battery during discharge of the battery and due to the current*

Here we define the dynamic response of the battery due to the current flowing through the cell during discharge of the cell using a similar approach to (Tremblay, and Dessaint 2009).

$$V_{baseD} = E0_d + E1_d + E2_d \quad (136)$$

Where:

V_{baseD} = *A sum of the base line voltage equations during discharge of the battery*

Here we define the base voltage due to the change in SOC during discharge.

$$V_{dynD} = E3_d + E4_d \quad (137)$$

Where:

V_{dynD} = *A sum of the dynamic voltage equations during discharge of the battery*

Here we define the dynamic voltage due to current flowing through the cell during discharge.

$$V_{cellD} = V_{baseD} + V_{dynD} \quad (138)$$

Where:

V_{cellD} = *The cell voltage of the battery during discharge of the battery*

Here we determine the cell voltage during discharge.

$$v_{cell} = \begin{cases} V_{cellC} \\ V_{cellD} \end{cases} \begin{cases} [for i_{batt} \leq 0] \\ [for i_{batt} > 0] \end{cases} \quad (139)$$

Where:

V_{cell} = *Determines which cell voltage characteristics dependant on the flow direction of current*

Here we determine which cell voltage to use by defining that the negative current represents charging and the positive current represents discharging the cell

$$v = v_{cell} * n_s \quad (140)$$

Where:

v = *The voltage of the battery pack*

Here we calculate the battery pack voltage by multiplying the cell voltage by the number of cells connected in series.

The main difference between the model developed in this thesis using Dymola, and the proposed model by (Tremblay, and Dessaint 2009), within MATLAB/Simulink, is the independent voltage equations for charge and discharge of the cell, and the

implementation of a parametric coulombic efficiency, shown in equation (118), that reduces the rate of stored charge. Due to the quantity of parameters proposed, this battery model can be adapted to suit other types of cell chemistry and cell age. It can be seen from equations (111) to (139) that there are different parameters which affect the voltage curve during charge and discharge of the battery model. The additional variables allow for slightly better curve fitting when either validating the model or using the model for slightly different lithium ion chemistries.

Another important area of the battery pack is the BMS. Typically, the BMS can be described as a resistor that is switched on, to each cell, when the cell voltages within the battery pack start to become un-balanced, in terms of inter-cell voltage variation. The BMS can be a difficult to model where the battery is modelled as "semi ideal". This means that one pack is represented as many cells which are of identical SOC, capacity, internal resistance and age. In reality this is not the case because when cells age the voltage characteristics can change and, dependent on the pack design, the cells can age at different rates which creates cell voltage variation within the battery pack. Therefore, comparing model simulation results against an aged battery pack can be arduous, as the battery pack will not respond as an ideal voltage source. This is especially true at high SOC and low SOC.

This means that when the battery pack has aged it will have the BMS switching in the balance resistors more often when charging at higher SOC's, to ensure that all the cells within the battery pack are balanced to the same voltage.

3.9 Battery Management System Model

The BMS model has been created using Dymola and is shown in Figure 3-16. The methodology used in creating the BMS model is based on the discussion at the end of the previous section, section 3.8 and complies with the discussion around the paper by (Daowd et al. 2013) in the literature review, in section 2.4. It consists of a buck-boost convertor connected to a resistor which will increase the current draw on the battery dependant on the request from the BMS Drain model.

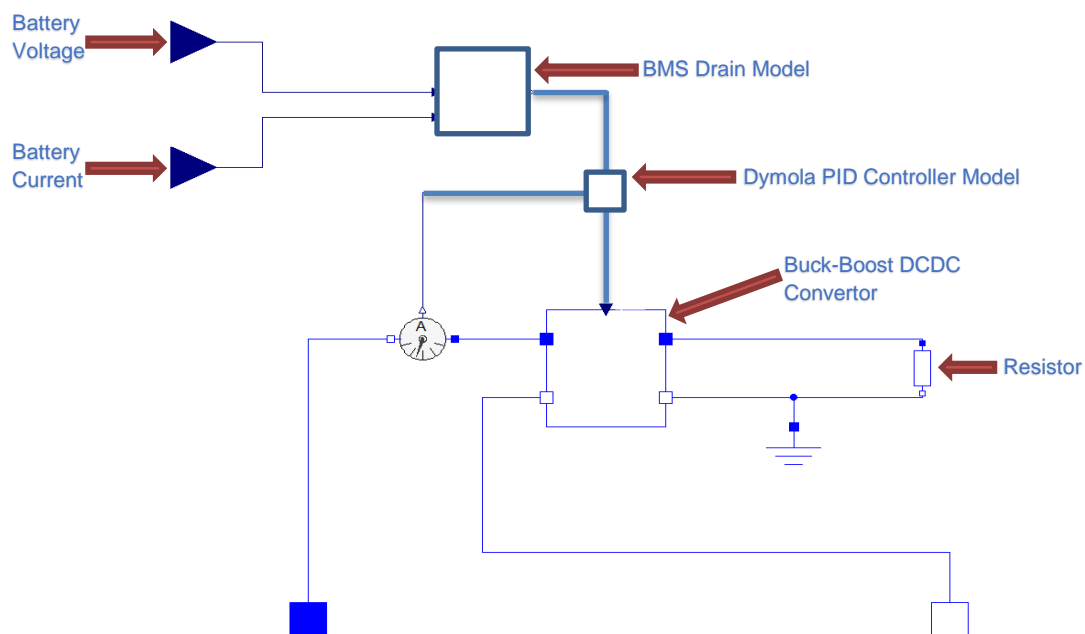


Figure 3-16 - Battery Management System Model

The BMS drain model consists of two main equations which have been generated and takes the voltage of the pack and the current flowing into the battery (charge current). It uses these two variables to decide the drain it should impose on the battery to prevent OVP's and reduce the current being supplied to the battery at the higher SOC values. The equations which have been created are presented below:

$$i_{loadI} = \left\{ \begin{array}{c} i_{minDrain} \\ \left(\left(\frac{i - i_{minDrainThres}}{i_{maxDrainThres} - i_{minDrainThres}} \right) * i_{maxDrain} \right) + i_{minDrain} * nS; \\ i_{maxDrain} * nS \end{array} \right\} \quad (141)$$

$$\left[\begin{array}{l} \text{for } i \leq i_{minDrain} \\ \text{for } i > i_{minDrainThres} \\ \text{for } i \geq i_{maxDrainThres} \end{array} \right]$$

Where:

- i = The current flowing through the battery
- i_{loadI} = The current load to be applied due to the current flowing through the battery
- $i_{minDrain}$ = The minimum current to draw from battery, a negligible amount of current
- $i_{maxDrain}$ = The maximum current to draw from the batter
- $i_{minDrainThres}$ = The current threshold which the the BMS starts applying a load
- $i_{maxDrainThres}$ = The current threshold where the maximum load is applied

Here we have created a parametric linear scale which increases the load from $i_{minDrain}$ to $i_{maxDrain}$ between $i_{minDrainThres}$ and $i_{maxDrainThres}$. We limit the i_{loadI} to the given $i_{minDrain}$ and $i_{maxDrain}$ to ensure that the load stays within the scale set by the parameters. Now that the load which is to be applied to the battery has been calculated, we can take the same approach to parametrically calculate when to apply that load based on the voltage of the battery, rather than current. This will ensure it is only active when the battery voltage is within its balancing voltage range.

$$i_{loadV} = \left\{ \begin{array}{c} i_{minDrain} \\ \left(\frac{v - (v_{thres} * nS)}{(v_{max} * nS) - (v_{thres} * nS)} * i_{loadI} \right) \\ i_{loadI} \end{array} \right\} \left[\begin{array}{l} \text{for } v \leq (v_{thres} * nS) \\ \text{for } v > (v_{thres} * nS) \\ \text{for } v \geq (v_{max} * nS) \end{array} \right] \quad (142)$$

Where:

- i_{loadV} = The current load to be applied due to the voltage at the battery terminals
- v_{max} = The maximum allowable voltage at the battert cell
- v_{thres} = The voltage threshold which the the BMS starts applying a load

Here the condition in which the BMS starts applying load on the battery has been determined via parameters. These two equations, i_{loadI} and i_{loadV} ensure that the load on the battery is only applied when the current is high as well as when the voltage is high. Therefore, if the voltage is high and the current is low, then negligible current will be loaded onto the cell.

$$y = i_{loadV} \quad (143)$$

Where:

- y = The output of the model which is sent to the Buck Boost converter which physically applies the load

'y' represents the output signal of the BMS drain which feeds a PID controller that controls the buck-boost convertor. These equations also allow for scenarios where zero current is being supplied to the battery, in this condition, only a negligible current will be drained by the BMS ensuring that the voltage of the battery can still reach the maximum voltage that the cell would when outside of the simulation environment.

The buck-boost DCDC convertor model has been formulated based on the Springers modelling approach as discussed in section 2.5 (Sira-Ramirez, and Silva-Ortigoza 2006). It uses a set of differential equations to determine the voltage and current output of the DCDC and has the resistance at the capacitor, resistance at the inductor, capacitance and inductance as the parameters. The model is set to calculate the resistance at both the input and the output to allow for versatility between different systems.

Figure 3-17 shows a simplified circuit diagram of a buck-boost DCDC convertor. The approach to create the DCDC model uses both of Kirchoff's first and second laws which is in conjunction with Springers modelling approach (Sira-Ramirez, and Silva-Ortigoza 2006) and (Dizqah, Busawon, and Fritzson 2012).

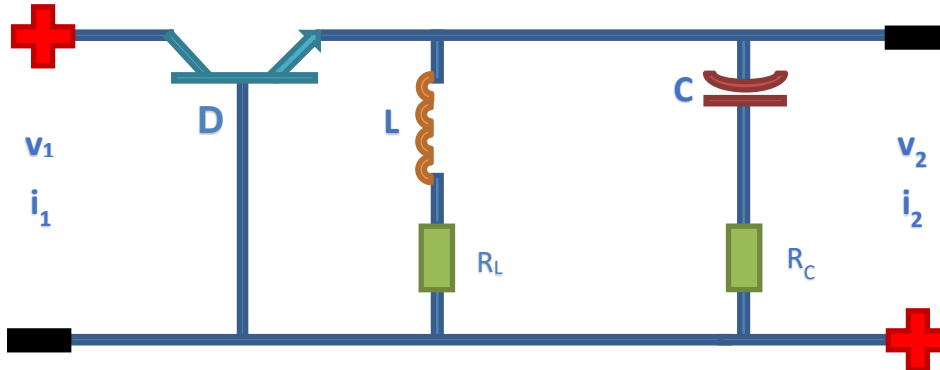


Figure 3-17 – Simplified Buck-Boost DCDC Schematic

The buck-boost DCDC convertor model has been modelled with the following formulation, in addition the model dynamically calculates the resistance of both the input and output device connected to the model:

$$R_2 = -v_2 / (i_2 + eps) \tag{144}$$

Where:

- R_2 = The resistance at the output of the DCDC
- v_2 = The voltage at the output of the DCDC
- i_2 = The current at the output of the DCDC
- eps = A negligible value to prevent divisions by zero

This is used to automatically calculate the resistance of the device connected to the output of the DCDC so that any electrical device can be connected to the output and the DCDC will retain its functionality.

$$R_{in} = -v_1 / (i_1 + eps) \quad (145)$$

Where:

R_{in} = The resistance at the input of the DCDC
 v_1 = The voltage at the input of the DCDC
 i_1 = The current at the input of the DCDC

This is used to automatically calculate the resistance of the device connected to the input of the DCDC so that any electrical device can be connected to the input and the DCDC will retain its functionality.

$$\frac{d}{dt} v_c = R_2 / ((R_2 + R_c) * C) * i_L - 1 / ((R_2 + R_c) * C) * V_c \quad (146)$$

Where:

v_c = The voltage at the capacitor
 R_c = The resistance at the DCDC capacitor
 C = The capacitance of the DCDC capacitor
 i_L = The current flowing through the inductor

Using Kirchhoff's Voltage Law, we can solve for the voltage at the capacitor using the same approach as (Dizqah, Busawon, and Fritzson 2012).

$$\frac{d}{dt} i_L = (- (R_L * R_2 + R_L * R_c + R_2 * R_c) / (L * (R_2 + R_c)) * i_L) - R_2 / (L * (R_2 + R_c)) * v_c + D / L * v_1 \quad (147)$$

Where:

i_L = The current flowing through the inductor
 R_L = The resistance at the inductor
 L = The inductance of the inductor
 D = The transistor state (input value 0 – 1)

Using Kirchhoff's Current Law we can solve for the current at the inductor using the same approach as (Dizqah, Busawon, and Fritzson 2012).

$$v_2 = v_c + R_c * C * \frac{d}{dt} v_c \quad (148)$$

Here we have calculated the output voltage due to the voltage at the capacitor using the same approach as (Dizqah, Busawon, and Fritzson 2012).

$$i_1 = D * i_L \quad (149)$$

Finally, we can determine what load is drawn from the input of the DCDC due to the value of the transistor state input (D) using the same approach as (Dizqah, Busawon, and Fritzson 2012).

Equation (144) to (149) show that the current is controlled by an input variable 'D', which is fed by a PID controller. This changes between 10^{-4} and 0.3 to regulate the current through the DCDC. The limitations of this model within Dymola are that it cannot be completely disconnected as divisions by zero occur and the model will fail to compile and simulate. Hence, the use of 10^{-4} as the minimum input for 'D' has been

CHAPTER 3 - Modelling

used and the repercussions of this, are that the DCDC will always draw a small amount of current. However, it is deemed negligible at this minimum value as only a value 0.01A is drawn from the battery pack.

3.10 Motor Model

The motor model has been developed using conventional modelling methods for electric motors (Gamazo-Real, Vázquez-Sánchez, and Gómez-Gil 2010). The model methodology which has been adopted provides the best characterisation of the motor when using parameters obtained from a manufacturer's datasheet. The model is based on the Modelica Electromotive Force (EMF) model which takes the current at the electrical pins and converts it to a torque at the flange by multiplying the current by an electrical torque constant (Modelica 2000-2013). However, the EMF model requires a switching type motor controller to apply the voltage and current to the EMF model. Therefore, the model was developed to include the motor controller model, within the motor itself. This means that the motor is to be supplied with a throttle signal, brake signal, electrical connector and rotation connector output. The final model can be seen in Figure 3-18, where two motors have been connected in parallel to represent the Coventry University Microcab H2EV.

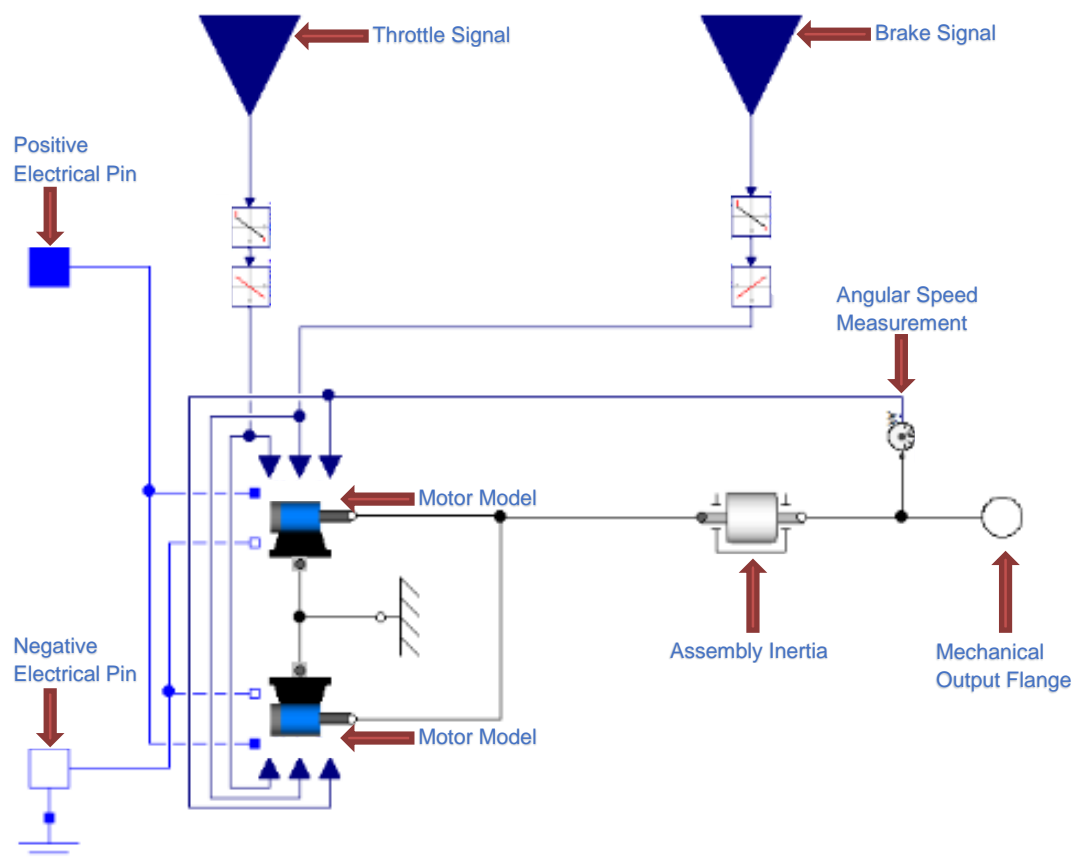


Figure 3-18 - Motor Model Overview

The motor controllers, in the Coventry University Microcab H2EV, can be set to apply regenerative braking, it was necessary to implement this into the model, as by doing so the energy recovered can be simulated by adjusting the regenerative braking

CHAPTER 3 - Modelling

strategy while testing the model. The model formulation used to create the motor models has been created using both first principles and checking the model results against manufacturer curves. The model formulation using this approach can be seen below:

$$\tau_{const} = \tau_{motorMaxP} / i_{motorMaxP} \quad (150)$$

Where:

- τ_{const} = *The electrical torque constant*
- $\tau_{motorMaxP}$ = *The maximum rotational torque supplied by the motor, parameter*
- $i_{motorMaxP}$ = *The maximum current supplied to the motor, to achieve the max torque, parameter*

Here we calculate the conversion between torque and current based on characteristics supplied by the most motor manufacturer datasheets.

$$k_{speed} = \left[\frac{RPM_{rated}}{v_{nominal}} - (RPM_{rated} * 0.001) \right] - \exp\left(\frac{RPM - RPM_{max}}{1000}\right) \quad (151)$$

Where:

- k_{speed} = *The characteristic of the back EMF of the motor (RPM/V)*
- RPM_{ratedP} = *The rated rotational speed of the motor, parameter*
- RPM_{maxP} = *The maximum rotational speed of the motor, parameter*
- RPM = *The rotational speed of the motor*
- $v_{nominalP}$ = *The rated working voltage of the motor, parameter*

Here we calculate the 'speed constant' which determines the back EMF of the motor. However, when the speed of the motor, in Revolutions per Minute (RPM), gets close to its maximum parameterised value, we reduce the speed constant using $\exp\left(\frac{RPM - RPM_{max}}{1000}\right)$ so that the EMF increases and ensures that the motor will not spin higher than the maximum speed.

$$v_{motor} = RPM / k_{speed} \quad (152)$$

Where:

- v_{motor} = *The back EMF of the motor*

Here we calculate the actual back EMF of the motor due to speed of the motor.

$$\tau = i_{Motor} * \tau_{const} \quad (153)$$

Where:

- τ = *The torque supplied or generated by the motor*
- i_{motor} = *The supplied or generated current at the motor*

Here the torque generated is calculated based on the current flowing through the motor. However, where the road can influence the torque applied to the motor, retardation of the vehicle without brakes, this also defines the law which generates current by the motor.

$$P_{motorOut} = \tau * RPM / 9.548 \quad (154)$$

Where:

- $P_{motorOut}$ = *The mechanical power at the motor*
- 9.548 = *A constant that converts RPM to frequency in hz*

Here we calculate the mechanical power which the motor produces, and this is used to determine the electromechanical efficiency of the motor.

$$P_{motorIn} = i_{motortotal} * v_{motor} \quad (155)$$

$$P_{motorIn} = v * i \quad (156)$$

Where:

$P_{motorIn}$ = The electrical power at the motor, and creates the relationship with i and v

$i_{motorTotal}$ = Determines the total current which is drawn across the electrical pin in the model

Here we have created the power relationship between some of the motor variables and the physical electrical connections of the model.

$$v = v_p - v_n \quad (157)$$

$$0 = i_p - i_n \quad (158)$$

$$i = i_p \quad (159)$$

Where:

v = The voltage between the positive pin and negative pin in the model

v_p = The voltage at the positive pin in the model

v_n = The voltage at the negative pin in the model

i = The current law across the positive pin and negative pin in the model

i_p = The current at the positive pin in the model

i_n = The current at the negative pin in the model

Here we define the electrical law between the physical electrical pin of the model and define the voltage potential between the pins and Kirchoff's current law.

$$i_{driveMotorCurve} = \left\{ \frac{[\tau_{motorMaxP} - \left(\exp\left(\frac{RPM - RPM_{maxP}}{1000}\right) * \tau_{motorMaxP}\right)]}{\tau_{const}} \right\} * Throttle \quad (160)$$

Where:

$i_{driveMotorCurve}$ = The current that the motor can provide based on RPM, the torque constant and the throttle

$Throttle$ = The throttle signal which is sent to the motor controller

This equation creates a torque limit which is determined by the motors speed to ensure that the motor cannot provide maximum torque as it reaches the maximum specified speed and is then scaled by the input of the throttle signal from the driver.

$$i_{MotorMax} = \left\{ \begin{array}{l} i_{DriveMotorCurve} \\ i_{MotorMaxP} \end{array} \right\} \left[\begin{array}{l} \text{for } i_{DriveMotorCurve} < i_{MotorMaxP} \\ \text{for } i_{DriveMotorCurve} \geq i_{MotorMaxP} \end{array} \right] \quad (161)$$

Where:

$i_{motorMax}$ = Limits the maximum current at the motor to that of the curve and the datasheet

This ensures that the motor will not draw more current than defined or if the motor current curve is more aggressive and allows for higher currents than specified, that the current is limited to the maximum value specified in the parameters.

$$Regen_{enable} = \left\{ \begin{array}{l} 0 \\ 1 \end{array} \right\} \left[\begin{array}{l} \text{for } |RPM| \leq RPM_{minSpeedP} \\ \text{for } |RPM| > RPM_{minSpeedP} \end{array} \right] \quad (162)$$

Where:

$Regen_{enable}$ = The boolean variable which enables the regenerative braking, when above a certain speed

$RPM_{minSpeedP}$ = The minimum speed which the motor can supply regenerative braking

This determines the speed in which the motor can provide regenerative braking and the production of current.

$$i_{regenMotorCurve} = \left\{ \frac{\left[\tau_{motorMaxP} - \left(\exp \left(\frac{RPM - RPM_{maxP}}{1000} \right) * \tau_{motorMaxP} \right) \right]}{\tau_{const}} \right\} * Brake \quad (163)$$

$* Regen_{enable}$

Where:

$i_{regenMotorCurve}$ = The current that the motor can provide based on RPM, the torque constant and the brake signal

Brake = The braking signal which is sent to the motor controller

Here we parameterise the regen curve the same way that we have characterised the drive curve.

$$i_{MotorBrakeMax} = \begin{cases} i_{regenMotorCurve} & \text{for } i_{regenMotorCurve} < i_{motorMaxP} \\ i_{motorMaxP} & \text{for } i_{regenMotorCurve} \geq i_{motorMaxP} \end{cases} \quad (164)$$

Where:

$i_{motorBrakeMax}$ = Limits the maximum current at the motor to that of the curve and the datasheet

Here we ensure that the motor will not provide more current than specified in the parameters during regenerative braking, essentially limiting the regen motor curve so that more aggressive curves can be parametrically implemented.

$$i_{Motor} = \begin{cases} -i_{regenMotorControllerLimitP} + i_{fan} \\ i_{motorMax} - i_{motorBrakeMax} \\ i_{maxMotorController} - i_{fan} \end{cases} \quad (165)$$

$$\begin{cases} \text{for } i_{motorMax} - i_{motorBrakeMax} \leq -i_{regenMotorControllerLimitP} + i_{fan} \\ \text{for } i_{motorMax} - i_{motorBrakeMax} > -i_{regenMotorControllerLimitP} + i_{fan} \\ \text{for } i_{motorMax} - i_{motorBrakeMax} \geq i_{maxMotorController} - i_{fan} \end{cases}$$

Where:

i_{motor} = Limits the current at the motor to that of the motor curve, the datasheet and includes the losses induced by the mechanical fan attached to the rotor

$i_{regenMotorControllerLimit}$ = Determines the regen current to apply when braking and infers a braking torque

i_{fan} = The electrical load induced by turning the mechanical fan

Here we calculate the actual current which flows across the motor which is either regenerated by road torque, retardation of the vehicle, or generated by pure current across the windings used to propel the vehicle. Here we introduce i_{fan} which is the electrical representation of the fan loss and is explained further after equation (167).

$$i_{motorTotal} = i_{Motor} + i_{fan} \quad (166)$$

Here the total current which is drawn by the motor is calculated. The current used to generate or regenerate torque and the current wasted which is used to turn the mechanical fan which is attached to the rotor.

$$P_{fan} = (RPM/RPM_{Max}) * P_{fanP} \quad (167)$$

Where:

P_{fan} = Determines an ideal loss of due to turning the mechanical fan, it is a linear relationship with RPM. Where the fan is used to remove heat from the motor, the power is used to determine maximum energy that this will be required to turn the fan at the motors maximum rotational speed

P_{fanP} = Sets the maximum equivalent cooling power of the mechanical fan attached to the rotor

Where the fan is a mechanical fan built into the rotor of the electric motor and is used to cool the motor windings during operation of the motor. The fan only spins at the speed of the motor and not independently of the motor, so it is not possible to use a typical electrical power equation like $P = i^2 * R$ to rotate the fan. The equivalent fan loss is higher at higher speeds, and the motor can draw high currents at low RPM. Thus, $P = i^2 * R$ inappropriate for the representation of this loss. However, $P = i^2 * R$ can be used alongside the armature resistance and the rated current of the motor to estimate the equivalent cooling power which the fan is likely to provide. Where, the equivalent cooling power is denoted as the parameter P_{fanP} . The fan has hereby been modelled as ideal, where the loss is linear in relation to the rotational speed of the motor.

$$i_{fan} = \frac{P_{fan}}{v} \quad (168)$$

Where:

i_{fan} = *Determines the current at the battery due to the loss of the mechanical fan attached to the rotor, due to the voltage across the motor*

Where the power consumption of the fan has been calculated the additional current, which is drawn at the electrical pins of the model can be calculated based on the input voltage of the motor.

$$\eta_{motor} = \frac{P_{motorOut}}{P_{motorIn}} \quad (169)$$

Where:

η_{motor} = *Calculates the efficiency of the motor*

Where both electrical power in and mechanical power out have been calculated earlier, here we can calculate the efficiency of the motor.

It can be seen from equation (156) that the drain on the battery is inferred by a combination of all the equations and by calculating both the back-EMF voltage, equation (151), and the torque conversion rate, the dynamic limit of the motor characteristics can be represented via a set of manufacturer datasheet parameters. Equation (161) determines the current to draw from the battery based on the motor characteristics, motor controller input settings and the throttle request. Equation (162) determines the current to charge the battery based on the motor characteristics, motor controller input settings, torque generated at the motor and the brake request. Equation (153) determines the torque provided by the motor and the regenerative braking energy created by the motor due to the inter-dependant equations shown above. To ensure model stability, dynamic rate limiters and the limiters have been applied to the brake and throttle signal so that no signals can instantaneously change, creating an event, or go out of range for the model. The full Dymola Motor Model code can be found in APPENDIX B – Model Code.

3.11 Control Model

Currently the Coventry University Microcab H2EV's VCU is dedicated to safety of the driver and is very basic in terms of dynamic handling control. However, as driver safety and sensor checking is not a main concern for this project the original H2EV VCU has not been implemented. Instead, a proposed VCU has been created so that throttle control algorithms can be tested to assess operational efficiency. Therefore, the following throttle control model has been created to determine if it would benefit the vehicle's overall range and efficiency. A control strategy that reduces the maximum throttle signal sent to the motor controller as the SOC of the battery is reduced would be of benefit to the client. This is where the given vehicle has a problem with battery LVP emergency shutdowns when the battery SOC is 45% and the vehicle has a high throttle demand from the driver. It suggests if a reduced throttle signal was implemented, then they would be able to consistently use more of the available capacity from the battery without creating an LVP emergency shutdown condition. Therefore, the following mathematical control model has been created and implement into the vehicle model:

$$\Delta T = T_{max} - T_{min} \quad (170)$$

Where:

ΔT = *The throttle range*
 T_{max} = *The maximum throttle value, typically 100%*
 T_{min} = *The lower value which the throttle will be limited to*

Here we calculate the range which the throttle will adjust.

$$\Delta SOC = SOC_{max} - SOC_{min} \quad (171)$$

Where:

ΔSOC = *The State of Charge range*
 SOC_{max} = *The SOC value which T_{max} is applied*
 SOC_{min} = *The SOC value which T_{min} is applied*

Here we calculate the SOC range where the throttle limiting is active.

$$\Delta TSOC = \Delta T / \Delta SOC \quad (172)$$

Where:

$\Delta TSOC$ = *The gain of the throttle limit*

Here we calculate the gain for which the dynamic limit on the throttle should operate based on both the SOC parameters and the throttle parameters.

$$Dyn_{soc} = \Delta TSOC * (SOC - (SOC_{max} - ((T_{max} - \Delta TSOC) / \Delta TSOC))) \quad (173)$$

Where:

Dyn_{soc} = *The result of the scaled and gained throttle limit*
 SOC = *The State of Charge of the battery*

Here we scale and gain the signal for the throttle limiter based on the SOC of the battery.

$$Dyn_{limSOC} = \begin{cases} T_{min} \\ Dyn_{soc} \\ T_{max} \end{cases} \left[\begin{array}{l} for\ Dyn_{soc} \leq T_{min} \\ for\ Dyn_{soc} > T_{min} \\ for\ Dyn_{soc} \geq T_{max} \end{array} \right] \quad (174)$$

Where:

Dyn_{limSOC} = The dynamic limit to be applied to the throttle

Here we saturate the value of the limit to the maximum and minimum throttle values set in the parameters.

$$T_{Out} = \begin{cases} 0 \\ T_{In} \\ Dyn_{limSOC} \end{cases} \left[\begin{array}{l} for\ T_{In} \leq 0 \\ for\ T_{In} > 0 \\ for\ T_{In} \geq Dyn_{limSOC} \end{array} \right] \quad (175)$$

Where:

T_{Out} = The limited throttle signal

T_{In} = The input throttle signal

Here we process the throttle signal and saturate it, if it is above the dynamic limit.

Through simulation and brief testing, Equations (170) to (175) provide an additional two miles to the total range of the vehicle. However, it can be seen from the equations that this limits the actual top speed of the vehicle rather than just the acceleration. Physical testing proved that the vehicle would still accelerate well when the throttle was limited to 60%, however, the control prevented the vehicle from achieving its top speeds when in this condition. Figure 3-19 shows how the throttle is limited as the SOC of the battery is reduced between the two thresholds.

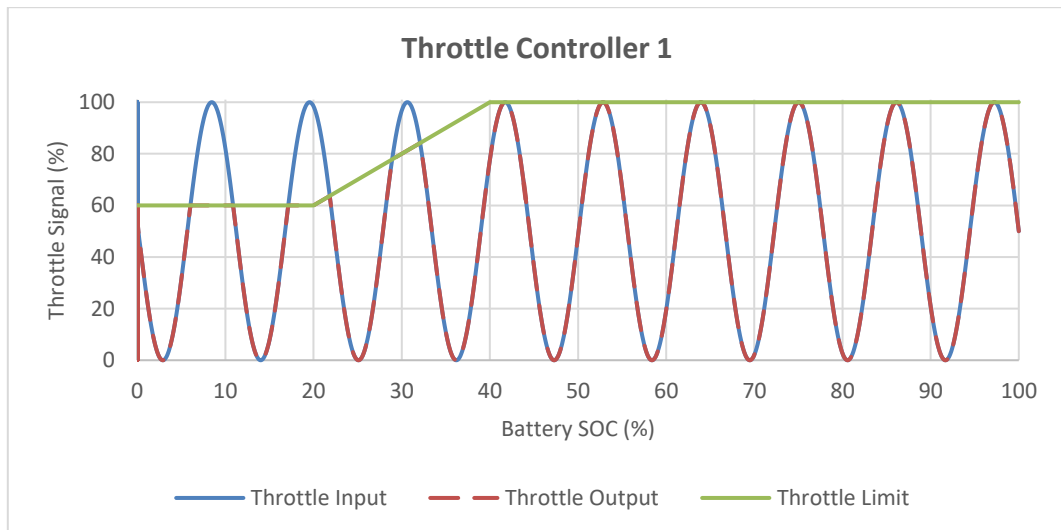


Figure 3-19 - SOC Throttle Restrictive Control Result

Figure 3-19 shows the input throttle request by the driver in blue. It shows that when the SOC of the battery is below 40% (X-Axis) the driver is still requesting more than the throttle limit which is shown as the green line in the chart. Figure 3-19 shows the output of the throttle as a dashed-line, which has been superimposed on the graph, and it can be seen that the input signal (blue) is being saturated to the throttle limit

shown in green and the saturated throttle output is the dashed-line. Therefore, the input is equal to the output unless it is above the throttle limit, if the input is greater than the throttle limit then the output is the throttle limit.

During an initial test, a further development on the created throttle algorithm was conducted and designed. This is to initially restrict the throttle to 60% until a speed of 20 mph then to gradually ramp up to the maximum throttle value, throughout the SOC of the battery. This strategy was implemented in the same manner as the previous one, except that the SOC was replaced with the vehicle speed. Therefore, the developed model formulation is presented below:

$$\Delta V = V_{max} - V_{min} \quad (176)$$

Where:

ΔV = The velocity range
 V_{max} = The velocity of the vehicle which T_{max} is applied
 V_{min} = The velocity of the vehicle which T_{min} is applied

Here we calculate the range, based on vehicle velocity, where the throttle limiting is active.

$$\Delta TV = \Delta T / \Delta V \quad (177)$$

Where:

ΔTV = The gain of the throttle limit

Here we calculate the gain for which the dynamic limit on the throttle should operate based on both the vehicle speed parameters and the throttle parameters.

$$Dyn_V = \Delta TV * (V - (V_{max} - ((T_{max} - \Delta TV) / \Delta TV))) \quad (178)$$

Where:

Dyn_V = The result of the scaled and gained throttle limit
 V = The velocity of the vehicle

Here we scale and gain the signal for the throttle limiter based on the velocity of the vehicle.

$$Dyn_{limV} = \begin{cases} T_{min} \\ Dyn_V \\ T_{max} \end{cases} \left[\begin{array}{l} \text{for } Dyn_V \leq T_{min} \\ \text{for } Dyn_V > T_{min} \\ \text{for } Dyn_V \geq T_{max} \end{array} \right] \quad (179)$$

Where:

Dyn_{limV} = The dynamic limit to be applied to the throttle

Here we saturate the value of the limit to the maximum and minimum throttle values set in the parameters.

$$T_{Out} = \begin{cases} 0 \\ T_{In} \\ Dyn_{limV} \end{cases} \left[\begin{array}{l} \text{for } T_{In} \leq 0 \\ \text{for } T_{In} > 0 \\ \text{for } T_{In} \geq Dyn_{limV} \end{array} \right] \quad (180)$$

Where:

T_{Out} = The limited throttle signal
 T_{In} = The input throttle signal

Here we process the throttle signal and saturate it, if it is above the dynamic limit.

Figure 3-20 shows how the throttle is limited dependant on the speed of the vehicle between the two thresholds.

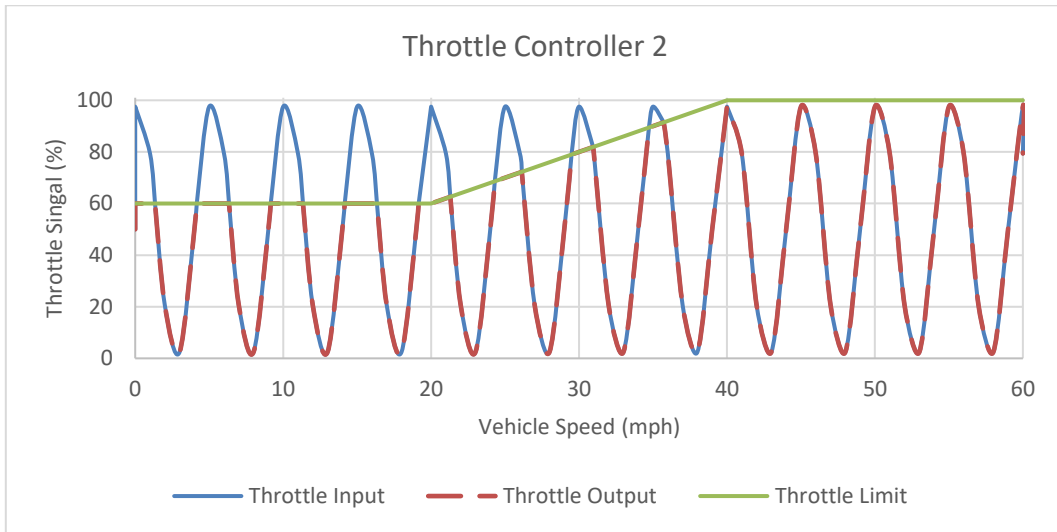


Figure 3-20 - Vehicle Speed Throttle Restrictive Control Results

Figure 3-20 shows the input throttle request by the driver in blue. It shows that when the speed of the vehicle is below 20 mph (X-Axis) the driver is still requesting more than the throttle limit which is shown as green in the chart. Figure 3-20 shows the output of the throttle as dashed-line, which has been superimposed on the graph, and it can be seen that the input signal (blue) is being saturated to the throttle limit shown in green and the saturated throttle output is the dashed-line. Therefore, the input is equal to the output unless it is above the throttle limit, if the input is greater than the throttle limit then the output is the throttle limit.

From discussing the previous vehicle control strategies with the clients, it was thought that the vehicle might benefit from both throttle control algorithms, where the initial SOC based algorithm provided a limp home mode that has the ability to advise the driver to stop and charge the batteries, by allowing the fuel cell to catch up and charge. The second control algorithm is likely to reduce the average energy consumption of the vehicle by preventing over acceleration and stalling the motors. Therefore, using equations (170) to (174) and equations (176) to (179) this led to the following model formulation:

$$Dyn_{lim3} = \begin{cases} Dyn_{limV} & \text{for } Dyn_{limV} < Dyn_{limSOC} \\ Dyn_{limSOC} & \text{for } Dyn_{limV} \geq Dyn_{limSOC} \end{cases} \quad (181)$$

Where:

Dyn_{lim3} = The dynamic limit to be applied to the throttle based on both Dyn_{limV} and Dyn_{limSOC}

Here we prioritise the SOC limit over the speed limit, the speed limit is always active, however, if the SOC limit is lower than that of the speed limiter then the SOC limiter takes priority.

$$T_{Out} = \begin{cases} 0 \\ T_{In} \\ Dyn_{lim3} \end{cases} \begin{bmatrix} \text{for } T_{In} \leq 0 \\ \text{for } T_{In} > 0 \\ \text{for } T_{In} \geq Dyn_{lim3} \end{bmatrix} \quad (182)$$

Where:

T_{Out} = The limited throttle signal

T_{In} = The input throttle signal

Here we process the throttle signal and saturate it, if it is above the dynamic limit.

Figure 3-21 shows how the maximum throttle is limited dependant on both the speed of the vehicle, between the two thresholds, and the SOC of the battery. The throttle is initially limited when the speed is below 20 mph and gradually ramps up as the speed increases to 40 mph where full throttle is allowed. It also shows how the throttle is then slowly reduced when the battery SOC hits the upper threshold and gradually reduces this to the lower throttle value at the lower SOC value. The dynamic limit can be seen below, as the green line, in the upper graph of Figure 3-21 and the parameters used for the example shown in Figure 3-21 are below:

T_{max}	=	100	%
T_{min}	=	60	%
SOC_{max}	=	60	%
SOC_{min}	=	40	%
V_{max}	=	40	mph
V_{min}	=	20	mph

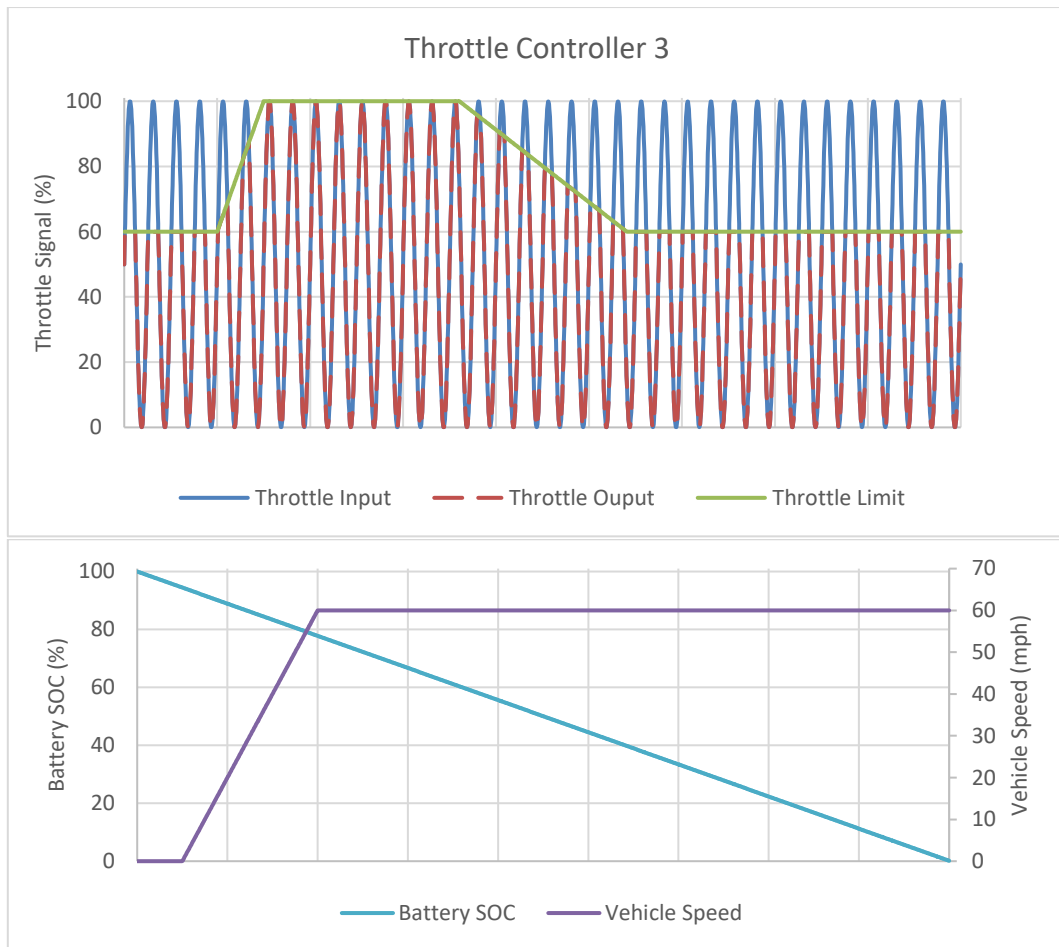


Figure 3-21 - SOC & Vehicle Speed Restrictive Control Results

Figure 3-21 can appear to be complicated, however, it is very useful to show the functionality of 'Throttle Controller 3'. The top chart within Figure 3-21 shows the same information as the previous examples, where the throttle input request by the driver *is* blue, the throttle limit of the controller *is* green, and the throttle output of the controller *is* the dashed-line, which has been superimposed on the graph. By comparing the values in the lower chart with that of the upper chart and the parameters, we can see that when the vehicle speed, in the lower chart, gets to 20 mph the throttle limit in the upper chart starts increasing the limit from 60% throttle until the vehicle speed, in the lower chart, reaches 40 mph and then the throttle limit, in the upper chart, reaches its maximum, 100%. It can also be seen that when the battery SOC in the lower chart reaches 60% the throttle limit, in the upper chart, starts reducing from 100% down to 60% throttle. The throttle is reduced to that 60% when the battery SOC, in the lower graph gets to 40% SOC. Thus, the graph is capable of quickly showing both the functionality of the controller and that the mathematics applied is functioning as expected.

3.12 Fuel Cell Model

The fuel cell model has been primarily based on the steady state model by (Benchouia et al. 2013). The justification for the adoption of this modelling technique is given in section 2.5.1, and a steady state model has been chosen because the fuel cell will be used under loads which are relatively stable. The intended model will be simulated with a vehicle which has a battery as a power buffer and the control of the fuel cell will be done by the DCDC which allows the fuel cell to run at a consistent power output. The fuel cell model which has been implemented into Dymola uses a set of differential equations to determine the voltage dependant on current draw (Benchouia et al. 2013). However, the way temperature has been implemented into the model has been developed to better reflect the processes within the fuel cell. Equations supplied by Ballard Power System have been used to determine the heat energy generated when producing current, which is then referenced from the fuel cell model (Ballard Power Systems Inc. 2014). This heat generated is fed to a Modelica heat port which outputs the temperature of the fuel cell. The temperature is then used back within the voltage equations so that the characteristics of the fuel cell will change dependant on the fan control of the fuel cell. Therefore, a PID fan controller is required to fully utilise the fuel cell model including thermal management. A Boolean parameter has been added so that if the heat port is not required, for a simulation, it can be disabled. Thus, the fuel cell model can run as a basic simulation that represents running at one constant temperature defined within the parameters. Equations (183) - (195) represent how the electrical side of the fuel cell model has been created and equations (196) - (198) represent the thermal characteristics of the fuel cell:

$$P_{O_2} = P_{cath} * \frac{(1 - X)}{1 \times 10^5} \quad (183)$$

Where:

P_{O_2} = The partial pressure of oxygen at the cathode
 P_{cath} = The pressure at the cathode
 X = The water content in the membrane

Here we calculate the partial pressure of oxygen at the cathode based on the pressure and the humidity of the of the air at the cathode by using the same approach as (Benchouia et al. 2013).

$$P_{H^2} = P_{anode} * \frac{(1 - 0.5 * X)}{1 \times 10^5} \quad (184)$$

Where:

P_{H^2} = The partial pressure of hydrogen at the anode
 P_{anode} = The pressure at the anode

Here we calculate the partial pressure of hydrogen at the anode based on the pressure and the humidity of the of the hydrogen at the anode by using the same approach as (Benchouia et al. 2013).

$$C_{O_2} = \frac{P_{O_2}}{5.08_{x10^6} * \exp(-498 / T)} \quad (185)$$

Where:

C_{O_2} = The concentration of oxygen dissolved in water
 T = The temperarute of the fuel cell in Kelvin

Here we calculate the concentration of oxygen which is in the water due to the temperature of the fuel cell by using the same approach as (Benchouia et al. 2013).

$$J = \begin{cases} 0 \\ \frac{I_{FC}}{I_{max}} * J_{max} \\ J_{max} \end{cases} \left[\begin{array}{l} \text{for } \frac{I_{FC}}{I_{max}} * J_{max} \leq 0 \\ \text{for } \frac{I_{FC}}{I_{max}} * J_{max} > 0 \\ \text{for } \frac{I_{FC}}{I_{max}} * J_{max} \geq J_{max} \end{array} \right] \quad (186)$$

Where:

J = The active current density of the cell
 I_{FC} = The current produced by the fuel cell
 I_{max} = The maximum current that the fuel cell can produce
 J_{max} = The maximum current density of the fuel cell

Here we calculate the current density of the fuel cell by using the same approach as (Benchouia et al. 2013). Then we ensure that it cannot exceed what is defined in the parameters by using a conditional statement.

$$r_m = 181.6 * \frac{1 + 0.03 * \frac{J}{J_{max}} + 0.062 * \frac{T^2}{303} * \frac{I_{FC}^{2.5}}{A}}{\left(X - 0.634 - 3 * \frac{I_{FC}}{A}\right) * \exp\left(4.18 * \frac{T - 303}{T}\right)} \quad (187)$$

Where:

r_m = The specific resistivity of the membrane for electron flow
 A = The active area of the membrane

Here we calculate the specific resistivity of the membrane based on the temperature, active area of the membrane and the current density of the membrane by using the same approach as (Benchouia et al. 2013).

$$R_m = r_m * \frac{t}{A} \quad (188)$$

Where:

R_m = The equivalent resistance of the membrane for electron flow
 t = The thickness of the membrane

Here we calculate the equivalent resistivity of the membrane due to it physical size by using the same approach as (Benchouia et al. 2013).

$$N_{ohm} = I_{FC} * (R_m + R_C) \quad (189)$$

CHAPTER 3 - Modelling

Where:

N_{ohm} = The ohmic voltage loss

R_c = The resistance to the transfer of protons through the membrane

Here we calculate the ohmic voltage loss due to the resistance for electron flow and the resistance to the transfer of protons. This represents a high proportion of the loss of voltage at high loads and the same approach as (Benchouia et al. 2013) has been used.

$$N_{con} = -B * \ln\left(1 - \frac{J}{J_{max}}\right) \quad (190)$$

Where:

N_{con} = The concentration voltage loss

B = A parametric coefficient, - 1.022

Here we calculate the concentration voltage loss due to the active area of the membrane. These assists ' R_m ' in characterising the loss of voltage at high loads. The same approach as (Benchouia et al. 2013) has been used.

$$N_{act} = \begin{cases} -S_1 + S_2 * T + S_3 * T * \ln|C_{O_2}| & \text{for } I_{FC} \leq 0.001 \\ -S_1 + S_2 * T + S_3 * T * \ln|C_{O_2}| + S_4 * T * \ln I_{FC} & \text{for } I_{FC} > 0.001 \end{cases} \quad (191)$$

Where:

N_{act} = The activation voltage loss

S_1 = A parametric coefficient, 1.215

S_2 = A parametric coefficient, 0.044

S_3 = A parametric coefficient, - 0.003

S_4 = A parametric coefficient, 0.012

Here we calculate the activation voltage loss based on coefficients obtained by curve fitting and use an if statement to ensure that logarithms of zero do not occur at zero loads. This represents a large quantity of the voltage loss over the whole current production range of the fuel cell. However, it is mostly responsible for the exponential voltage loss at low currents. To achieve this, the same approach as (Benchouia et al. 2013) has been used.

$$N_{diff} = 2 * (1 - \exp(I_{FC} - I_{max})) - |(1 - \exp(I_{FC} - I_{max}))| \quad (192)$$

Where:

N_{diff} = The gas diffusion voltage loss

Here we calculate the gas diffusion voltage loss, where the voltage is rapidly reduced when more current is drawn from the fuel cell than it can provide using the same approach as (Benchouia et al. 2013).

$$E_{nerst} = 1.229 - 8.5_{x10^{-4}} * (T - 298.15) + 4.31_{x10^{-5}} * T * (\ln|P_{H_2}| + 0.5 * \ln|P_{O_2}|) \quad (193)$$

Where:

E_{nerst} = The thermodynamic potential of the cell

Here we calculate the thermodynamic potential of the cell, Nernst voltage, which is typically the open circuit voltage of the fuel cell, irrespective of current, when the fuel

cell is operating under normal conditions using the same approach as (Benchouia et al. 2013).

$$v_{cell} = \left\{ \frac{E_{nerst} * n_s - N_{ohm} - N_{con} - N_{act} - N_{diff}}{n_s} \right\} \quad (194)$$

$$\left[\begin{array}{l} \text{for } \frac{E_{nerst} * n_s - N_{ohm} - N_{con} - N_{act} - N_{diff}}{n_s} \leq 0 \\ \text{for } \frac{E_{nerst} * n_s - N_{ohm} - N_{con} - N_{act} - N_{diff}}{n_s} > 0 \end{array} \right]$$

Where:

v_{cell} = The voltage of a single cell within the fuel cell
 n_s = The number of cells in series within the fuel cell

Now we can calculate the cell voltage for the fuel cell using the same approach as (Benchouia et al. 2013).

$$v_{fc} = v_{cell} * n_s \quad (195)$$

Where:

v_{fc} = The voltage of the whole fuel cell

Now we can calculate the voltage for the fuel cell.

$$\frac{d}{dt} Q_{created} = n_s * (E_{nerst} - V_{cell}) * \frac{I_{FC}}{3600} \quad (196)$$

Where:

$Q_{created}$ = The heat produced by fuel cell

Now we can calculate the heat that the fuel cell produces and apply it to the heat port to calculate dynamic temperature of the fuel cell (Ballard Power Systems Inc. 2014).

$$Q_{fan} = -P_{fan} * V_{fan} * \eta_{fan} \quad (197)$$

Where:

Q_{fan} = The heat removed by by fuel cell's cooling fan
 η_{fan} = The efficiency of the fuel cell cooling fan
 P_{fan} = The power of the fuel cell cooling fan
 V_{fan} = The velocity of the cooling fan as a percentage from max

Now we can calculate the heat that is removed by the fuel cell's cooling fan and apply it to the heat port to calculate the dynamic temperature of the fuel cell.

$$Q_{loss} = Q_{created} + Q_{fan} \quad (198)$$

Where:

Q_{loss} = The heat lost at the thermal connector of the fuel cell

Here we have added the production and removal of heat to the thermal connector of the fuel cell, which can affect and be affected by ambient conditions.

The other area of fuel cell modelling which is of interest is the hydrogen (H₂) consumption. Therefore, the implementation of gas flow via the tools found in the Dymola packages, 'Smart Electric Drive' package and the 'Pneumatics' package, enabled the use of dynamic hydrogen flow. The H₂ system has been implemented via

an enabled Boolean parameter and has been modelled as an extended model. This allows, the option to disable the H₂ system, within the model, to reduce simulation time if the user is not concerned about the H₂ consumption. The extended model consists of a H₂ tank, 1st stage pressure regulator, 2nd stage pressure regulator, stack resistance, purge valve, reacted hydrogen non-return valve, a standard non-return valve and an exhaust to atmosphere. One of the non-return valves is used on the purge line which sole use is to prevent any gases flowing backwards into the system when fuel cell stack pressures are low. The second, reacted hydrogen, non-return valve is used to represent the reacted H₂ gas by the fuel cell and is essentially modelled as a dynamic leak.

The reacted H₂ gas model (modified non-return valve) has an additional input which takes a reference current from the fuel cell and uses equation (199) to determine the mass flow rate of the of the non-return valve. The relationship between the mass flow rate and the current output of the fuel cell was established by a combination of test data and published data from Ballard (Ballard Power Systems Inc. 2014). In equation (199) \dot{m} represents the mass flow rate of the non-return valve and determines the hydrogen consumption based on both the output current of the fuel cell and the number of cells in series (Ballard Power Systems Inc. 2014).

$$\dot{m} = i * n_s * 1.04_{x10^{-8}} \quad (199)$$

Where:

\dot{m} = *The mass flow rate of hydrogen due to current production of the fuel cell*

Figure 3-22 shows the layout of the H₂ system model. The example shown in Figure 3-22 uses the test data to feed the fuel cell controller and the reacted consumption model. This enabled the validation of the H₂ system model prior to the implementation of the full fuel cell system model, both, the pressure within the hydrogen tank and the H₂ volume flow rate between the 5 bar regulator and the 1.5 bar regulator, can be directly compared to that of the H₂ tank pressure and the H₂ volume flow log file during post processing. Additionally, equations (200) and (201) have been created and added into the H₂ system model to display the percentage difference between the simulation and the test data as an error.

$$\varepsilon_{PH2} = \left| 1 - \frac{P_{tankTest}}{P_{tankSim}} \right| * 100; \quad (200)$$

Where:

ε_{PH2} = *The error between the simulation and test data*

$P_{tankTest}$ = *The pressure at the hydrogen tank during testing*

$P_{tankSim}$ = *The pressure at the hydrogen tank during the simulation*

Here we calculate the error for the hydrogen pressure between the simulation and the test environment.

$$\varepsilon_{vFlow} = \left| 1 - \frac{VFR_{5barTest}}{VFR_{5barSim}} \right| * 100 \quad (201)$$

Where:

- ε_{vFlow} = The error between the simulation and test data
 $VFR_{5barTest}$ = The volume flow rate at the 5bar regulator during testing
 $VFR_{5barSim}$ = The volume flow rate at the 5bar regulator during the simulation

Here we calculate the error for the hydrogen flow rate between the simulation and the test environment.

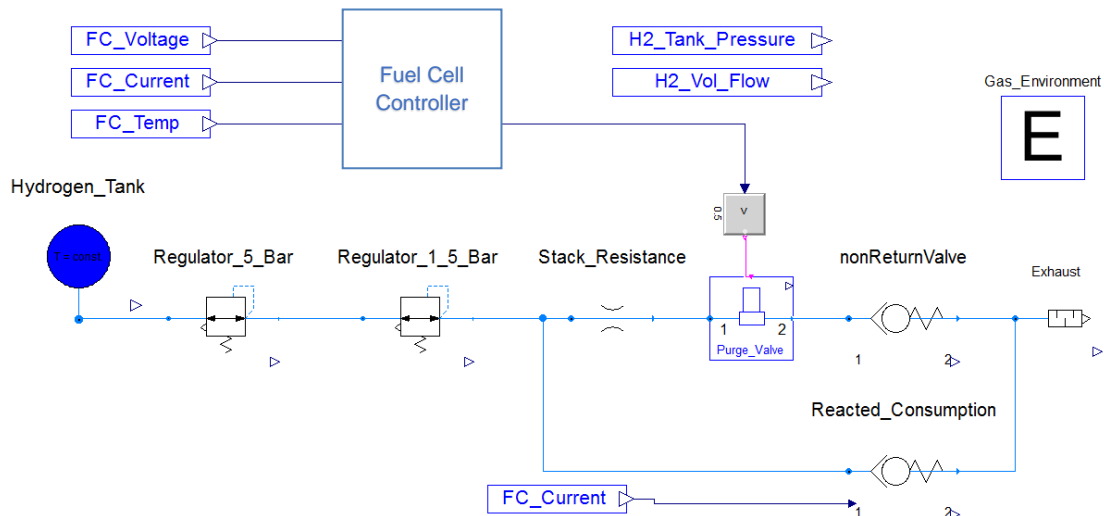


Figure 3-22 - Hydrogen System Model

As the original Dymola 'Pneumatics', 'airVolumelsotherm' tank model was designed to only represent air, the addition of hydrogen density has been implemented as a parameter and equations (202) to (205) have been developed, in order, to define the start condition as a pressure, rather than a mass, so that the initial conditions matching that of the test data can be met. The implementation of volume flow rate as a variable was also necessary in order to provide a direct comparison between the volume flow rate sensor and the simulation results.

$$m(start = \frac{P_{initial} * v}{R * T_{environment}}) \quad (202)$$

Where:

- m = The mass of hydrogen in the tank
 $start$ = This ensures that the equation is only used at the start of the simulation
 $P_{initial}$ = The start pressure of the hydrogen tank for the simulation, parameter
 v = The physical volume of the hydrogen tank
 R = The specific gas constant of hydrogen
 $T_{environment}$ = The ambient temperature of the environment

Here we determine the start conditions for the hydrogen tank by using the ideal gas law to calculate the mass of hydrogen in the tank based on the initial pressure, the volume of the tank and the temperature of the environment.

$$\frac{d}{dt}m = \dot{m}_{tank} \quad (203)$$

Where:

\dot{m}_{tank} = *The mass flow rate at the tank*

Here we calculate the mass remaining in the tank due to the flow of hydrogen during the operation of the fuel cell.

$$V_{slpm} = \frac{-\dot{m}_{tank} * 1000}{\rho_{H2}} * 60 \quad (204)$$

Where:

V_{slpm} = *The volume flow rate at the tank*

ρ_{H2} = *The density of hydrogen*

Here we can calculate the hydrogen volume flow rate out of the hydrogen tank in standard litres per minute for comparison with the test results by using a derivative of the ideal gas law

$$m_{used} = \frac{P_{initial} * v}{R * T_{environment}} - m \quad (205)$$

Where:

m_{used} = *The hydrogen used since the start of the simulation*

Here we can calculate the hydrogen used within the simulation in kg. This is achieved by using the ideal gas law with the start parameters and the mass of hydrogen in the tank throughout the simulation.

3.13 Fuel Cell Controller Model

Figure 3-23 shows the contents of fuel cell controller model. This has been modelled in accordance to the 'Ballard Power Systems 1080AC fuel cell user integration guide'. The guide is a document supplied by Ballard Power Systems and dictates how their '1080AC series' fuel cells should be controlled (Ballard Power Systems Inc. 2014). As the fuel cell which will be used in the validation stage of the project is a Ballard Power Systems 1080AC fuel cell, it is necessary to control the fuel cell model in the same manner.

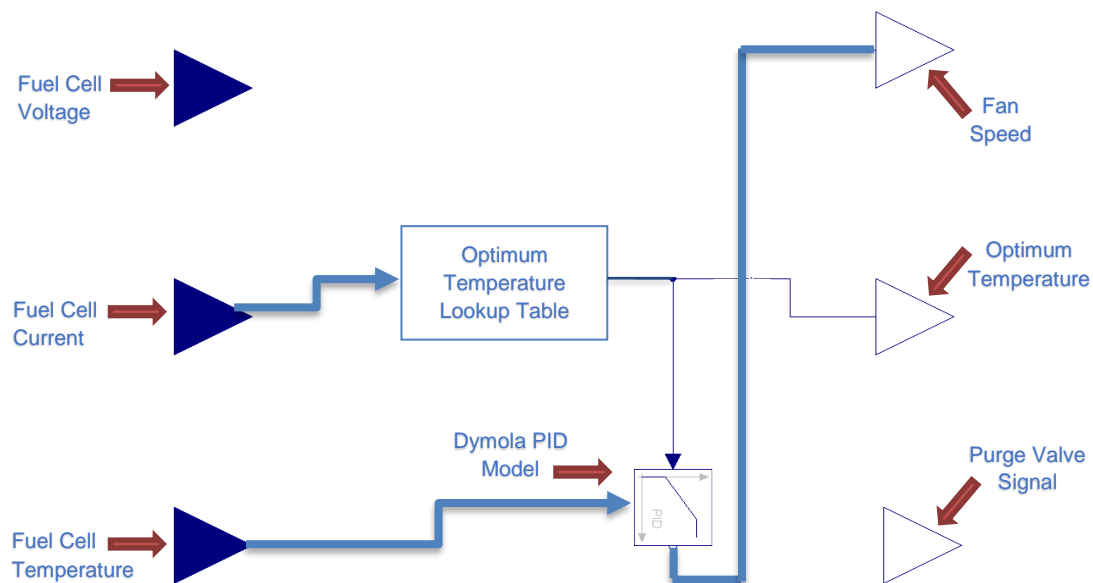


Figure 3-23 - Fuel Cell Controller Model

The fuel cell controller model's main purpose is to control the fuel cell fan and the purge interval of the hydrogen purge valve. The temperature range in which the fuel cell should be operated, is determined by the fuel cell current output. Therefore, it takes a reference current from the fuel cell and feeds it to a parametric lookup table which outputs the correct temperature to operate the fuel cell, based on Ballard's 1080AC user manual, to the reference input of the PID controller. The PID controller increases or decreases the output of the fan speed dependant on this, with a delay of 2 seconds to enable some hysteresis in the results and to aid the reality of the simulation results. The purge control is based on a coulomb count of the current which the fuel cell is producing. The model will use the integral of current until a parameterised value of 2300 As has been reached, at this point the controller will output a value of 1, on the purge output, for the parameterised purge duration of 0.2s. After 0.2s of a purge duration has been reached the model then resets both the coulomb count and the

purge output to 0 to restart the procedure (Ballard Power Systems Inc. 2014). Where Ballard Power Systems only provide written description of how to operate the fuel cell, equations (206) to (209) have been created and are presented below. These equations define the purge output control mathematically.

$$\frac{d}{dt}y = i \quad (206)$$

Where:

y = *The Integral of current*
 i = *The current produced by the fuel cell*

Here we create a coulomb counter to count the current which is produced by the fuel cell.

$$\left. \begin{array}{l} \text{when, } y < y_{interval} \\ \text{when, } y \geq y_{interval} \ \& \ t \leq y_{duration} \\ \text{when, } t > y_{duration} \end{array} \right\} \quad (207)$$

$$= \left[\begin{array}{lll} reinit(t,0) & f = 0 & \frac{d}{dt}t = 0 \\ reinit(t,0) & f = 1 & \frac{d}{dt}t = \Delta t \\ reinit(t,0) & reinit(y,0) & f = 0 \end{array} \right]$$

Where:

$y_{interval}$ = *The interval in which the purge valve is closed, parameter*
 $y_{duration}$ = *The duration in which the purge valve is open, parameter*
 t = *The time counter*
 $reinit(,)$ = *A Modelica function which resets the first input variable by the second*
 f = *The value to set the purge valve condition, 1 is open, 0 is closed*

Here we set the condition to open the purge valve. When the current count goes greater than the interval it will open the purge valve for the purge duration time and then will reset both the current counter and the time counter to zero as instructed by (Ballard Power Systems Inc. 2014).

$$Purge = f \quad (208)$$

Where:

$Purge$ = *The signal sent to the purge valve*

Here we send signal to open the purge valve.

$$Coulumb_{count} = y \quad (209)$$

Where:

$Coulumb_{count}$ = *The coulomb count of current sent to the ouput signal*

Here we use an output to send the coulomb count to other areas of the model.

3.14 Buck-Boost DCDC Model

The buck-boost DCDC model is based on that of the Springer averaging buck-boost converter model (Sira-Ramirez, and Silva-Ortigoza 2006) for reasons stated in both section 2.5 and section 3.9. The model has primarily been developed by Arash Moradinegade Dizqah (Dizqah, Busawon, and Fritzsion 2012), where in comparison to (Sira-Ramirez, and Silva-Ortigoza 2006) an additional resistor at both the capacitor and the inductor have been implemented into the model, to improve the representation of the losses which occur within the converter. The procedure to depict the averaging DCDC model equations, are first, to apply Kirchhoff Voltage Law and Kirchhoff Current Law to both conditions of the DCDC's transistor in the 'On' state and in the 'Off' state. Secondly, check to see if both sets of equations are still coherent during a range of the duty cycle of the transistor. Then each set of equations can be multiplied by the weight of the duty cycle input and then added together to create the voltage and current at the other side of the DCDC converter (Sira-Ramirez, and Silva-Ortigoza 2006).

Equations (210) to (217) define the mathematics to determine the characteristics of the buck-boost DCDC model by (Dizqah, Busawon, and Fritzsion 2012);

$$R_{out} = \frac{v_2}{|i_2| + eps} \quad (210)$$

Where:

R_{out} = The resistance at the output of the DCDC
 v_2 = The voltage at the output of the DCDC
 i_2 = The current at the output of the DCDC
 eps = A negligible value to prevent divisions by zero

This is used to automatically calculate the resistance of the device connected to the output of the DCDC so that any electrical device can be connected to the output and the DCDC will retain its functionality.

$$R_{in} = \frac{v_1}{|i_1| + eps} \quad (211)$$

Where:

R_{in} = The resistance at the input of the DCDC
 v_1 = The voltage at the input of the DCDC
 i_1 = The current at the input of the DCDC

This is used to automatically calculate the resistance of the device connected to the input of the DCDC so that any electrical device can be connected to the input and the DCDC will retain its functionality.

$$\frac{d}{dt} v_c = R_{out} * \frac{1 - D}{(R_{out} + R_c) * C} * i_L - \frac{1}{(R_{out} + R_c) * C} * v_c \quad (212)$$

Where:

v_c = The voltage at the capacitor
 D = The averaged transistor state (input value range 0 – 1)
 R_c = The voltage at the DCDC capacitor
 C = The capacitance of the DCDC capacitor
 i_L = The current flowing through the inductor

CHAPTER 3 - Modelling

Using Kirchhoff's Voltage Law we can solve for the voltage at the capacitor (Dizqah, Busawon, and Fritzsion 2012).

$$\frac{d}{dt}i_L = - \frac{R_L * (R_{Out} + R_C) - R_{Out} * R_C * (1 - D)}{L * (R_{Out} + R_C)} * i_L - R_{Out} * \frac{(1 - D)}{L * (R_{Out} + R_C)} * v_c + \frac{D}{L} * v_1 \quad (213)$$

Where:

R_L = The resistance at the inductor
 L = The inductance of the inductor

Using Kirchhoff's Current Law we can solve for the current at the inductor (Dizqah, Busawon, and Fritzsion 2012).

$$v_2 = v_c - R_C * \left(R_{Out} * \frac{1 - D}{R_{Out} + R_C} * i_L - \frac{1}{R_{Out} + R_C} * v_c \right) \quad (214)$$

Here we have calculated the output voltage due to the voltage at the capacitor, resistance at the capacitor, resistance at the output, current across the inductor and the transistor state condition (Dizqah, Busawon, and Fritzsion 2012) .

$$i_1 = D * i_L \quad (215)$$

Now we can determine what load is drawn from the input of the DCDC due to the value of the transistor state input (D) (Dizqah, Busawon, and Fritzsion 2012).

$$P_{in} = i_1 * v_1 \quad (216)$$

Where:

P_{in} = The power at the input of the DCDC

Here we calculate the power at the input of the DCDC so that DCDC efficiency can be calculated if required.

$$P_{out} = \frac{v_2^2}{R_{Out}} \quad (217)$$

Where:

P_{out} = The power at the output of the DCDC

Here we calculate the power at the output of the DCDC so that DCDC efficiency can be calculated if required.

3.15 Driver Model

The decision to adopt the Dymola driver model shown in Figure 3-24 has been taken, as it is a closed loop model with comprehensive tracking functions that can operate the vehicle model in relation to the data stored in the road model (Deuring, Gerl, and Wilhelm 2010).

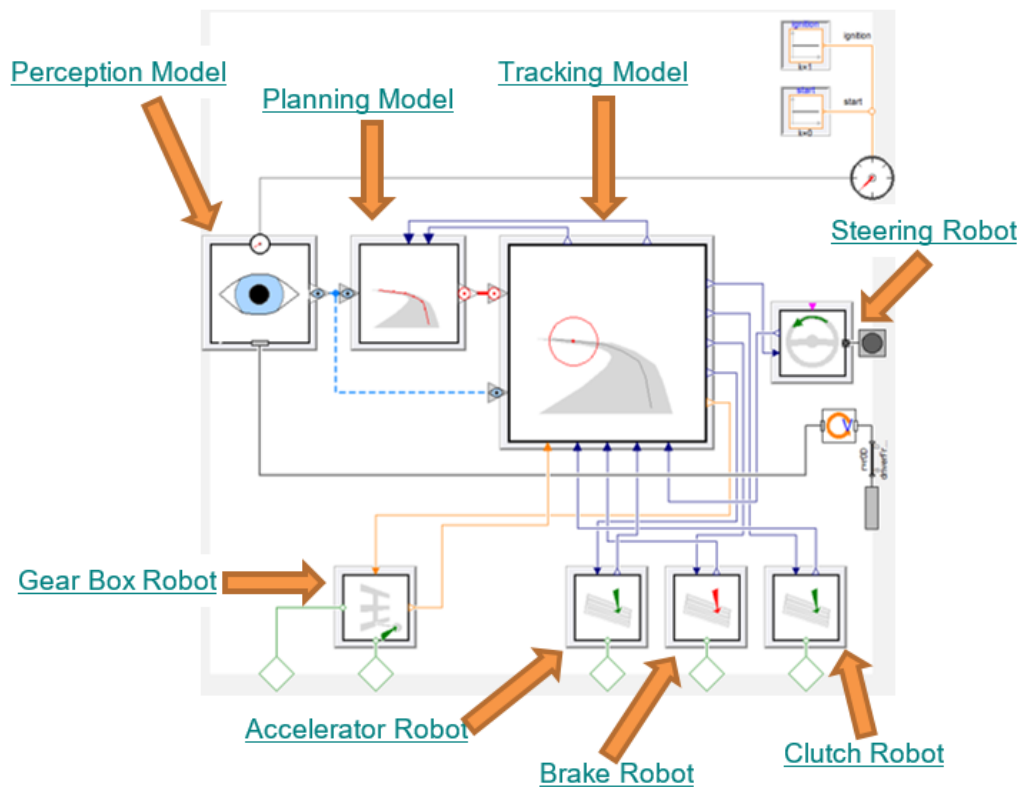


Figure 3-24 - Driver Model Overview

The Dymola driver model takes information from both the road profile and the vehicle simultaneously to determine how to manipulate the vehicle to meet the demands of the road. Figure 3-24, consists of the following sub-models which make this possible (Modelon 2012-2013);

- Perception Model - The perception model takes the following variables with respect to the world resolve frame, angular velocity of the vehicle, longitudinal velocity of the vehicle, longitudinal acceleration of the vehicle and the x, y, z position of the vehicle.
- Planning Model - The perception model looks a set distance along the road profile model to initiate the drive conditions and creates path point information, so that the driver can gradually turn the vehicle into corners and allow for smoother throttle and brake conditions.
- Tracking Model - The tracking model consists of a lateral tracker model, longitudinal tracker, single point gear selection model and a gear shifter model.

- The lateral tracker model can adjust the steering inputs based on a combination of the preview distance and time from the perception model information and the path point information from the planning model.
- The longitudinal tracker model uses the same information as the lateral tracker, however, it uses a feedback loop of the accelerator pedal position and the brake pedal position to calculate if the driver should apply more to the accelerator, or to the brake to achieve the correct speed conditions set by the perception model information and the planning model information.
- The single point gear selection model uses the motor/engine speed, current gear position and vehicle speed to determine if a gear shift is required, based on variables set by the programmer.
 - The gear selector conditions are as follows, maximum gear, minimum gear, lowest engine speed when accelerating, highest engine speed when accelerating, lowest engine speed when cruising, highest engine speed when cruising, lowest engine speed when retarding, highest engine speed when retarding and a shift delay.
- Steer Robot Model – The steer robot model uses a steering wheel reference angle from the tracking model's lateral tracker to change the position of the 3-dimensional rotational output flange connected to the vehicles steering rack model which in turn affects the trajectory of the vehicle about the world frame.
- Gear Robot Model – The gear robot outputs a gate and cross-gate position to the gearbox model of the vehicle, as previously mentioned, the decision of which gear the vehicle should be in is defined by the single point gear selection model.
- Accelerator Robot Model – This determines an accelerator position based on the decision of the longitudinal tracker model and provides no dynamics so that the accelerator response is instantaneous between the decision and the output.
- Brake Robot Model – This operates in the same manner as the accelerator robot model, however, it outputs an instantaneous brake signal rather than an accelerator signal.
- Clutch Robot Model – This operates in the same manner as the accelerator robot model, however, it outputs an instantaneous clutch signal rather than an accelerator signal.

3.16 Road Models

Dymola provides three roads as standard, which are, a straight and flat road, a scenario of driving over a crest and a large circular road (a large roundabout). The software provides a 3D road builder function so that the user can create their own road models which the driver model can operate the vehicle around. The 3D road builder is a set of function calls which can interpolate a series of set points. The road model then consists of x, y and z positions in metres about a zero position. It is from the x, y and z position in which the rest of the road variables are created and the following set points are defined in reference to the global x, y and z position in the model; banking, width, path position and velocity. Each of these vectors can be imported via a *.MAT file or *.CSV file. Therefore, implementation of a real-world driving data can be done without too much difficulty. A limitation of the road builder function, supplied by Dymola, is that it can create a road profile that folds upon itself when multiple coordinate points are close together. To prevent this from occurring, prior to importing the *.CSV file into Dymola some precision rounding and filtering is required. The following complex conditional statement was created using Microsoft Excel to achieve this rounding and filtering.

Cell E2 = (218)

$$\left[\text{AND} \left(\begin{array}{l} \text{OR} \left(\begin{array}{l} \text{MROUND}(B2,0.1) <> \text{MROUND}(B1,0.1), \\ \text{MROUND}(B2,0.1) <> \text{MROUND}(B3,0.1) \end{array} \right), \\ \text{OR} \left(\begin{array}{l} \text{MROUND}(C2,0.1) <> \text{MROUND}(C1,0.1), \\ \text{MROUND}(C2,0.1) <> \text{MROUND}(C3,0.1) \end{array} \right), \\ \text{OR} \left(\begin{array}{l} \text{MROUND}(D2,0.1) <> \text{MROUND}(D1,0.1), \\ \text{MROUND}(D2,0.1) <> \text{MROUND}(D3,0.1) \end{array} \right) \end{array} \right) \right]$$

$$\left[\begin{array}{l} \text{for true} \\ \text{for false} \end{array} \right] = \left\{ \begin{array}{l} \text{"KEEP"} \\ \text{" " } \end{array} \right\}$$

Where:

- E2** = The cell adjacent to any logged signal which prints the result
- B2** = The first value for X position of the logged GPS data
- C2** = The first value for Y position of the logged GPS data
- D2** = The first value for Z position of the logged GPS data
- <>** = is a not equal to operator
- MROUND** = This rounds the value in the cell by the second entry (0.1)
- OR** = Boolean statement which returns true if either condition is true
- AND** = Boolean statement which returns true when all conditions are true

The statement *MROUND*, rounds the number in each defined cell to one decimal place and then compares the value before and after in column B to determine both values are different to the middle cell, Cell B2. If the values are different in both, column B, column C and column D then it will return "KEEP" within Cell E2 and if each cell is the same then it will return a blank cell. The 'OR' conditions within the 'AND' statement can be repeated multiple times for conditions that require more than 3 variables.

3.17 Summary of Modelling

This chapter of the thesis has shown the approach to creating a novel multi-disciplinary FECV model which can simulate a range of different vehicle scenarios. This has been achieved by using state-of-the-art modelling techniques for each critical area of the vehicle model so that objective 1, “To create a multi-disciplinary FCEV model with the following complex subsystems: ...”, in section 1.3 could be met. By integrating the state-of-the-art modelling techniques, which were identified in the literature review, into Dymola and developing them to interact with each other’s domains the first objective was met. The modelling section has addressed the limitations, specified in the literature review, of using Dymola by creating a parametric battery model, a parametric fuel cell model, and a parametric combined motor and motor controller model in the Modelica modelling language. The use of existing state-of-the-art models and the method which Dymola uses to create each model has been described, thus meeting each sub-objective within the first objective in section 1.3. The limitations concerning the current state-of-the-art parametric battery modelling technique, discussed in section 2.4.1, have been addressed by implementing a parametric Coulombic efficiency and by populating equations to represent different charge and discharge characteristics of a battery. The limitations concerning current state-of-the-art parametric fuel cell modelling techniques, discussed in section 2.5.1, have been addressed by creating a thermodynamic model of a fuel cell hydrogen system, so that hydrogen consumption and gas flow characteristics can be represented. Additionally, care has been taken to make each area of the model parametric, so that the model can be used as a development tool within industry and to meet objective 2, in section 1.3, “Provide parametric modelling capability for versatility of vehicle design and simulation”. The model is specifically aimed as a virtual prototype, where the design of the vehicle inherently would require testing and development. Due to the multi-disciplinary and parametric nature of the proposed model, this can be achieved in the simulation environment so that developments to the vehicle can be tested and their effects on the whole vehicle can be determined simultaneously. This provides a better design process for integrated vehicle systems and a system optimisation tool for FCEVs thus meeting the overall aim set out in section 1.3, to determine if a novel multi-disciplinary fuel cell vehicle model can accurately predict energy consumption for EVs and FCEVs. Therefore, such a model can be used for system optimisation in the virtual environment to improve upon the energy consumption of the vehicle and system performance.

CHAPTER 4 - DATA COLLECTION, EXPERIMENTS AND TESTING

At the whole vehicle level energy consumption is typically associated with several aspects of vehicle design and construction. Therefore, creation of a representative model requires careful investigation of the geometry of the vehicle and several physical properties and characteristics, especially those relating to vehicle mass and tyre performance. This data was acquired by static physical measurements, controlled experimental work and collation of field data. Where direct measurements were not possible, this has been highlighted and explained in the text. Similarly, detailed investigation is required for the vehicle propulsion system which includes the battery and the fuel cell, where data relating to quasi steady state performance of electrical, thermal and fluid systems is required. The careful definition of road and route characteristics which relies heavily on information in the public domain is also important. Such data has been used in both model definitions and in correlation studies. Questions of accuracy, repeatability of experimental work and its results have been addressed in the text, as has its significance in terms of model definitions and in correlation studies. Wherever possible SI-Units have been used however, industry standards have also been adopted where appropriate. This section of the thesis presents the most relevant experiments and the resulting test data which has been conducted throughout the project. A list of equipment used to complete all the test can be found in APPENDIX E – Test Equipment List.

4.1 Component Mass and Positioning Collection

Figure 4-1 shows the Catia CAD model of the Coventry University Microcab H2EV. The areas of this CAD model have been provided by multiple sources and are shown below:

Microcab Industries Ltd	Exterior bodywork and interior models
Coventry University	Chassis model
Michael Apicella	Battery, fuel cell, hydrogen tank, wheels, electric motor and wiring models

Where multiple models were not available in CAD it was necessary to measure each missing component and use reverse engineering on these vehicle components so that the full CAD model shown in Figure 4-1 could be generated by the author of this thesis.



Figure 4-1 - Coventry University Microcab H2EV CAD

The coordinate system used to define the model was located on the centre line of the vehicle at the front axle position. For clarity the axis system is shown in front of the vehicle in Figure 4-1. This is the vehicle which the Dymola simulation model has been based on. From the data in the CAD file it is possible to determine the centre of mass position of each component that has been manufactured in house and this has been used to create a parametric vehicle mass model. The procedure to acquire this data, required opening each component model separately in the 3D engineering modelling tool Dassault Systems Catia V5 (Catia) and using the Measure Inertia tool. The Measure Inertia tool provides a mass of the object and the global x, y and z positions of the object. Therefore, the Measure Inertia tool is capable of providing all the component data required to fulfil the mass model requirements. The data collected from the Catia CAD model was implemented in a Microsoft Excel document so that the local inertias, and centre of mass could be calculated and implemented in the mass model. A portion of each table within the Excel document can be seen in Table 4-1, Table 4-2 and Table 4-3. All the data collected to achieve this can be found in APPENDIX A – Model Data.

Table 4-1 - Vehicle Component Database Example

Component Name	Mass (kg)	Centre of Mass (mm)		
		X	Y	Z
Roof	38.9	1325	0	1136
Rear Left Hand Window	1.5	1954	-586	1078
Rear Right Hand Window	1.5	1954	586	1078
Boot Outer	10	2590	0	813

From this data we can use the equations (89)-(91) from section 3.3 to determine the centre of mass position of the vehicle and then equations (92)-(94) to determine X, Y and Z component positions in relation to the centre of mass, shown in Table 4-2:

Table 4-2 - Component Positions in Relation to the Centre of Mass

Component Name	Centre of Mass (mm)		
	X	Y	Z
Roof	66	-11	776
Rear Left Hand Window	695	-597	718
Rear Right Hand Window	695	574	718
Boot Outer	1331	-19	453

Now the component locations in relation to the vehicle's centre of mass have been determined, the component mass moments of inertia can be calculated using equations (96)-(98). These are shown in Table 4-3.

Table 4-3 - Vehicle Component Inertia Example

Component Name	Mass Moment of Inertia (kg m ²)		
	I _{xx}	I _{yy}	I _{zz}
Roof	23.5	23.6	0.18
Rear Left Hand Window	1.30	1.50	1.26
Rear Right Hand Window	1.27	1.50	17.7
Boot Outer	2.06	19.8	18.2

Now that the component mass moments of inertias have been calculated, equations (96)-(98) can be used to determine the moment of inertia for the vehicle. These equations give:

$$I_{XX,CM} = 155 \text{ kg m}^2$$

$$I_{YY,CM} = 378 \text{ kg m}^2$$

$$I_{ZZ,CM} = 350 \text{ kg m}^2$$

Where:

$I_{XX,CM}$ = The vehicle's moment of inertia about the longitudinal axis

$I_{YY,CM}$ = The vehicle's moment of inertia about the lateral axis

$I_{ZZ,CM}$ = The vehicle's moment of inertia about the vertical axis

Having determined the vehicle mass and centre of mass positions, the following data can be added to Table 4-4 so that a better presentation of the data acquired from the CAD model can be presented.

Table 4-4 - Vehicle Mass Calculations

Calculations		
Component	Value	Units
Sprung Mass	676	kg
Mass Total On Ground	729	kg
X Body Centre of Mass to Front Wheel Centre	1.18	m
Y Body Centre of Mass to Front Wheel Centre	0.015	m
Z Body Centre of Mass to Front Wheel Centre	0.37	m
Mass Bias Front	0.54	-
Front Mass	399	kg
Rear Mass	330	kg
Front Axle load	370	kg
Rear Axle Load	306	kg

The results shown in Table 4-4 were then validated using a set of corner scales to weigh the real vehicle, to determine the error between the CAD Model and manufacturing. Table 4-5 shows both the results from the corner scales and the error between the estimating mass using the CAD model and the physical test.

Table 4-5 - Vehicle Measurements

Physical Vehicle Measurements		
Component	Value	Units
Front Left Wheel	196	kg
Front Right Wheel	206	kg
Rear Left Wheel	169	kg
Rear Right Wheel	159	kg
Total Front Mass	402	kg
Total Rear Mass	328	kg
Mass Bias Front	0.55	-
Front Weight CAD Error	0.69	%
Rear Weight CAD Error	0.77	%
Weight Bias Error	0.66	%
Total Weight Error	0.03	%

Table 4-5 shows the mass values which were taken and that when using data from the CAD model we can accurately represent the total vehicle mass to an error of 0.03% and mass distribution to approximately 0.7%.

4.2 Battery Testing

4.2.1 Battery Pack Discharge Testing

Figure 4-2 shows the setup of the experiment with the 72 V 4 kWh Goodwolfe battery pack connected to the load and with the Lifebatt monitoring software loaded onto the laptop. The specific battery cell layout of this 72 V 4 kWh Goodwolfe battery pack is discussed further in Section 4.2.3. This test has been set up and carried out by the author of this thesis and can be used to validate the battery model's voltage against the SOC of the battery during a steady state discharge condition.

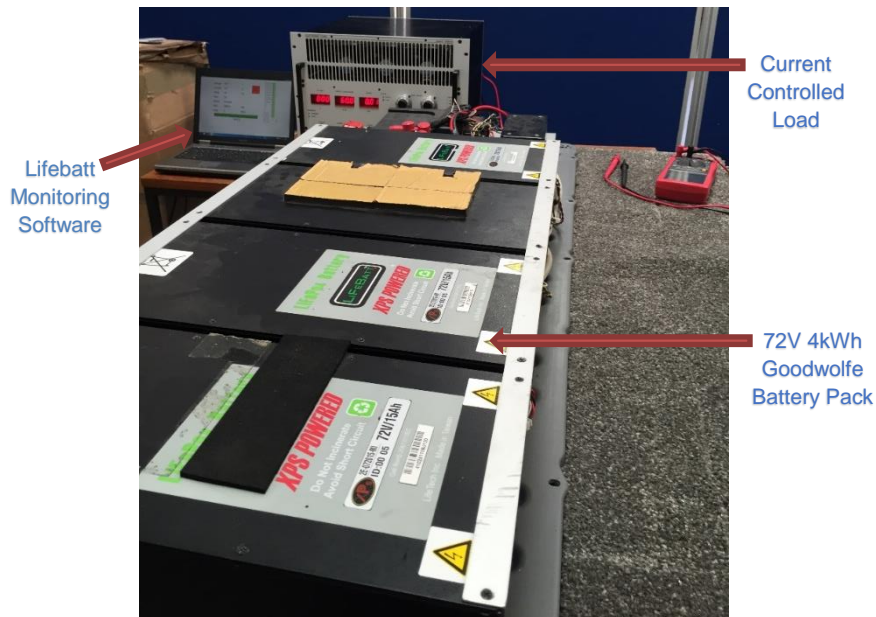


Figure 4-2 - Battery Discharge Test Setup

In addition to what is shown in Figure 4-2, a Kvaser Memorator Professional HS/HS datalogger was attached to the battery Controller Area Network (CAN) bus to log the results and a switchbox to the control lines of the battery in order to switch on the BMS as shown by the test schematic in Figure 4-3.

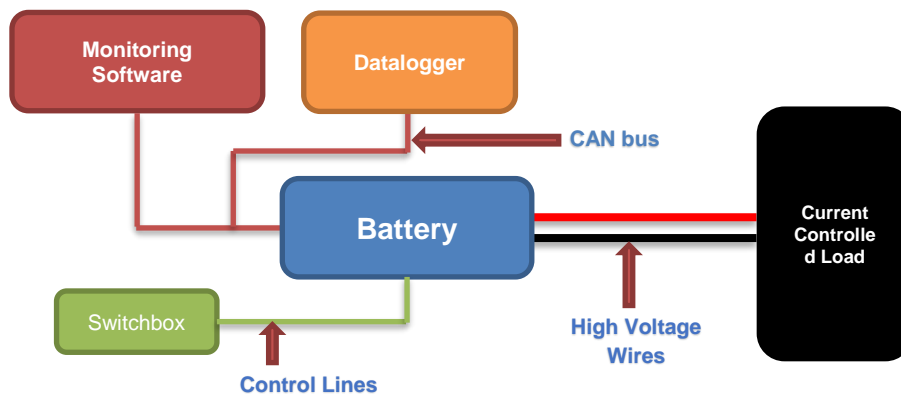


Figure 4-3 - Battery Discharge Test Schematic

The battery pack was initially charged to 100% SOC and then a load current of 50 A was applied to the battery pack, and this was done until an LVP flag was raised by the BMS and displayed on the monitoring software. All the battery parameters were logged during the procedure and a list of the main concerns are presented in Table 4-6.

Table 4-6 - Logged Battery Test Variables

Parameter Name	Variable Range	Granularity	Unit
SOC	0 – 100	0.01	%
Voltage	0 – 100	0.3	V
Current	-500 to 500	0.5	A
LVP	0 – 1		Boolean
OVP	0 – 1		Boolean
OTP	0 – 1		Boolean
Cell Variation	0 – 1	300mv threshold	Boolean

Due to the voltage of the battery, 50 A is the maximum current which can be drawn when using the specified test equipment. The voltage characteristics during this test can be seen against the battery pack’s SOC in Figure 4-4.

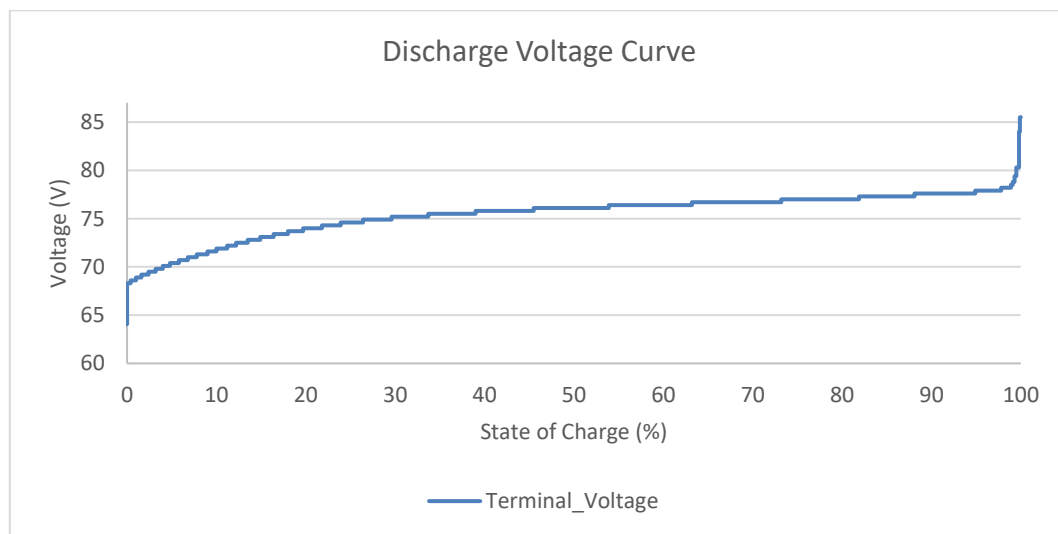


Figure 4-4 – 50 A Constant Current Battery Discharge Voltage vs SOC

The exponential voltage characteristics at both high and low SOC can be seen in Figure 4-4. However, the battery test had to be stopped due to a LVP flag at 64 V, which is 2.66 V/cell, where there is 24 cells connected in series.

Figure 4-5 shows the same graph, although, the voltage is plotted against time rather than SOC. The small spike at the end of the curve where the voltage rises, is where the load is switched off prior to stopping the datalogger. The results show that on a

50A load, the battery takes 3950 s (65.8 minutes) to reach an LVP flag and requires the procedure to be stopped.

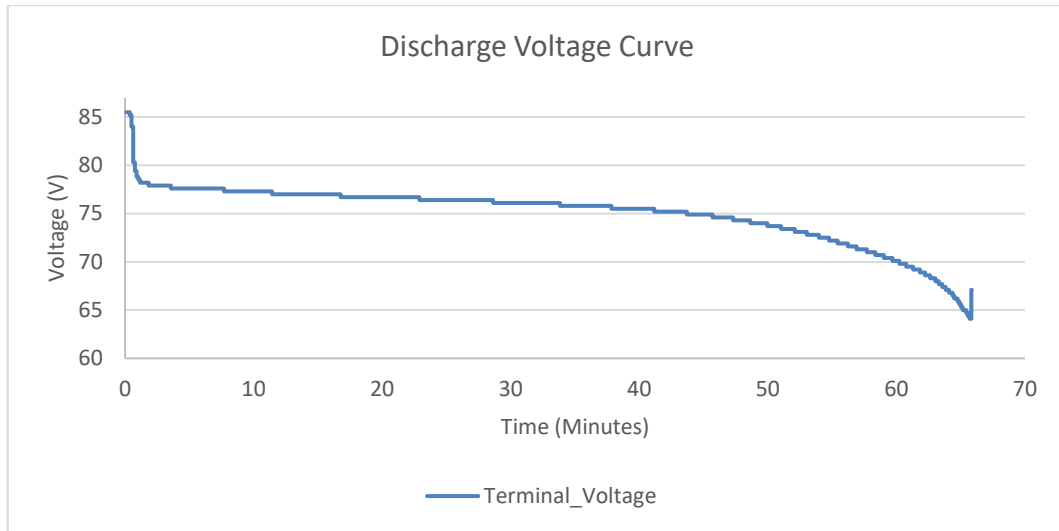


Figure 4-5 – 50 A Constant Current Battery Discharge Voltage vs Time

The main difference between these two graphs, Figure 4-4 and Figure 4-5, is the ability to see the exponential concentration voltage loss at low SOC. This is because the BMS does not track the SOC well, this is clear when the SOC reaches zero but the voltage continues to reduce because the test is still being conducted. If the BMS is able to track the SOC well, the LVP flag would occur at exactly 0% SOC and the test would be concluded at that point.

4.2.2 Battery Pack Charge Testing

Figure 4-6 shows the Zivan NG1 10 A charger which is used to charge the Goodwolfe 72 V 4 kWh battery packs. It is directly connected to the fused positive terminal and the negative contactor of the battery.



Figure 4-6 – 72 V Zivan NG1 Charger

The charger will not initiate until it receives a Charge-Enable signal which comes from the BMS. Therefore, the switchbox is also required within this procedure. The experimental test setup is shown by the schematic in Figure 4-7. This test has been set up and carried out by the author of this thesis and can be used to validate the battery model's voltage against the SOC of the battery during a typical lithium ion battery charge profile.

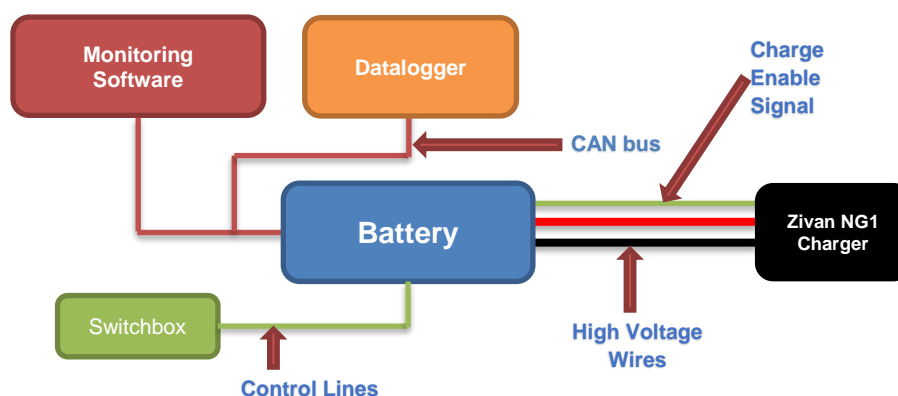


Figure 4-7 - Battery Charge Test Schematic

The BMS in the battery pack can deactivate the charger by disabling the Charge Enable line if there is a scenario where the cell variation gets too large or cells reach an Over Temperature Protection (OTP) or an OVP. OVP occurs when any cell voltage goes 1 mV over 3.65 V. Therefore, in the given battery pack where there are 96 cells in total, the chance of any one of the 96 cells going out of range at high SOC is very likely, especially if there is any variance in cell capacity or internal resistance across the battery pack. This typically creates long balancing durations at high SOC as the BMS can disable and enable the charger often, to ensure all cells within the pack are charged fully and to the same SOC.

The charge procedure of the Goodwolfe developed Zivan NG1 charger is shown below in Figure 4-8.

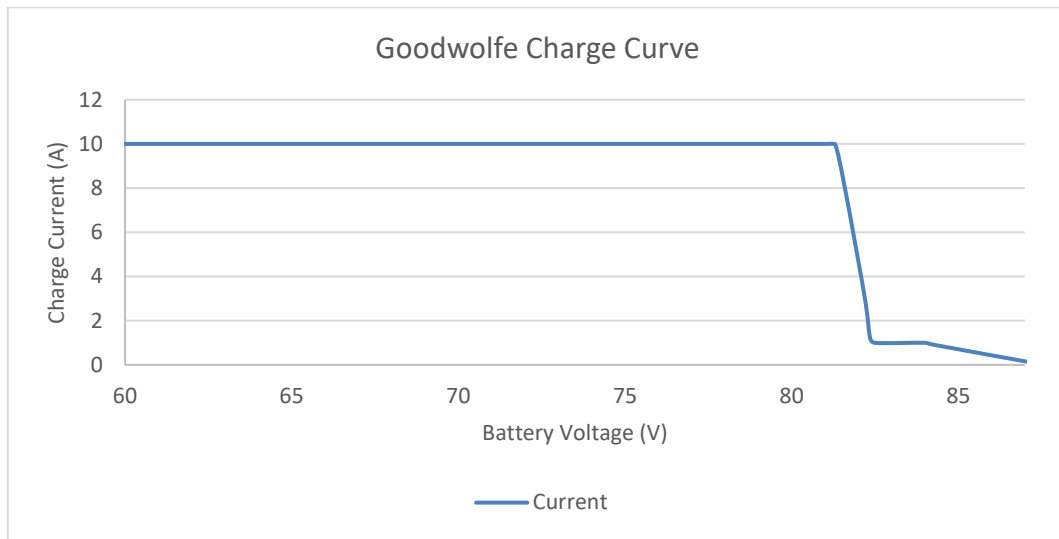


Figure 4-8 - Goodwolfe Charge Curve

It can be seen in Figure 4-8 that the Goodwolfe charge curve consists of four charge procedures, Constant Current (CC) at 10 A to 82 V, Constant Voltage (CV) to 83 V, CC at 1 A to 84 V then CV to 87.6 V. The charger must reduce the current when the voltage of the battery is high due to safety concerns. This is in relation to the maximum cell voltage of the battery. Therefore, to ensure that the batteries does not exceed this manufacturer limit when being charged, most chargers finish the charging profile with a CV charging method. The constant voltage charging method is complete when the battery voltage and the DC supply voltage are equal and therefore, reached equilibrium. Exceeding this maximum voltage limit will typically result in a battery fire (McDowall 2014).

Figure 4-9 shows the characteristics of the battery pack voltage whilst being charged by the Goodwolfe Charge Curve. When the battery is at 96.4% SOC the battery pack voltage is at 84 V and at this point the BMS starts enabling and disabling the charger as the Battery Management Module (BMM) cannot keep all the cells at an equal voltage below the OVP threshold. Therefore, at this point the test was concluded and defines the duration of this test at just over eight hours.

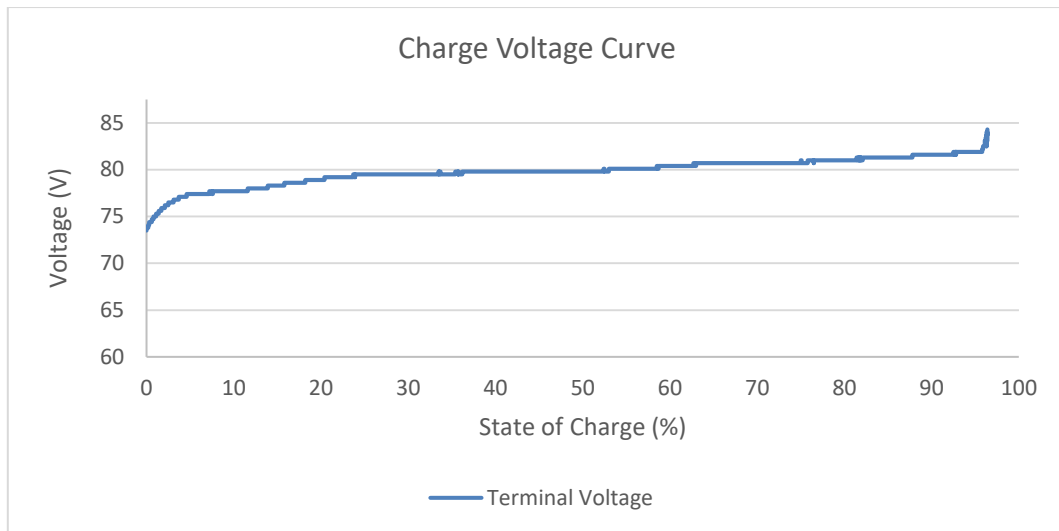


Figure 4-9 - Battery Charge Test, Voltage vs SOC

It can be seen in Figure 4-9 that both the high and low SOC exponential voltage characteristics are present due to the lithium ion phosphate battery chemistry. Figure 4-10 shows the battery pack takes just over 8 hours to charge to 96.4% SOC and this also shows that there is cell variation present within the pack. Further evidence of cell variation during this charge test is presented in APPENDIX C – Battery Pack Cell Variation.

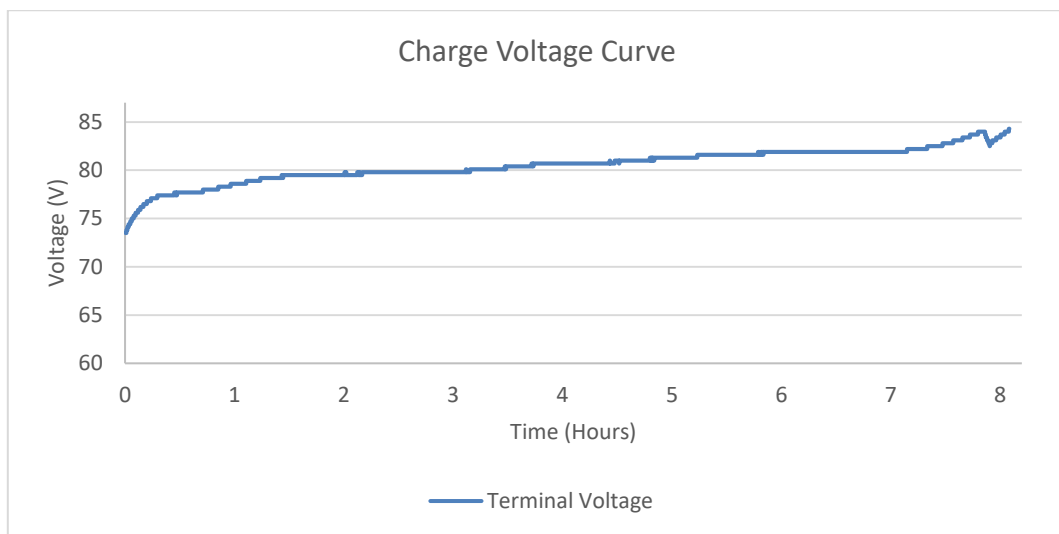


Figure 4-10 - Battery Charge Test, Voltage vs Time

Figure 4-10 indirectly shows how the variation of cell voltage can seriously affect the performance of the battery, in most simulations batteries are modelled as ideal and this is not considered. The main reason for not considering this effect is because it is necessary to characterise each cell independently and the ability to characterise the aging of a cell. These results can be used for some battery pack validations but it would be more appropriate to obtain cell data so that the model can be validated at both a cell and pack level. This is because both tests, described in section 4.2.1 and

section 4.2.2, were carried out multiple times. However, repeatable results were difficult to achieve, where the BMS would display LVP flags at different voltages on the discharge test and the BMS would disable the charger at different voltages during the charge test, therefore, supporting the tests conducted in the following sections.

4.2.3 Individual Cell Discharge Test

From the results in section 4.2.2 it was necessary to test the battery pack at a cell level to better represent the behaviour of the battery. The test results can be used to validate discharge characteristics against the battery model at a cell level and to identify if the reason for intercell variation is due to the battery pack consisting of multiple cells with varying capacitance. Therefore, a battery pack was disassembled and each cell was labelled from 1 to 96 as shown in Figure 4-11.

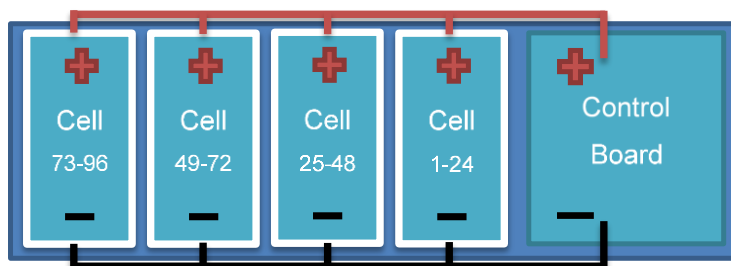


Figure 4-11 - Goodwolfe 72v 4kWh Battery Pack Layout

Figure 4-12 shows the internal layout of each sets of cells. From testing multiple batteries at pack level, it was clear that out of eight battery packs repeatable tests were difficult to achieve. This is likely to be because of a variation between cell capacity within the pack. It can be seen from Figure 4-11 and Figure 4-12 that the battery packs are initially connected in series and then connected in parallel.

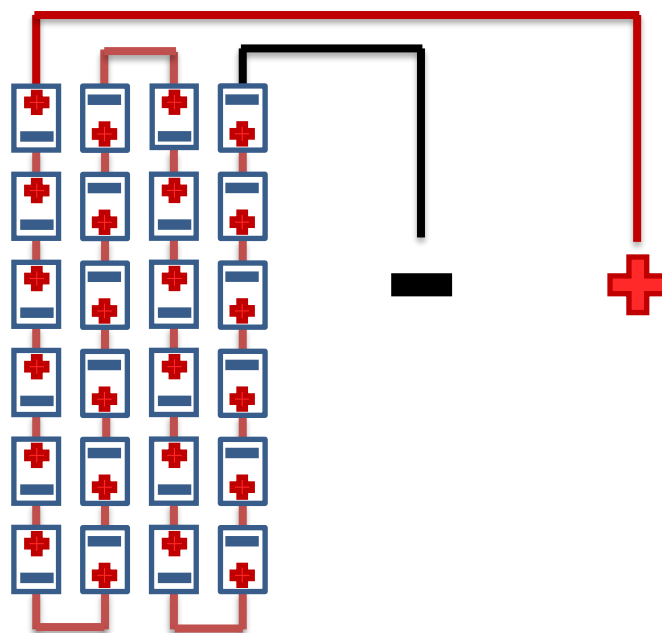


Figure 4-12 - Goodwolfe 72v 4 kWh Battery Pack, Cell Configuration

It is clear from Kirchhoff's Voltage Law that when two batteries are electrically connected in parallel that there cannot be any difference in voltage between them. Therefore, in the case of the Coventry University Microcab H2EV battery packs, each

group of 24 cells will be held to the same high voltage, but out of the 96 cells there can be large variation. It is possible for one group of twenty cells to be balanced to 3.2 V equating to 64 V while another 4 cells could be very low in SOC and sit at 2 V, making the group of 24 cells be a total of 72 V.

The test procedure required each cell to be initially charged to 3.6 V and then let rest for an hour prior to connecting the cell to the load and performing a 3 C (three times the nominal rated capacity of the cell, 45 A) discharge to 2.3 V. In theory, a 3 C discharge should take exactly 20 minutes. From this test we can determine the capacity of the cell by using first principles around the measurement of electrical charge. We know that electrical charge is the integral of current and measured in Coulombs with a SI Unit of *As*. Thus, giving equation (219).

$$C (As) = \int_{time(0)}^{time(end)} Current (A) * \Delta time (s) \quad (219)$$

Where:

- C* = The Coulombic electrical charge in *As*
- time(end)* = The end point of time for the integration
- time(0)* = The start point of time for the integration
- Current* = The current during the integration
- Δtime* = The change in time during the integration

If constant direct current is used then the current will not vary and equation (219) can be simplified to equation (220).

$$C (As) = Current(A) * time(s) \quad (220)$$

Where:

- C (As)* = The Coulombic electrical charge in *As*
- Current* = The current during the test
- time* = The time taken to perform the constant direct current test

However, when discussing batteries, this unit of charge can be very large, so batteries have adopted a nonstandard unit for representing battery charge as *Ah*. This unit of electrical charge is achieved by changing the unit of time from seconds to hours. We know there are 3600 *s* in an hour, so by dividing the Coulombic electrical charge by 3600 *s* we appropriately convert the units, giving equation (221).

$$C (Ah) = \frac{C (As)}{3600 (s)} \quad (221)$$

Where:

- C (Ah)* = The Coulombic electrical charge in *Ah*
- 3600 (s)* = The amount of seconds within an hour

Therefore, so that this can be used to determine the capacity of a battery due to a constant direct current test, we can write the equation in long hand as shown in equation (222).

$$C (Ah) = \frac{Current (A) * time (s)}{3600 (s)} \quad (222)$$

As these tests will be conducted with a direct constant current load at 45 A the value of current in equation (222) will be equal to 45 A and the only difference between testing the cells will be the time.

When testing the battery cells, it was advised to discard any cells which were below 2.5 V resting, which resulted in 10 cells out of the 96 cells in total, being discarded. Figure 4-13 shows the experimental test setup for the capacity tests which have been conducted by the author of this thesis.

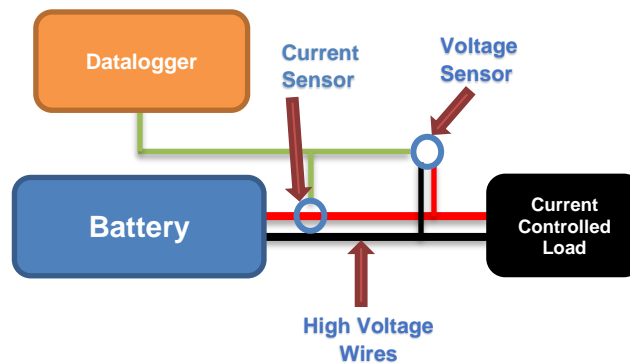


Figure 4-13 - Battery Cell Discharge Test Schematic

Using the test setup defined in Figure 4-13 and the test procedure described prior to equation (219), all the cells could be tested, and a key result is shown in Figure 4-14. Figure 4-14 show that there was a maximum variation, disregarding the rejected cells, in capacity of 1.003 Ah across the tested cells, it can also be seen, that the cell voltage variation is present across the cells when comparing the discharge graphs of the highest capacity cell against the lowest.

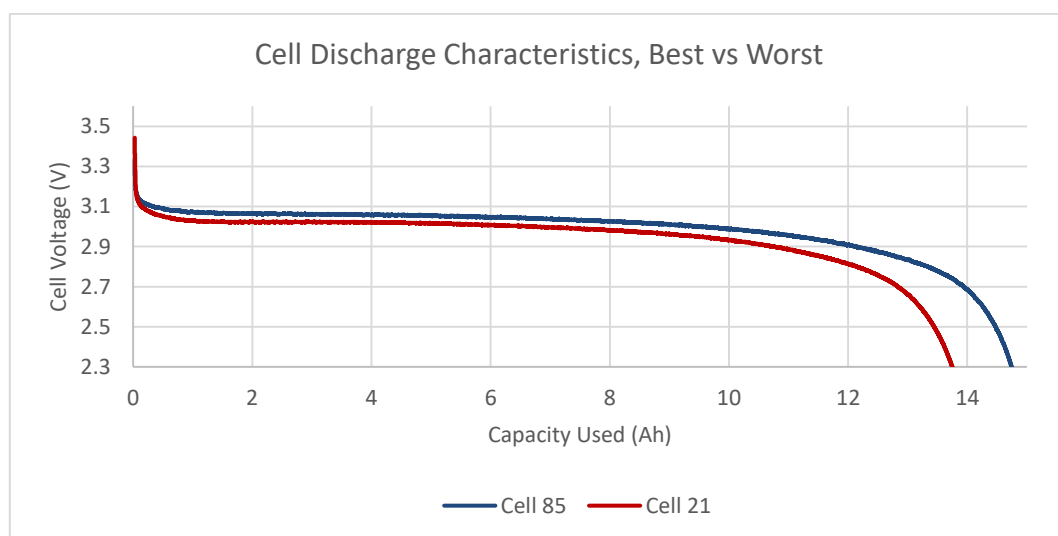


Figure 4-14 – 3 C Discharge Cell Characteristics

The variation of capacity with this battery pack is likely to be present among the other available packs. Therefore, this could present issues with validating the battery pack models, as to get a theoretical 0% error, the model would have to be made of 96 individual cells models which all have the same capacity and cell characteristics of each cell within the tested battery pack. It is also not possible to know which cells get recharged by the other sub-packs when the vehicle rests, as the four sub-packs will ensure that they all maintain the same voltage. Therefore, the chance of a low cell showing a higher voltage is possible, as the cell's voltage would be boosted by the effect of charging and internal resistance. This could result in the higher capacity cells having their SOC reduced. The result of this is that when the battery pack is recharged, the lower capacity cells reach their own 100% SOC quicker than that of the others. This results in the battery pack voltage spiking exponentially prior to that of the entire battery pack reaching 100% SOC and the charger switching off. Evidence of this can be seen in Figure 4-9 of the previous section where the charger is disabled when the battery pack only reaches 96.4%.

Figure 4-15 shows the variation in battery cell capacity across one of the Coventry University Microcab H2EV battery packs.

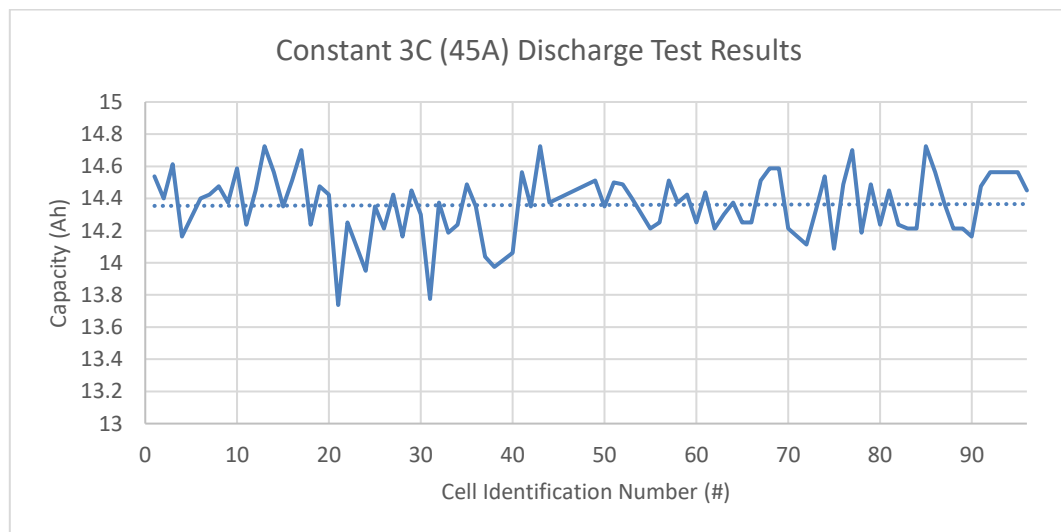


Figure 4-15 - Battery Pack, Cell Capacity Results

By looking at the linear trend line set in Figure 4-15, the average cell capacity of the battery pack is 14.35 Ah, which is 95% of the rated capacity of each cell. However, it should be noted that the worst cell is 91% of the rated capacity for this battery. APPENDIX D – Battery Cell Results provides Figure 8-4 and Figure 8-5 where the capacity and RMS voltage over each discharge of 361 cells are presented.

4.2.4 Individual Cell Direct Current Internal Resistance Testing

Another point of interest was the internal resistance of the cells and how they may vary compared to that of the manufacturer's stated variables. This test was performed in accordance with the battery pack manufacturer's recommendation to BS EN 61960:2011 (BS EN 61960:2011: 2011) and can be used to direct the battery model's parameter for internal resistance. The test procedure is presented below;

- The battery is charged to 3.5 V until the current falls below 100 mA.
- The battery should be stored at an ambient temperature of 20 °C ±5 °C, for a minimum of 1 hour and maximum of 4 hours.
- The measurement should be performed at an ambient temperature of 20 °C ±5 °C.
- The battery should be discharged at $i_1 = 0.2 * i_2$, for 10 seconds
- The discharge current should then be immediately increased to i_2 for a duration of 10 seconds
- The load should be removed from the battery
- The voltage and current at the battery should be measured at the end of each battery discharge procedure
- The voltage and current Measurements should be measured independently of the contacts which are used to draw the current (BS EN 61960:2011: 2011)

Equation (223) is used to calculate the internal resistance of the battery (BS EN 61960:2011: 2011).

$$DCIR = \frac{V_1 - V_2}{I_2 - I_1} * 1000 \quad (223)$$

Where:

- DCIR** = *The Direct Current Internal Resistance of the battery in mOhms*
- V₁** = *The voltage at I₁ in V*
- V₂** = *The voltage at I₂ in V*
- I₁** = *The load current, I₂ * 0.2 in A*
- I₂** = *The maximum load current in A*

The author of this thesis has designed the experimental test setup and conducted the physical tests which provide the results within this section. The experimental test setup for the Direct Current Internal Resistance (DCIR) tests can be seen in Figure 4-16.

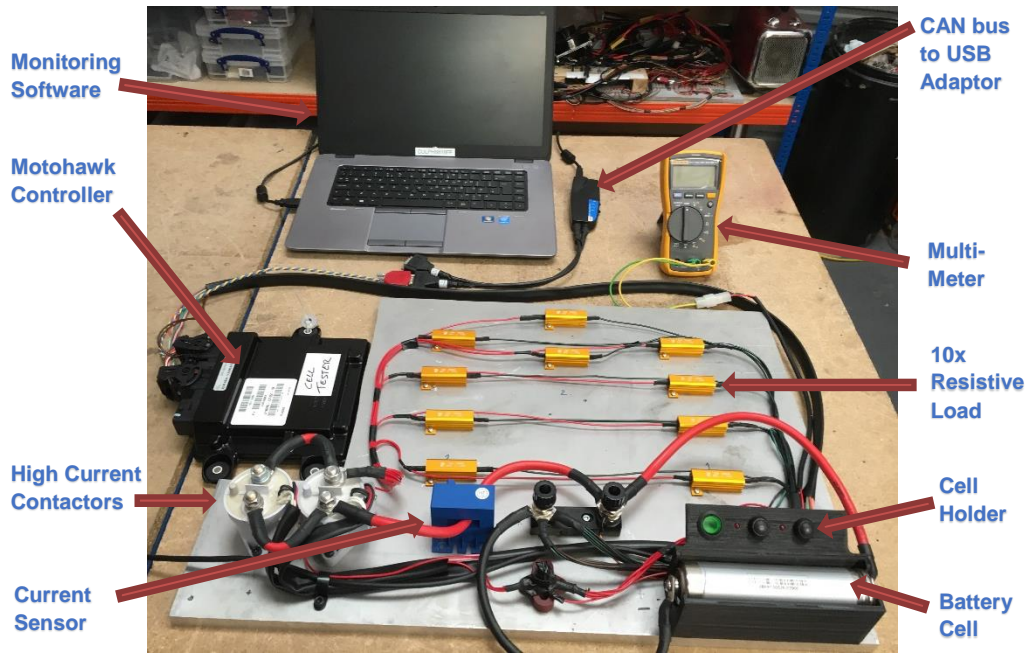


Figure 4-16 - Battery Cell DCIR Test Setup

The Motohawk controller was programmed by the author of this thesis to automate the test defined in (BS EN 61960:2011: 2011) and the cell holder was also designed by the author of this thesis and fabricated using Coventry University’s 3D printing facilities. The voltage is measured by the controller and the controller performs the test cycle once the far right button is pressed on the cell holder. Additionally a calibration process was completed to ensure the correct voltage was measured by the controller. The controller has a resolution of 12 bits, and an input range of 0-5 V. Therefore, we can measure cell voltage to a resolution of 1.2 mV (Woodward 2015). It is from this test setup, shown in Figure 4-16, that the results shown in Figure 4-17 could be obtained.

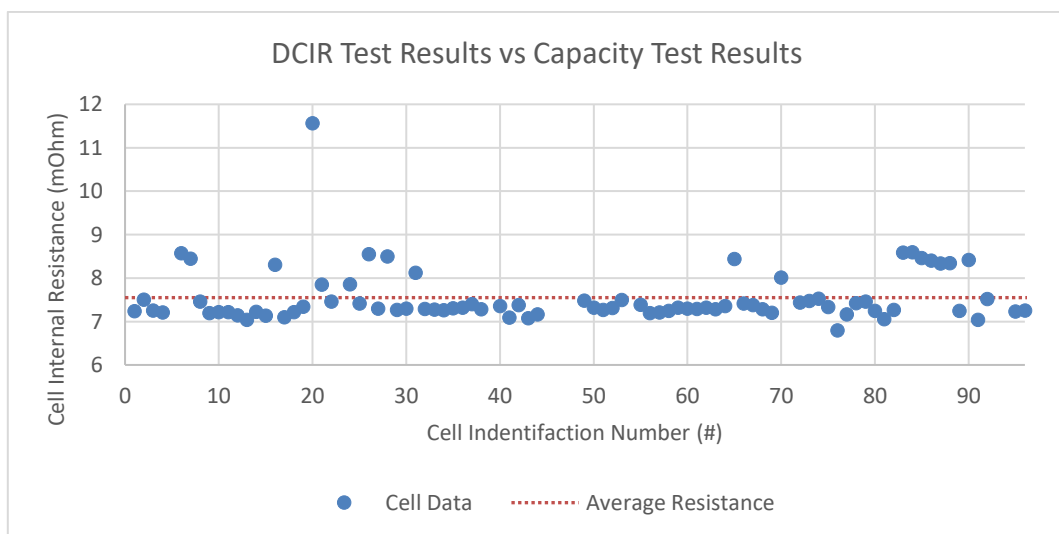


Figure 4-17 - Battery Pack, Cell DCIR Results

Figure 4-17 shows the results of the DCIR test on the cells from one of the Goodwolfe 72 V 4 kWh Battery Packs that was dismantled and tested. There is a variation of 4.77 mΩ between the cells and an average internal resistance of 7.55 mΩ. When comparing the results of the previous test 'Individual Cell Discharge Test', shown in Figure 4-15, to the results of this test, shown in Figure 4-17, it can be seen that there is no obvious correlation between the internal resistance of the cell and cell capacity. This can be seen clearly in Figure 4-18, where the DCIR results have been plotted against the corresponding battery cells tested capacity.

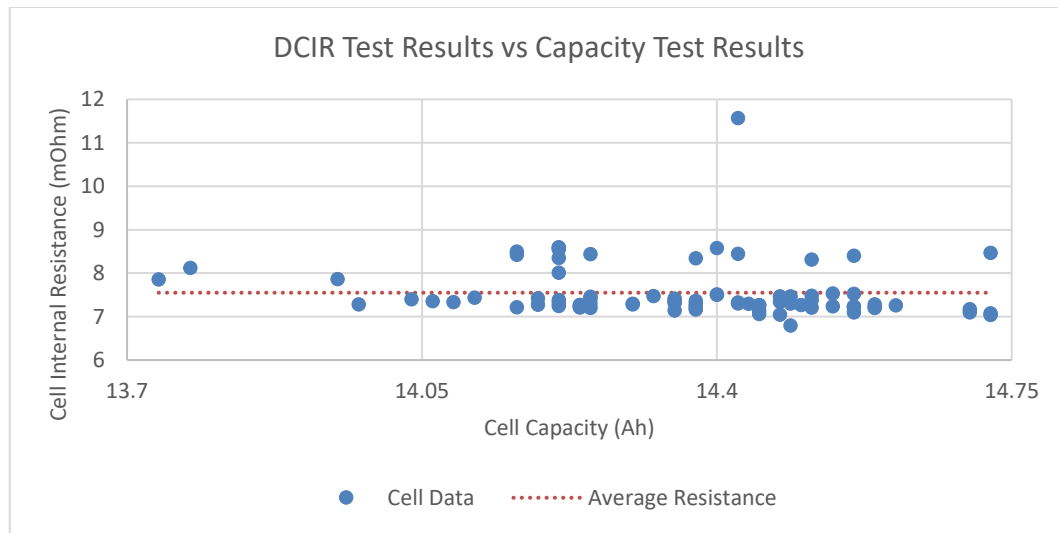


Figure 4-18 - Cell Internal Resistance vs Cell Capacity

It can be seen within Figure 4-18, that the cell with the highest internal resistance does not have the worst capacity and that the cells with the best capacity are not substantially different to the cells with the worst capacity. Table 4-7 presents the capacity and the internal resistance of the two cells presented in the previous section, in Figure 4-14.

Table 4-7 - Presented Cells Internal Resistance and Capacity

Cell ID	Cell Capacity [Ah]	Cell Internal Resistance [mΩ]
85	14.764	8.466
21	13.761	7.854

A full table of these results can be found in APPENDIX D – Battery Cell Results, Table 8-5.

4.3 Fuel Cell Testing

4.3.1 Fuel Cell Fracture Testing

A point of interest in the modelling was determining failure modes of the fuel cell due to vibration and impact on the fuel cell from semi-normal driving conditions, such as curb strikes. An impact test on a 3 kW 72 cell Horizon fuel cell was performed to determine the point at which it would fracture when subjected to a kerb strike event. The fuel cell was mounted via the mounting points provided by Horizon in a 10 mm steel cage, which bolted to the MTS 4-Post Shaker Rig with little to no attenuation. This enabled the force from the 4-Post Shaker Rig to directly travel through the mounting points of the fuel cell. The fuel cell was subjected to a 100 mm vertical movement at a rate of 0.981 m/s^2 (0.1 g) to 29.43 m/s^2 (3 g) in 0.981 m/s^2 (0.1 g) increments whilst the fuel cell was pressurised with nitrogen at 0.55 barg (1.55 bar absolute) via a regulator. The pressure was monitored during the experiment by using two pressure gauges. This test was designed and conducted by the author of this thesis. The experimental test setup can be seen in Figure 4-19.

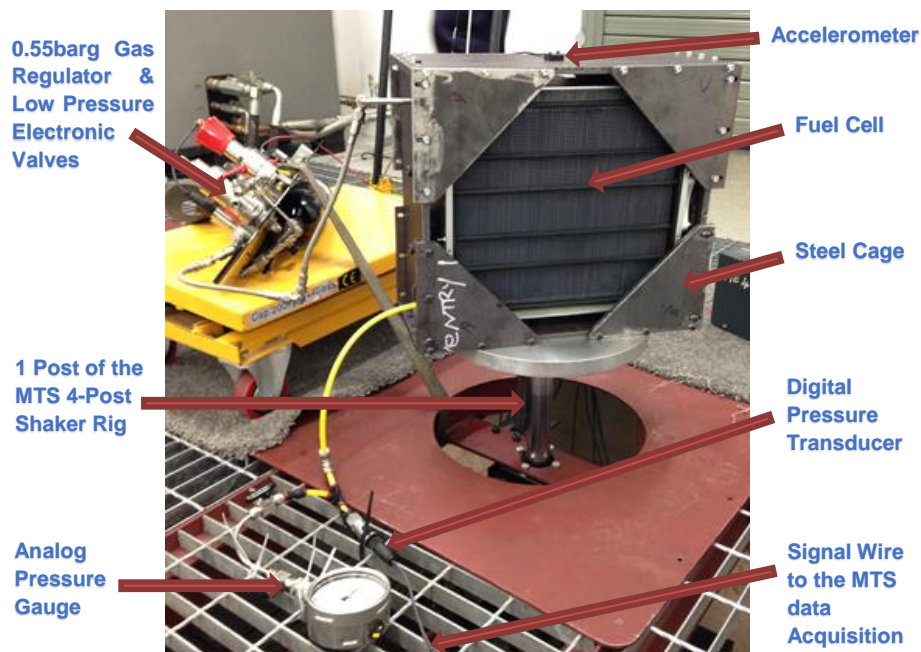


Figure 4-19 - Fuel Cell Fracture Test Rig

Figure 4-19 shows how the fuel cell has been mounted in the steel cage with the gas tray fitted in place to ensure that the correct nitrogen pressure is supplied. It can also be seen that an analogue pressure gauge has been used alongside a digital pressure transducer which has been fed into the MTS data acquisition software to ensure that two pressure readings can be taken for validation. Also, one accelerometer has been installed on the cage to confirm that the correct acceleration has been applied to the

fuel cell. Prior to the excitation of the shaker rig post, pressure is fed to the fuel cell and then the low pressure electronic valves are switched off to ensure there is only the pressure inside the stack during the test. This ensured that if a small leak occurred that it would be visible via both pressure gauges. After each impact the system was left for five minutes to determine if the system had developed a leak. The tests determined that the fuel cell retained pressure within the system throughout all of the tests and the fuel cell can be established as gas tight up to 29.43 m/s^2 (3 g) impacts on the mounting points. Therefore, this test suggests that it would not be necessary to implement a failure mode within the fuel cell model for high amplitude bump scenarios. The fuel cell which was tested already had electrical performance degradation present. The 3 kW Horizon fuel cell was originally fitted to a Coventry University Microcab H2EV. This study led to an additional study into the torsion at the chassis mounting points for the fuel cell, to identify if torsion at the mounting points is significant enough to cause a failure. The second investigation found that insignificant opposing forces were found at either mounting points during the series of tests and that it is unlikely to be the cause of the degraded cells. As conclusive evidence to the reason for fuel cell failures could not be identified, a torsion related failure mode was also not required to be implemented into the fuel cell model. A report of the tests conducted for the second investigation can be found in APPENDIX G – Vehicle Attenuation.

4.3.2 Fuel Cell, Battery & Hydrogen Consumption Testing

To validate the fuel cell model, DCDC model, battery model and hydrogen model the following test and logged variables were required. The test procedure required modifying the Coventry University Microcab H2EV's VCU power request parameter in increments of 250 W from 1000 W to 3000 W prior to each test, where the fuel cell was operated for a total of 10 purges on the 3 kW 70 cell Ballard 1080AC fuel cell. From this, sufficient hydrogen consumption data could be collected and used for validation. After each test the battery was drained at 30 A for eleven and a half minutes, so that a similar SOC start condition for the battery could be achieved for each test. The electrical charge which would be transferred to the battery during each test can be calculated using equations (224) and (225), and the time required to achieve a similar SOC between tests has been calculated using equation (227).

$$\frac{2,300 (As/purge)}{3600 (s)} = 0.6389 (Ah/purge) \quad (224)$$

Where:

- 2,300 = *The Coulombic purge interval As/purge*
- 3,200 = *The number of seconds in an hour*
- 0.6389 = *The electrical charge transferred to the battery in Ah/purge*

Here the amount of charge per fuel cell purge has been calculated by dividing the coulombic purge interval by an hour to change the units to *Ah*. This can also be used to determine how many purges from the fuel cell it would take to charge the battery, if there were no losses involved.

$$0.6389 (Ah/purge) * 10 = 6.389 (Ah) \quad (225)$$

Where:

- 10 = *The number of purges conducted during the experimental test*
- 6.389 = *The electrical charge transferred to the battery during the test in Ah*

Here the amount of charge transferred to the battery during the experimental test has been calculated.

$$\frac{60 (Ah)}{0.6389 (Ah/purge)} = 93.9 \quad (226)$$

Where:

- 60 = *The electrical charge of the battery in Ah*
- 93.9 = *The number of fuel purges required to charge the battery from 0 to 100% SOC*

Here the number of fuel cell purges required to charge the battery from 0 to 100% SOC has been calculated. By rearranging equation (220) presented in section 4.2.3, so that we solve for time, and using the result from equation (225), the time required to drain the battery when using the vehicle's 30 A heaters can be calculated.

$$\frac{6.389 (Ah) * 3600(s)}{30 (A)} = 766 (s) \quad (227)$$

Where:

6.389 = The electrical charge transferred to the battery during the test in Ah

3,200 = The number of seconds in an hour

30 = The electrical current of the vehicles heater in A

681 = The time required to drain the battery to the same SOC in s

Here electrical charge has been converted back into the SI units of As, by multiplying by 3,600s and then dividing by the current of the vehicle's heaters.

To conduct the tests within this section of the thesis, a tool that can merge up to three separate CAN bus's and analogue inputs was required Figure 4-20 shows the tool that has been created and the manufactured wiring loom.

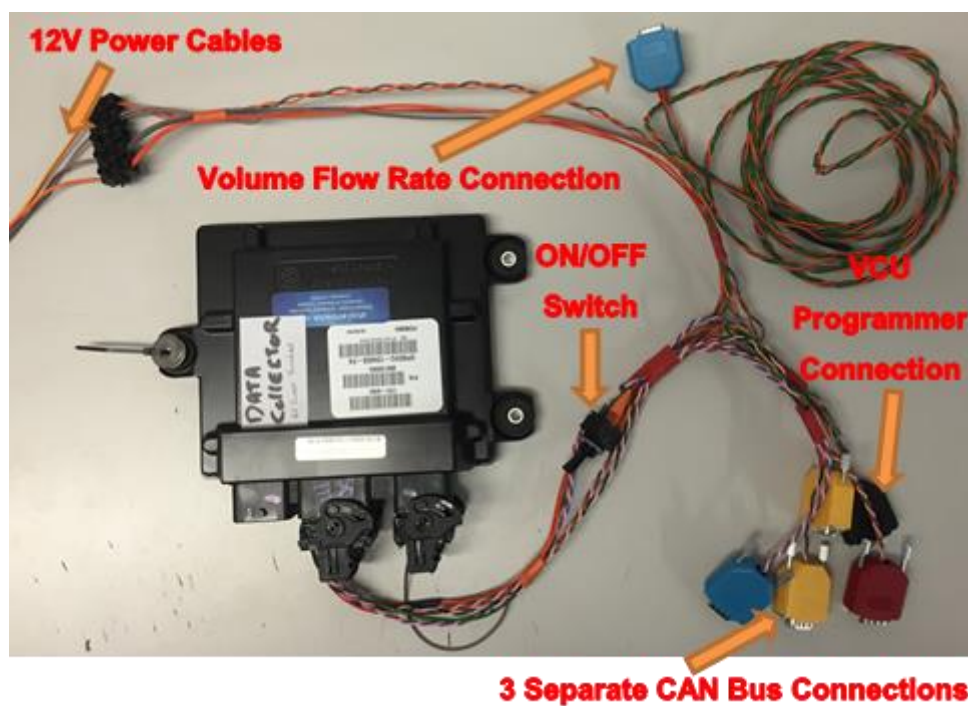


Figure 4-20 - Programmed Motohawk VCU and Wiring Loom for Data Acquisition Purpose

This controller and wiring loom shown in Figure 4-20 have both been programmed and built by the author of this thesis. A spare un-flashed VCU was used as the controller. The VCU which was used to perform this task was a Motohawk ECM-5554-112-0904xD. To make this useful, a Motohawk Simulink model was created within MATLAB/Simulink to receive the analogue 5 V signal from the volume flow rate sensor, 3 CAN databases had to be written to M-Code and the model compiled and flashed to the VCU. Once this was performed a wiring loom was required to interface between the volume flow rate sensor, the three vehicle CAN bus's and the Kvaser Memorator Professional HS/HS CAN bus logger. The experimental test setup used for this section can be seen in Figure 4-21.

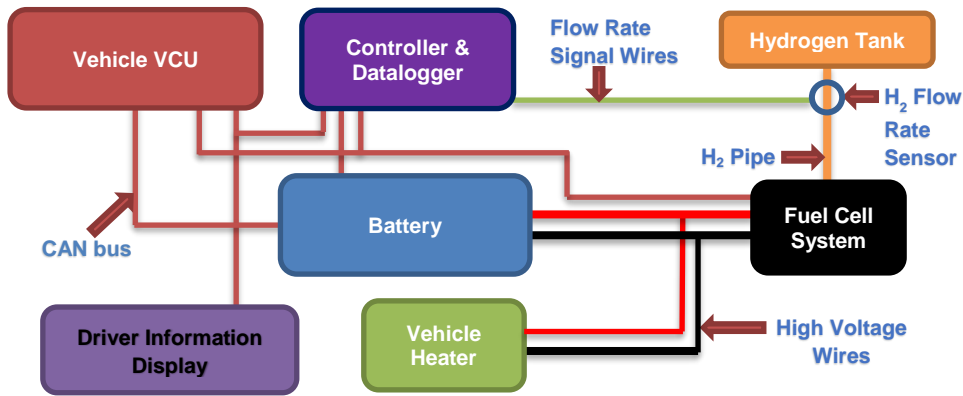


Figure 4-21 - Vehicle Test Schematic

Figure 4-21 shows each CAN bus in dark red, high voltage wiring in red and black, the hydrogen pipe in orange and the signal wires in green. This shows how the controller which has been programmed sits above the vehicle's platform, listening for all the data which is available on each CAN bus. The datalogger has been incorporated into the controller for simplicity within the schematic. The creation of this controller allows for all of the data from the different sub systems to be recorded with the same timestamp, thus, removing the post-processing procedure for aligning the data with regard to time. Figure 4-22 to Figure 4-29 show all the test data that was captured during this test. Figure 4-22 shows the voltage of the fuel cell for each of the power request tests.

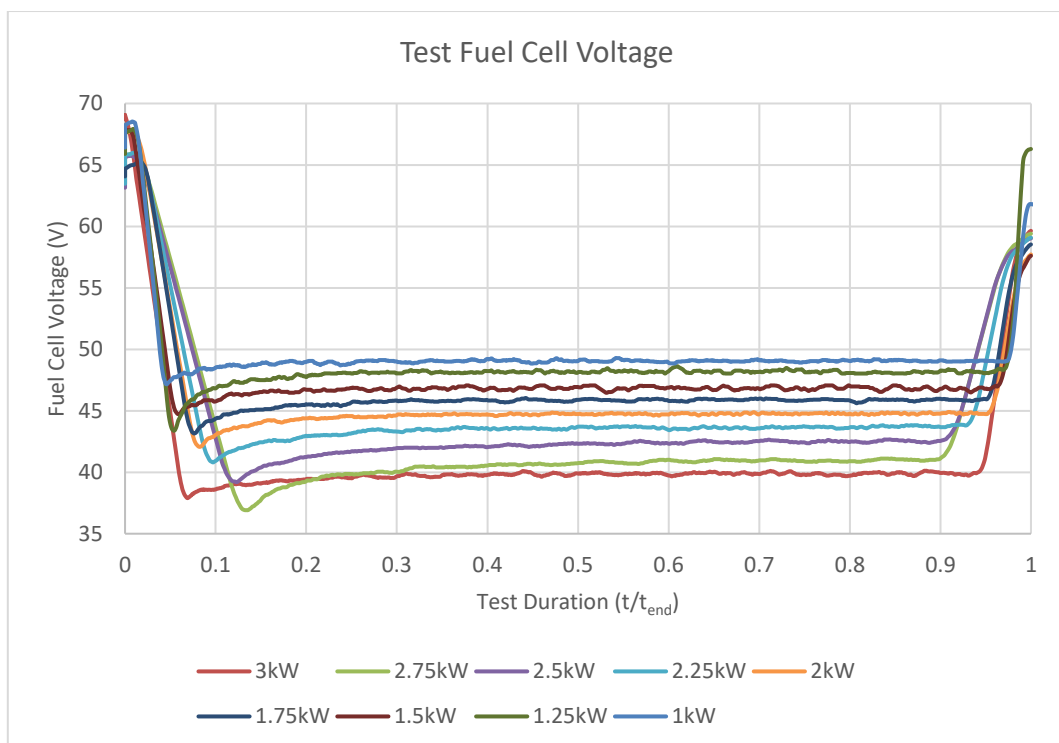


Figure 4-22 - Fuel Cell Voltage at Each Test Increment

Where the test criteria is to operate the fuel cell for 10 purges, or as shown by equation (225), $6.389 Ah$, the time taken to complete each test will not be the same. Therefore,

data has been presented against the test duration rather than the specific time of the test, this allows for better representation of the data in one single graph. Figure 4-22 shows that the open circuit voltage of the fuel cell varies, by as much as 5 V at the start of the test and the voltage of the fuel cell tends to be low at the start of the test, compared to half way through the test. Figure 4-23 shows the current of the fuel cell for each of the power request tests.

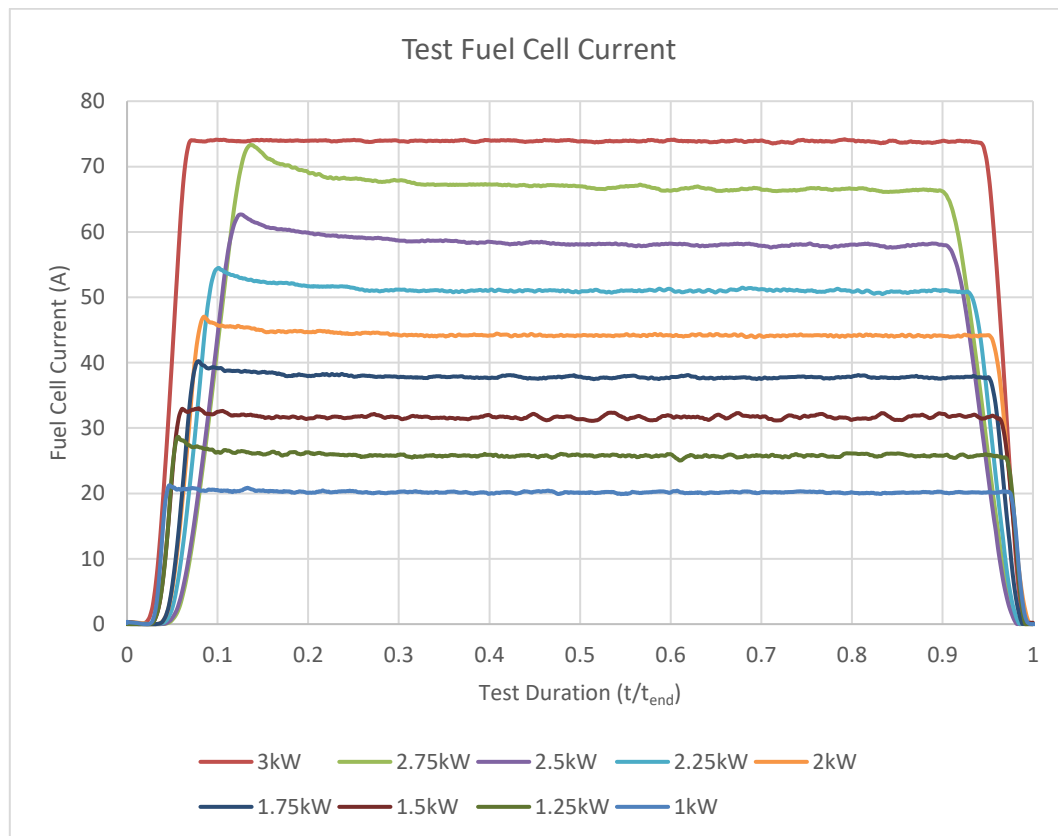


Figure 4-23 - Fuel Cell Current at Each Test Increment

Figure 4-23 shows that the fuel cell's controller draws more current from the fuel cell and then settles once the test is approximately one third of the way through. This is present for each test except for the 3 kW test, where the DCDC is at its current limit. This happens because the fuel cell controller is controlling the fuel cell to a power request, thus, where the voltage drops it increases the current to achieve the power output request. From the literature review, the published fuel cell modelling techniques required the implementation of temperature to represent the fuel cell voltage and this has also been included in the modelling technique used for this thesis. Therefore, the reduced fuel cell voltage at the start of the tests is likely to be due to a lower temperature, whilst the fuel cell is heating up. This can be checked by analysing the fuel cell temperature shown in Figure 4-24.

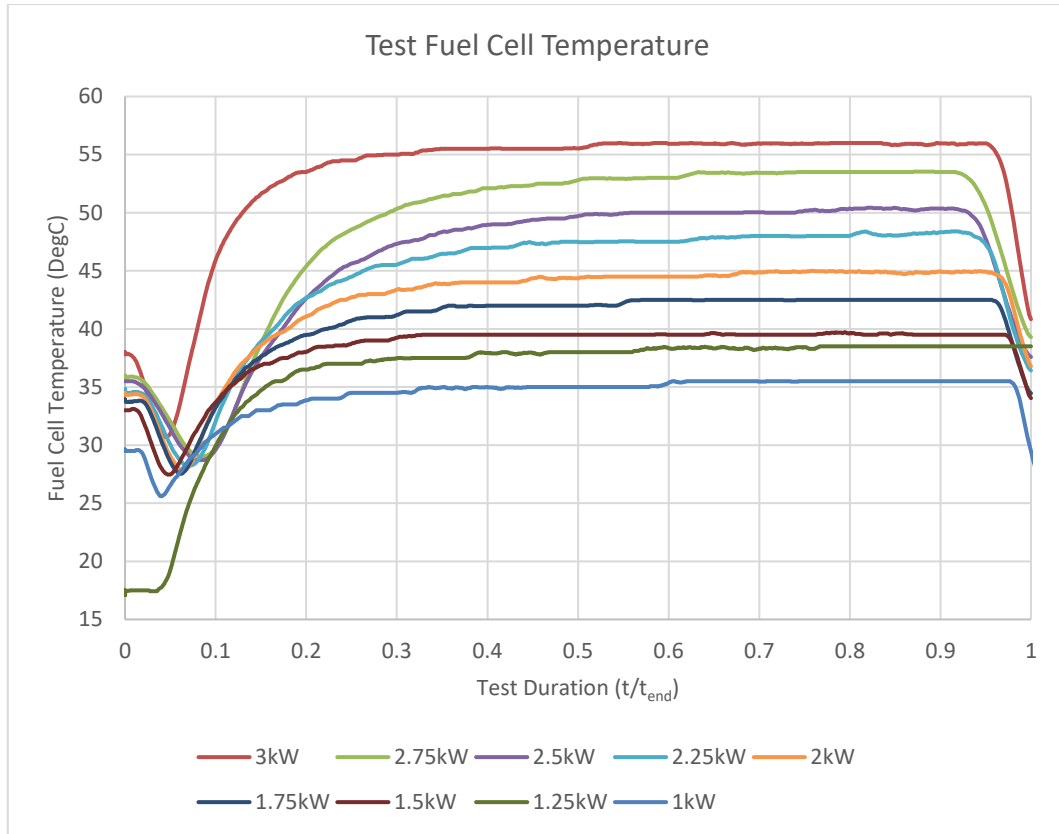


Figure 4-24 - Fuel Cell Temperature at Each Test Increment

Figure 4-24 shows that the temperature takes a large proportion of the test duration to settle therefore this could account for the lower voltage of the fuel cell early in the tests. It can also be seen that the PID which controls the fan in the fuel cell controller, appears to be heavily damped as at no point does the temperature overshoot or oscillate. Figure 4-22 shows the voltage at the battery for each of the fuel cell power request tests.

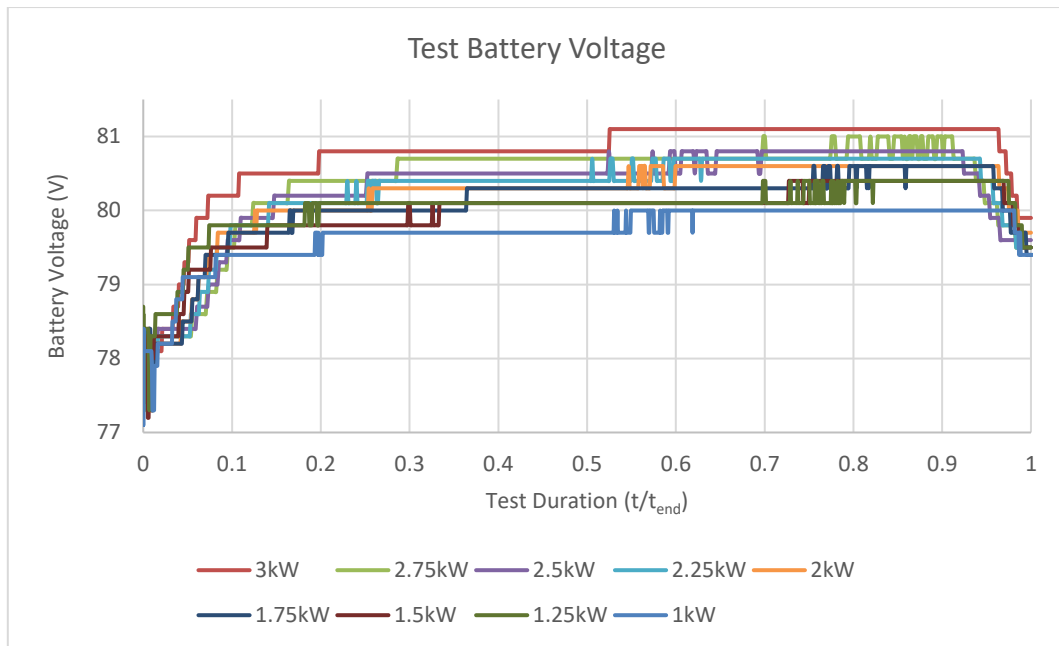


Figure 4-25 - Battery Pack Voltage at Each Test Increment

The test data shown in Figure 4-25 shows how the battery voltage increases as the fuel cell charges the battery at different rates. The data is particularly granular as the resolution on the battery packs voltage signal is 0.3 V. This creates the spikes in the voltage signal, as when the battery voltage is half way between the resolution the signal will switch between the two and can bounce if there is any noise on the signal, this is a limitation when using the Goodwolfe battery's BMS voltage signal to log the battery pack voltage. Figure 4-26 shows the current at the battery for each of the fuel cell power request tests.

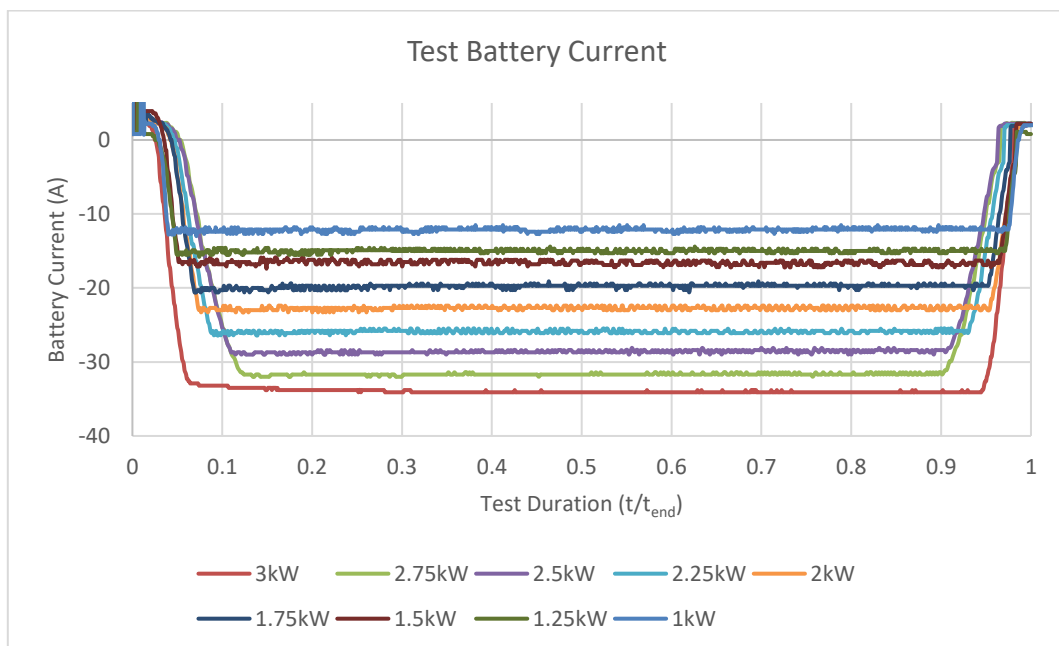


Figure 4-26 - Battery Pack Current at Each Test Increment

Figure 4-26 shows that the charge current of the battery is negative and that the DCDC in the fuel cell system provides a consistent current for the duration of the test. However, what looks like noise on the current signal is actually the DCDC buck-boost converter chopping the signal via transistors to regulate the current, this creates a very fast ripple which can appear as noise on a signal. Figure 4-27 shows the SOC of battery for each of the fuel cell power request tests.

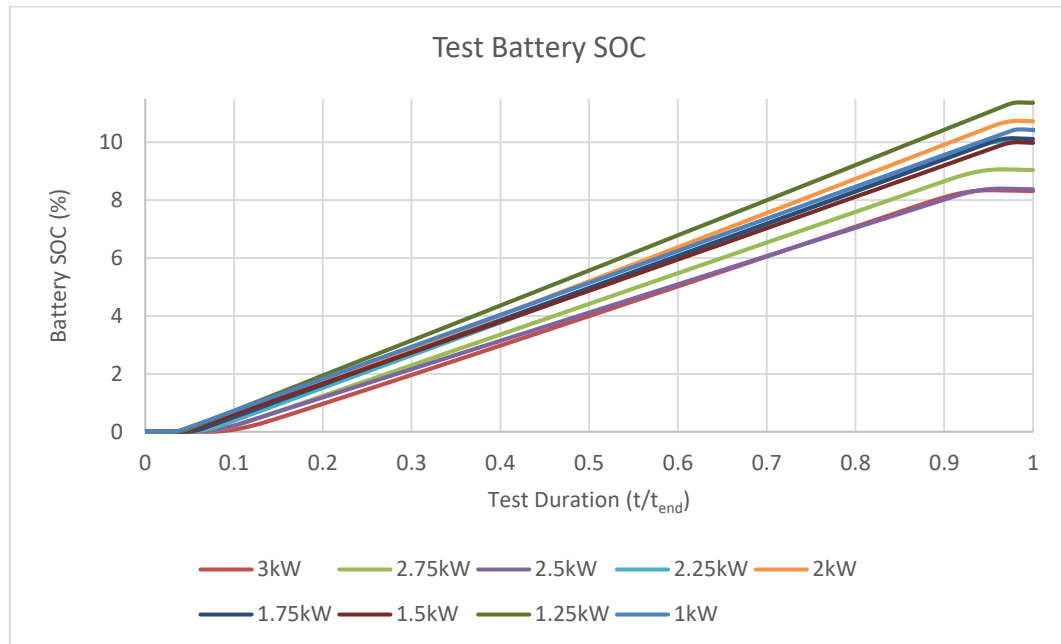


Figure 4-27 - Battery Pack SOC at Each Test Increment

Due to an error within the battery pack's BMS the SOC occasionally gets reset to 0% upon shutdown of the vehicle. Therefore, the battery pack within the test was not actually at 0% SOC, but the change in SOC is still correct, in regard to Coulombic current counting. Figure 4-27 shows that the amount of energy transferred from the fuel cell to the battery varies between tests, this is because the test has not been automated and required the action of starting and stopping the fuel cell manually.

Figure 4-28 shows the hydrogen tank pressure during each of the experiments.

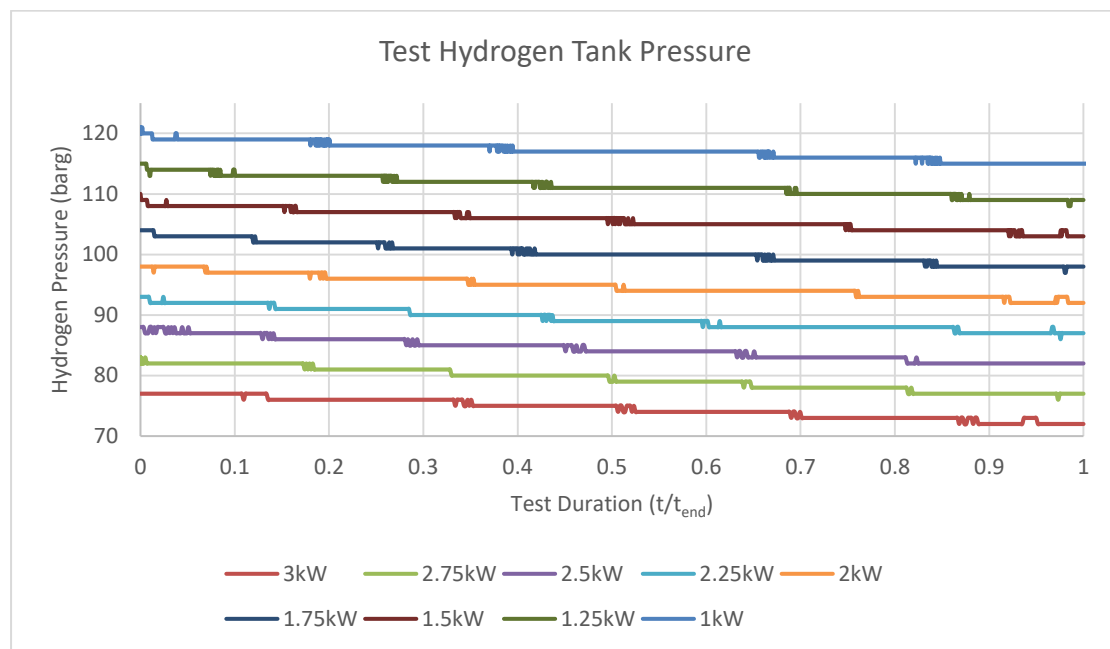


Figure 4-28 - Hydrogen Tank Pressure at Each Test Increment

Figure 4-28 shows the hydrogen tank pressure throughout each of the test procedures. Figure 4-28 shows that, during each test procedure the fuel cell uses between five and six bar of hydrogen from the tank to generate roughly 6.389 Ah over the duration of 10 purges. Figure 4-29 shows the hydrogen flow rate, in Standard Litres per Minute (slpm) for a small duration of each test.

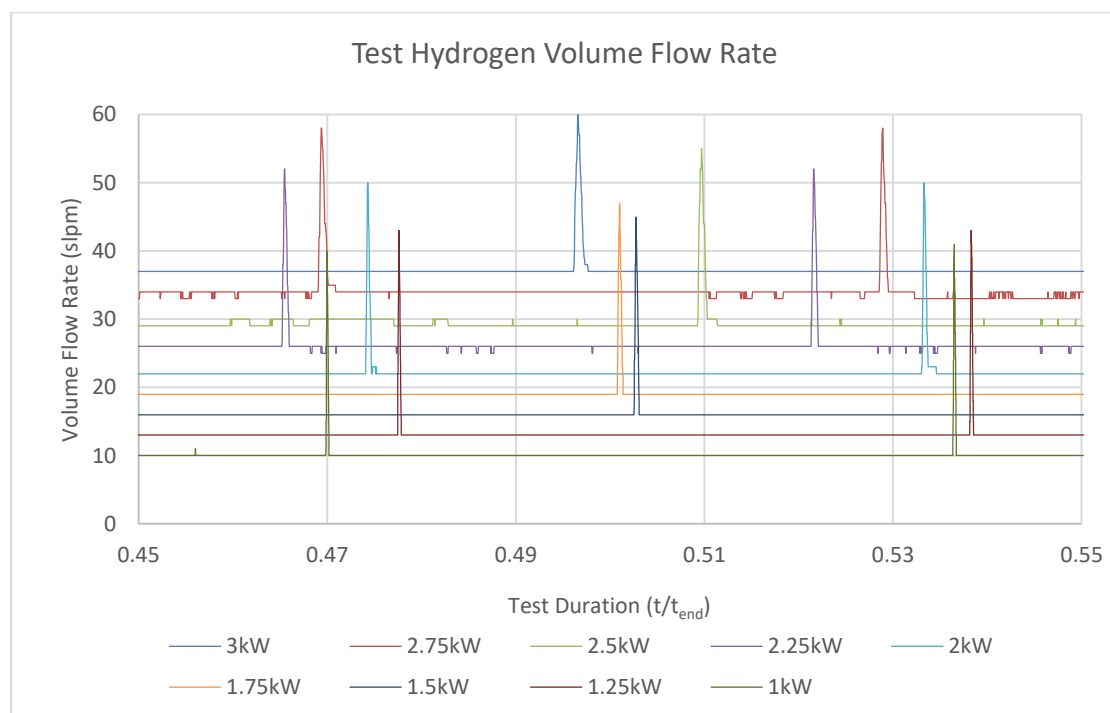


Figure 4-29 - Hydrogen Volume Flow Rate at Each Test Increment

Only a selected part of the data has been shown here as the hydrogen flow rate is consistent throughout each of the tests. Also the spike in flow rate during each fuel cell purge compromises the clarity and interpretation of the graphs. Figure 4-29 shows that when the fuel cell is operating at a higher output power the reacted hydrogen is increased. However, the volume flow rate during each purge is approximately an 27slpm larger than the reacted volume flow rate for the given power output. Figure 4-30 show the hydrogen volume flow rate on the 3 kW test during the shutdown procedure for the fuel cell.

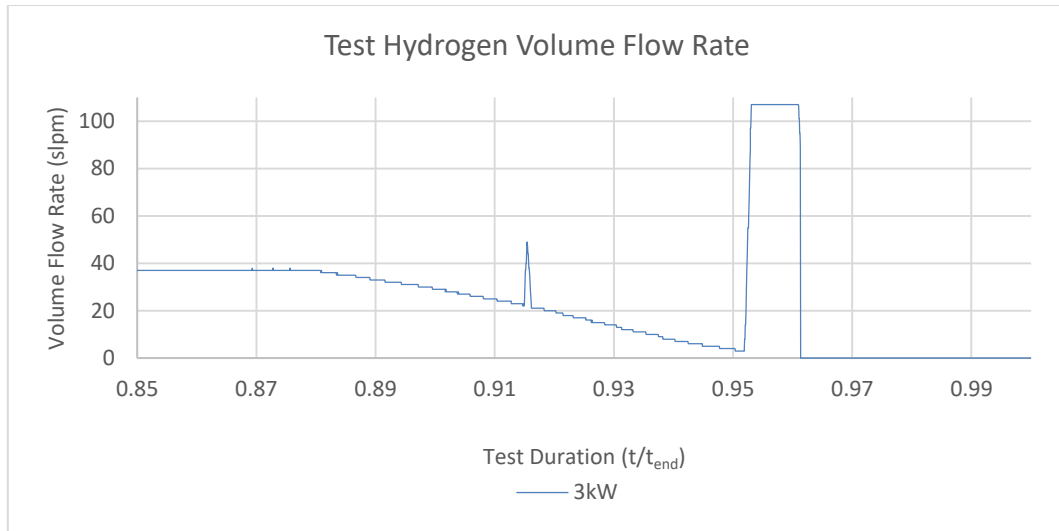


Figure 4-30 - 3kW Fuel Cell Hydrogen Flow Rate during Shutdown

There are two large purges when operating the fuel cell, one at the start and another at the end of each period of operating the fuel cell. These are the start-up purge and shutdown purge and they occur for approximately 2 seconds and reach the maximum volume flow rate of 107 slpm. This can be seen in Figure 4-30 where the shutdown purge has been used for the example. This also shows that as the fuel cell power is reduced, the reacted hydrogen consumption is also reduced.

4.4 Road Data Acquisition

4.4.1 NEDC Rolling Road Test

The NEDC is a ‘highly stylised’ test schedule, used to compare vehicle emissions between different vehicles and this test has been performed on a rolling road at MIRA. This test can be used for validating the vehicle model against dyno data for energy consumption of the battery when operating as an EV. The author was present for the duration of the test, but the physical test was carried out by MIRA at their test facility in Nuneaton, West Midlands, UK. Due to security reason, no photos are allowed whilst on the MIRA premises, thus, a written description of the test procedure is provided here. The test consisted of driving the vehicle on a chassis dynamometer at the speed/time defined in Figure 4-31, which is eight cycles of the Urban Cycle part of the NEDC, as seen in section 2.6, Figure 2-20. Whilst performing this test the battery voltage, battery current, force at the wheel and dynamometer speed were all measured and recorded for the following graphs to be created. Figure 4-31 shows the speed versus time profile which was used during the test.

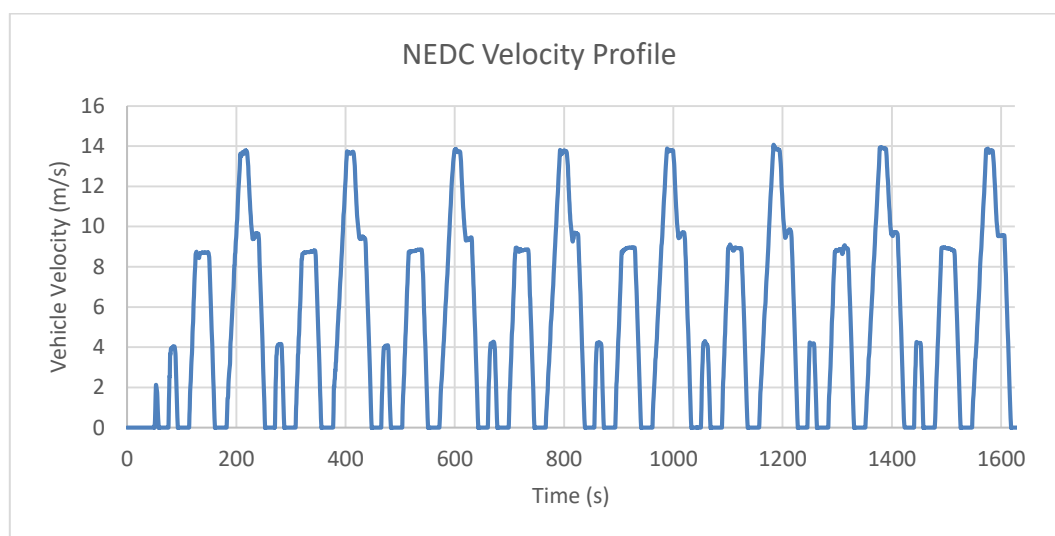


Figure 4-31 - NEDC Velocity Procedure

The highway-driving part of the NEDC which was discussed in the literature review was not carried out within this test. This is because the Coventry University Microcab H2EV, which was used for the test, is not able to achieve the higher speeds involved in the highway-driving section of the NEDC. Therefore, the NEDC urban driving section was used twice. The distance travelled over the test procedure is shown in Figure 4-32.

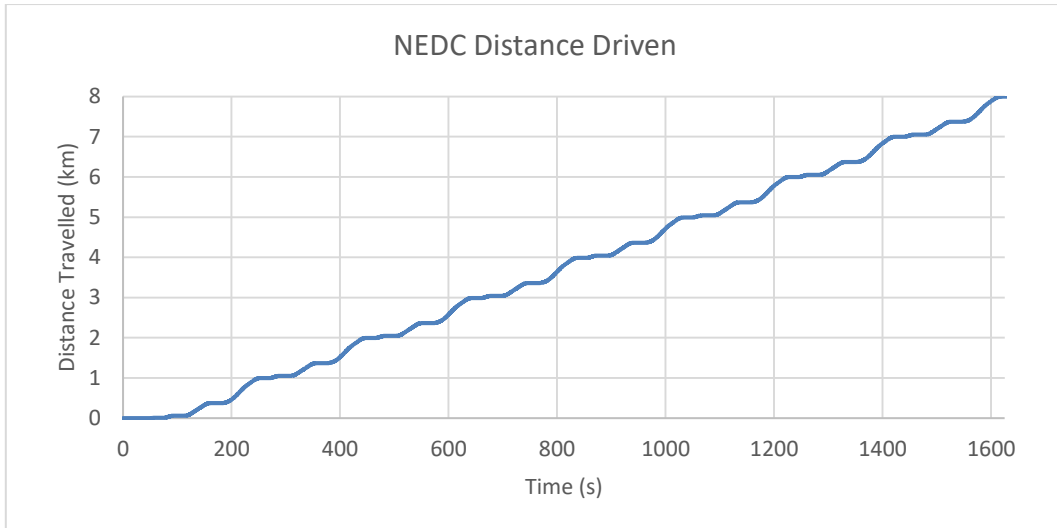


Figure 4-32 - NEDC Distance Driven

Figure 4-32 shows that the distance driven on the NEDC is 7.997 km, thus, each urban cycle of the NEDC accounts for approximately 1 km of driving. Figure 4-33 shows the energy consumption at the battery over the NEDC test.

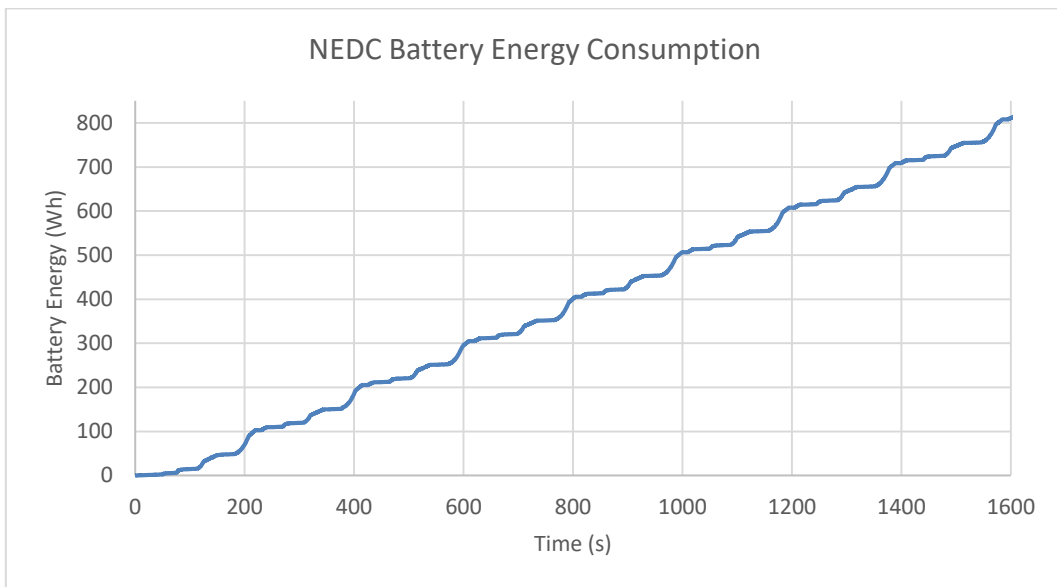


Figure 4-33 - NEDC Battery Consumption

Figure 4-33 shows that the vehicle uses a total of 815 Wh from the battery on the NEDC test procedure which has been described here. Therefore, an average energy consumption per km can be calculated using the sum of the energy supplied from the battery divided by the distance travelled. This gives an energy consumption of 101.9Wh/km. Where the force and speed of the vehicle's wheels is measured by the chassis dynamometer, the power which the vehicle produces at the wheels is also provided by the chassis dynamometer. Figure 4-34 shows the integral of vehicle power i.e. the power needed to move the vehicle, during the NEDC test.

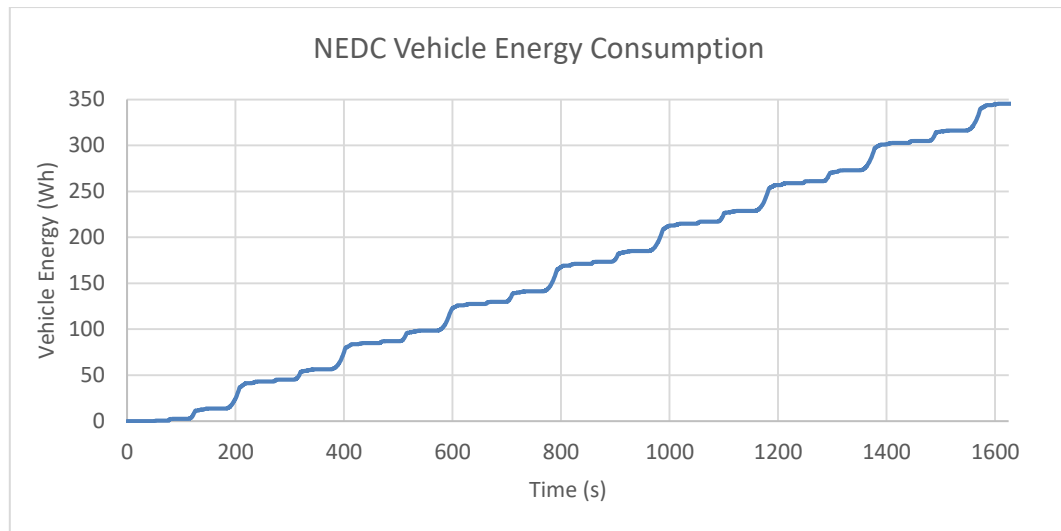


Figure 4-34 - NEDC Vehicle Consumption

Figure 4-34 shows that by the end of the NEDC test procedure the vehicle has provided 345 Wh of energy from the wheels. Therefore, the efficiency of the Coventry University Microcab H2EV powertrain can be calculated by dividing the energy provided, by the energy consumed. Thus, the average efficiency of the vehicle's powertrain is 42.3%.

4.4.2 Coventry University Drive Cycle

Figure 4-35 shows the physical locational data of the CUDC. The drive cycle has been overlaid on google maps (Google Maps 2015) and is the red route on the map.

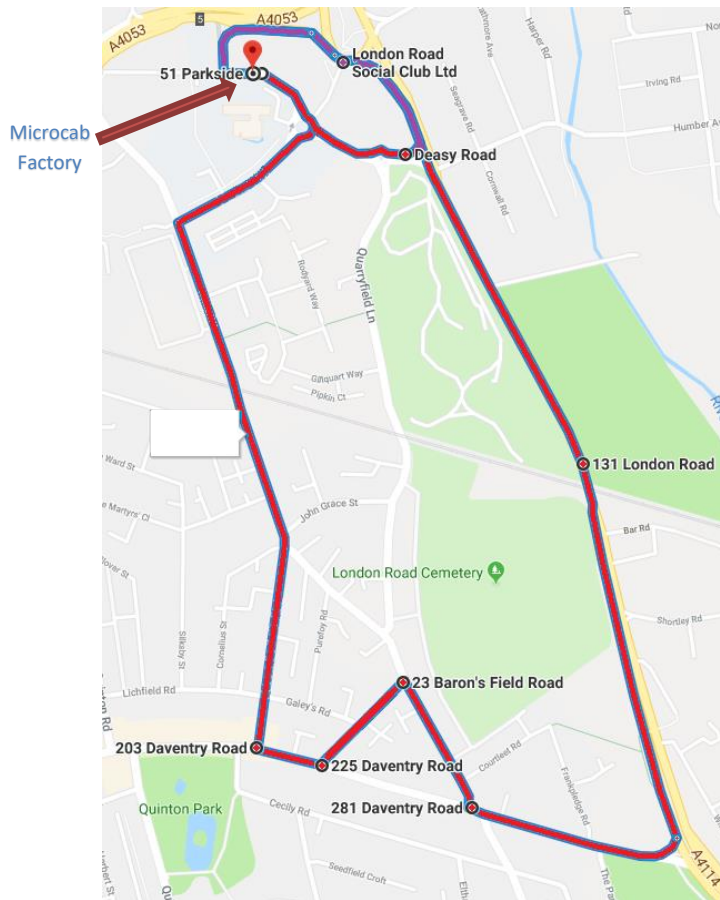


Figure 4-35 - Coventry University Drive Cycle Map

This drive cycle was designed by (Ryan et al. 2014) with the Coventry University Microcab H2EV in mind due to the inability to achieve the higher speeds of the NEDC and to incorporate a set of realistic real-world driving conditions, such as, stop-go traffic, round-a-bouts and variable altitude. This development of the drive cycle allowed for road testing of a vehicle with comparable speeds to that of the urban cycle of the NEDC (Ryan et al. 2014). However, within Dymola the road profiles are preferably circuits, where longer simulations can carry on running in a loop. The point at which the CUDC starts and ends is too close together to generate a turning point and therefore creates simulation issues. To overcome this issue, the drive cycle was changed and shown as the purple extension at the top of Figure 4-35. The test data in this section was obtained by physically driving the Coventry University Microcab H2EV on the CUDC in Coventry, West Midlands, UK. This was done by the author of this thesis and has been repeated multiple times to ensure that the results which are presented here, are hereby an accurate representation of the energy consumption of

the vehicle when driving this real world urban route. This test can be used for validating the whole vehicle model as a 3D energy prediction model and to compare real world driving data and energy consumption against current the type approval method, the NEDC. A combination of data acquisition devices has been used. A Race Technology DL1 CAN Data logger has been programmed and used for the acquisition of the vehicle data as well as the GPS positioning. However, where over a few tests the CAN feature of the DL1 proved to be unreliable a Kvaser Memorator Professional HS/HS was used in addition to ensure that the vehicle data could always be obtained. Figure 4-36 shows the velocity of the vehicle when performing the CUDC test.

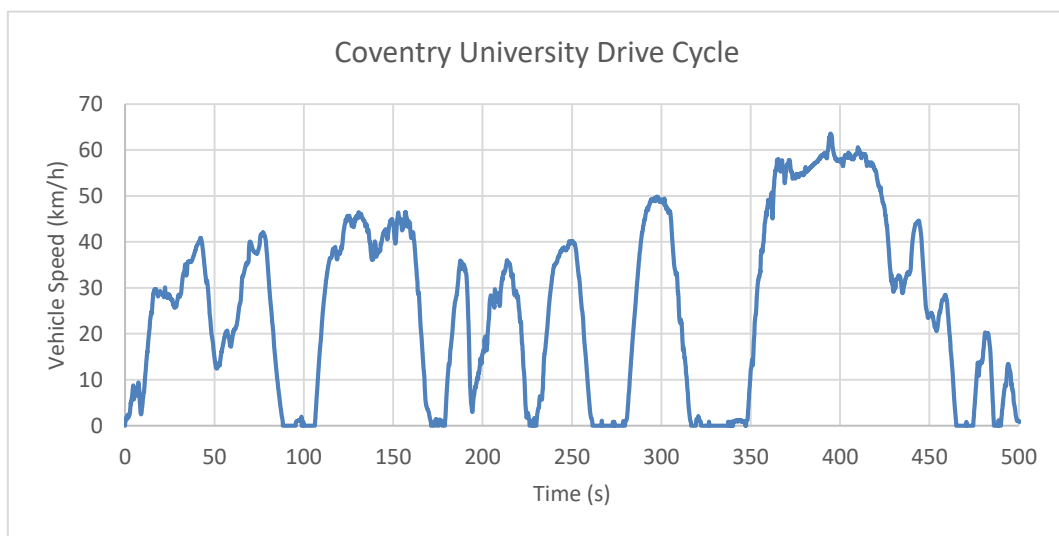


Figure 4-36 - Coventry University Drive Cycle Velocity Profile

Figure 4-36 shows that the CUDC consists of seven stop/start scenarios with several periods of up to 49 km/h (30 mph). It has one higher speed section which is up to 65 km/h (40 mph) for around 75s, and the Root Mean Square (RMS) of the CUDC velocity profile is 32.4 km/h. Figure 4-37 shows the battery voltage of the Goodwolfe 72V 4kWh battery pack during the CUDC test procedure.

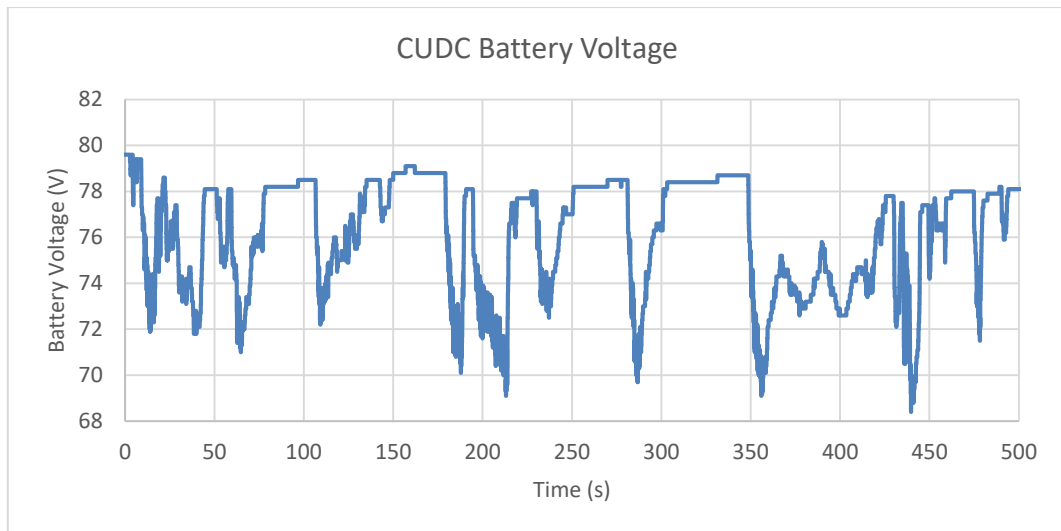


Figure 4-37 - Coventry University Drive Cycle - Battery Voltage Results

By comparing Figure 4-37 to Figure 4-36 it can be seen that when the vehicle is accelerating the battery voltage drops to as low as 68.4 V (2.85 V/cell) and when the vehicle is at rest the battery voltage returns to approximately 78 V (3.25 V/cell). Figure 4-38 shows the battery current of the Goodwolfe 72 V 4 kWh battery pack during the CUDC test procedure.

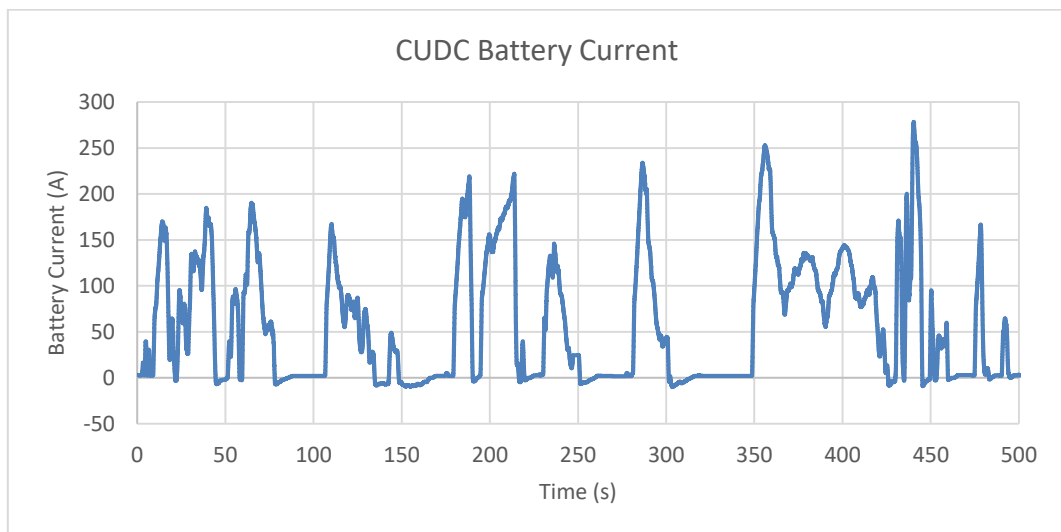


Figure 4-38 - Coventry University Drive Cycle - Battery Current Results

Figure 4-38 shows that the battery current reaches peaks of approximately 275 A and the RMS of the battery current over the CUDC is 90.3 A. The energy consumption over the test can be derived from Figure 4-39 where the battery SOC during the CUDC test is presented.

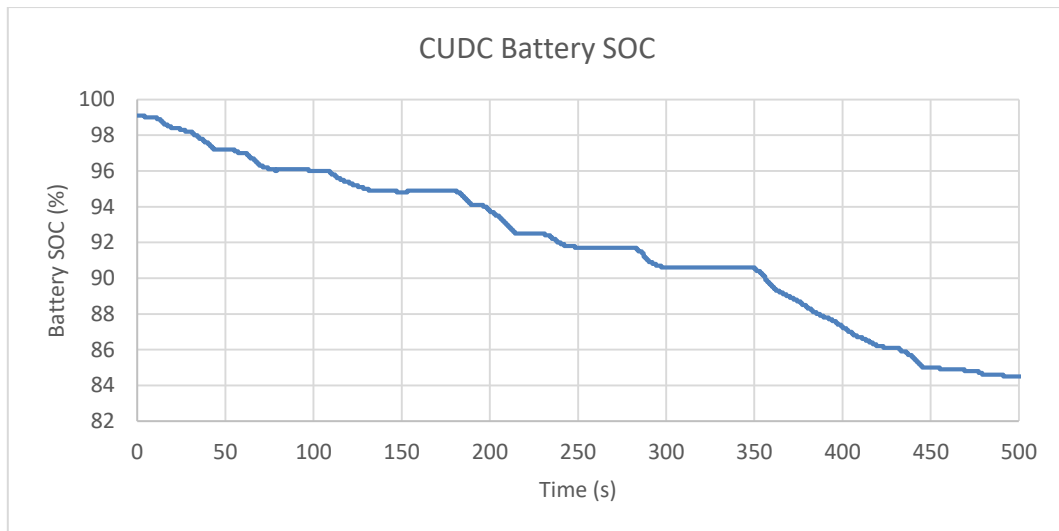


Figure 4-39 - Coventry University Drive Cycle - Battery SOC Results

Figure 4-39 shows that the CUDC test started with a battery SOC of 99.1% and finished the test with a battery SOC of 84.5%. Therefore, the vehicle required 14.6% SOC from the battery to perform the drive cycle. Thus, using the percentage of SOC used for the test and multiplying this by the battery capacity in Wh (4 kWh), the energy consumption over the test can be derived as 584 Wh. The altitude along the CUDC test is presented in Figure 4-40.

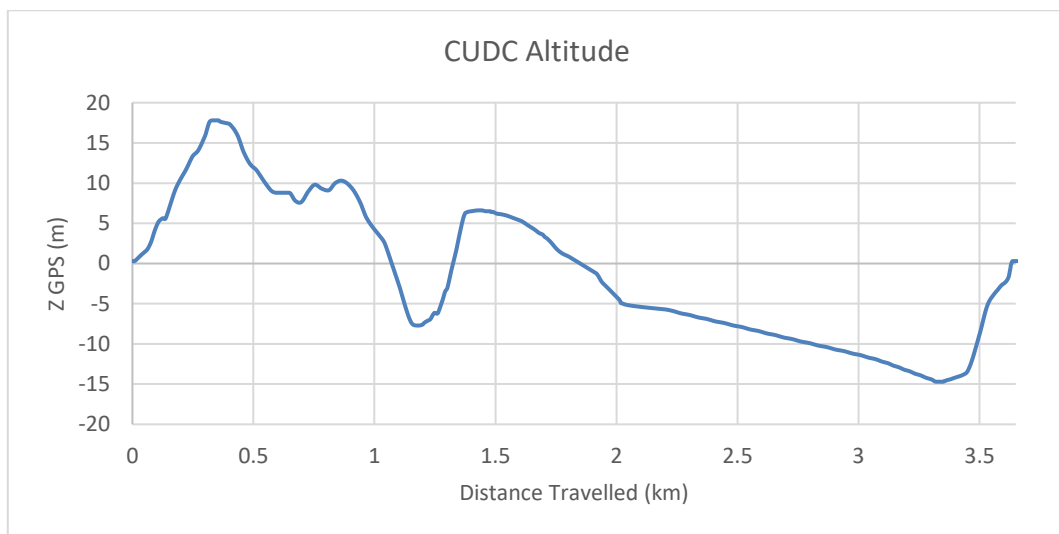


Figure 4-40 - Coventry University Drive Cycle, Altitude Profile

Figure 4-40 shows that the altitude changes significantly over the drive cycle and although these appear steep on the graph, the steepest incline is 7.5 degrees. Now the average energy consumption per km can be calculated by dividing the derived energy consumption, 584 Wh, by the distance travelled, 3.65 km, which gives 160 Wh/km. Figure 4-41 shows the X and Y GPS data which has been recorded during the CUDC test.

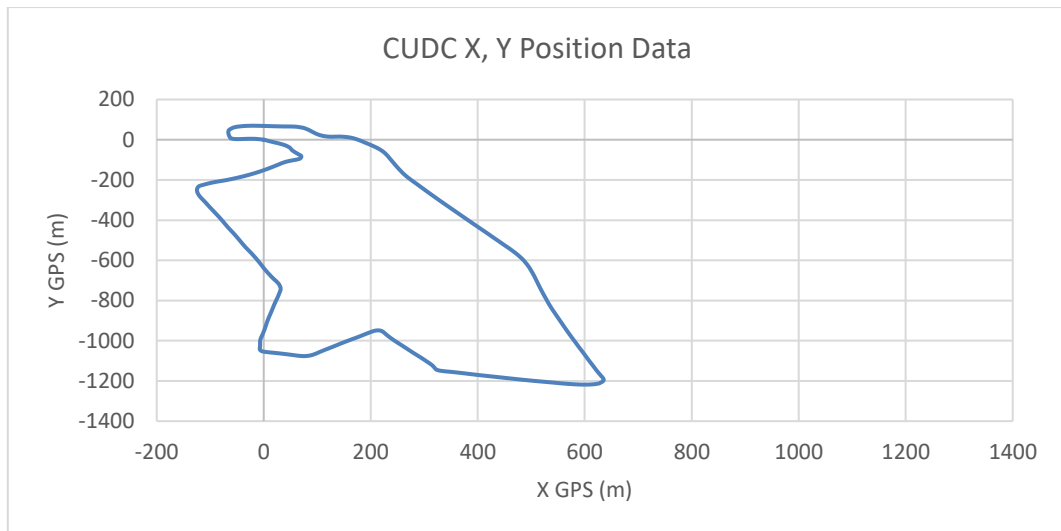


Figure 4-41 - Coventry University Drive Cycle, X, Y GPS Positioning

It can be seen that Figure 4-41 accurately represents the CUDC which is shown earlier in Figure 4-35. The discussion around Figure 4-40 shows that the energy consumption over the CUDC is 160 Wh/km and the discussion around Figure 4-33, in Section 4.4.1, shows the energy consumption for the NEDC test to be 101.9 Wh/km. Using these two measurements to determine the percentage difference, there is a 36.3% difference in energy used per kilometre between the two drive cycle tests.

4.5 Summary of Tests

Using the tests presented within this chapter validation can be made at a subsystem level as well as at the full vehicle level. Wherever possible each test has been performed under controlled conditions. However, even where it was possible to run controlled tests, it has not always been possible to perform repeated experiments to create statistical significance. In other cases, data has been normalised to compare results from field trial data. Where key data, such as energy consumption is common. By normalising some of the test results specific test data can be used to actuate the simulation to validate the results of the modelled system against the test data. This ensures that the simulated test can be the same as the comparable physical experiment.

This chapter has shown the approach taken for each test: Where the vehicle geometry has been acquired through virtual and physical measurements; The batteries were tested under a set of steady state operating conditions at both the whole battery pack level and at the battery cell level; The fuel cell has been tested under a set of steady state operating conditions to determine the hydrogen consumption, fuel cell voltage characteristics and the response from the battery; The whole vehicle has been tested by using both a rolling road at MIRA to perform the NEDC test, where MIRA members of staff performed the test, and through physically driving the vehicle on the CUDC in Coventry, United Kingdom. The tests conducted within this chapter have provided the data required so that objectives 3 and 4, in section 1.3, “subsystem validation” and “whole vehicle level validation” can be achieved.

The set of tests provides the data to establish how accurate the vehicle model will be at representing real life conditions.

CHAPTER 5 – SIMULATION RESULTS, CORRELATION AND VALIDATION

Simulation models can sometimes be useful in isolation. However, it is generally important to address their accuracy by reference to experimental data, and this should be collected to represent the same test conditions used for the model simulation. This approach has been taken wherever possible within the project. Where such analysis has revealed differences between predicted and measured results, these have been investigated and used to identify sources of error within the model, leading to refinement and convergence. Generally, within this investigation, experimental results have been accepted as the reference, and correlation errors are assumed to lie within the model rather than the experimental work. A wider view of validation within this project also requires confirmation from the client groups of the usefulness and practicability of the results. This has been particularly important in the cases where control implementation has been recommended, reflecting the important goals of safety, reliability and usability. Implementation of recommended changes arising from the investigation and modelling exercise has been achieved for four distinct aspects;

- Vehicle Dynamics - Suspension and Steering
- Vehicle Dynamics - Motor Control
- Battery Management - Charge and Discharge
- Fuel Cell - Thermal Management

The first two of these have been fully implemented, assessed and validated, whilst the last two are partially implemented but not fully assessed at the present time. Therefore, the approach in these cases has been validated by the client group. This section of the thesis will compare the simulation results of the model with the comparable tests defined in CHAPTER 4 - Data Collection, Experiments and Testing, demonstrating a level of accuracy for the difference systems within the model. A summary of the RMS error of the models have been presented in section 5.6 and a tabulated version of the results are shown in APPENDIX H – Tabulated Validation Results.

5.1 Sub-System Validation

5.1.1 Battery Pack Steady State Discharge Validation

This validation procedure is used to compare the battery model's ability to represent the voltage and SOC of the 72 V 4 kWh Goodwolfe battery pack by using the results from section 5.1.1. The model simulation environment can be seen in Figure 5-1.

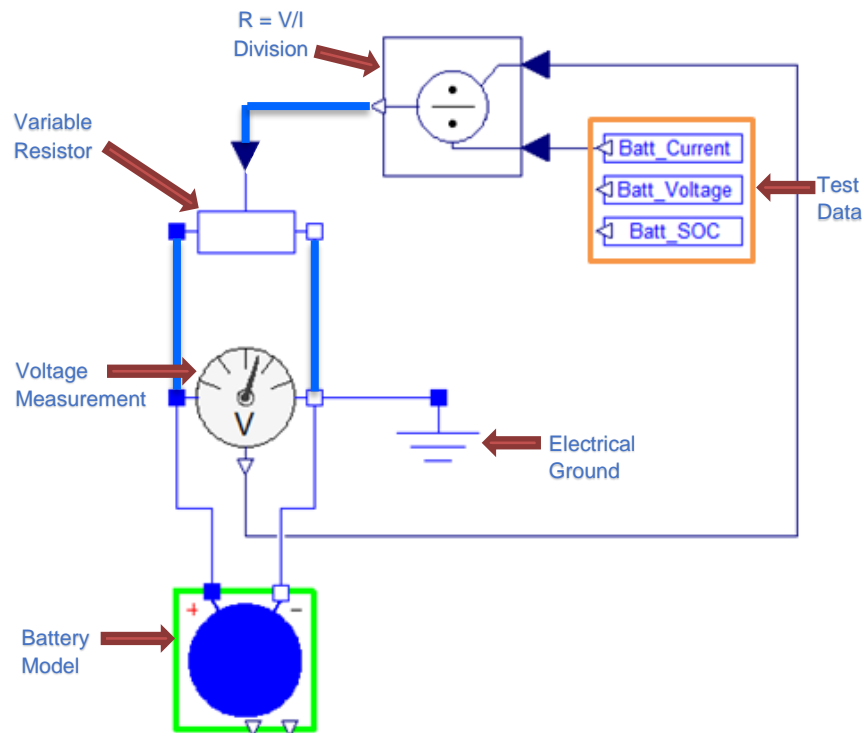


Figure 5-1 - Steady State Battery Discharge, Simulation Setup

Within this validation procedure, the model has been set up to use a variable resistor and a division so that the voltage at the battery pack divided by the logged test current data will produce the correct resistance to apply equal current draw from the battery to that of the physical test. The test data has been imported in the three sub-models, within the highlighted orange section of the figure, to enable direct validation between the simulation results and the test results. Thus, the duration of the experimental test determines the duration of the simulation. To ensure that the simulation setup is functioning as expected, the test battery current has been plotted against the simulation battery current in Figure 5-2.

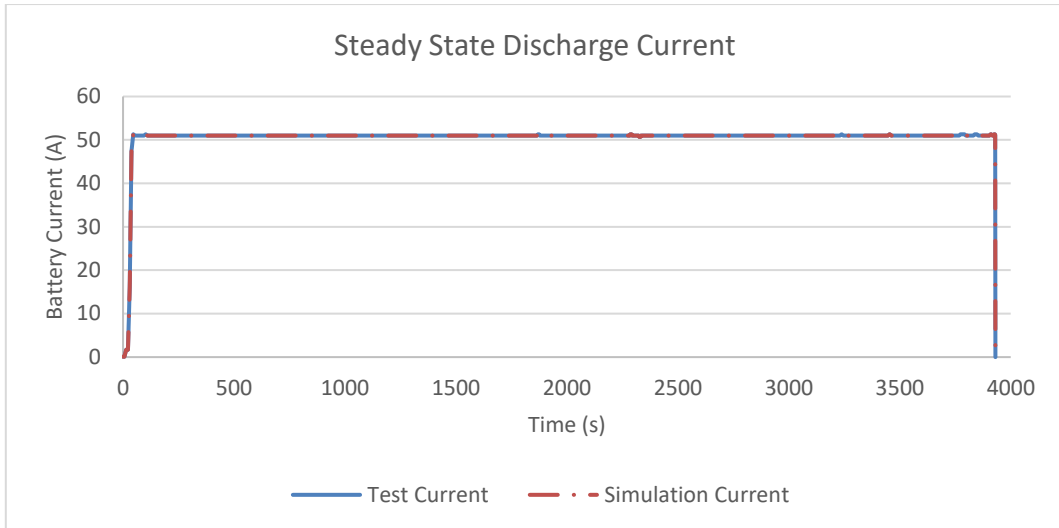


Figure 5-2 - Steady State Battery Discharge Current Simulation Results

Figure 5-2 shows the simulation current superimposed on the test current and it shows that they are equal, thus, showing that the simulation setup functions as intended. As previously stated the simulation duration of 3931s is dictated by the duration which the experimental test took, where the test data is the driving factor of the simulation. Both the test and simulation battery voltage are plotted against the battery SOC and are shown in Figure 5-3 to show the correlation between results.

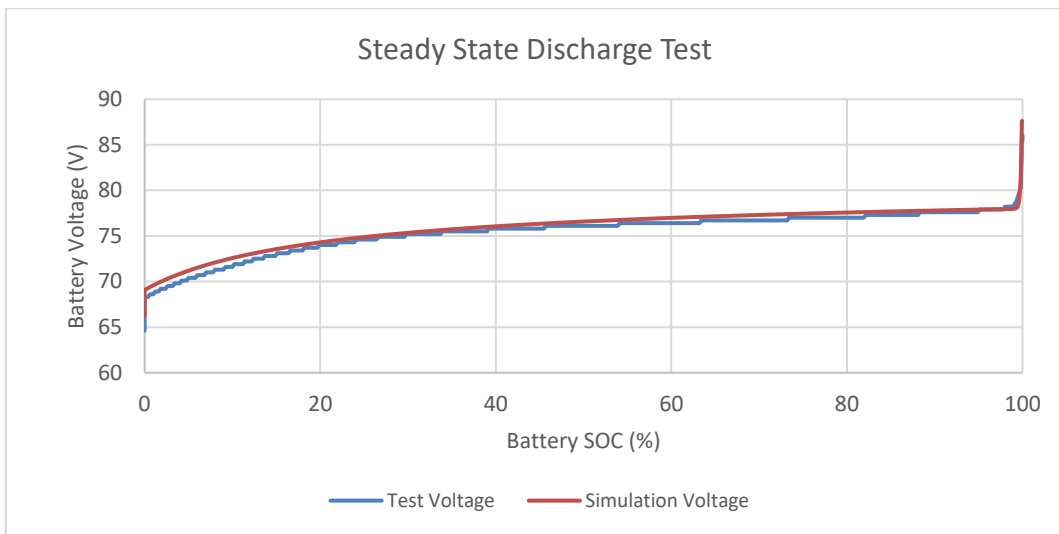


Figure 5-3 - Steady State Battery Discharge Voltage Simulation Results

Figure 5-3 shows that the battery model presented in this thesis can represent the battery voltage well over the majority of the battery's SOC. It shows a correlation to the test scenario of approximately 1 V over the simulation. To ensure that the capacity of the battery model represents that of the physical battery, the SOC for both the test results and the simulation results have been plotted about the simulation duration. This is shown in Figure 5-4.

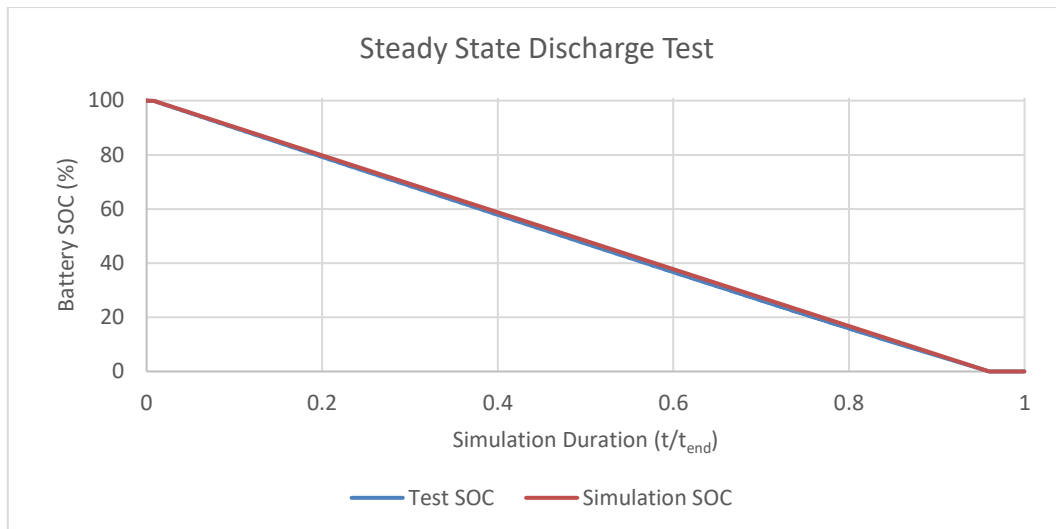


Figure 5-4 - Steady State Battery Discharge SOC

It can be seen in Figure 5-4 that the simulated SOC shows similar capacity to that of the physical test. This shows that the battery SOC can be represented very well over the course of the simulation with a highest difference in SOC of 1.19%. From the results, the percentage error between the simulation results and the test data can be obtained to get the instantaneous error over the simulation and then the RMS of the error, to determine a level of confidence in the model. This is shown in Figure 5-5 where both the voltage and SOC errors are presented.

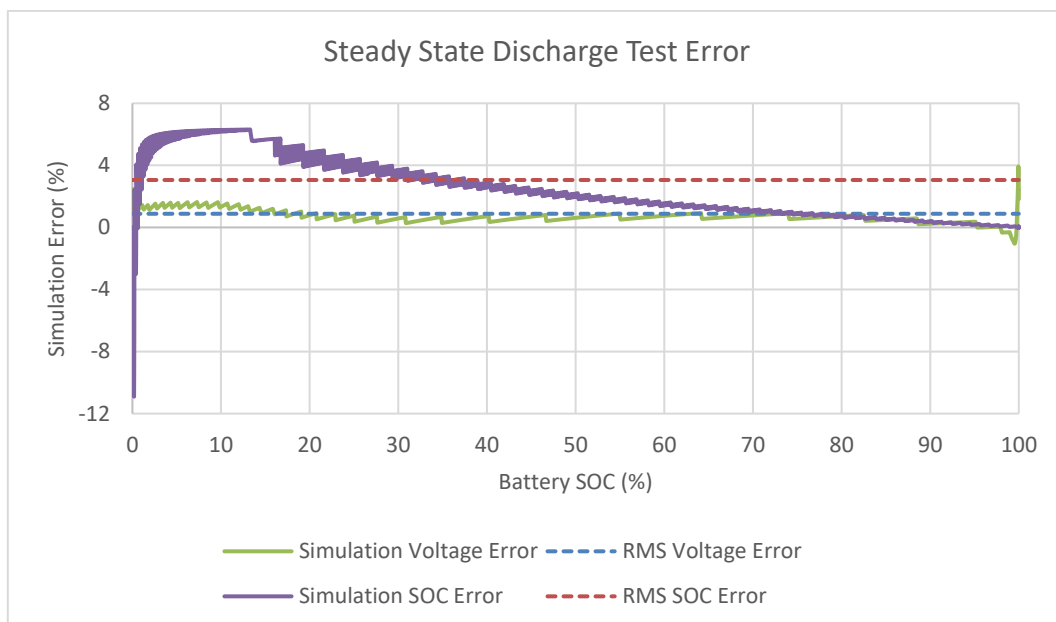


Figure 5-5 - Steady State Battery Discharge Simulation Results

Figure 5-5 shows that the RMS error of the battery voltage is 0.88%, therefore the model can represent the battery voltage to a RMS average of 99.1%. The minimum accuracy of the battery voltage during this simulation is 96%, which occurs during the exponential range of the battery voltage, near 100% SOC. Figure 5-5 shows a

relatively high percentage error in SOC estimation when the battery is low in SOC, however, this is where the battery SOC is close to zero, thus, small differences in battery SOC results in larger percentage errors. The RMS error of battery SOC has been calculated as 3.05%, therefore the model can estimate the battery SOC to an average of 96.9%.

5.1.2 Battery Pack Goodwolfe Charge Simulation

This validation procedure is to compare the battery model's ability to represent the voltage and SOC of the 72 V 4 kWh Goodwolfe battery pack by using the results from section 4.2.2. The model simulation environment can be seen in Figure 5-6.

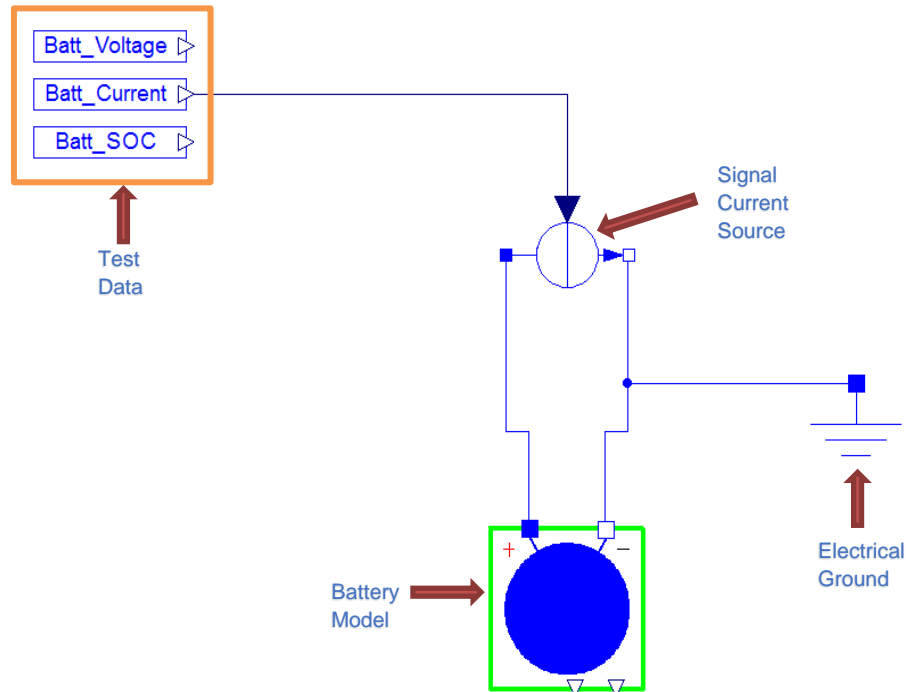


Figure 5-6 - Goodwolfe Battery Charge, Simulation Setup

Figure 5-6 shows how model simulation has been created to use a signal current source so that the current provided to the battery pack is equal to that of the physical test data. The test data has been imported, via the three sub-models, within the highlighted orange section of the figure and Figure 5-6 shows how the battery current from the test data is the driving factor of the simulation, thus, the test duration dictates the duration of the simulation. This has been implemented to allow for direct validation between the simulation results and the test results. To ensure that the simulation setup functions as expected, the test battery current has been plotted against the simulation battery current in Figure 5-7.

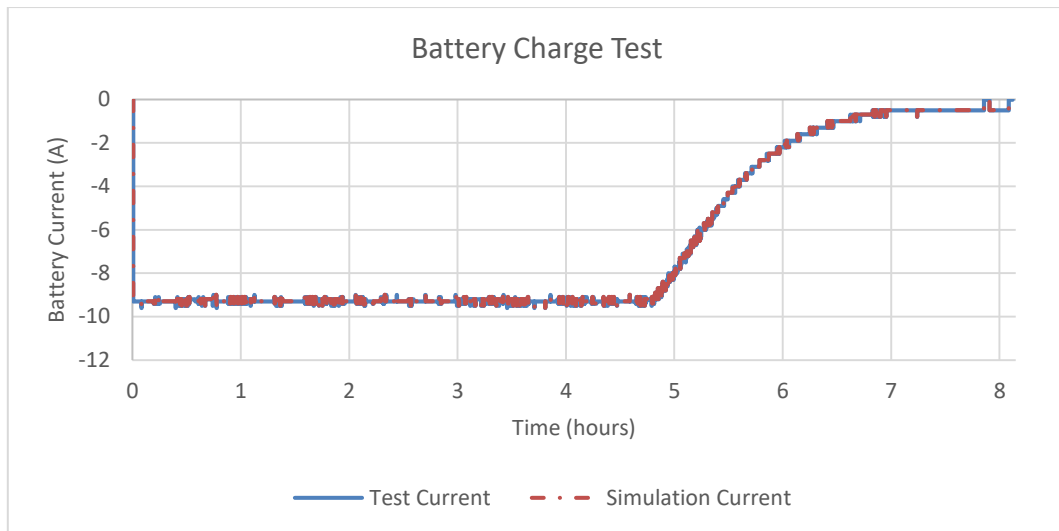


Figure 5-7 - Battery Charge Current Simulation Results

Figure 5-7 shows the simulation battery current overlaid on the test battery current and it shows that they are equal, thus, showing that this simulation setup functions as intended. As stated in section 4.2.2, the battery took just over 8 hours to charge until the BMS disabled the charger and where the test data is the driving factor of the simulation, this dictates the duration of this simulation. Both the test and simulation battery voltage are plotted against the time of both the test and simulation respectively. Figure 5-8 is presented to show the correlation between these two results.

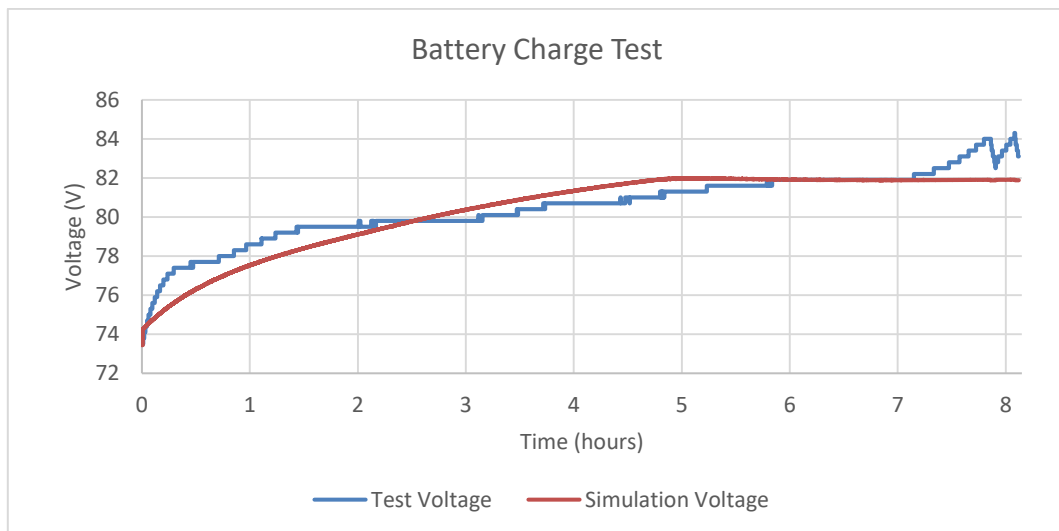


Figure 5-8 - Battery Charge Voltage Simulation Results

Figure 5-8 shows that the battery model presented in this thesis can represent the battery voltage to approximately 1V over most of the simulation. However, towards the end of the simulation the representation is not as good and a difference of up to 2.5V can be seen. To ensure that the capacity of the battery model represents that of the physical battery, the SOC for both the test results and the simulation results have been plotted against the simulation duration. This is shown in Figure 5-9.

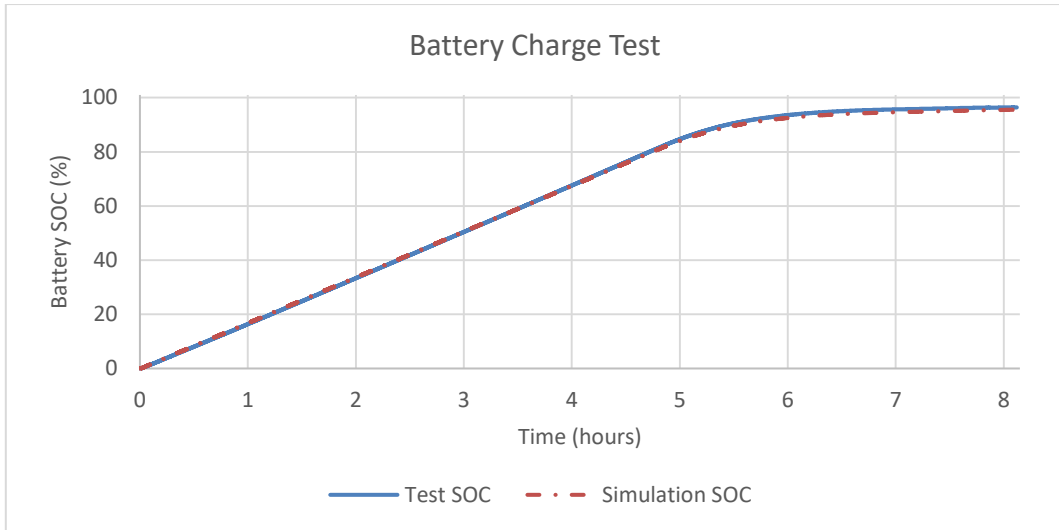


Figure 5-9 - Battery Charge SOC Simulation Results

It can be seen in Figure 5-9 that the simulated SOC shows similar capacity to that of the physical test where the SOC trace follows that of the test very closely over the entire simulation. From the results, the percentage error between the simulation results and the test data can be obtained to get the instantaneous error over the simulation and then the RMS of the error, to determine a level of confidence in the model. This is shown in Figure 5-10 where both the voltage and SOC errors are presented.

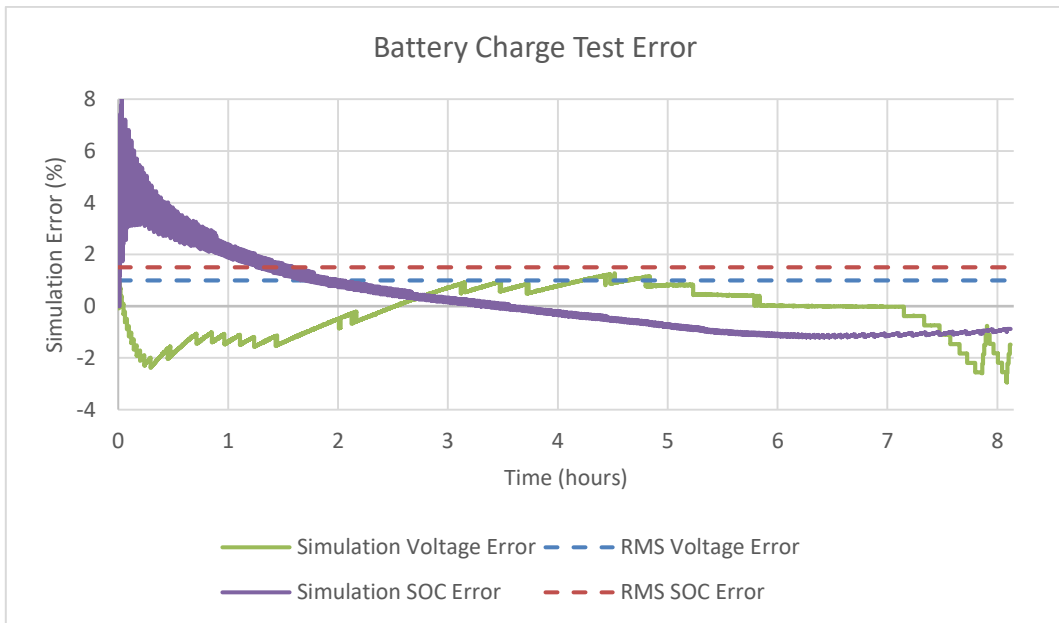


Figure 5-10 - Battery Charge Simulation Results

Figure 5-10 shows the error when directly comparing the simulation results against the test results in real-time throughout the simulation. The RMS error of the battery voltage is 0.99%, therefore, the battery voltage can be represented to an average of 99.1% for this test scenario and there is a minimum accuracy of 97% during the high voltage

exponential range of the battery voltage towards the end of the simulation. The RMS error of the battery SOC estimation is 1.5%, with a peak error of 8% when the SOC is low. Therefore, the model can estimate the battery SOC to an average of 98.5%.

5.1.3 Single Cell Model Validation

This section of the thesis shows the accuracy of representing a single cell's voltage characteristics during a range of steady state discharge procedures. The section will focus on the accuracy of the voltage measurement against the battery's SOC at different discharge rates (C) and will then go on to present an ideal form of representing battery pack voltage characteristics and the limitations in doing so. The simulation layout can be seen in Figure 5-11.

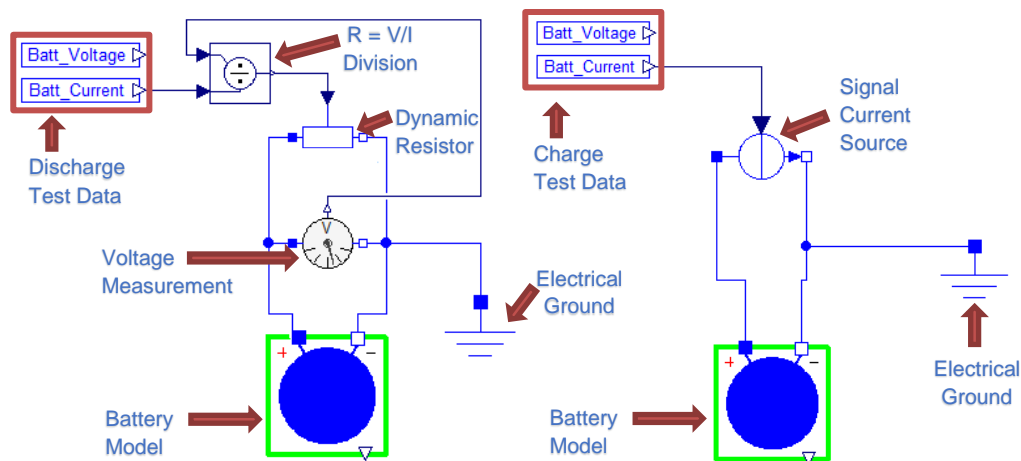


Figure 5-11 - Single Cell Test Simulation Layout

The discharge simulation can be seen on the left of Figure 5-11, where the battery is connected to a dynamic resistor which divides the simulation battery voltage by the test battery current to apply the correct resistance to the battery. This ensures that the battery is discharged by the exact same current in which the cell was tested. The charge simulation can be seen on the right of Figure 5-11, where the test current is fed into the signal current source to ensure that the same current used to charge the cell in the test is used to charge the simulated cell. These two tests have been split into the following sub sections where section 5.1.3.1 covers the battery cell discharge simulations and section 5.1.3.2 covers the battery cell charge simulations. Where each simulation has been simulated for a different period of time, dictated by the duration of the test, the results have been plotted against a normalised x axis, which is the instantaneous time divided by the end time. This allows for a better presentation of the results and where each test has been conducted over the entire SOC range of the cell, the x axis of the graphs can be thought of as either depth of discharge or SOC for the results presented in section 5.1.3.1 and section 5.1.3.2 respectively.

5.1.3.1 Single Cell Steady State Discharge Simulations, Cell ID C08, Capacity 13.1Ah.

Figure 5-12 shows both the test and simulation results for discharging a single battery cell at different discharge rates.

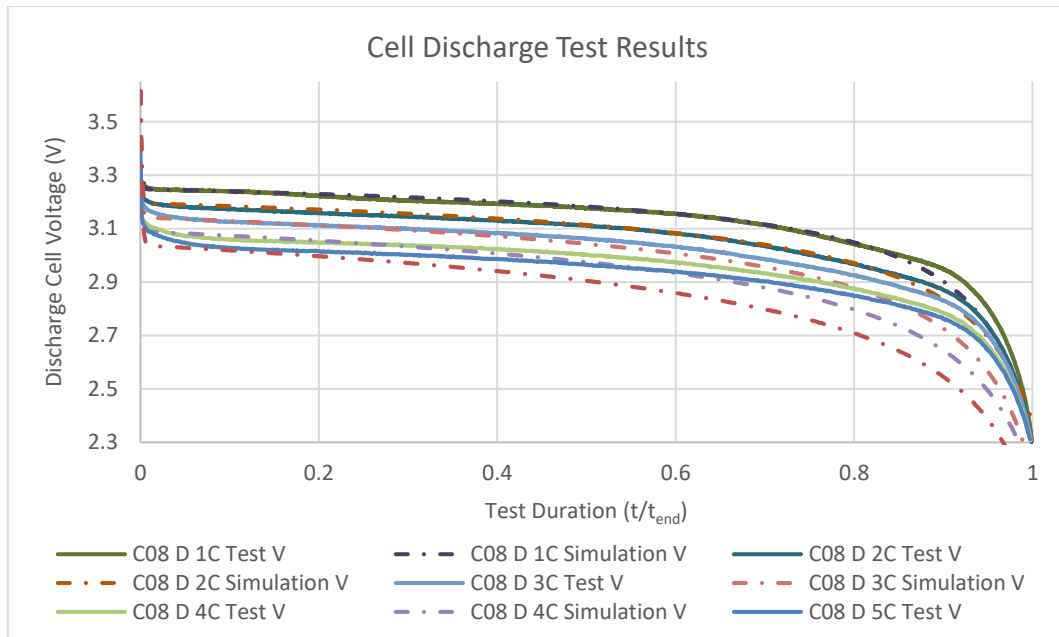


Figure 5-12 - Cell Discharge Voltage Simulation Results

Figure 5-12 shows the results against the test duration so that better presentation of the results can be achieved. The simulation cell voltages have been overlaid, with a dotted line, for direct comparison and the battery model tends to have a more linear decrease in voltage over the range of the battery's SOC. Figure 5-12 shows that when discharging the cell at higher currents as the real cell tends to maintain a slightly flatter curve. Figure 5-13 shows the percentage error between the simulation results and the test data.

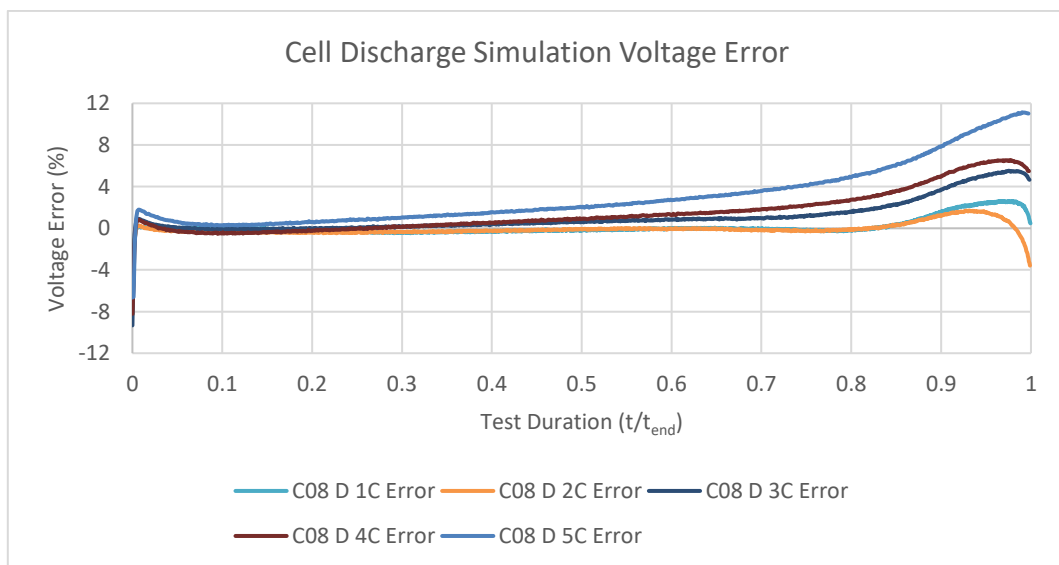


Figure 5-13 - Cell Discharge Voltage Simulation Errors

Figure 5-13 shows the instantaneous error of the cell voltage at each discharge rate for the battery model. The graph shows that the battery model can represent the cell voltage well over the flat region of the battery voltage. However it can be noted, that as the discharge current is increased the error is also increased, thus suggesting that the internal resistance of the battery model is slightly different to that of the physical cell. Figure 5-13 shows that the highest error is approximately 11% towards the end of the simulation. This is where the cell SOC is near zero.

5.1.3.2 Single Cell Steady State Charge Simulations, Cell ID C08, Capacity 13.1Ah.

Figure 5-14 shows the current applied to each cell during the charge testing. The current seen in Figure 5-14 is the same current used to charge the battery model in the cell charging simulations.

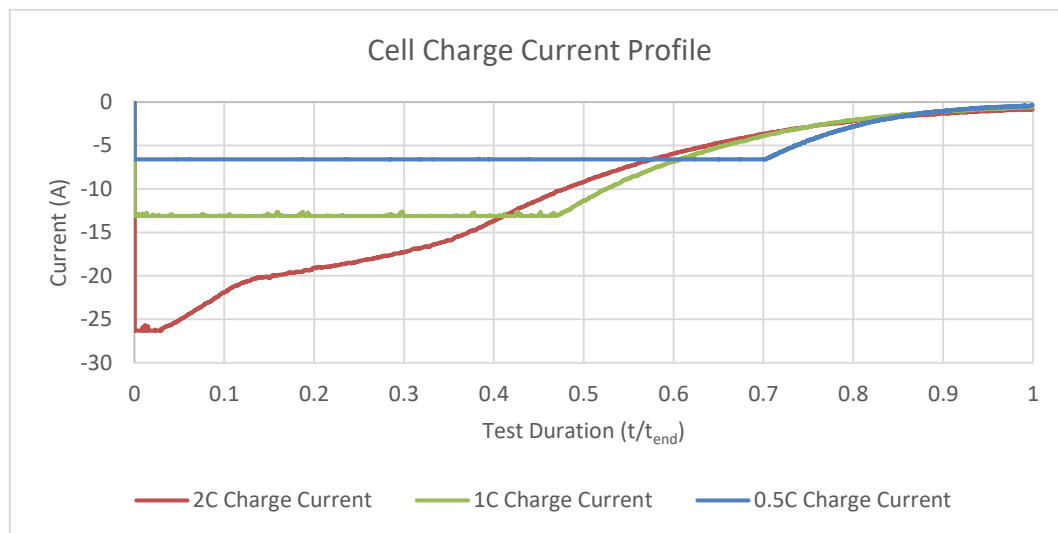


Figure 5-14 - Cell Charge Currents

As stated in section 4.2.2, the battery cannot be continuously charged at a fixed current to the maximum voltage due to both concerns regarding safety and the internal resistance within a cell, which causes the voltage to increase where current is flowing through the battery. Therefore, any charging procedure consists of at least two charging phases, the first CC and the second CV. The CC phase is what is used to denote the C rate in which the battery is being charged. Figure 5-14 shows that when charging at 1C, one times the battery capacity, that the CC phase is just less than half the test duration, 0.5C is three quarters of the test duration and 2C is approximately one twentieth of the test duration. This shows that even when increasing the C rate of charge that there are some limitations to physically charging a cell at higher currents, and that the battery chemistry would need to be developed to reduce the internal charge resistance so that the CC phase can be in operation for longer. Figure 5-15

shows both the test and simulation results for charging a single battery cell at the discussed discharge rates.

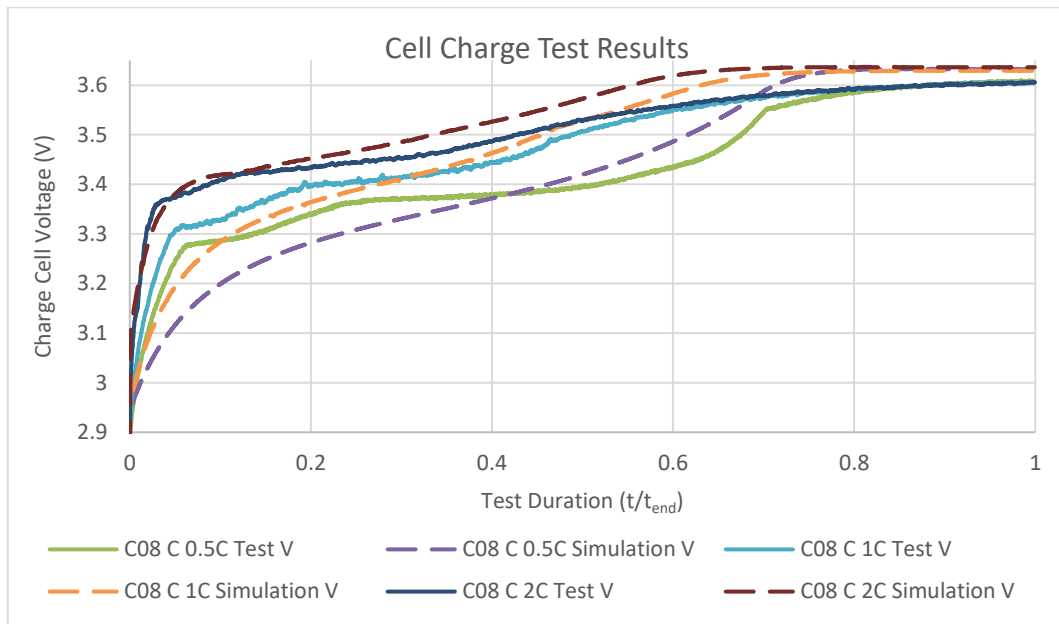


Figure 5-15 - Cell Charge Voltage Simulation Results

Figure 5-15 shows the cell voltage results against the test duration, where the simulation cell voltages have been overlaid, using dotted lines, on top of the test data for a direct comparison. Figure 5-15 shows that when charging the cell at low currents, the real cell tends to have a higher resistance early in the simulation and the battery models has a more linear response over the battery's SOC range. Figure 5-16 shows the percentage error between the simulation results and the test data.

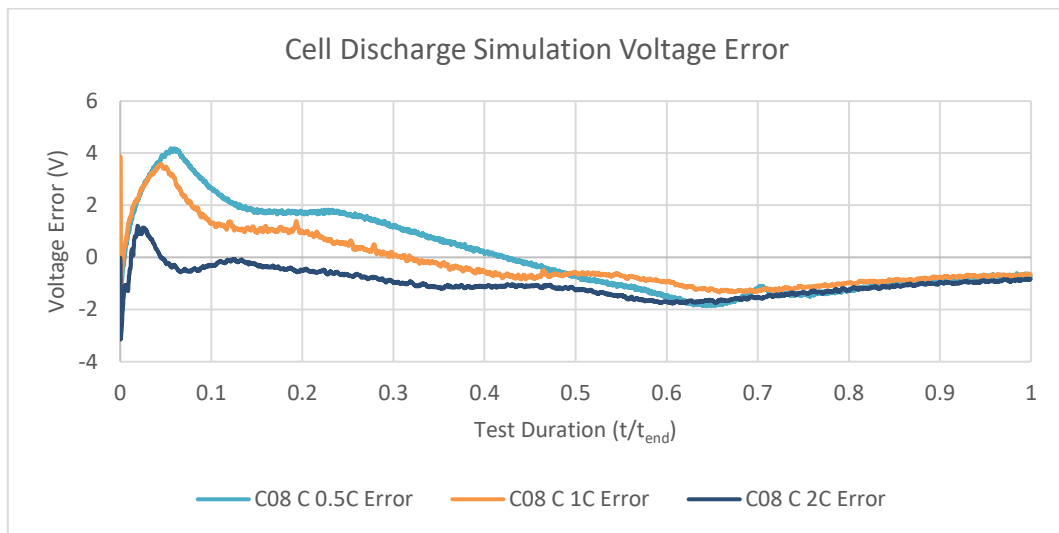


Figure 5-16 - Cell Discharge Voltage Simulation Errors

Figure 5-16 shows the instantaneous error of the cell voltage at each charge rate for the battery model. The graph shows that the battery model can represent the cell voltage better when the charge current is higher, thus, as the charge current is

increased the error is decreased. Figure 5-16 shows that the highest error is approximately 4% at the beginning of the 0.5C simulation and that the battery model can represent the battery voltage better at higher SOC, towards the end of each test.

5.1.3.3 *Single Cell Simulations Summary, Cell ID B08, Capacity 13.1Ah.*

From the percentage error results which have been presented, the RMS average error for each simulation can be used to determine a level of confidence in the model. Figure 5-17 shows the RMS error for each simulation and the RMS average error over all the battery cell simulations.

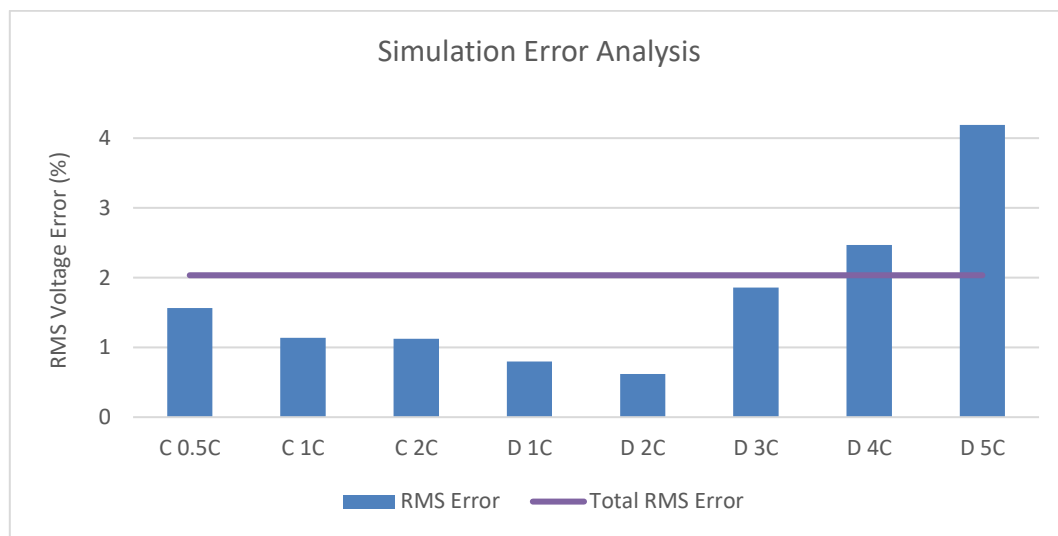


Figure 5-17 - Single Cell Validation Error Analysis

Figure 5-17 shows that the average RMS error across all the simulations is approximately 2%, the highest correlation achieved by the battery model is 0.6% and the worst is 4.2% during the high current discharge simulations. Therefore, by using the RMS average of all the simulations, the battery model can be averaged to a value of 98% accurate when validating the voltage characteristics for different charge and discharge rates.

5.1.4 Fuel Cell Model Validation

This section of the thesis, shows the accuracy of representing the 70 cell Ballard 1080AC fuel cell voltage characteristics during a range of steady state discharge procedures. The section will focus on the accuracy of the voltage measurement and the hydrogen consumption against the different tested power outputs of the fuel cell. The simulation layout can be seen in Figure 5-18.

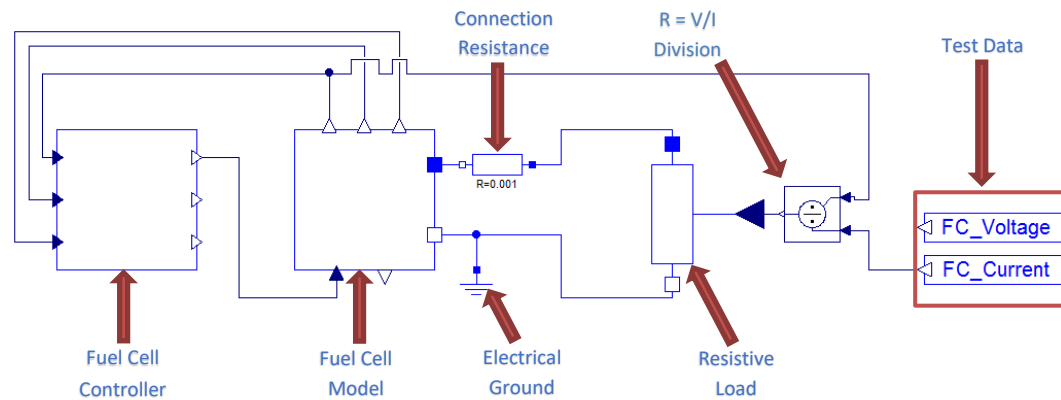


Figure 5-18 - Fuel Cell Voltage Validation, Simulation Layout

Figure 5-18 shows that the fuel cell model is connected to a variable resistor which divides the simulation fuel cell voltage by the test fuel cell current to apply the correct resistance to the fuel cell model. This ensures that the fuel cell model has the exact same load applied during the simulation to which was applied during the tests. The current drawn from the fuel cell and the fuel cell voltage at each power increment can be seen in section 4.3.2, Figure 4-23 and Figure 4-22. Due to the quantity of tests which have been conducted, only the fuel cell simulation results have been presented in this section. Figure 5-19 shows the model voltage of the fuel cell when producing the same current as each test conducted in section 4.3.2.

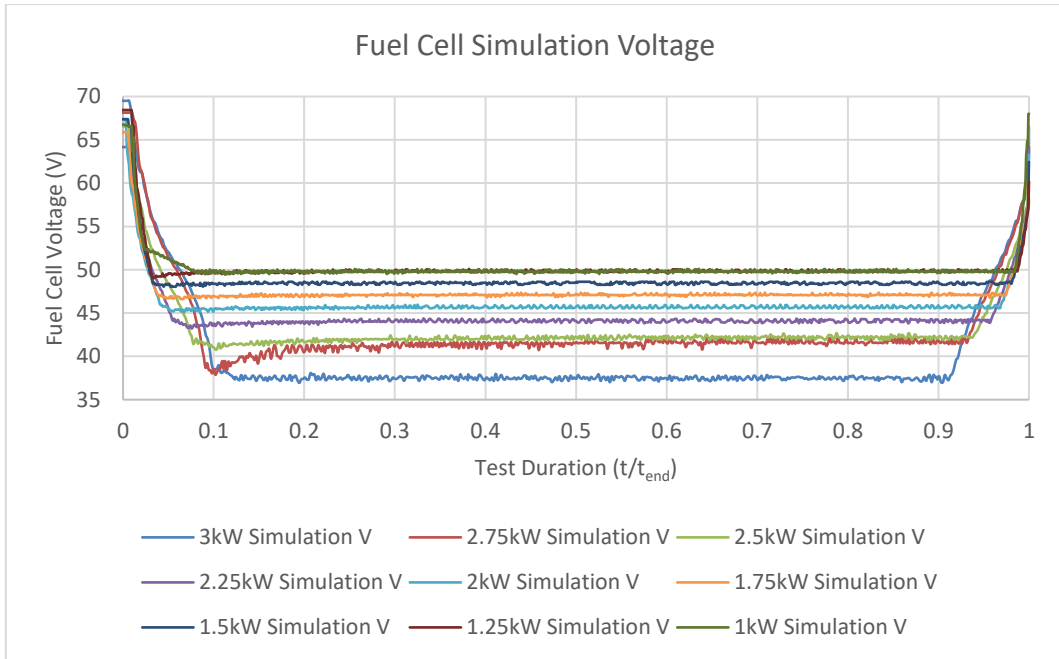


Figure 5-19 - Fuel Cell Voltage Simulation Results at Each Power Output

Figure 5-19 shows the model voltage of the fuel cell when producing the same current as each test. Using the test fuel cell voltage and the simulation fuel cell voltage, the average RMS percentage error has been calculated and is presented in Figure 5-20.

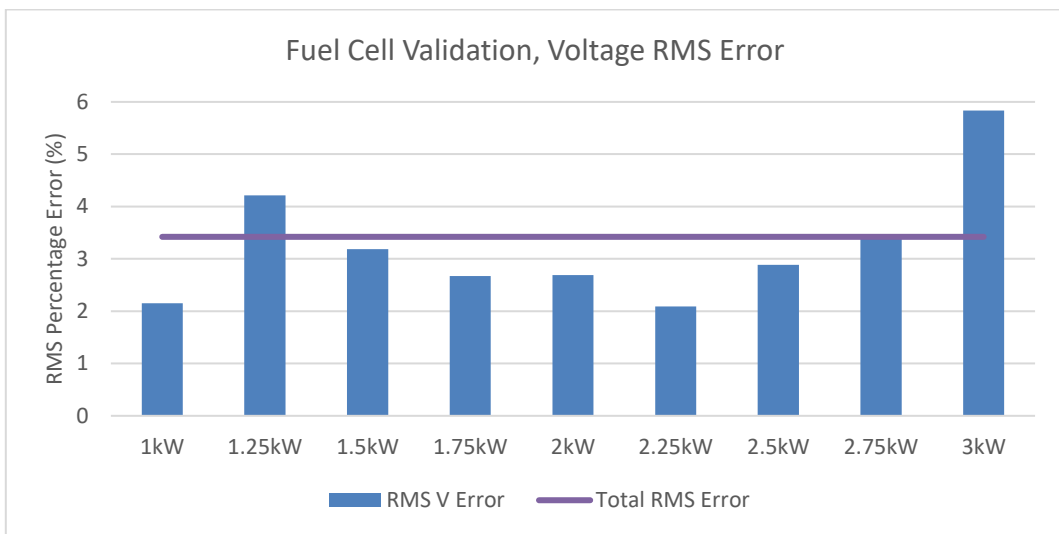


Figure 5-20 - Fuel Cell Validation, RMS Voltage Error

Figure 5-20 shows the RMS Error of the simulated fuel cell voltage against the tested results. The figure shows that the model can track the voltage of the 70 cell Ballard fuel cell to between 2% and 6% for the tested scenarios with an average RMS error of 3.4% across all the scenarios. Thus, giving an average model accuracy of 96.6% for steady state fuel cell simulations. To validate the hydrogen consumption part of the fuel cell model, an additional simulation setup has been created and is shown in Figure 5-21.

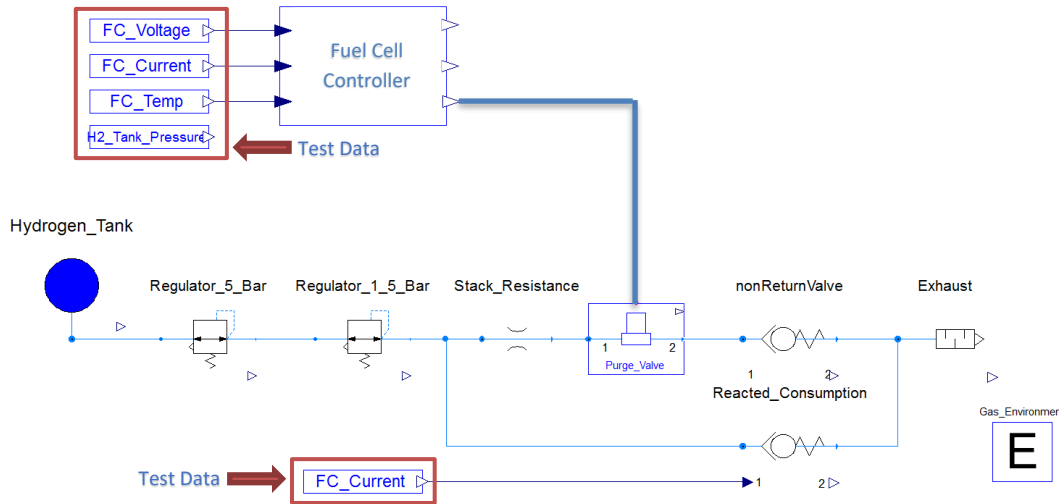


Figure 5-21 - Fuel Cell Hydrogen Consumption Validation, Simulation Layout

Figure 5-21 shows that the test voltage, current and temperature of the fuel cell are fed into the fuel cell controller model, which determines the timing of the purge valve operation, whilst the reacted consumption model determines the quantity of hydrogen used based on the same test current, which influences the purge duration. Figure 5-22 shows the hydrogen tank pressure over the first five tests.

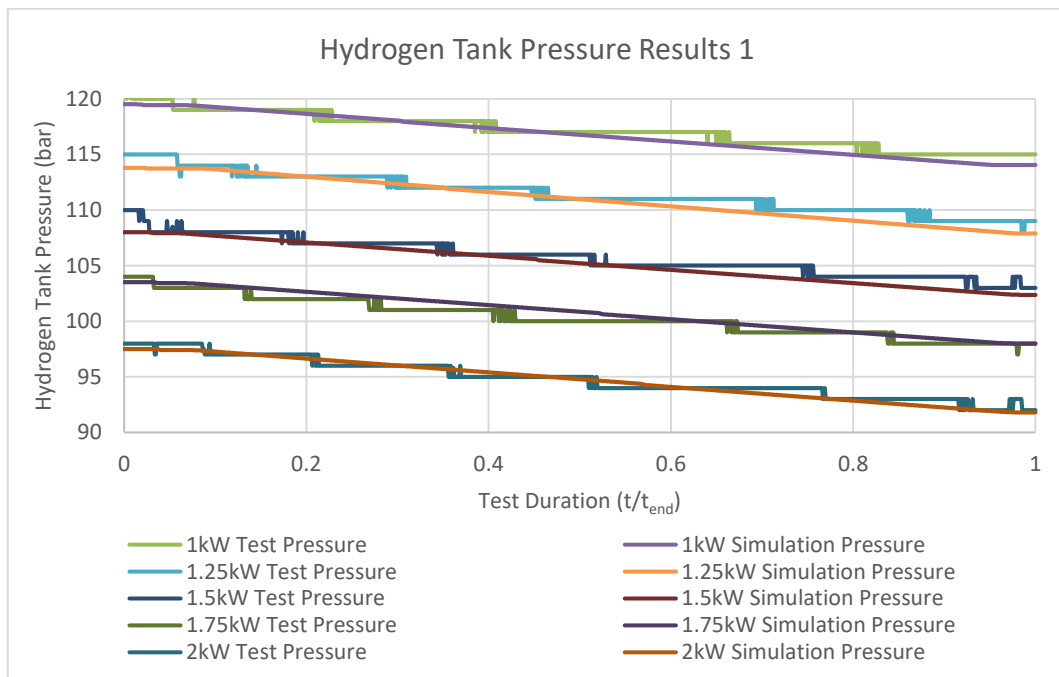


Figure 5-22 - Hydrogen Tank Pressure Results 1

Figure 5-23 shows the hydrogen tank pressure for the remaining tests.

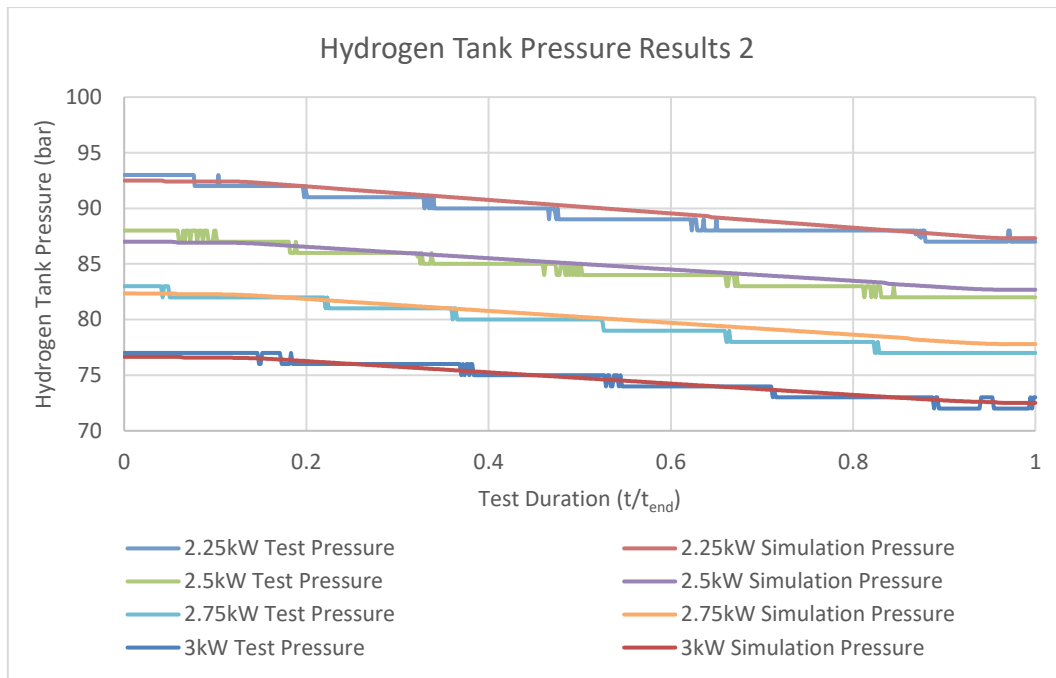


Figure 5-23 - Hydrogen Tank Pressure Results 2

Figure 5-22 and Figure 5-23 show a direct comparison of the test data against the simulation results, showing the hydrogen pressure within the tank over the course of each scenario. The two figures show close correlation between the logged data and the gas consumption model. Figure 5-24 presents the RMS percentage error between the simulated hydrogen pressure and the test data.

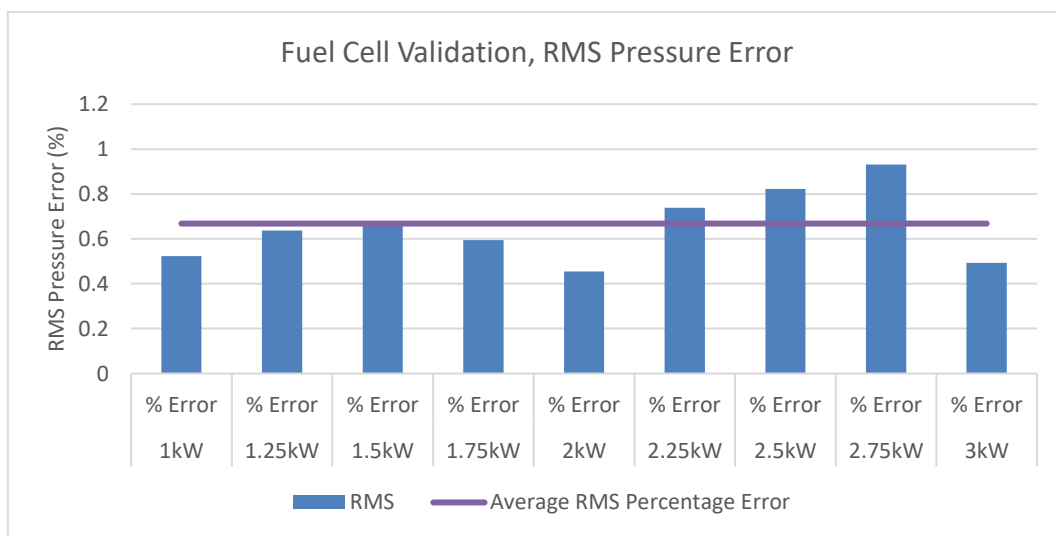


Figure 5-24 - Fuel Cell Validation, Hydrogen Consumption Error

Figure 5-24 shows that the gas consumption model can represent the hydrogen consumption of the fuel cell to an average of 0.7% across all of the scenarios and therefore, is approximately 99% accurate at representing the test data.

5.1.5 DCDC System Model Validation

This section of the thesis describes the validation of the system as a whole, via the DCDC, where the difference between the fuel cell power and the battery power will be compared to that of the simulation. Therefore, the presented data in this section will use both equation (228) and (229) to show the error within the DCDC Model.

$$P_{DCDCLoss} = P_{FuelCell} - P_{Battery} \quad (228)$$

$$\varepsilon_{Model} = P_{TestDCDCLoss} - P_{ModelDCDCLoss} \quad (229)$$

Where:

- $P_{DCDCLoss}$ = The amount of power that is lost by the DCDC when converting the voltage and current
- $P_{FuelCell}$ = The power that the fuel cell produces, a product of voltage and current
- $P_{Battery}$ = The power at the battery, a product of voltage and current
- ε_{Model} = The error between the test and simulation
- $P_{TestDCDCLoss}$ = The amount of power that is lost by the DCDC during the test
- $P_{ModelDCDCLoss}$ = The amount of power that is lost by the DCDC during the simulation

Figure 5-25 shows the simulation setup which is used in this section of the simulation results.

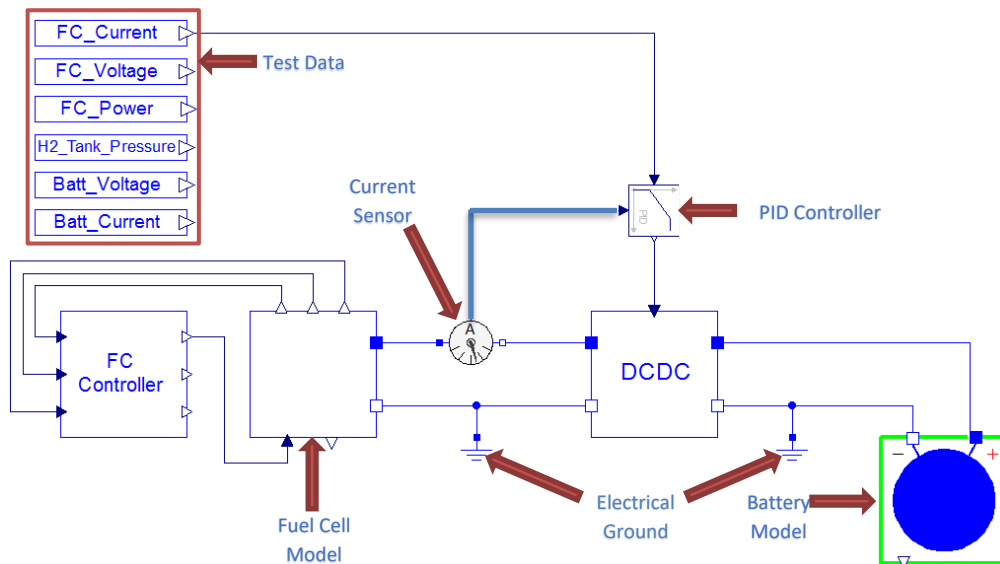


Figure 5-25 - Fuel Cell System Validation, Simulation Layout

Figure 5-25 shows how the fuel cell current from the test data is the driving factor for these simulations. The fuel cell current is fed to the PID controller as its setpoint and the current sensor that measures the fuel cell model's current is the PID controller's reference. This PID controller determines the operation of the DCDC and adjusts the DCDC model's 'D' value, discussed in section 3.14, to manipulate the rate at which it charges the battery. Figure 5-26 shows the typical power loss for two simulations.

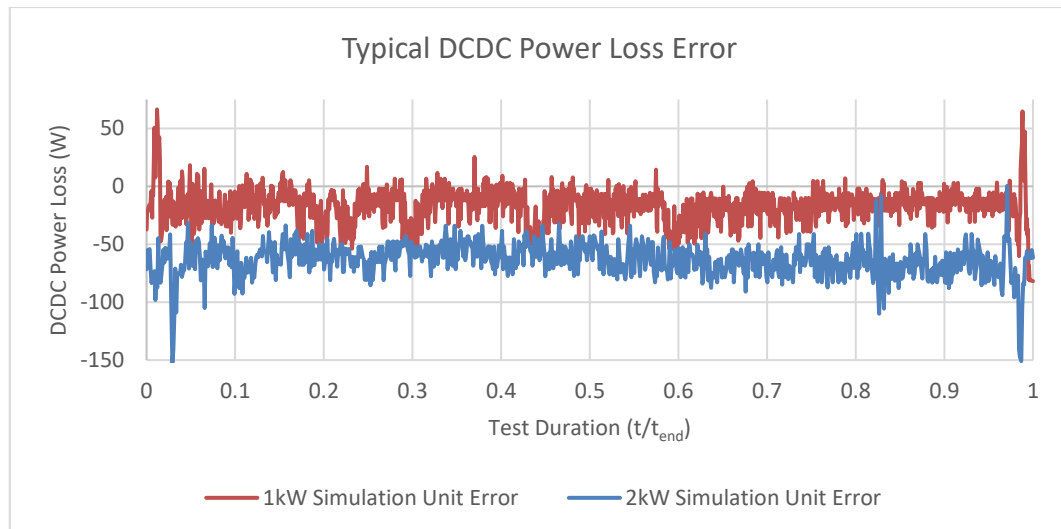


Figure 5-26 - DCDC Power Loss Error Results

Figure 5-26 shows the typical error of the DCDC model for two of the test scenarios. Only two have been presented as the similarity in results across all the simulations make the graph difficult to read. The results fluctuate frequently due to the PID controller’s fast response to changing the ‘D’ value of the DCDC model. Figure 5-26 shows that the DCDC model tends to produce a less efficient DCDC conversion than the real system, where the value is consistently negative. Figure 5-26 shows peak errors of up to 150 W for brief scenarios. However, where this is at the start and the end of the simulation it is likely to be the small delay within the PID controller acting on the DCDC to track the current of the fuel cell test data. Figure 5-27 shows the RMS average error of the DCDC model against the test data.

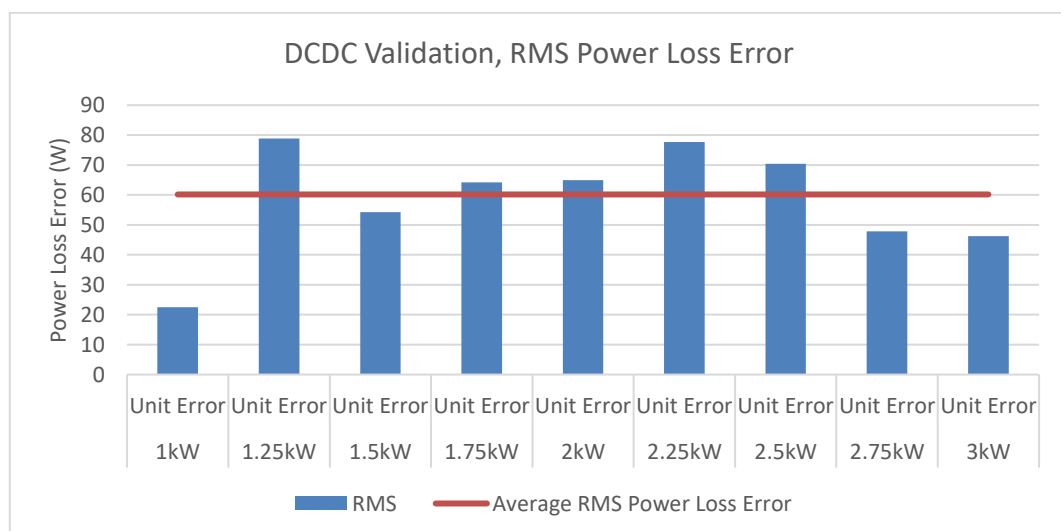


Figure 5-27 - DCDC Validation, RMS Power Error

Figure 5-27 shows that over all of the scenarios the model has an average RMS error of 60 W, where this is typically 60 W less than the test data. Using these results, the efficiency of the DCDC during each test has been presented in Figure 5-28, using the

RMS of energy produced by the fuel cell divided by the RMS of the energy absorbed by the battery.

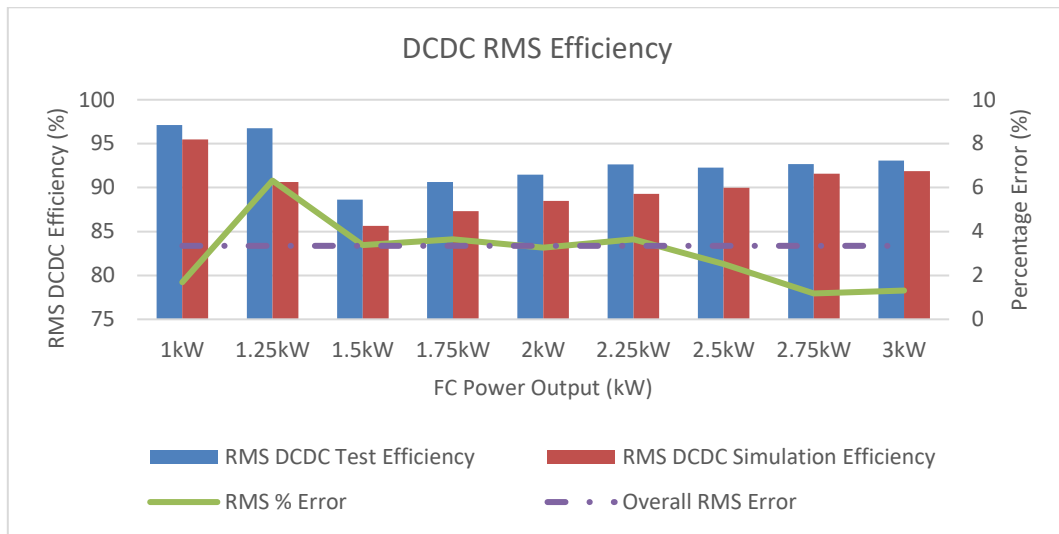


Figure 5-28 - DCDC Efficiency Validation

Figure 5-28 shows the DCDC RMS efficiency of each test and simulation, it shows that over all the tests, the model has an average error of 3.4% and with a peak error of 6% on the 1.25 kW simulation. Figure 5-28 suggests that when using this DCDC model a pessimistic value of charge transferred to the battery would be estimated, where the model would show that the DCDC model would waste more energy than it would. However, in terms of a percentage error this is relatively low.

5.1.6 Motor Model Validation

The test results of the motor were provided by the motor manufacturer, Lynch Motor Co. The manufacturer applied 72.2 V to the motor whilst sequentially applying 10 different torques to the output shaft and taking measurements. Table 5-1 shows the results of the measurements taken during the tests provided by Lynch Motor Co alongside the results of the simulated motor model.

Table 5-1 - Lynch Data Vs Simulation Results

Test #	Voltage Motor [V]		Current [A]		Power In [kW]		Speed [RPM]		Torque [Nm]		Power Out [kW]		Efficiency [%]	
	Test	Simulation	Test	Simulation	Test	Simulation	Test	Simulation	Test	Simulation	Test	Simulation	Test	Simulation
1	72.2	72.3	16.0	15.5	1.2	1.1	3923	3925	2	2	0.8	0.8	69.3	71.5
2	71.3	71.2	57.3	57.1	4.1	4.1	3804	3811	9.1	9.1	3.5	3.5	86.3	87.0
3	70.5	70.4	80.0	80.6	5.6	5.7	3732	3741	13.1	13.1	5.0	5.0	88.4	88.1
4	69.3	69.3	108.7	109.9	7.5	7.6	3637	3645	18.1	18.1	6.7	6.7	89.1	88.4
5	68	67.9	138.0	139.8	9.4	9.5	3536	3537	23.2	23.2	8.4	8.4	89.1	88.2
6	67.1	67.0	156.0	157.4	10.5	10.5	3469	3468	26.2	26.2	9.3	9.3	88.5	87.9
7	66.4	66.1	169.0	171.5	11.2	11.3	3414	3409	28.6	28.6	10.0	9.9	88.7	87.7
8	65.5	65.3	181.0	184.3	11.9	12.0	3357	3351	30.8	30.8	10.5	10.5	88.9	87.4
9	64.2	64.0	199.7	203.1	12.8	13.0	3271	3261	34	34	11.3	11.3	88.5	87.1
10	63.1	63.3	209.0	211.9	13.2	13.4	3220	3216	35.5	35.5	11.7	11.6	88.4	86.9

Figure 5-29 shows the simulation layout which has been used to validate the motor model to the test data provided by Lynch Motor Co.

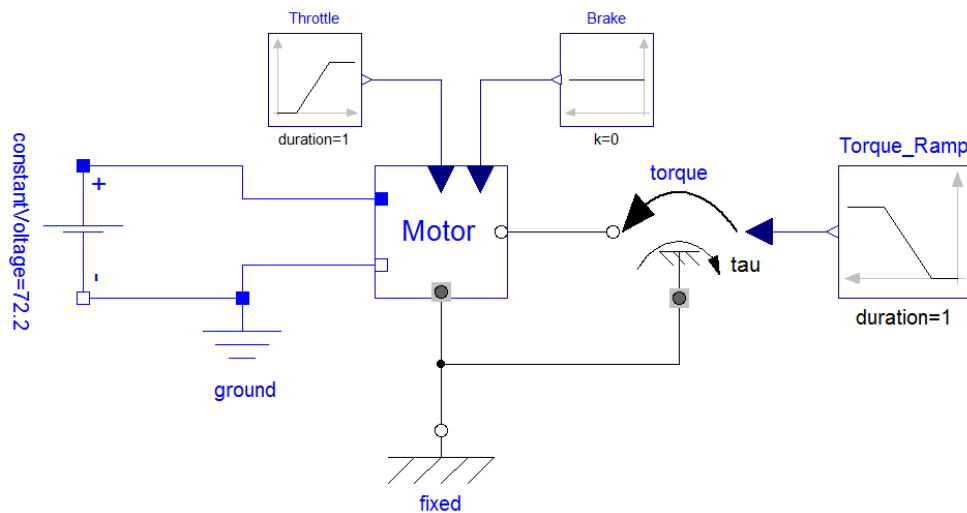


Figure 5-29 - Motor Model Validation, Simulation Layout

As shown in Figure 5-29, the simulation consists of the motor model being supplied with 100% throttle with 0Nm of opposing torque for the first 5s, allowing the motor to reach maximum angular velocity, then the torque is applied, and the measurements

are taken once the motor angular velocity settles to a steady state. Figure 5-30 shows the efficiency of the motor in relation to the input electrical power and output mechanical power.

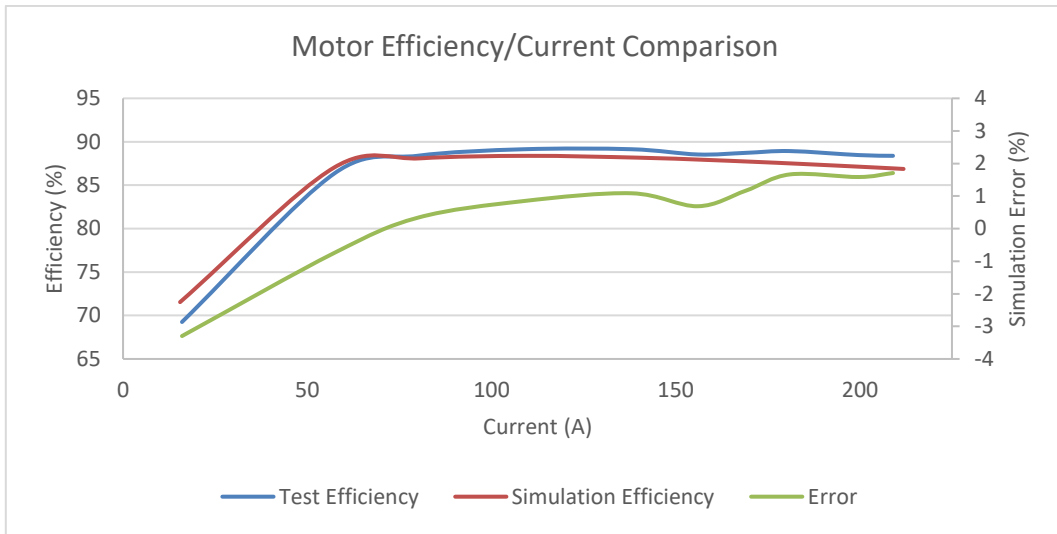


Figure 5-30 – Motor Validation, Efficiency Error

Figure 5-30 shows the motor model can represent the losses of the motor with a maximum error of $\pm 4\%$. This occurs when the current is low, at 16 A and the motor is at the maximum RPM of the motor. Figure 5-31 shows the back-EMF of the motor on the X-axis and the motor speed on the Y-axis.

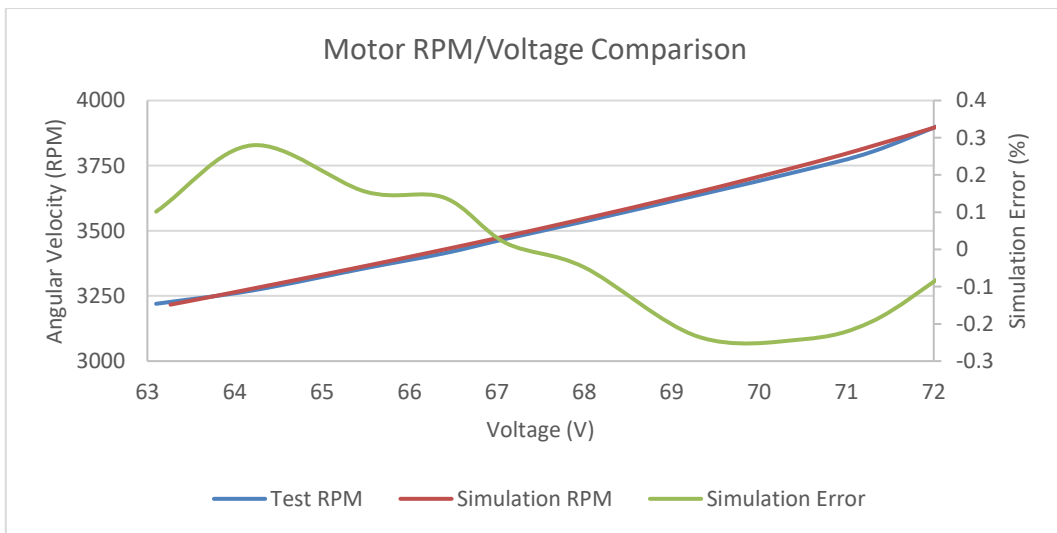


Figure 5-31 – Motor Validation, Speed & Back Voltage Error

Figure 5-31 shows that the back-EMF voltage of the motor can be represented well over the provided RPM range to an average of $\pm 0.25\%$. The relationship between the back-EMF and the current is shown in Figure 5-32.

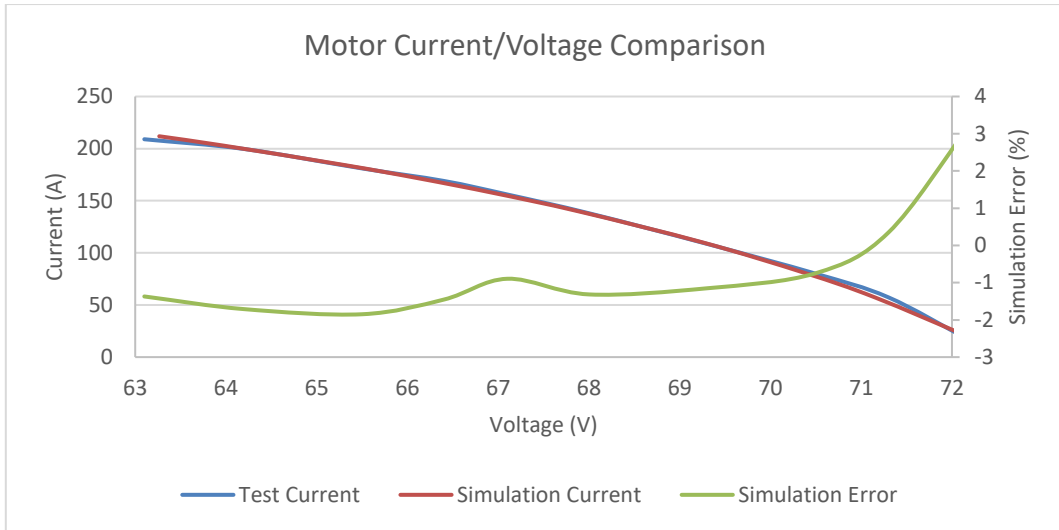


Figure 5-32 – Motor Validation, Current Error

Figure 5-32 shows a peak simulation error of 3.5%, at the maximum motor RPM where the back-EMF is its greatest. However, the model can represent the current versus back-EMF to average error of approximately 2% for most of the simulation. The mechanical output power of the test and simulation is presented in Figure 5-33.

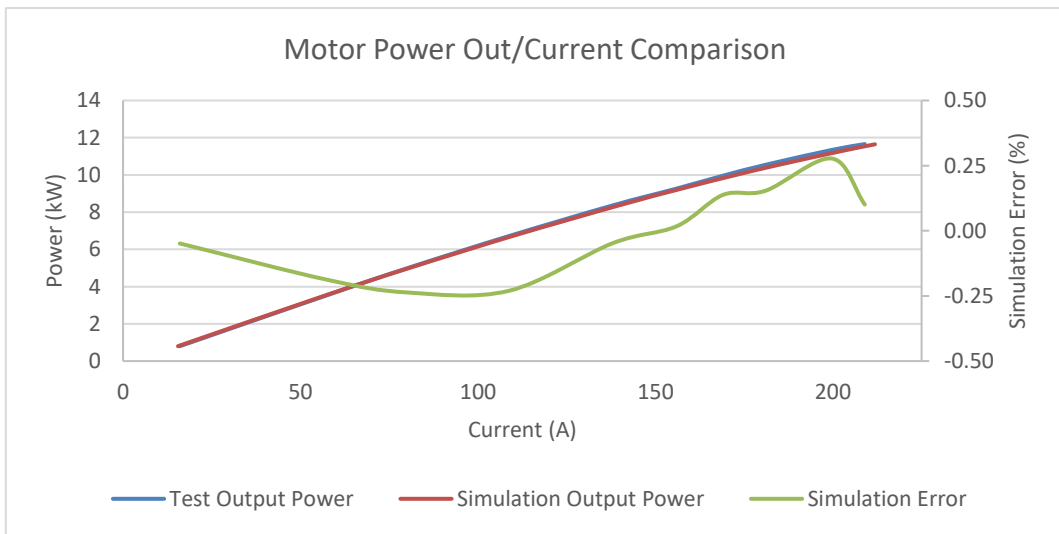


Figure 5-33 - Motor Validation, Output Power Error

The output power of the motor can be represented to an average error of approximately $\pm 0.2\%$ across the tested range as shown in Figure 5-33. It's important to note that, due to the way that Lynch Motor Co has conducted the test, the results are technically from 3800 RPM to 3225 RPM as well as 16 A to 210 A. Thus, this curve also shows how the power is reduced due to both back-EMF and losses within the motor. Figure 5-34 shows the torque versus current at the motor for both the simulation and test results.

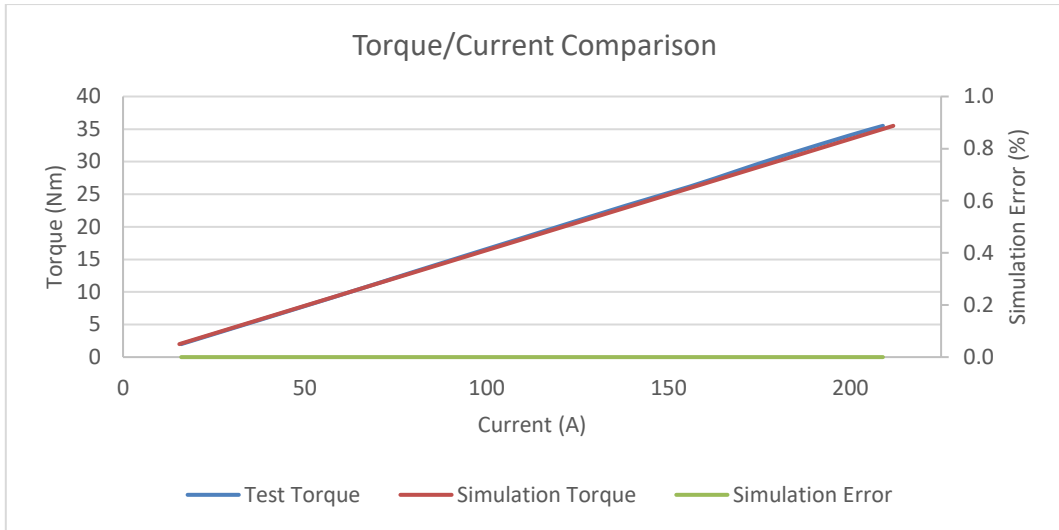


Figure 5-34 - Motor Validation, Torque Error

It can be seen from Figure 5-34 above, that the torque in the simulation is equal to that of the torque in the test. This is because the test torque is the actuator in the simulation as explained at the start of this section. Figure 5-35 shows the RMS percentage error between the model and the test data.

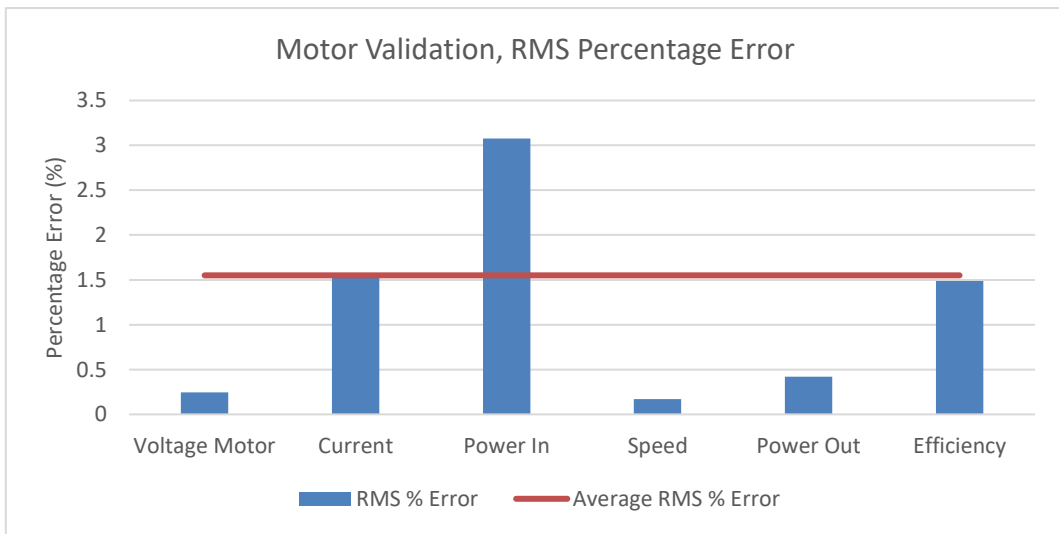


Figure 5-35 - Motor Validation, RMS Percentage Errors

Figure 5-35 shows that over all the scenarios the model has an average error of 1.55% and shows a peak RMS error of $\pm 3\%$ for the given scenarios. The peak error is in relation to the input electrical power to the motor, and the simulation showed that at the maximum torque, test 10 in Table 5-1, the motor model required 200 W more than the test data.

5.2 NEDC Vehicle Validation

5.2.1 NEDC Electric Vehicle Simulation

To create comparable results between the test data and the simulation, the driver model has been changed to a closed loop driver which replaces the ground vehicle speed lookup function, within the planner model, to a time-based lookup table. The second area of comparison is the calculation of vehicle energy consumption. The energy consumption calculation has been formulated via the power of the battery and speed of the vehicle at each time interval. Therefore, equations (230) to (234) define the method of calculating a comparable energy consumption figure in Wh/km .

$$P_{battery} = (i_{battery} * v_{battery})/1000 \quad (230)$$

Where:

$P_{battery}$ = The instantaneous power at the battery in kilowatts

$i_{battery}$ = The instantaneous battery current in Amperes

$v_{battery}$ = The instantaneous battery voltage in Volts

Here the power at the battery during the simulation is calculated

$$Q_{battery} = \int_{t-1}^t P_{battery} \quad (231)$$

Where:

$Q_{battery}$ = The energy used from the battery in kilojoules or kilowatts

t = Time in seconds

Here the integral of the battery power has been used to calculate the energy provided by the battery pack.

$$Q_{usedbattery} = \frac{Q_{battery}}{3.6} \quad (232)$$

Where:

$Q_{usedbattery}$ = The energy used from the battery in kilowatt hours

Here the energy provided by the battery pack has been converted from kW to kWh to follow the conventional units which have been used throughout this thesis.

$$S_{travelled} = \frac{\int_{t-1}^t V_{vehicle}}{1000} \quad (233)$$

Where:

$S_{travelled}$ = The distance travelled over the simulation in kilometers

$V_{vehicle}$ = The speed of the vehicle in meters per seconds

Here the distance travelled is calculated in km from the integral of vehicle speed.

$$Q_{consumption} = \frac{Q_{usedbattery}}{S_{travelled}} \quad (234)$$

Where:

$Q_{consumption}$ = The amount of energy per kilometer provided by the battery in kilowatt hours per kilometer

Finally, the energy consumption of the vehicle can be calculated in kWh/km , using the energy provided by the battery divided by the distance travelled.

Figure 5-36 shows the simulation layout of the NEDC tests.

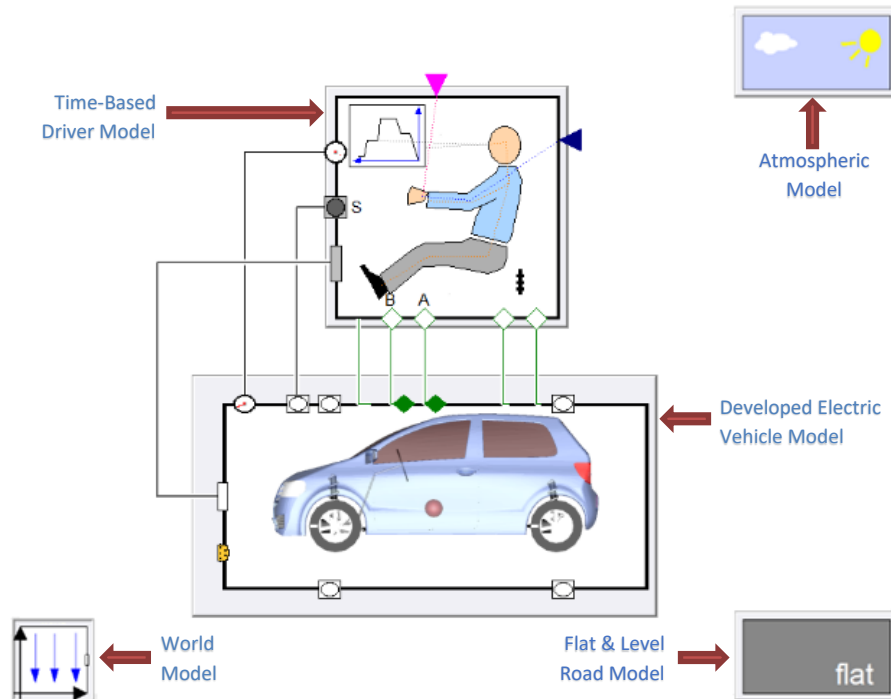


Figure 5-36 - NEDC Simulation Layout

As shown in Figure 5-36, this simulation is conducted with the flat and level road to represent the same conditions as that of a chassis dynamometer. The driver model has the same time versus velocity data from the test in section 4.4.1, so that the driver will control the vehicle to the same conditions as the test. As the test was conducted with the Coventry University Microcab H2EV operating in electric vehicle mode only, the fuel cell model has been removed for this validation procedure. Figure 5-37 shows the speed of the vehicle during the laboratory test and the speed of the vehicle during the simulation.

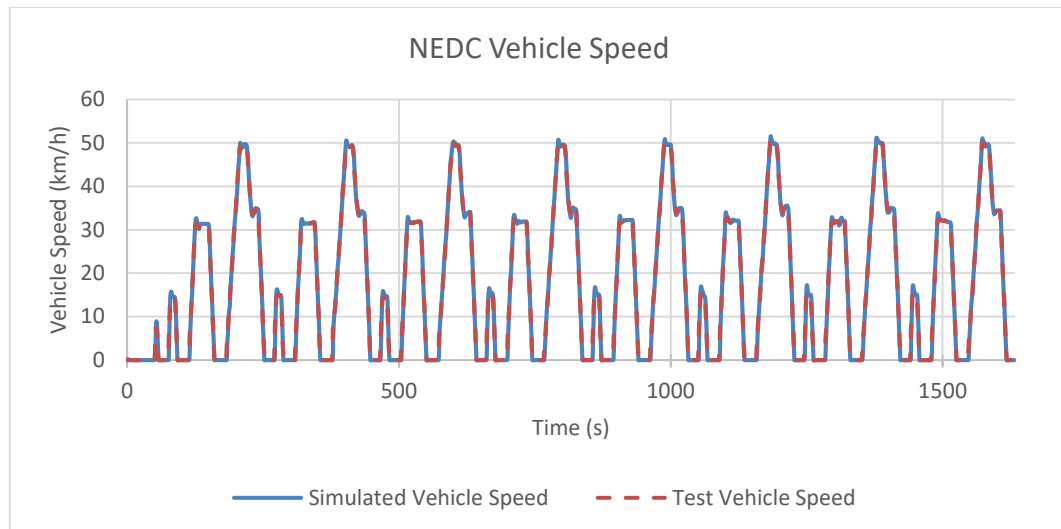


Figure 5-37 - NEDC Vehicle Speed Validation

Figure 5-37 shows that the driver can closely match the speed which is requested by the drive cycle. However, there is a slight over and undershoot when high accelerations stop or start. This shows that the driver model can closely represent a typical driver’s responses to speed change requests. Figure 5-38 shows the energy consumption of both the simulation and the test data.

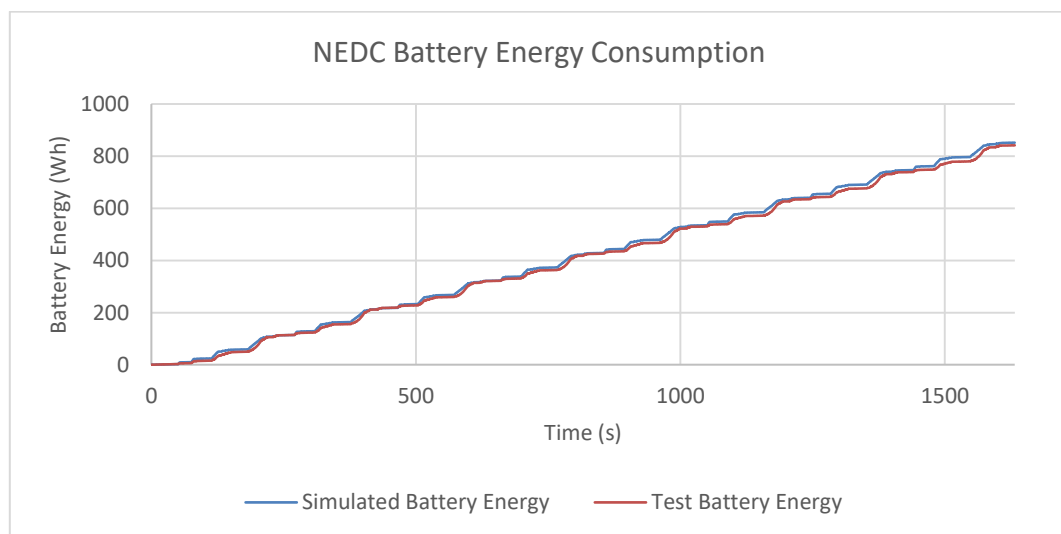


Figure 5-38 - NEDC Energy Consumption Validation

From the test data in section 4.4.1 we know that the whole tested urban NEDC requires 841.9 Wh from the battery. Figure 5-38 shows that the model predicts that the battery would have to supply 852 Wh of energy to the vehicle to complete the same test procedure and it can also be seen that the simulation results follow the energy consumption test results closely. Using these two results the percentage difference is calculated as 1.2% and this shows that the model can represent dynamometer laboratory tests to an error of 1.2%. When analysing the data from Figure 5-38 we can

estimate the range the vehicle would be able to drive, based on the battery capacity. The tested vehicle has a nominal battery capacity of 4 kWh. From using equations (235) and (236) it can be calculated that the battery would be able to power the vehicle for 37.554 km, based on the NEDC.

$$Q_{consumptionNEDC} = \frac{Q_{NEDC}}{S_{NEDC}} \quad (235)$$

$$106.513 \left[\frac{Wh}{km} \right] = \frac{851.89 [Wh]}{7.998 [km]}$$

Where:

$Q_{consumptionNEDC}$ = The amount of energy per kilometer provided by the battery in kilowatt hours per kilometer
 Q_{NEDC} = The energy used from the battery over the NEDC simulation in kilowatt hours
 S_{NEDC} = The distance travelled over the NEDC simulation in kilometers

Here the energy consumption of the vehicle has been calculated as 106.513 Wh/km.

$$S_{rangeNEDC} = \frac{Q_{batterynominal}}{Q_{consumptionNEDC}} \quad (236)$$

$$37.554 [km] = \frac{4000 [Wh]}{106.513 [Wh]}$$

Where:

$S_{rangeNEDC}$ = The estimated range of the vehicle based on the battery capacity and NEDC test result in km
 $Q_{batterynominal}$ = The nominal battery capacity in Wh

Here the total distance which the vehicle should be able to drive has been calculated.

The terminology 'should' has been used where the NEDC is the type approval process for the vehicles and therefore, should be capable of providing an accurate value for the energy consumption of a vehicle. Therefore, we could use this data to calculate the power that would be required from a fuel cell so that battery SOC is maintained and seamless driving can be conducted until the hydrogen tank is depleted. This is calculated by using equations (237) and (238).

$$Q_{FC} = \frac{Q_{consumptionNEDC}}{\left(\frac{t_{NEDC}}{3600} \right)}, \quad (237)$$

$$1879.2 [Wh] = \frac{851.89 [Wh]}{\frac{1632 [s]}{3600 [s]}}$$

Where:

Q_{FC} = The estimated energy requirement for continuous driving in Wh
 t_{NEDC} = The time taken to complete the NEDC test in s

Here the requirement of electrical energy to provide continuous driving is calculated as 1879.2 Wh. Equation (238) can be used to determine the requirement from the fuel cell if a simplified efficiency is incorporated into charging the battery.

$$P_{FC} = Q_{FC} + (2 - \varepsilon_{DCDC}) \quad (238)$$

$$1935.5 [Wh] = 1879.2 + (2 - 0.97)$$

Where:

P_{FC} = The estimated continuous power requirement from the fuel cell in W
 ε_{DCDC} = The efficiency of the DCDC at the given power.

CHAPTER 5 – Simulation Results, Correlation and Validation

Here the DCDC efficiency has been incorporated into the estimation of required the power from the fuel cell. This has been calculated as $1935.5 Wh$, where a fuel cell will provide continuous power until the hydrogen tank is depleted a hydrogen consumption model would be required to determine the time which the vehicle could drive for based on the size of the hydrogen tank to determine the range.

5.2.2 NEDC Fuel Cell Electric Vehicle Simulation

Using the results in section 5.2.1 and equation (237) and (238) the vehicle can be simulated with the fuel cell power output set to 1935.5 W as an estimate to determine seamless driving with the fuel cell operational. Figure 5-39 shows the battery energy consumption from the test, the energy provided by the fuel cell over the simulation and the equivalent energy used from the battery. The same simulation setup shown in Figure 5-36 has been used, however, the fuel cell system included into the vehicle model, thus, the following results are the first of the fuel cell vehicle model which has been created and discussed throughout this thesis.

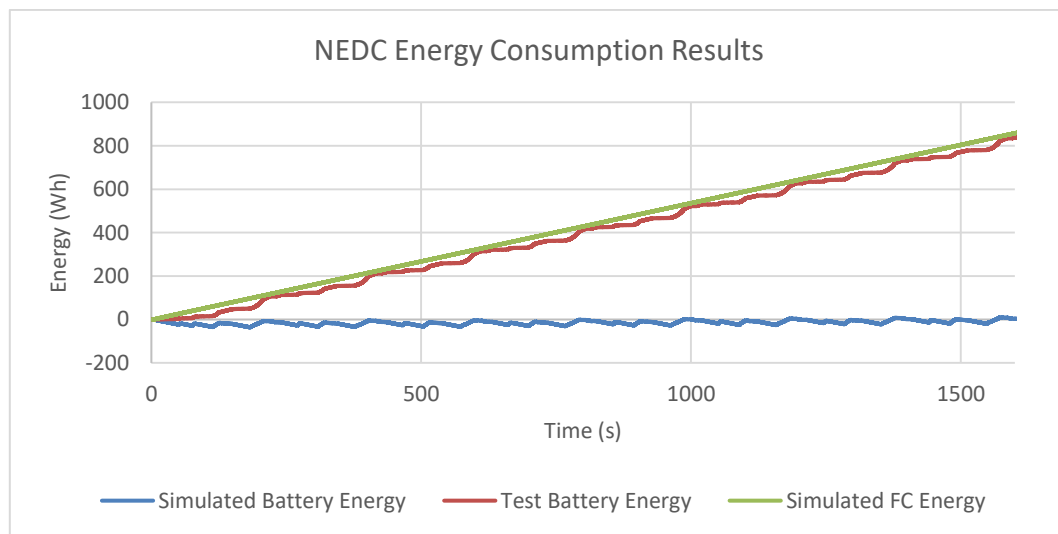


Figure 5-39 - NEDC Fuel Cell Energy Consumption Estimation

Figure 5-39 show the energy consumption of the battery, in blue, and the energy provided by the fuel cell, in green. When the fuel cell is delivering 1935.5 W then most of the energy which was previously being provided by the battery is now being provided by the fuel cell. This suggests that equations (237) and (238) are correct for estimating this value of continuous driving over the NEDC. However, as stated in section 2.6, the NEDC is a highly-stylised drive cycle and does not realistically represent real world driving conditions and a common misconception is to take these values as a rule of thumb. In section 4.4.2 it was established that there is a 36% difference in energy consumption between the NEDC and the CUDC. Therefore, it can be assumed that the actual fuel cell power requirement would be larger for real world driving conditions.

5.3 CUDC Vehicle Validation

Within this section of the thesis the difference between straight line modelling and 3D modelling is explained, where one simulation will be done in accordance with the NEDC type of simulation and the other using the full Dymola road generator tool so that the 3D road is created. This takes more dynamic forces into account including road altitude, cornering dynamics, chassis suspension dynamics and tyre force dynamics, all of which consume energy when the vehicle is moving. It shows the inaccuracies in predicting battery consumption using current type approval methods.

5.3.1 CUDC Straight Line Electric Vehicle Simulation

The same simulation setup shown in Figure 5-36 has been used for the straight-line simulation of the CUDC. Figure 5-40 shows the battery energy consumed during the CUDC test against the distance travelled during the test. The figure presents the test data against that of the simulation results and presents a clear distinction of the error, by using the unit difference throughout the simulation of a straight line and flat drive cycle.

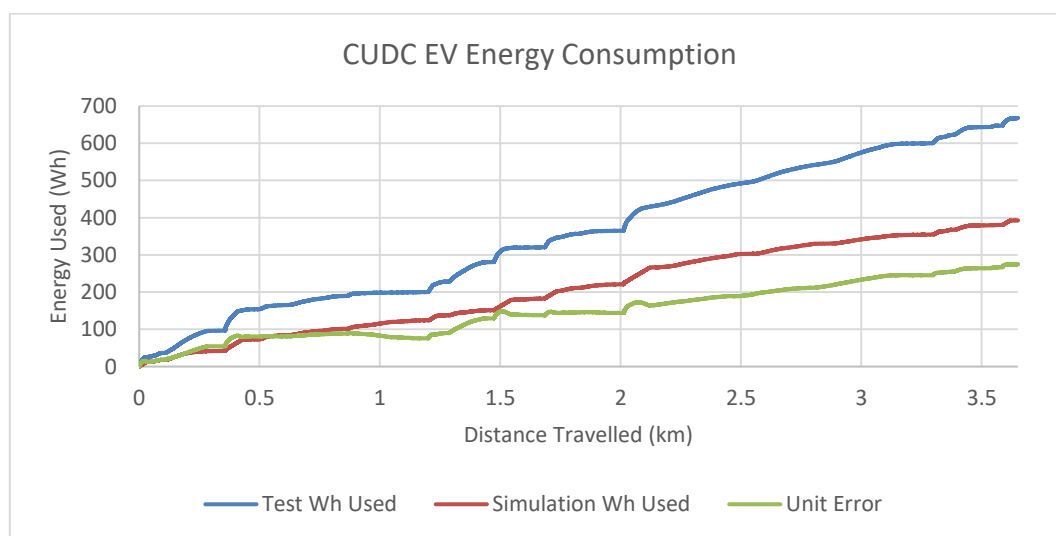


Figure 5-40 – Flat & Straight CUDC EV Simulation, Battery Energy Consumption Estimation Results

Figure 5-40 shows that by the end of the simulation there is a difference of 275 Wh between the simulation and the test data. The distance travelled in both the test and the simulation was 3.65 km. Therefore, the test showed that the vehicle requires 179.9 Wh/km and the simulation results shown in Figure 5-40, indicate that the vehicle requires only 107.5 Wh/km. Using the percentage difference on these two results, it suggests that the simulation has a 40% error. From this data we would assume that the model is at fault and there are large inaccuracies present in the modelling technique that has been used. However, it is interesting to note that the NEDC

simulation shows the vehicle requires 106.5 Wh/km which is comparable to the NEDC test data with an error of 1.2%, but the NEDC requires 36% less energy than the CUDC which is a real-world driving test. Therefore, where the model shows close correlation with the NEDC, the 40% error in this CUDC simulation it is more likely due to the road characteristics not being represented in the simulation, such as, deviations from a straight line and changes in altitude. The RMS unit error of this simulation is 162.7 Wh, by dividing this by the distance of the CUDC a unit error per km is calculated to be 44.6 Wh/km. To determine if the representation of the road is at fault for the simulation error, the full Dymola road generator tool and the closed loop driver should be used to simulate the real-world drive cycle.

5.3.2 CUDC 3D Road Electric Vehicle Simulation

The simulation setup is shown in section 3.2, Figure 3-1. This section of the thesis shows the results of the vehicle model over the 3D CUDC and has made use of the Dymola road generator tool and the Dymola closed loop driver. Figure 5-41 shows the battery energy consumed during the CUDC for both the test and the simulation against the distance travelled.

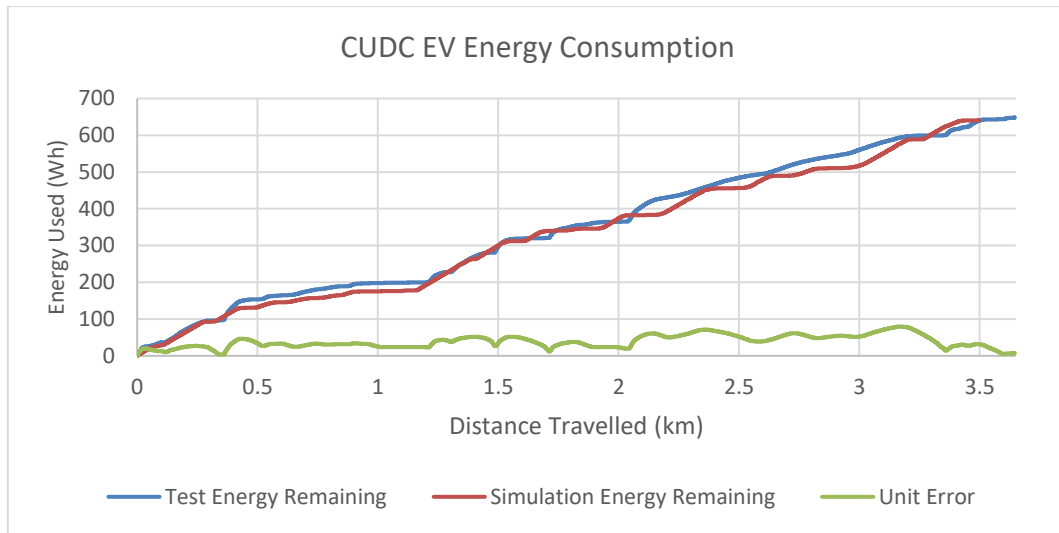


Figure 5-41 – 3-Dimensional CUDC EV Simulation, Battery Energy Consumption Estimation Results

Figure 5-41 shows that the simulation results track those from the test results well and at the end of the simulation there is difference of 6.73 Wh between the simulation and test data. As stated in section 4.4.2, the distance travelled at the end of the test is 3.65 km and the vehicle requires 179.9 Wh/km. The simulation results shown in Figure 5-41 state that the vehicle requires 648.8 Wh over the CUDC, 177.6 Wh/km, suggesting that the model has an error of 1.3%. This confirms the suspicions that the representation of the road characteristics is the reason that the previous simulation, in section 5.3.1, had such a high error, of 40%, where the only difference between these two simulations is the representation of the road. The RMS unit error of this simulation is 39 Wh. Therefore, this approach to representing the vehicle and simulating the drive cycle, provides an RMS unit error of 10.7 Wh/km.

Using the following equations we can estimate the power requirement from the fuel cell for continuous driving on the CUDC.

$$Q_{FC} = \frac{Q_{consumptionCUDC}}{\left(\frac{t_{CUDC}}{3600}\right)} \quad (239)$$

$$5928.1 \text{ [Wh]} = \frac{648.8 \text{ [Wh]}}{\frac{394 \text{ [s]}}{3600 \text{ [s]}}}$$

Where:

Q_{FC} = The estimated energy requirement for continuous driving in Wh
 t_{CUDC} = The time taken to complete the CUDC test in s

Here the requirement of electrical energy to provide continuous driving is calculated as 5928.1 Wh. Equation (240) can be used to determine the requirement from the fuel cell if a simplified efficiency is incorporated into charging the battery.

$$\begin{aligned} P_{FC} &= Q_{FC} + (2 - \varepsilon_{DCDC}) \\ 6106 [Wh] &= 5928.1 + (2 - 0.97) \end{aligned} \quad (240)$$

Where:

P_{FC} = The estimated continuous power requirement from the fuel cell in W
 ε_{DCDC} = The efficiency of the DCDC at the given power.

Here the DCDC efficiency has been incorporated into the estimation of the required power from the fuel cell. This has been calculated as 6106 Wh, where a fuel cell will provide continuous power until the hydrogen tank is depleted a hydrogen consumption model would be required to determine the time which the vehicle could drive for based on the size of the hydrogen tank to determine the range. Previously section 5.2.1 showed that the vehicle would require a fuel cell to provide a continuous 1935.5 W of power so that full driving range can be achieved. However, this section shows a substantial difference in this result, where the CUDC would require 6106 W of continuous power to achieve full range without stopping to recharge the batteries. Therefore, specifying a FCEV based on the NEDC would lead to reduced vehicle range when driving in real world conditions.

$$S_{rangetest} = \frac{Q_{batterynominal}}{Q_{consumptionTest}} \quad (241)$$

Where:

$S_{rangeNEDC}$ = The estimated range of the vehicle based on the battery capacity and test result in km
 $Q_{batterynominal}$ = The nominal battery capacity in Wh
 $Q_{consumptiontest}$ = The energy consumption from either a test or a simulation in Wh/km

Figure 5-42 was created using equation (241) and presents the vehicle range based on both test data and simulation data.

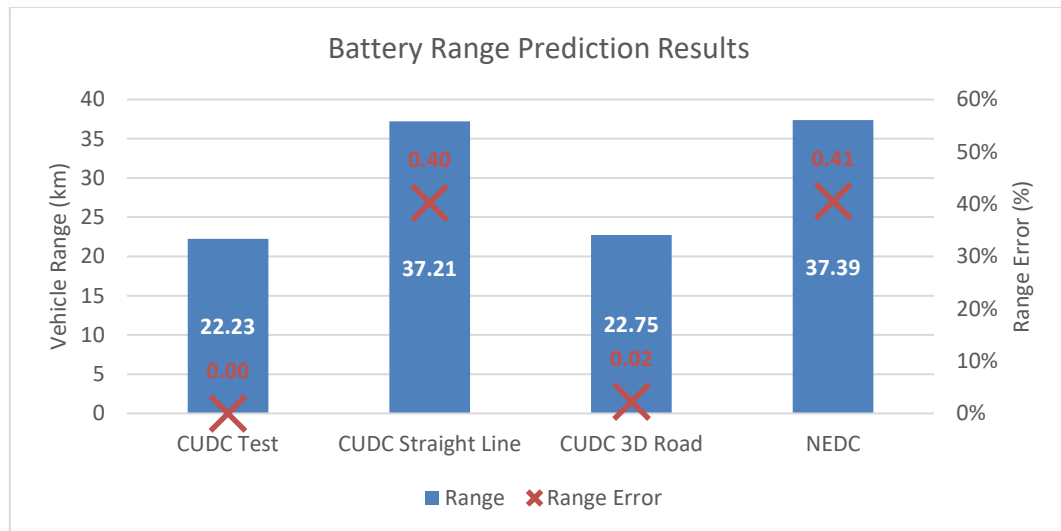


Figure 5-42 - CUDC EV Battery Range Prediction Results

Figure 5-42 shows that the range of the vehicle estimated from the test result of the CUDC is 22.23 km, the CUDC straight line simulation is 37.21 km, the CUDC 3D road simulation is 22.75 km and the NEDC test results is 37.39 km. Figure 5-42 shows that taking the time to model both the vehicle and the drive cycle correctly can lead to range accuracies of 97.7% where the range estimation error of the CUDC 3D road is only 2.3% against real world data. The results shown within this section also confirm the assumption made, that the 40% error of the Flat and Straight CUDC, was due to the lack of a properly characterised road modelled and that the estimation of range or vehicle behaviour cannot be concluded within a simulation environment without the implementation of a characterised road.

5.3.3 CUDC 3D Road Fuel Cell Vehicle Simulation

This section of the thesis shows the results of the proposed vehicle model on the 3D CUDC road profile. The fuel cell has been set to 1500 W power output, equal to that of the test conditions, and Figure 5-43 shows the energy consumption of the vehicle for the simulation and the test results.

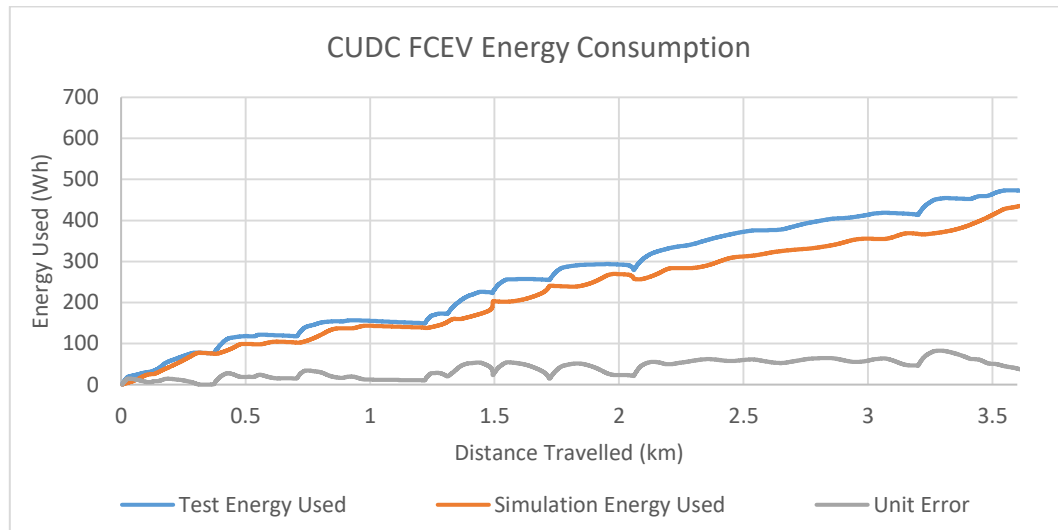


Figure 5-43 – 3-Dimensional CUDC FCEV Simulation, Battery Energy Consumption Estimation Results

Figure 5-43 shows that the energy of the vehicle can be represented well to an RMS unit error of 10.34 Wh/km. The fuel cell was set to 1500 W during the test due to concerns about the fuel cell control system ability to operate the stack within manufacturer specified limits. Further definition of this can be found in APPENDIX F – Improper Fuel Cell Control. Figure 5-43 shows that even with the fuel cell providing approximately 1500 W of continuous power, energy is still being primarily drawn from the battery, where 434 Wh of energy is used over the CUDC. Therefore, during the CUDC the FCEV requires 116 Wh/km from the battery, and by applying equation (241), the vehicle's range is now 34 km, an improvement of 11.7 km by using the fuel cell as a 1.5 kW range extender. When considering operational issues, this improvement in range is small and would require the driver to stop and charge the vehicle prior to using all the available hydrogen energy remaining in the system. However, if the fuel cell could be controlled correctly and operated at 3 kW, then the continuous range performance of the vehicle would be increased. Figure 5-44 shows the energy consumption from the battery and the hydrogen tank pressure over the CUDC simulation when operating the fuel cell at a 3 kW power output.

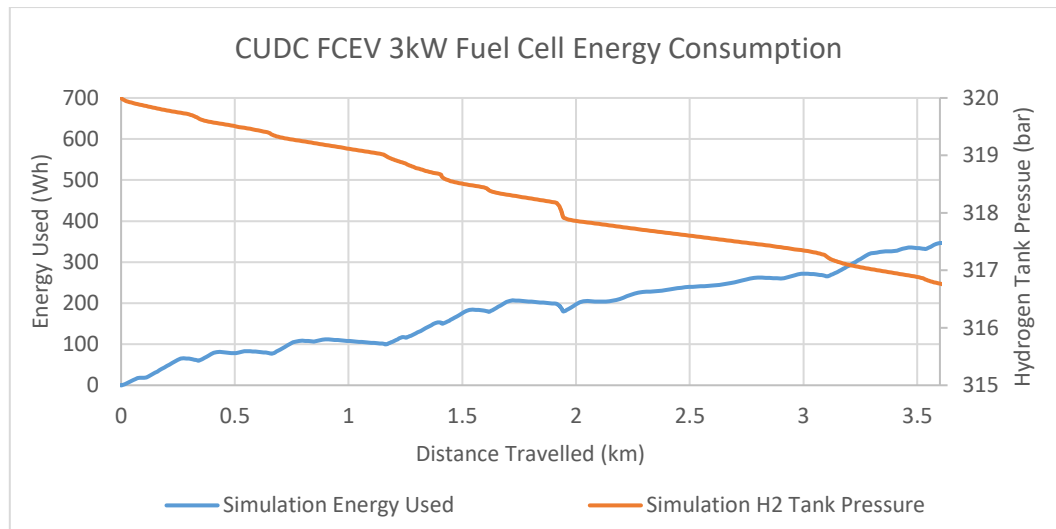


Figure 5-44 - 3-Dimensional CUDC FCEV 3kW FC Simulation, Battery Consumption Estimation and Hydrogen Consumption Estimation

The simulation results in Figure 5-44 show that at the end of the simulation the battery has supplied 364 Wh of energy and the has used 3.245 bar (0.0201 kg) of hydrogen. By dividing these values by the distance travelled the consumption rates can be calculated, thus, the battery energy consumption is reduced to 99.7 Wh/km and the hydrogen consumption is 0.889 bar/km (0.00552 kg/km). Applying equation (241) to this data, suggests that the vehicle range would be increased to 40.1 km, a 17.8 km increase compared to the EV and a 6 km increase compared to the 1.5 kW fuel cell operation. However, the Coventry University Microcab H2EV does not allow the fuel cell to operate when the battery SOC is above 80%, in order to prevent OVP events occurring on the battery. Therefore, the calculated range is likely to be less upon installation. Because of this, the first 4.55 km will require 177.6 Wh/km whilst waiting for the fuel cell to start up. An additional 32.1 km of range is available whilst the fuel cell is operating at 3 kW, providing a total of 36.55 km rather than the initial 40.1 km estimated. Section 5.3.2, proposed, using mathematical estimation and simulation results, that the vehicle would require a fuel cell which can provide 6.1 kW, so that continuous driving is available to the driver until the hydrogen and battery pack is depleted. This proposal is presented further in section 5.5.

5.4 Throttle Controller Simulation Results

This section of the thesis includes the results of the throttle control algorithms which were presented within section 3.11. The findings within this section were presented to both the clients and resulted in the implementation of these control algorithms. However, this was not a simple implementation as the client did not have access to modify the Coventry University Microcab H2EV VCU code. Therefore, to implement the control algorithm in the vehicle an in-depth study of the existing VCU safety functions and the operational processes was required, so that the VCU in terms of usability and to make the vehicle more user friendly could be achieved at the same time. Therefore, the task of creating a VCU model using Motohawk was conducted, whilst introducing ISO26262 compliance into both the VCU model and the new hardware (BS ISO 26262-12011: 2011). During the discussions of VCU development, findings regarding the battery and fuel cell system were also presented and the client saw the opportunity to revise the current vehicle platform within their budget. This led to a battery redesign and fuel cell system design. The implementation of all the new sub-systems to the vehicle is still in progress. An agreement with the client was made to conduct the control strategy investigation on the EV platform as any improvements to energy consumption on the EV platform will directly benefit the FCEV. Therefore, the results within this section will only include the modelling and simulation as the vehicle developments are still in progress. The simulations were performed over the 3D CUDC and from this point forward within the thesis the term CUDC will imply the 3D representation of the road rather than the straight and flat speed profile version.

5.4.1 CUDC EV SOC Throttle Controller Simulation

This simulation has been performed with the following parameter settings on the 'Throttle Controller 1' algorithm which was proposed in section 3.11:

Battery SOC Start	=	40%
Maximum Throttle Limit	=	100%
Minimum Throttle Limit	=	60%
SOC Throttle Limit Start	=	40%
SOC Throttle Limit End	=	20%

The simulation of the CUDC consumes approximately 15% of the battery SOC and the simulation has been initiated with the battery SOC set to 40%. Figure 5-45 shows the difference of implementing the SOC-dependant throttle control algorithm between the driver model and the motor model. Figure 5-45 shows the simulation results, regarding energy consumption, when implementing the control strategy into the vehicle model.

To ensure that only the effects of the control strategy are presented, the results have been presented against the results of the same simulation without the control strategy, thus, eliminating any correlation errors between test data and simulation results.

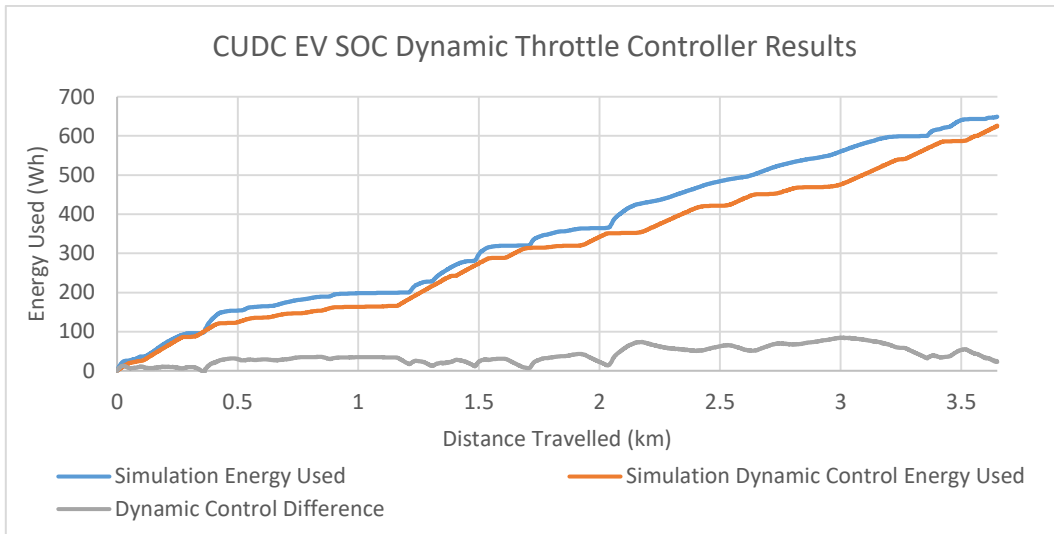


Figure 5-45 - CUDC EV SOC Dynamic Throttle Controller Results

Figure 5-45 shows, within the first 0.4 km a similar trend in energy consumption and as the controller begins to limit the throttle then the energy consumption starts reducing over the drive cycle. The total energy consumption over the CUDC simulation is reduced by 22.8 Wh with a RMS difference of 45 Wh less. In relation to distance the control algorithm could save an average of 12 Wh/km when limiting between the two SOC thresholds.

Where the acceleration of the vehicle is being limited by this control algorithm it is inevitable that the vehicle will take longer to complete the CUDC. The difference in time to complete the CUDC with the controller is an additional 29.4s which is an average of 8 s/km slower as the vehicle has not used enough energy from the battery to reach the 60% hard limit of the control algorithm. Figure 5-46 shows the results of the EV on the CUDC when the battery SOC is initially set to 20% prior to compiling the simulation. Therefore, the controller will limit the maximum throttle to 60% over the entirety of the presented simulation results in Figure 5-46.

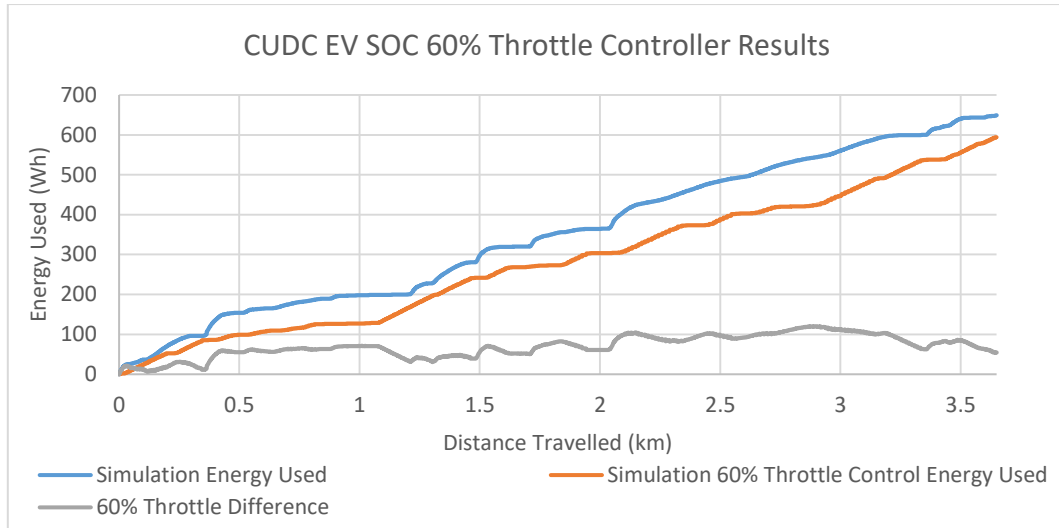


Figure 5-46 - CUDC EV SOC 60% Throttle Limit Controller Results

Figure 5-46 shows that the total energy consumption over the CUDC simulation is reduced by 54.4 Wh with an RMS difference of 75 Wh. In relation to distance, the control algorithm could save an average of 20.6 Wh/km when limiting the throttle to 60% past the second SOC threshold. The difference in time to complete the CUDC without the controller is 35.1s, which is an average of 9.6 s/km slower.

5.4.2 CUDC EV Speed Throttle Controller Simulation

This simulation has been performed with the following parameter settings on the 'Throttle Controller 2' algorithm which was proposed in section 3.11:

Battery SOC Start	=	100%
Maximum Throttle Limit	=	100%
Minimum Throttle Limit	=	60%
Speed Throttle Limit Start	=	32km/h
Speed Throttle Limit End	=	48km/h

Figure 5-47 shows the result of implementing the speed-dependant throttle control algorithm between the driver model and the motor model.

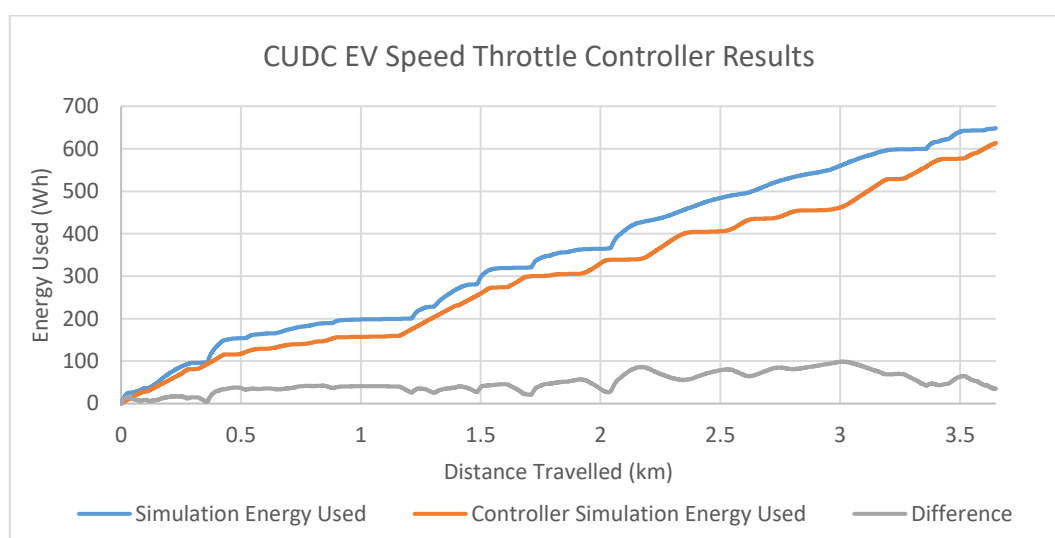


Figure 5-47 - CUDC EV Speed Throttle Controller Results

Figure 5-47 shows that the simulation results present a reduced energy consumption over the CUDC. The total energy consumption during the simulation is reduced by 35.1 Wh with an RMS difference of 54 Wh. In relation to distance the control algorithm could save an average of 15 Wh/km. By applying equation (241) to this data, where the battery consumption averages at 168.1 Wh/km, the range of the vehicle would be 23.8 km an estimated gain of 1.3 km in range.

The difference in time to complete the CUDC with the controller is an additional 43s, which is an average of 11.8 s/km slower. However, it is clear from the results in Figure 5-47 that a FCEV could both benefit and suffer from this control algorithm. Its implementation into any vehicle should be dependent on the nature of the drive cycle which the vehicle is designed for, since when the vehicle is required to travel up a large incline there is the potential for stalling of the motor due to the controller limiting the current to the motors. However, developments in this area could be of great interest

and the concept of route planning dependant control algorithms would be an area of new research and innovation.

5.4.3 CUDC EV Dual Throttle Controller Simulation

This simulation has been performed with the following parameter settings on the 'Throttle Controller 3' algorithm which was proposed in section 3.11:

Battery SOC Start	=	100 %
Maximum Throttle Limit	=	100 %
Minimum Throttle Limit	=	60 %
Speed Throttle Limit Start	=	32 km/h
Speed Throttle Limit End	=	48 km/h
SOC Throttle Limit Start	=	40 %
SOC Throttle Limit End	=	20 %

Due to the nature of this throttle algorithm it was necessary to simulate the EV on the CUDC continuously until the battery model is fully depleted. Therefore, this was performed for the EV with and without the 'dual' throttle controller implemented into the model. The results for this simulation are presented in Figure 5-48.

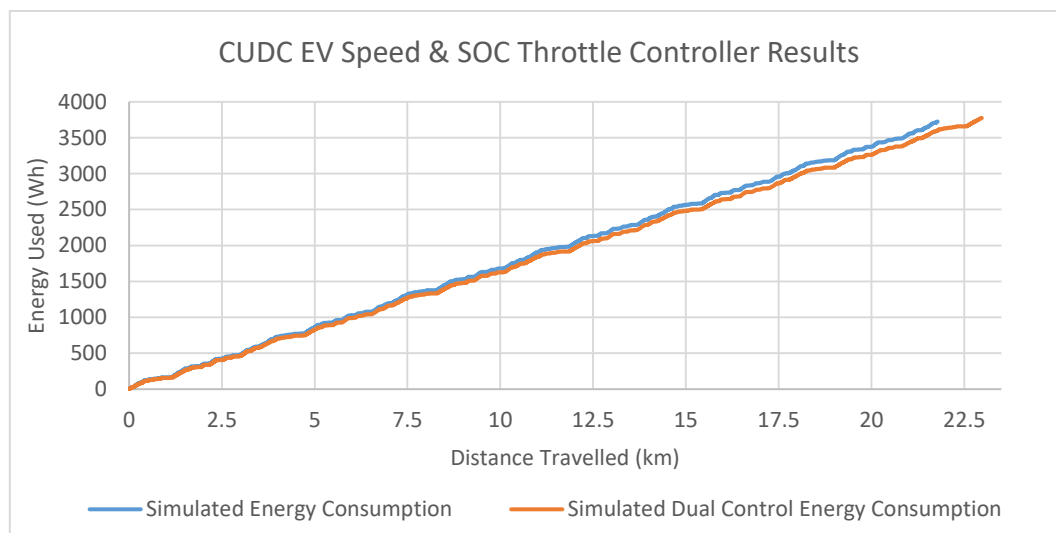


Figure 5-48 - CUDC EV Speed and SOC Throttle Controller Results

Figure 5-48 shows the simulation results and how the implementation of both control algorithms allows the EV vehicle to achieve an additional 1.2 km, similar to what was estimated in the previous section. However, the vehicle takes an additional 114s to drive the same 21.8 km, which is 5.2 s/km slower with the control algorithms implemented. From Figure 5-48 we can calculate that the EV without the throttle controller requires 171 Wh/km and the EV with the throttle controller requires 164.2 Wh/km. Therefore, an improvement of 6.8 Wh/km was achieved by implementing this controller.

5.5 Continuous CUDC Fuel Cell Electric Vehicle Simulation Results

This simulation has been performed without throttle control algorithms to verify if the estimation made in section 5.3.3, that the vehicle can achieve 32.1 km of range whilst the fuel cell is operating at 3 kW, between 80% battery SOC and 0% battery SOC. Figure 5-49 presents the simulation results when the FCEV is simulated on the CUDC continuously until the battery SOC is equal to zero.

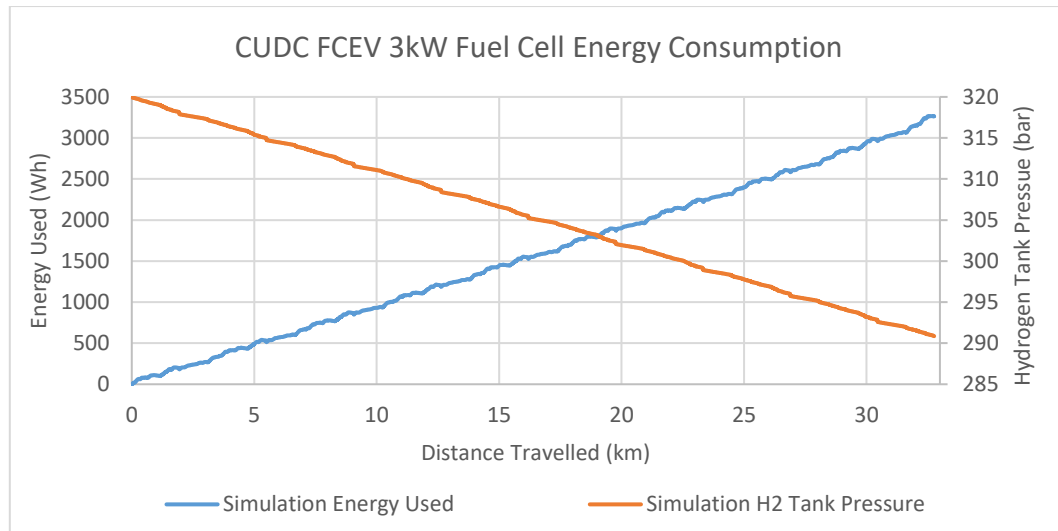


Figure 5-49 - Continuous CUDC FCEV 3kW FC Simulation, Battery Consumption Estimation and Hydrogen Consumption Estimation

Figure 5-49 shows that the model estimates a range of 32.8 km whilst the fuel cell is operating at approximately 3 kW. A 29.1 bar pressure drop and 0.18 kg of hydrogen was used to achieve the range of 32.8 km, and that there is plenty of remaining hydrogen in the tank. Therefore, it would suggest that this is the range limit of the given Coventry University Microcab H2EV, when performing drive cycles similar to that of the CUDC.

The FCEV has been simulated with the throttle control algorithm described in section 5.4.3 over the CUDC to present the benefits of throttle control algorithm whilst operating the fuel cell at 3 kW. The results are shown in Figure 5-50 and simulation was performed with the following parameter settings:

Battery SOC Start	=	80 %
FC Power Output Setting	=	3000 W
Maximum Throttle Limit	=	100 %
Minimum Throttle Limit	=	60 %
Speed Throttle Limit Start	=	32 km/h
Speed Throttle Limit End	=	48 km/h
SOC Throttle Limit Start	=	40 %

SOC Throttle Limit End = 20 %

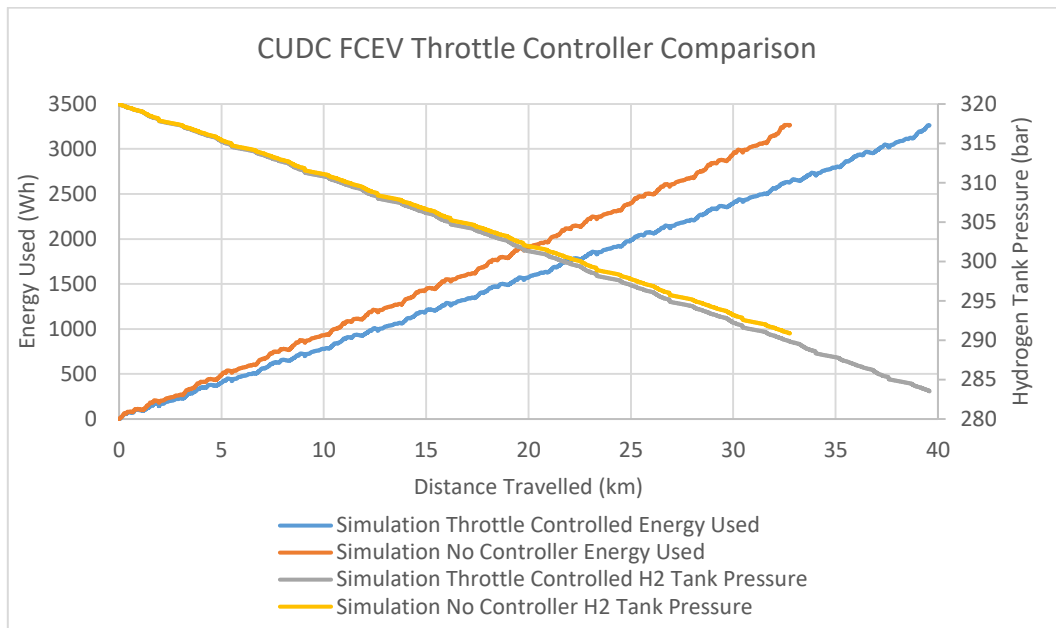


Figure 5-50 - Continuous CUDC FCEV 3kW FC Simulation, Battery Consumption Estimation and Hydrogen Consumption Estimation, Throttle Controller Comparison Results

Figure 5-50 shows that by implementing the throttle control algorithm into the FCEV model a vehicle range gain of 6.8 km can be achieved. This improved the battery consumption to 82.45 Wh/km, a 17 Wh/km reduction. Figure 5-50 presents the hydrogen consumption in relation to the 75 litre tank pressure and it shows that 36.5 bar of hydrogen is used over the simulation and that 0.921 bar/km (0.0057 kg/km) is required. Therefore, the total available range from hydrogen is reduced from 360.5 km to 347.4 km. However, to achieve this the user would need to use the plug-in charging facility on the vehicle, rather than the fuel cell, to recharge the batteries between 39.5 km drives.

Section 5.3.2 proposed, via equation (239) and (240), that the vehicle would require a fuel cell to operate at approximately 6.1 kW in order to provide continuous driving until hydrogen energy and battery energy is depleted. By applying equations (239) and (240) to the simulation results in section 5.4.3, Figure 5-48, it can be estimated that the vehicle with the Dual Throttle Controller implemented would require a 5.55 kW fuel cell to achieve this. As the client agreed to the implementation of a new VCU with this throttle control, all the following simulation results will all include the use of the dual throttle controller proposed in section 3.11 and have the following parameter settings:

Maximum Throttle Limit = 100 %
 Minimum Throttle Limit = 60 %
 Speed Throttle Limit Start = 32 km/h

Speed Throttle Limit End = 48 km/h
 SOC Throttle Limit Start = 40 %
 SOC Throttle Limit End = 20 %

Initially the simulation was done with the fuel cell power output set to approximately 6.1 kW and then 5.55 kW, to identify if the given theories presented, based on the simple mathematics of equations (239) and (240), are accurate enough to be used for the continuous CUDC simulations when the throttle controller is implemented. The following simulations have been performed with parameter settings presented below:

Battery SOC Start = 80 %
 FC Power Output Setting 1 = 5550 W
 FC Power Output Setting 2 = 6100 W
 FC Power Output Setting 3 = 5800 W
 Number of Cells in the FC Model = 140

Figure 5-51 shows the power produced by the fuel cell model and the power at the battery model.

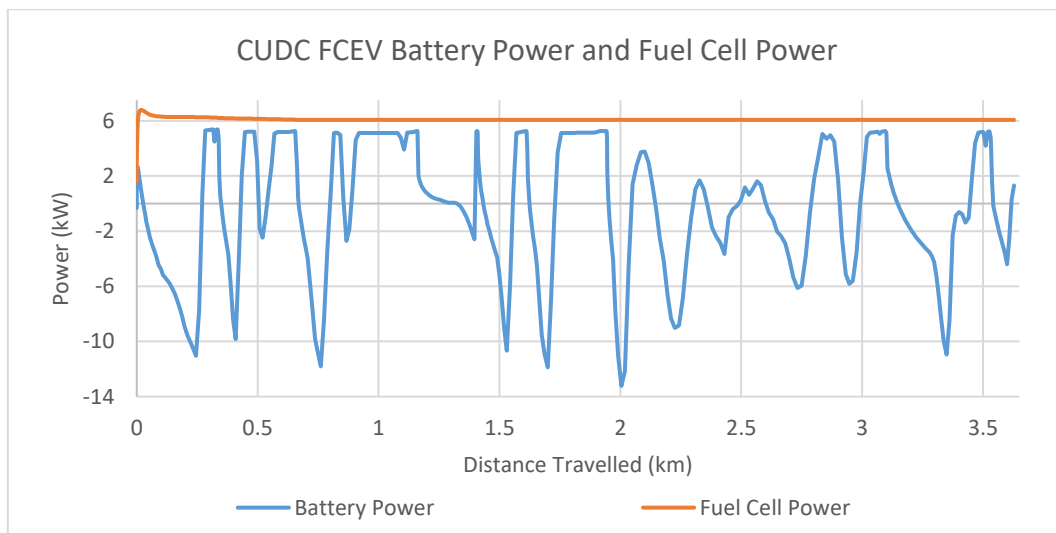


Figure 5-51 - CUDC FCEV Battery Power and Fuel Cell Power, Simulation Results

Figure 5-51 shows the simulation results when the fuel cell is set to the higher power setting of 6.1 kW, this shows that 5.3 kW is transferred to the battery, which can be seen when the vehicle is stationary. At these higher fuel cell current outputs, the DCDC model adjusts based on its parameter setting and results in reduced efficiency when comparing data against the 3 kW system model. Figure 5-52 shows the energy consumption over one cycle of the CUDC when the fuel cell is operating at both 'FC Power Output Setting 1' and 'FC Power Output Setting 2'.

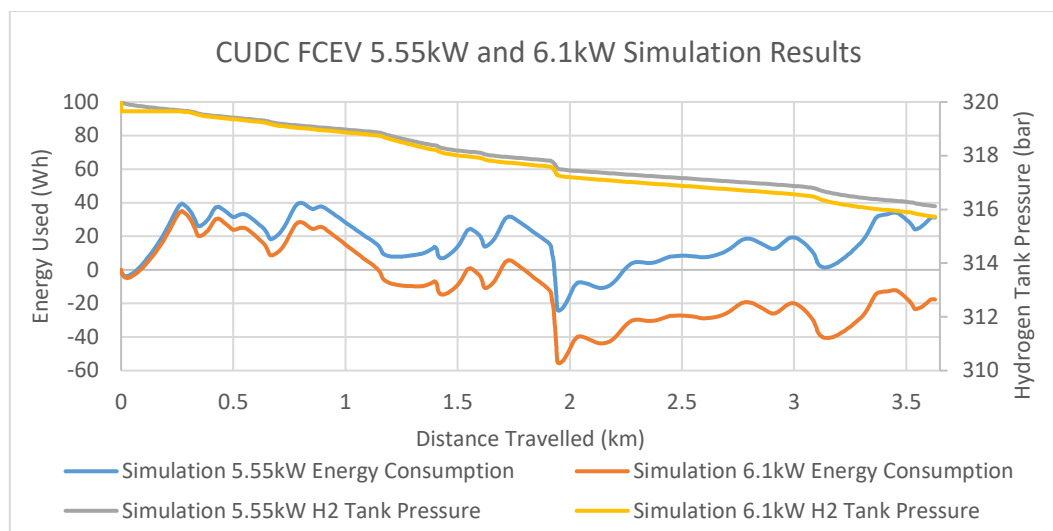


Figure 5-52 - CUDC FCEV Battery Energy Consumption Estimation and Hydrogen Consumption Estimation, Simulation Results at FC Outputs Power of 5.55kW and 6.1kW

Figure 5-52 shows that the fuel cell is over charging the battery when set to operate at 6.1 kW. This is shown where the energy consumption of the battery is negative at the end of the CUDC. Therefore, equations (239) and (240) can only be used to provide a good starting point to specifying a fuel cell. Figure 5-52 shows when the fuel cell is operated at 5.55 kW that 31.1 Wh of energy was consumed from the battery at the end of the CUDC. Therefore, with the 5.55 kW fuel cell power output the battery only needs to provide 8.5 Wh/km, a reduction of 166.4 Wh/km at the battery. Using the results in Figure 5-52 the hydrogen consumption can be calculated for the two operating conditions of the fuel cell. At 5.55 kW the hydrogen consumption is 1.07 bar/km, a range of 280 km and, at 6.1 kW the hydrogen consumption is 1.18 bar/km, a range of 254 km. However, from the results in Figure 5-52 if a 6.1 kW fuel cell is used, then a control strategy would need to be implemented to prevent overcharging the batteries. Therefore, the following simulation results have been performed with a fuel cell power, between the two presented values, of 5.8 kW to establish the range if the fuel cell is tailored specifically to the CUDC.

Figure 5-53 shows the simulation results when operating the fuel cell at constant power of 5.8 kW over the CUDC, with the following parameter settings in the model:

Battery SOC Start	=	80 %
FC Power Output Setting	=	5800 W
Number of Cells in the FC Model	=	140

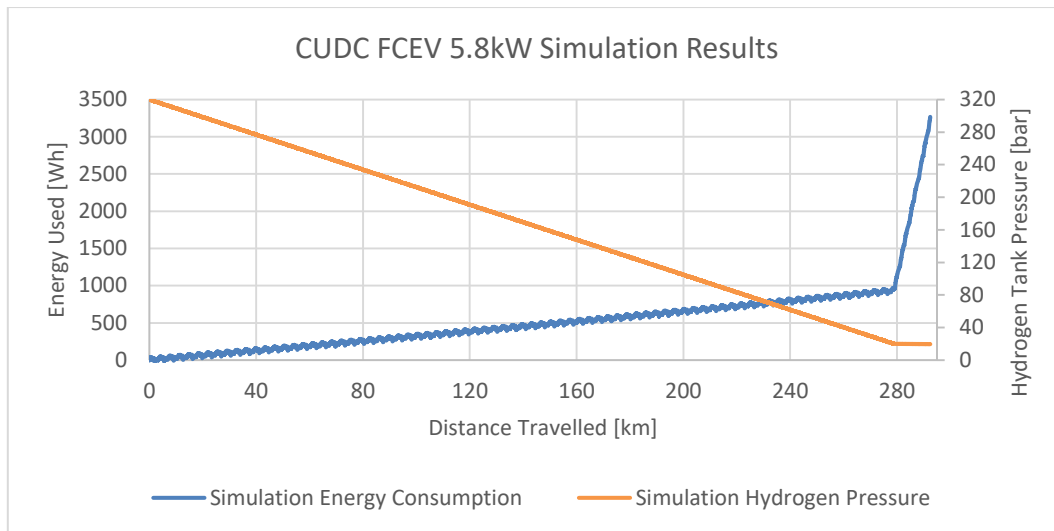


Figure 5-53 - CUDC FCEV 5.8kW Battery Energy Consumption Estimation and Hydrogen Consumption Estimation

Figure 5-53 results show the FCEV can achieve a range of 292 km over the CUDC which is achieved in 9.09 hours (32,714 s). It shows, when using 80% of the battery capacity and operating the fuel cell at 5.8 kW that the energy requirement from the battery is an average 11.17 Wh/km. The reason this is larger than the results from Figure 5-52 is because those results do not consider using the remaining battery capacity when the hydrogen is depleted. Figure 5-53 shows that the range whilst the 5.55 kW fuel cell is in operation is 279 km and the energy required from the battery is 951 Wh, therefore, the average energy requirement from the battery during fuel cell operation is 3.41 Wh/km. The hydrogen consumption is also improved, as the battery accounts for the extended range of 13 km, to 1.03 bar/km (0.0064 kg/km). This concludes that by replacing the 3 kW fuel cell with a 5.8 kW fuel cell, into the FCEV, there is a range increase of 253 km to made. However, it could easily be argued that not all conditions of real world driving are similar to that of the CUDC and that other drivers may demand more from their vehicles, which can be due to locational circumstances and driver characteristics. Therefore, creating a vehicle specification on one drive cycle could be deemed inappropriate and could potentially result in an under specified vehicle. This was shown when comparing the range results of the NEDC test data against that of the CUDC test data in section 5.3.2, Figure 5-42 and through the literature review (Ryan et al. 2014). To account for the possibility of under specification, the simulation has been performed with an 8 kW fuel cell to provide head room for more strenuous drive cycles. An 8 kW fuel cell has been chosen because the maximum charge rate of the battery is 2C and this is then the limiting factor for increasing fuel cell power output.

Figure 5-54 shows the simulation results when operating the fuel cell at a power of 8 kW over the CUDC. To ensure that the 8 kW fuel cell would not over charge the battery, a simple controller has been implemented into the model which switches the fuel cell on when the battery SOC falls below 20% and then switches the fuel cell off when the battery SOC rises above 80%. Therefore, the CUDC FCEV simulation results presented in Figure 5-54 have been performed with the following parameter settings:

Battery SOC Start	=	80 %
FC Power Output Setting	=	8000 W
Start FC at Battery SOC	=	20 %
Stop FC at Battery SOC	=	80 %
Number of Cells in the FC Model	=	170

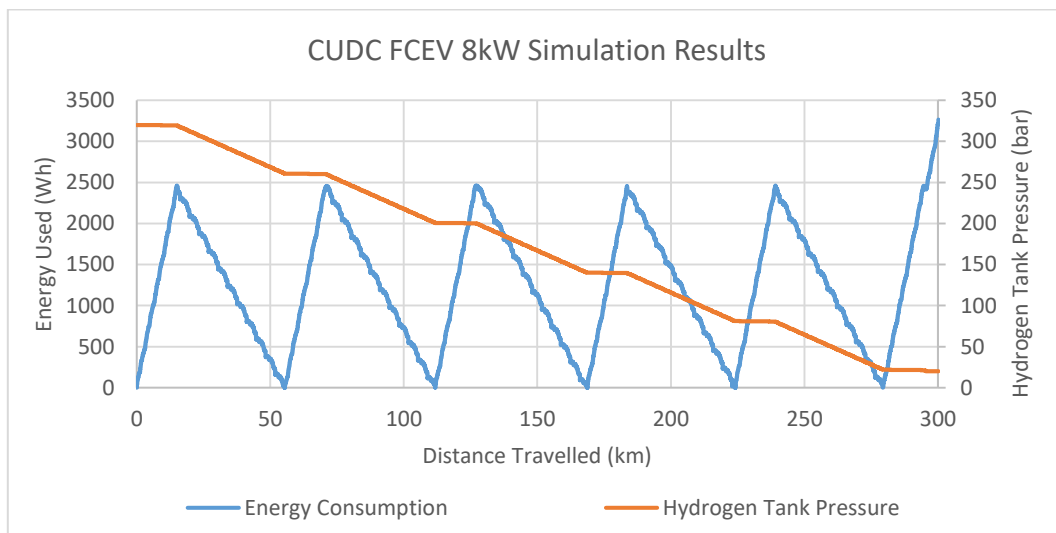


Figure 5-54 - CUDC FCEV 8kW Battery Energy Consumption Estimation and Hydrogen Consumption Estimation

Figure 5-54 results show the FCEV can achieve a range of 300 km over the CUDC which is achieved in 9.27 hours (33,388 s). It shows, when using 80% of the battery capacity and operating the fuel cell at 8 kW that the energy requirement from the battery is an average 10.8 Wh/km. The hydrogen consumption is 0.99 bar/km (0.0062 kg/km). This concludes that by replacing the 3 kW fuel cell with an 8 kW fuel cell, into the FCEV, provides range increase of 261 km and an improvement of 8 km over the 5.8 kW fuel cell. Although the improvement over the 5.8 kW fuel cell is small, the system will allow for more demanding drive cycles as it can recharge the vehicle without having to stop driving. Therefore, the 8 kW fuel cell system can accommodate a larger range of users for the proposed vehicle. It can be estimated that the range could be larger than this, depending on the user, as it is unlikely that 300 km of urban driving would be done in one trip and on/off events for the vehicle would be present.

Therefore, the vehicle may be switched off and then on again between the two thresholds of the fuel cell controller. This would allow for battery to provide energy again for a short distance prior to the fuel cell switching on and using the hydrogen energy thus, resulting in a range increase.

5.6 Summary of Results

The results shown within this chapter have demonstrated the validation procedure and the level of accuracy which the proposed multi-disciplinary FCEV model can provide. A list of RMS errors for each simulation has been tabulated, this is shown in APPENDIX H – Tabulated Validation Results, Table 8-7. Test data from chapter 4 has been used to validate each subsystem of the model and the whole vehicle model.

The battery model can represent both the battery pack capacity and the voltage to 1.1% and 0.82%, respectively, for discharge and charge scenarios. The battery model can represent a battery's cell voltage over a range of different charge and discharge scenarios to an average of 2.03%. The fuel cell model can represent the fuel cell voltage and hydrogen consumption to an average error of 2.1% over a range of different steady state operating conditions. Using the fuel cell test results, data regarding the DCDC efficiency was derived and the DCDC model can represent the losses to an error of 3.3%. The motor model has been validated against data provided by the manufacturer, where an average error of 1.5% is present over the given tests. This meets objective 3.1, in section 1.3, "subsystem validation".

The vehicle model can represent the vehicle energy consumption on the NEDC test cycle to 1.2% and the energy consumption of the CUDC test cycle to 2.3%. The RMS error of each simulation in chapter 5 is 2.5%, thus showing good representation of the vehicle and meeting objective 3.2, in section 1.3, "whole vehicle level validation".

A key finding in this chapter is across section 5.3.1 and section 5.3.2 where the vehicle model is simulated driving the CUDC via two methods.

The first simulation is presented in section 5.3.1, where the vehicle model is simulated using a typical type approval drive cycle simulation method and speed versus time is fixed during the simulation. In this simulation the vehicle is driven along a flat and straight road.

The second simulation is presented in section 5.3.2 where the vehicle model is simulated using the proposed drive cycle method, and speed versus distance is fixed during the simulation. In this simulation the vehicle is driven along a 3D road that incorporates deviations from a straight line and changes in altitude. These inputs were obtained via test data. Both of the simulations take the same duration to complete and cover the same distance travelled.

The results show that when the road is not represented appropriately the model is not able to predict the energy consumption of the vehicle for real-world driving to a high level of accuracy.

This is shown where the first method of simulating the vehicle model on the CUDC with a flat and straight road under predicts energy consumption by 40%. The second method of simulating the CUDC using a 3D road greatly improves on this by under predicting energy consumption by only 1.3%. This shows that typical type approval methods should not be used to predict energy consumption of a vehicle in a simulation. It has been shown here that the road model representation can introduce an error of 38.7% (40% - 1.3%). This meets objectives four and five, in section 1.3, “provide predictive energy consumption capability” and “compare real-world driving data and energy consumption against current type approval methods”.

This does not invalidate the NEDC method because these tests are useful for direct comparison of vehicle performance, especially between different vehicles, and can be used as a practical test method for a quickly obtaining powertrain efficiency. However, from these results, it is felt that it should not be used to obtain values regarding energy consumption, vehicle range figures or for specifying vehicle powertrain requirements.

The chapter goes on to demonstrate how controllers can be implemented into the FCEV model and then tested to improve vehicle energy consumption on the CUDC through the virtual environment.

The end of this chapter shows the approach taken to optimise the test vehicle, Coventry University Microcab H2EV, fuel cell system requirements. It shows that the current 3 kW fuel cell system is limited to a range of 40.1 km, and that specifying a fuel cell size based on the CUDC would give a range of 292 km. However, using an 8 kW fuel cell would comfortably provide a range of 300 km. This shows how the proposed novel multi-disciplinary FCEV model can be used to optimise system performance and meets the goal described in section 1.3, “The model will allow FCEV manufactures to optimise system performance”

CONCLUSIONS & RECOMMENDATIONS FOR FURTHER WORK

6.1 Conclusions

The work presented in this thesis has shown a logical approach to creating a novel multi-disciplinary FCEV model which is capable of simulating a range of different driving scenarios. This has been done to show how such a model can be used to predict energy consumption for EVs and FCEV's and to meet the gap in current literature.

The first objective set out in section 1.3 was to create a multi-disciplinary FCEV model with appropriate subsystems. This objective has been met by using current state-of-the-art modelling techniques to represent the different subsystems of a FCEV.

The second objective set out in section 1.3 was to make each model parametric so that versatility for vehicle design can be achieved. This objective has been met by using parameters throughout the modelling process, where focus on parameterising common differences in subsystems has been made. This ensures that the subsystem models can be easily changed to analyse the effects of different sized systems. Additionally, standard Modelica connectors have been used so that the subsystem models are 'truly reusable'.

The third object set out in section 1.3 was to validate the FCEV model at a subsystem level. This objective has been met by testing each area of a physical vehicle to gain characteristic data for each subsystem. This data has been used to recreate the test within the virtual environment in order to directly compare the simulation results with the physical test data.

The fourth objective set out in section 1.3 was to validate the FCEV model as a whole. This objective has been met by obtaining energy consumption data from real-world driving and controlled rolling road testing. Data from these tests have been used to recreate the test within the virtual environment to directly compare the simulation results with the test data.

The fifth objective set out in section 1.3 was to ensure the FCEV model can predict the energy consumption of a vehicle. This has been met though the validation process for the FCEV model, and the proposed model can predict vehicle energy consumption to an error of 1.3% for real-world driving scenarios.

The final objective set out in section 1.3 was to compare real world driving data and energy consumption against the current type approval method. This object has been met, where the NEDC rolling road test was compared to that of the CUDC real-world

CONCLUSIONS & RECOMMENDATIONS FOR FURTHER WORK

test. This showed that the NEDC test required 36% less energy consumption compared to the CUDC test.

The aim of the project was to determine if a novel multi-disciplinary FCEV model can accurately predict energy consumption for EVs and FCEVs. This aim has been met using test data for both an EV and a FCEV, where the Coventry University Microcab H2EV was used in both cases. This was achieved by simulating both vehicle types on a real-world drive cycle, the CUDC, and by comparing the test data against the simulation results. The results showed that the model proposed here can predict the energy consumption of the EV to an error of 1.3% and the FCEV to an error of 8%. This gives a good representation of both vehicle types and meets the overall aim of the project.

A brief summary of these major conclusions is:

- To accurately represent the energy consumption of EVs and FCEVs a dynamic vehicle model and road which can represent deviations from a straight line and changes in altitude is a minimum requirement.
- The proposed model can be used for virtual vehicle development to improve upon energy consumption and to optimise vehicle powertrain specifications.
- The proposed model can be used to develop nearly all aspects of the vehicles handling and performance characteristics in the virtual environment due to its multi-disciplinary nature.

This main contributions to knowledge for this work include:

- The work conducted has provided Coventry University and Microcab Industries Ltd with a more in-depth insight as to what their vehicle platform can achieve in terms of energy consumption and hydrogen usage. Specifically, the simulation results have influenced their development schedule and the collaborative partnership have decided to work on the integration of an 8 kW fuel cell due to the benefits discussed and the knowledge provided in this thesis.
- The work here has provided a state-of-the-art modelling approach to EVs and FCEVs using Dymola as the simulation tool and novel models for an EV and a FCEV which were not previously available.
- The work here has shown that the current type approval methodology is not suitable as a process to determine the energy consumption and range estimation for EVs and FCEVs in a simulation environment.

6.2 Discussion and Future Work

The model development in this thesis provides a comprehensive base for further developments and extensions. The future work that could follow this project and the reasons for pursuing these investigations are listed below:

- i. An initial study would be to establish the scalability of the model and if it can represent other existing vehicles to the same level of accuracy. So, that multi vehicle validation could be achieved and the quantity of work required to gain that same degree of confidence in the model could be established. However, theoretically the model would hold a similar level of accuracy if the same technology is used in a new vehicle design due to the methodology taken to generate this model.
- ii. A database of three-dimensional drive cycles, obtained through real world driving, could be collated to better improve the virtual proving ground concept.
- iii. An investigation to identify the need for high powered motors in EV's and FCEV's is of interest and to determine if the benefits of a multi-speed gearbox can overcome the losses in a gearbox by reducing motor power requirements.
- iv. Where life expectancy of air cooled fuel cells is a concern, the development of a validated parametric water cooled fuel cell system model would be of interest to cater for larger vehicles and increased longevity.
- v. An investigation of battery sizes in relation to fuel cell sizes, how small can you go in relation to the vehicle specification?
- vi. An investigation into route dependant throttle control algorithms, where a satellite navigation system interacts with the vehicle to determine the most efficient way to operate the vehicle. The client's response to this type of controller, which was also presented in this thesis, was receptive as any period of driving which reduces the energy consumption will provide extra time for the fuel cell to apply more charge to the battery and could significantly improve range. Therefore, the client recognises the benefits of this type of controller and shows enthusiasm to see future work into route dependant control algorithms.
- vii. Finally a development task to the model to work as a real-time simulation, so that not only can scenarios be programmed, but real characteristics of both the controller and the vehicle can be virtually tested with human interaction.

REFERENCES

- Andersson, R. (2012) *Online Estimation of Rolling Resistance and Air Drag for Heavy Duty Vehicles*. Stockholm: KTH Industrial Engineering and Management
- André, M., Keller, M., Sjódin, Á., Gadrat, M., Mc Crae, I., and Dilara, P. (2009) 'The ARTEMIS European Tools for Estimating The Transport Pollutant Emissions'. *18th International Emissions Inventories Conference*, (1:18), 1-10
- Aston, R. (2015) 'DCDC Modelling Methodologies' [Interview by Apicella, M] in n, e. (2015) *n.b*. Coventry: n.p
- AVL LIST GmbH (2013) *AVL Cruise M* [Online] available from <https://www.avl.com/web/guest/simulation> [19/04/2013]
- Bakker, E., Nyborg, L., Volvo Car, C., Pacejka, H., and Delft University of Technology, . (1987) *Tyre Modelling for Use in Vehicle Dynamic Studies*. Detroit, Michigan: SAE The Engineering Society for Advancing Mobility Land Sea Air and Space: Technical Paper Series
- Bakker, E., Pacejka, H., and Lidner, L. (1989) *A New Tire Model with an Application in Vehicle Dynamics Studies*. Monte Carlo: SAE In: 4th Auto Technologies Conference
- Ballard Power Systems Inc. (2014) *FCgen - 1020ACS Fuel Cell Stack - Product Manual and Integration Guide*. Burnaby, Canada: Ballard Power Systems Inc.
- Barlow, T., Latham, S., McCrae, I., and Boulter, P. (2009) *A Reference Book of Driving Cycles for use in the Measurement of Road Vehicle Emissions*. London, UK: TRL Limited
- Barreras, J., Schaltz, E., Andreasen, S., and Minko, T. (2012) 'Datasheet-Based Modeling of Li-Ion Batteries'. in Barreras, J. (ed.) *Proceedings of Vehicle Power and Propulsion Conference*, 'IEEE'. held on 9-12/10/2012 at Seoul, 830-835

- Benchouia, N., Hadjadj, A., Derghal, A., Khochermane, L., and Mahmah, B. (2013) 'Modeling and Validation of Fuel Cell PEMFC'. *Revue des Energies Renouvelables*, (16:2), 365-377
- Besselink, I., Schmeitz, A., and Pacejka, H. (2010) 'An Improved Magic Formula/Swift Tyre Model that can Handle Inflation Pressure Changes'. *Vehicle System Dynamics*, (48:1), 337-352
- Blundell, M. (2004) 'A Low Parameter Tyre Model for Handling Simulation'. *The European Conference for Tire Design and Manufacturing Technology*, (4:1),
- Blundell, M., and Harty, D. (2004) *The Multibody Systems Approach to Vehicle Dynamics*. Oxford: Elsevier Ltd.
- Blundell, M., and Harty, D. (2007) 'Intermediate Tyre Model for Vehicle Handling Simulation'. *IMEchE Multi-body Dynamics*, (221:1), 41-62
- BMW (2015) 'Technical Data: BMW i3'. *BMW* [Online] n.d./n.m./2015. Available from http://www.bmw.com/com/en/newvehicles/i/i3/2013/showroom/technical_data.html#m=i3 [15/11/2015]
- Bogosyan, S., Gokasan, M., and Goering, D. (20017) 'A Novel Model Vatisation and Estimation Approach for Hybrid Serial Electric Vehicles'. *IEEE Transactions on Vehicular Technology*, (56:4), 1485
- Boscaino, V., Miceli, R., Capponi, G., and Casadei, D. (ed.) (2013) *Fuel Cell Modelling and Test: Experimental Validation of Model Accuracy*. 'Power Engineering, Energy and Electrical Drives (POWERENG)'. held on 13-17/05/2013 at Istanbul, Turkey: IEEE
- Bosch, R. (2007) *Bosch Automotive Handbook*. Cambridge, Massachusetts: Bentley Publishers
- Boursin, P. (2004) '*HISTOIRE DE LA VOITURE ELECTRIQUE*'. [Electronic Source] from Philippe Boursin:

References

- Brooker, A., Haraldsson, K., Hendricks, T., Johnson, V., Kelly, K., Kramer, B., Markel, T., O'Keefe, M., Sprik, S., Wipke, K., and Zolot, M. (2013) *ADVISOR Documentation* [Online] available from http://adv-vehicle-sim.sourceforge.net/advisor_doc.html [15/12/2013]
- BSI Standards, P. (2011) *BS EN 61960:2011 Secondary Cells and Batteries Containing Alkaline or Other Non-Acid Electrolytes - Secondary Lithium Cells and Batteries for Portable Application*. United Kingdom Patent BS EN 61960:2011
- BSI Standards, P. (2011) *Road Vehicles - Functional Safety, Part 1: Vocabulary*. United Kingdom Patent BS ISO 26262-1:2011
- BSI Standards, P. (2011) *Road Vehicles - Functional Safety, Part 2: Management of Functional Safety*. United Kingdom Patent BS ISO 26262-2
- BSI Standards, P. (2011) *Road Vehicles - Functional Safety, Part 3: Concept Phase*. United Kingdom Patent BS ISO 26262-3
- BSI Standards, P. (2011) *Road Vehicles - Functional Safety, Part 4: Product Development at the System Level*. United Kingdom Patent BS ISO 26262-4
- BSI Standards, P. (2011) *Road Vehicles - Functional Safety, Part 5: Product Development at the Hardware Level*. United Kingdom Patent BS ISO 26262-5
- BSI Standards, P. (2011) *Road Vehicles - Functional Safety, Part 6: Product Development at the Software Level*. United Kingdom Patent BS ISO 26262-6
- BSI Standards, P. (2011) *Road Vehicles - Functional Safety, Part 7: Production and Operation*. United Kingdom Patent BS ISO 26262-7
- BSI Standards, P. (2011) *Road Vehicles - Functional Safety, Part 8: Supporting Processes*. United Kingdom Patent BS ISO 26262-8
- BSI Standards, P. (2011) *Road Vehicles - Functional Safety, Part 9: Automotive Safety Integrity Level (ASIL)-Oriented and Safety-Oriented Analyses*. United Kingdom Patent BS ISO 26262-9

- BSI Standards, P. (2012) *Road Vehicles - Functional Safety, Part 10: Guideline on ISO 26262*. United Kingdom Patent BS ISO 26262-10:2012
- Chen, M., and Rincón-Mora, G. (2006) 'Accurate Electrical Battery Model Capable of Predicting Runtime and I-V Performance'. *IEEE Transactions on Energy Conversion*, (21:2), 504-511
- Claytex (2010-2013) *Customer Stories* [Online] available from <http://www.claytex.com/category/customer-stories/page/1/> [28/10/2013]
- Clean Fleets (2014) 'Vehicle Test Cycles'. *Clean Fleets Factsheet* [Online] 10/07/2014. Available from http://www.clean-fleets.eu/fileadmin/files/documents/Publications/Test_cycles_-_Clean_Fleets_factsheet.pdf [22/08/2014]
- Daowd, M., Antoine, M., Omar, N., Van den Bossche, P., and Van Mierlo, J. (2013) 'Single Switched Capacitor Battery Balancing System Enhancements'. *Energies*, (6:1), 2149-2174
- Dassult Systems (2002-2013) *Dymola* [Online] available from <http://www.3ds.com/products-services/catia/capabilities/systems-engineering/modelica-systems-simulation/dymola> [28/10/2013]
- Deuring, A., Gerl, J., and Wilhelm, H. (2010) '*Multi-Domain Vehicle Dynamics Simulation with Dymola*'. [Electronic Source] from Vehicle Dynamics Expo: Stuttgart
- Dizqah, A., Busawon, K., and Fritzson, P. (2012) 'Acausal Modeling and Simulation of the Standalone Solar Power Systems as Hybrid DAEs'. *International Conference of the Scandinavian Simulation Society (SIMS)*, (1:53), 1 - 7
- Dorling, R. (ed.) (2005) *Model Validation and the Modelica Language*. 'The 4th International Modelica Conference'. held on 7-8/03/2005 at Hamburg: Modelica

References

- Drogies, S., and Bauer, M. (2000) 'Modeling Road Vehicle Dynamics with Modelica'. in Drogies, S. (ed.) *Proceedings of Modelica Workshop Proceedings*, 'Modelica'. held on 23-24/10/2000 at Lund, 161-168
- ECOpaint (2011) *Common Artemis Driving Cycles (CADC)* [Online] available from <https://www.dieselnet.com/standards/cycles/artemis.php> [2013/12/15]
- Einhorn, M., Conte, F., Kral, C., Niklas, C., Popp, H., and Fleig, J. (2011) 'A Modelica Library for Simulation of Electric Energy Storages'. *Proceedings of the 8th International Modelica Conference*, (8:1), 0-10
- Feroldi, D., and Basualdo, M. (2012) *Description of PEM Fuel Cell System*, Description of PEM Fuel Cell System. London: Springer, 49-72.
- Fiala, E. (1954) 'Seitenkräfte am rollenden Luftreifen'. *VDI-Zeitschrift*, (96:973),
- Forsyth, A., and Mollov, S. (1998) 'Modelling and Control of DC-DC Converters'. *IEE - Power Engineering Journal*, (12:5), 229-236
- Gallo, D., Landi, C., Luiso, M., and Morello, R. (2013) 'Optimization of Experimental Model Parameter Identification for Energy Storage Systems'. *Energies*, (6:9), 4572-4590
- Gamazo-Real, J., Vázquez-Sánchez, E., and Gómez-Gil, J. (2010) 'Position and Speed Control of Brushless DC Motors Using Sensorless Techniques and Application Trends'. *Sensors - Open Access Journal*, (10:1), 6901-6947
- Gillespie, T. (1992) *Fundamentals of Vehicle Dynamics*. Warrendale, PA: Society of Automotive Engineers, Inc.
- Goodwolfe (2014) 'About Microcab Batteries' [Interview by Apicella, M] in n.e. , (2014) *n.b.* London: Goodwolfe Ltd
- Goodwolfe Energy (2012) *X2E 15Ah 40166 Cell Technical Specification* [Online] available from <http://www.goodwolfe.com/documents/GWEX2E15AhCellTechnicalSpecification.pdf> [17/06/2014]

- Google Maps (2015) [Online] available from <https://www.google.com.au/maps/@-23.3394728,150.5201386,12z?hl=en> [01/06/2015]
- Gould, C., Bingham, C., Stone, D., and Bentley, P. (2009) 'New Battery Model and State-of-Health Determination Through Subspace Parameter Estimation and State-Observer Techniques'. *Vehicular Technology, IEEE Transactions*, (58:8), 3905-3916
- Growtham Raj, S., Mahesh Kumar, S., Sakthivel, C., Tamilmaran, R., Saravan, B., and Kondusamy, V. (2016) 'Analysis on Bus Body Aerodynamics & Fuel Efficiency in City Buses'. *IJESC*, (12:6), 3788-3793
- He, H., Xiong, R., Guo, H., and Li, S. (2012) 'Comparison study on the battery models used for the energy management of batteries in electric vehicles'. *The International Renewable Energy Congress - Energy Conversion and Management*, (64:5), 113-121
- Heisler, H. (2002) *Advanced Vehicle Technology*. Oxford: Butterworth-Heinemann
- Hirano, Y., Inoue, S., and Ota, J. (ed.) (2015) *Model Based Performance Development of a Future Small Electric Vehicle using Modelica*. 'Society of Instrument and Control Engineers of Japan (SICE)'. held on 28-30/07/2015 at Hangzhou, China: IEEE
- Honda (2008) *Fuel Cell Evolution* [Online] available from <http://automobiles.honda.com/fcx-clarity/fuel-cell-evolution.aspx> [25/10/2013]
- Horizon Fuel Cell Technologies (2013) *3000W Fuel Cell Stack User Manual* [Online] available from http://resources.arcolaenergy.com/docs/Manuals/Manual_FCS-C3000_V1.1_EN.pdf [15/07/2015]
- Hulsebusch, D., Schwunk, S., Caron, S., and Propfe, B. (2010) *Modeling and Simulation of Electric Vehicles - The Effect of Different Li-Ion Battery Technologies*. Shenzhen: The 25th World Battery, Hybrid and Fuel Cell Electric Vehicle Symposium & Exhibition

References

- Hyundai Motor UK (2016) *Hydrogen Fuel Cell History* [Online] available from <http://www.hyundai.co.uk/about-us/environment/hydrogen-fuel-cell#history> [25/01/2016]
- Johnson Matthey Plc (2013) *History* [Online] available from <http://www.fuelcelltoday.com/history> [25/10/2013]
- Jossen, A. (2005) *Fundamentals of Battery Dynamics*. Germany: Journal of Power Sources
- Jostins, J. (1999) 'Greenheart MicroCab Project - The question of hybrid power: Combining human and electric power in an ultra lightweight vehicle'. in Jostins, J. (ed.) *Proceedings of Assisted Human Powered Vehicles*, 'Future Bike Switzerland'. held on 18/08/1999 at Liestal, 66-93
- Jostins, J. (2017) 'About Microcab and Coventry Univeristy' [Interview by Apicella, M] in n, e. (2017) *n.b.*. Coventry: n.p.
- Kantola, K. (2004) *Hydrogen Fuel Cars 1807 - 1998* [Online] available from <http://www.hydrogencarsnow.com/index.php/1807-1986/> [15/11/2015]
- Kvaser (2014) [Online] available from <http://www.kvaser.com/products/kvaser-memorator-professional-hshs/> [15/07/2015]
- Markel, T., Brooker, A., Hendricks, T., Johnson, V., Kelly, K., Kramer, B., O'Keefe, M., Sprik, S., and Wipke, K. (2002) 'ADVISOR: A Systems Analysis Tool for Advanced Vehicle Modeling'. *ELSEVIER - Journal of Power Sources*, (110:2), 255-266
- McDowall, J. (2014) *A Guide to Lithium-Ion Battery Safety*. SAFT: Battcon
- McPhee, J. (2014) *Multibody System Dynamics: Research Activity* [Online] available from <http://real.uwaterloo.ca/~mbody/#Software> [06/09/2014]
- Microcab Industries ltd (2016) *History: Microcab, life without oil* [Online] available from <http://www.microcab.co.uk/history/> [12/07/2017]

- Microcab Industries ltd (2016) *Home: Microcab, life without oil* [Online] available from <http://www.microcab.co.uk/> [12/7/2017]
- Modelica (2000-2013) *Modelica and the Modelica Association* [Online] available from <https://www.modelica.org/> [25/10/2013]
- Modelica (2013) *Modelica User Guide - Connectors*. Linköping: Modelica
- Modelica Association (2000) *Modelica - A Unified Object-Oriented Language for Physical Systems Modelling*. Linköping: Modelica
- Modelon (2012-2013) *Dymola Success Stories* [Online] available from <http://www.modelon.com/products/dymola/dymola-success-stories/> [28/10/2013]
- Modelon AB (2004-2014) '*Uncoupled Aerodynamics of body front and side*'. [Electronic Source] from Modelon: München
- Morus, I. (2004) 'Grove, Sir William Robert (1811-1896)'. *Oxford Dictionary of National Biography* [Online] 19/08/2004. Available from <https://doi.org/10.1093/ref:odnb/11685> [25/10/2013]
- Muthuvel, A., Murthi, M., Sachin, N., Koshy, V., Sakthi, S., and Selvakumar, E. (2013) 'Aerodynamic Exterior Body Design of Bus'. *International Journal of Scientific & Engineering Research*, (4:7), 2453-2457
- New York State Energy Research and Development Authority (2005) *Hydrogen Fact Sheet* [Online] available from <http://www.fuelcelleducation.org/wp-content/themes/sandbox/pdf/History%20of%20Hydrogen.pdf> [25/10/2013]
- Nissan (2015) [Online] available from http://www.nissan.co.uk/content/dam/services/gb/brochure/Nissan_Leaf.pdf [17/11/2015]
- NREL (2010) *Welcome to SAM* [Online] available from <https://sam.nrel.gov/> [15/12/2013]

References

- Omar, N., Bossche, P., Coosemans, T., and Mierlo, J. (2013) 'Peukert Revisited—Critical Appraisal and Need for Modification for Lithium-Ion Batteries'. *Energies*, (6:11), 5625-5641
- Ommi, F., Pourabedin, G., and Nekofa, K. (2009) 'Evaluation of Model and Performance of Fuel Cell Hybrid Electric Vehicle in Different Drive Cycles'. *World Academy of Science, Engineering and Technology*, (50:2), 582 - 588
- Pacejka, H. (1995) 'The role of tyre dynamic properties, Seminar on Smart Vehicles, Delft'. *Vehicle System Dynamics*, (Special Issue:1), 55-68
- Pacejka, H. (2002) *Tire and Vehicle Dynamics*. Oxford: Elsevier Science
- Pacejka, H. (2006) *Tire and Vehicle Dynamics*. Oxford: Elsevier
- Pacejka, H. (2012) *Tire and Vehicle Dynamics*. Oxford: Elsevier
- Pacejka, H., and Bakker, E. (1992) 'The Magic Formula Tyre Model'. *Vehicle Systems Dynamics*, (21:1), 1-18
- Pacejka, H., and Besselink, I. (1997) 'Magic Formula tyre model with transient properties'. *Vehicle System Dynamics*, (27:1), 145-155
- Pacejka, H., and Sharp, R. (1991) 'Sheer force generation by pneumatic tyres in steady state conditions: A review of modelling aspects'. *Vehicle System Dynamics*, (20:1), 121-176
- PLANET GbR (2013) *SWARM* [Online] available from <http://swarm-project.eu/home.html> [25/10/2013]
- Pop, O., and Lungu, S. (2010) *Modelling of DC-DC Converters*, Modelling of DC-DC Converters. Rijeka: Sciyo, 125-150.
- Race Technology (2014) *DL1 MK3/Club Hardware Help Map* [Online] available from <http://www.race-technology.com/wiki/index.php/Hardware/DL1MK3> [15/07/2015]

- Raga, C., Barrado, A., Lázaro, ., Fernández, C., Valdivia, V., and Quesada, I. (2012) 'Black-Box Model and Identification Methodology for PEM Fuel Cell with Overshooting Transient Response'. *IEEE: Energy Conversion Congress and Exposition*, (29:10), 3168-3174
- Raga, C., Barrado, A., Lazaro, A., Fernandez, C., Valdivia, V., Quesada, I., and Gauchia, L. (2014) 'Black-Box Model, Identification Technique and Frequency Analysis for PEM Fuel Cell with Overshoot Transient Response'. *IEEE Transactions on Power Electronics*, (29:10), 5334 - 5346
- Rendus, C. (1839) ' Weekly reports of the sessions of the Academy of Sciences / published by MM. perpetual secretaries'. *Gallica: Academy of Sciences (France)* [Online] 06/01/1839. Available from <http://gallica.bnf.fr/ark:/12148/bpt6k2967c/f503.table> [25/10/2013]
- Ryan, D., Shang, J., Quillivic, C., and Porter, B. (ed.) (2014) *Performance and Energy Efficiency Testing of a Lightweight FCEV Hybrid Vehicle*. 'European Electric Vehicle Congress'. held on 3-5/12/2014 at Brussels, Belgium: EEEV
- Senger, R. (1997) *Validation of ADVISOR as a Simulation Tool for a Series Hybrid Electric Vehicle Using the Virginia FutureCar Lumina*. Virginia: SAE
- Shepherd, C. (1965) 'Design of Primary and Secondary Cells'. *Journal of the Electrochemical Society*, (112:1), 657-664
- Sherman, D. (2014) 'Drag Queens: Five Slippery Cars Enter a Wind Tunnel; One Slinks Out A Winner'. *Tesla* [Online] n.d./06/2014. Available from https://www.tesla.com/sites/default/files/blog_attachments/the-slipperiest-car-on-the-road.pdf [15/07/2016]
- Simic, D., Dvorak, D., Lacher, H., and Kuehnelt, H. (2014) *Modeling and Validation of Lithium-ion Battery Based on Electric Vehicle Measurement*. Technical Paper 1850: SAE
- Sira-Ramires, H., and Silva-Ortigoza, R. (2006) *Control Design Techniques in Power Electronic Devices*. London: Springer-Verlag London

References

- Sira-Ramirez, H., and Silva-Ortigoza, R. (2006) *Modelling of DC-to-DC Power Converters*, Modelling of DC-to-DC Power Converters. London: Springer-Verlag, 11 - 58.
- Souleman, N., Tremblay, O., and Dessaint, L. (ed.) (2009) *A Generic Fuel Cell Model for the Simulation of Fuel Cell Vehicles*. 'Vehicle Power Propulsion Conference'. held on 7-10/09/2009 at Dearborn, MI: IEEE
- Spotnitz, R. (2005) *Battery Modeling*. California: The Electrochemical Society
- Thanheiser, A., Kohler, T., and Herzog, H. (2012) 'Virtual Electric Vehicle Design using Real-World Coupled Realtime Simulation'. *World Electric Vehicle Journal*, (5:1), 51-57
- The Hydrogen Bubble (2012) *Hydrogen: Moving into the present* [Online] available from <http://thehydrogenbubble.blogspot.com/> [23/11/2013]
- TNO Automotive (2008) 'User Manual'. *MF-Tyre & MF-Swift 6.1* [Online] 08/02/2008. Available from <https://www1.ethz.ch/biomed.ee/intranet/support/madymo/Tyremodels.pdf> [13/05/2014]
- Toyota Motor Corporation (2016) *FCV Fuel Cell Vehicle* [Online] available from http://www.toyota-global.com/innovation/environmental_technology/fuelcell_vehicle/ [26/01/2016]
- Tremblay, O., and Dessaint, L. (2009) 'Experimental Validation of a Battery Dynamic Model for EV Applications'. *World Electric Vehicle Journal*, (3:1), 1-41
- Tremblay, O., Dessaint, L., and Dekkiche, A. (ed.) (2007) *A Generic Battery Model for the Dynamic Simulation of Hybrid Electric Vehicles*. 'Vehicle Power and Propulsion Conference'. held on 9-12/09/2007 at Arlington: IEEE
- Tsinias, V. (2014) *A Hybrid Approach to Tyre Modelling based on Modal Testing and Non-Linear Tyre-Wheel Motion*. Loughborough: Loughborough University

- Ural, Z., and Gencoglu, M. (ed.) (2010) *Mathematical Models of PEM Fuel Cells*. '5th International Ege Energy Symposium and Exhibition'. held on 27-30/06/2010 at Denizli, Turkey: IESE-5
- Verbugge, B., Heremans, Y., Van Mulders, F., Culcu, H., Van den Bossche, P., and Van Mierlo, J. (2009) 'Modelling the RESS: Describing Electrical Parameters of Batteries and Electric Double-Layer Capacitors through Measurements'. *World Electric Vehicle Journal*, (3:1), 803-811
- Vock, C., Hubel, J., Tsokolis, D., Samaras, C., Ntziachristos, L., Tola, R., Ricci, C., and Samaras, Z. (2014) *Deliverable D.3.2: Report on the Development and Use of the Vehicle Energy/Emission Simulator*. Thessaloniki: ICT-EMISSIONS Consortium
- Wang, C., Nehrir, M., and Shaw, S. (2005) 'Dynamic Models and Model Validation for PEM Fuel Cells Using Electrical Circuits'. *IEEE Transactions on Energy Conversion*, (20:2), 442-451
- Wipke, K., Cuddy, M., Bharathan, D., Burch, S., Johnson, V., Markel, A., and Sprik, S. (1999) *Advisor 2.0: A Second-Generation Advanced Vehicle Simulator for Systems Analysis*. Cole Boulevard, Golden, Colorado 80404-3393: National Renewable Energy Laboratory
- Woodward (2015) *MotoHawk Control Solutions ECM-5554-112-0904-C/F*. Fort Collins: Woodward
- Zhang, H., and Chow, M. (ed.) (2010) *Comprehensive Dynamic Battery Modeling for PHEV Applications*. 'Power and Energy Society General Meeting'. held on 25-29/07/2010 at Providence: IEEE
- Zupančič, B., and Sodja, A. (2013) 'Computer-Aided Physical Multi-Domain Modelling: Some Experiences from Education and Industrial Applications'. *Elsevier - Simulation Modelling Practice and Theory*, (33:1), 45-67

APPENDICES

APPENDIX A – Model Data

Table 8-1 - Model Data, Steering Geometry

Dymola Parameter	Description	Coventry University Microcab H2EV Values
r0R_1[3]	Position of left rack end, resolved in vehicleFrame [m]	{-0.117, 0.4, 0.191}
r0R_2[3]	Position of right rack end, resolved in vehicleFrame [m]	{-0.117, -0.4, 0.191}
r0PR[3]	Position of pinion-rack center rotation center (gear wheel center), resolved in vehicleFrame [m]	{-0.117, 0, 0.191}
r0PZ[3]	Position of lower steering column joint, resolved in vehicleFrame [m]	{-0.217, 0.3, 0.25}
r0QZ[3]	Position of upper steering column joint, resolved in vehicleFrame [m]	{-0.517, 0.3, 0.35}
r0Q[3]	Position of steering wheel centre, resolved in vehicleFrame [m]	{-0.617, 0.3, 0.35}
iPR	Ratio from pinion to rack (effective pinion radius) [m/rad] [m]	-0.0075

Table 8-2 - Model Data, Front Suspension Geometry

Dymola Parameter	Description	Coventry University Microcab H2EV Values
r0H[3]	Position of hub centre, resolved in vehicle frame [m]	{0, 0.688, 0}
r0X[3]	Position of origin of steerLinkFrame, resolved in vehicleFrame [m]	{-0.117, 0.4, 0.05}
r0A[3]	Position of origin of stabilizerFrame, resolved in vehicleFrame [m]	R0H
r0CL1[3]	Position of front link mount in chassis, resolved in vehicleFrame [m]	{0.068, 0.231, -0.091}
r0CL2[3]	Position of rear link mount in chassis, resolved in vehicleFrame [m]	{-0.208, 0.231, -0.082}
r0CS[3]	Position of spring mount in chassis, resolved in vehicleFrame [m]	{-0.032, 0.517, 0.503}
r0CD[3]	Position of strut/damper mount in chassis, resolved in vehicleFrame [m]	R0CS
r0SU[3]	Position of spring mount in upright, resolved in vehicleFrame [m]	{0, 0.596, 0}
r0DU[3]	Position of damper mount in upright, resolved in vehicleFrame [m]	R0SU
r0L1L2U[3]	Position of upright-strut joint, resolved in vehicleFrame [m]	{0.009, 0.619, -0.146}
r0L3X[3]	Position of steer link inner joint, resolved in vehicleFrame [m]	R0X

r0L3U[3]	Position of outer ball of steering rod, resolved in vehicleFrame [m]	{-0.105, 0.536, 0.05}
----------	--	-----------------------

Table 8-3 - Model Data, Rear Suspension Geometry

Dymola Parameter	Description	Coventry University Microcab H2EV Values
r0H_1[3]	Position of left hub centre, resolved in vehicleFrame [m]	{2.157,0.653,0}
r0L2U_1[3]	Position of left link attachment to upright, resolved in vehicleFrame [m]	{2.150,0.553,0}
r0CL2_1[3]	Position of left link attachment to chassis, resolved in vehicleFrame [m]	{1.740,0.577,0.042}
r0L1L2_1[3]	Position of left twist beam, resolved in vehicleFrame [m]	{2.09,0.62,0}
r0SU_1[3]	Position of left spring mount in upright, resolved in vehicleFrame [m]	{2.186,0.579,-0.106}
r0DU_1[3]	Position of left damper mount mount in upright, resolved in vehicleFrame [m]	{2.186,0.579,-0.106}
r0CS_1[3]	Position of left spring mount in chassis, resolved in vehicleFrame [m]	{2.01,0.517,0.256}
r0CD_1[3]	Position of left damper mount in chassis, resolved in vehicleFrame [m]	{2.01,0.517,0.256}
r0H_2[3]	Position of right hub centre, resolved in vehicleFrame [m]	{2.157,-0.653,0}
r0L2U_2[3]	Position of right link attachment to upright, resolved in vehicleFrame [m]	{2.150,-0.553,0}
r0CL2_2[3]	Position of right link attachment to chassis, resolved in vehicleFrame [m]	{1.740,-0.577,0.042}
r0L1L2_2[3]	Position of right twist beam, resolved in vehicleFrame [m]	{2.09,-0.62,0}
r0SU_2[3]	Position of right spring mount in upright, resolved in vehicleFrame [m]	{2.186,-0.579,-0.106}
r0DU_2[3]	Position of right damper mount mount in upright, resolved in vehicleFrame [m]	{2.186,-0.579,-0.106}
r0CS_2[3]	Position of right spring mount in chassis, resolved in vehicleFrame [m]	{2.01,-0.517,0.256}
r0CD_2[3]	Position of right damper mount in chassis, resolved in vehicleFrame [m]	{2.01,-0.517,0.256}

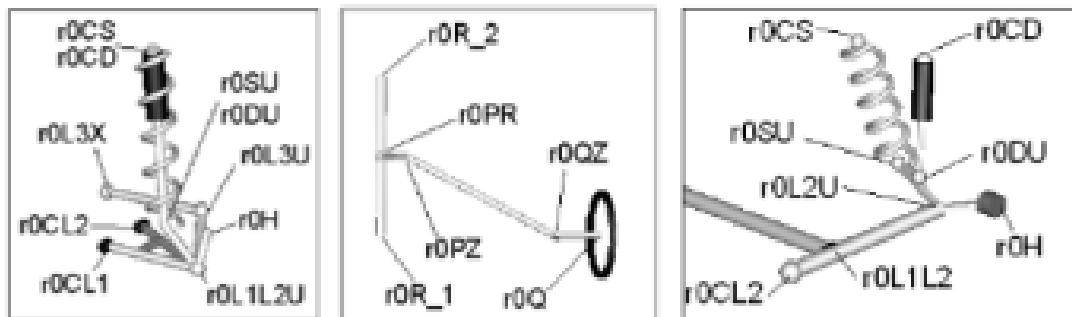


Figure 8-1 - Suspension Nomenclature (Dassult Systems 2002-2013)

Table 8-4 - Model Data, Component Centre of Mass

Vehicle Components, Reference to Front of Body							
Component Description	Mass	Centre of Mass About the Global Coordinate System			Centre of Mass About the Front Centre Axle		
	(kg)	X (mm)	Y (mm)	Z (mm)	X (mm)	Y (mm)	Z (mm)
Exterior							
Roof	38.9	2220	0	1233	1325	0	1136
Rear Left Hand Window	1.5	2849	-586	1175	1954	-586	1078
Rear Right Hand Window	1.5	2849	586	1175	1954	586	1078
Boot Outer	10	3485	-8	910	2590	-8.6	813
Boot Inner	11	3441	0	892	2546	0	795
Boot Window	5	3439	0	1162	2544	0	1065
Boot Inner Cover Panel	2.1	3483	0	620	2588	0	523
Rear Right Hand Outer Body	16.5	2494	681	492	1599	681	395
Rear Left Hand Outer Body	16.5	2494	-681	492	1599	-681	395
Rear Bumper Surround	8.1	3544	0	298	2649	0	201
Front Right Side Small Glass	1.1	1348	-649	954	453	-649	857
Front Left Side Small Glass	1.1	1348	649	954	453	649	857
Front Sealing Panel	3.9	972	0	785	77	0	688
Front Clip	25.2	660	0	445	-234	0	348
Bonnet Cover	0.8	558	0	696	-336	0	599
Windscreen	8	1226	0	1096	331	0	999
Rear Bumper Centre	1.5	3529	4	62	2635	4	-34
Interior Assembly (Upper)							
Front Interior Header	3.8	1780	0	1366	885	0	1269
Fuel Filler Bucket	3	2750	683	658	1856	683	561
Front Head Lining	0.5	2221	0	1450	1327	0	1353
Rear Head Lining	0.55	2857	0	1441	1963	0	1344
Interior Roof Trim	20.4	2283	0	1145	1389	0	1048
Middle Interior Header	1.5	2522	0	1463	1627	0	1366
Rear Interior Header	1.1	3155	0	1414	2260	0	1317
Front Centre Roof Console	0.2	1781	0	1346	887	0	1249
Interior Assembly (Lower)							
Boot Closure Panel	2	3509	0	439	2614	0	342
Dashboard Bracket FWD	1.5	1289	0	749	394	0	652
Dashboard Bracket RWD	0.8	1406	0	772	511	0	675
Dashboard Recess LHS	0.6	1262	-396	773	367	-396	676
Dashboard Recess RHS	0.6	1222	494	779	328	494	682
Dashboard Support	0.8	1130	-100	478	236	-100	381
Driver Instrument Cover	0.3	1360	310	856	465	310	759

Driver Instrument Inner	0.2	1399	311	832	504	311	735
Dashboard	6	1285	-8	750	390	-8	653
Fuse Box + Bracket	6	1240	-381	662	346	-381	565
H2 Inlet Pipe Cover	0.3	2725	632	514	1830	632	417
Interior Rear LHS Cover	0.8	2954	-567	653	2060	-567	556
Interior Rear RHS Cover	0.8	2954	567	653	2060	567	556
Rear Quarter Trim LHS	0.25	2485	-611	272	1591	-611	175
Rear Quarter Trim RHS	0.25	2485	611	272	1591	611	175
Rear LHS Wheel Arch Cover	1.7	3025	-613	460	2131	-613	363
Rear RHS Wheel Arch Cover	1.7	3025	613	460	2131	613	363
Front LHS Seat Plinth	6	1881	-308	279	986	-308	182
Front RHS Seat Plinth	6	1881	308	279	986	308	182
Rear LHS Seat Plinth	0.8	2792	-422	418	1898	-422	321
Rear RHS Seat Plinth	0.8	2792	422	418	1898	422	321
Doors							
LHS Door	25	1987	-651	657	1093	-651	560
RHS Door	25	1987	651	657	1093	651	560
Chassis							
Chassis + Subframe	325	1950	46	315	1056	46	218
Fuel Cell Splash Guard	4	3306	0	109	2412	0	12
Front Clip Floor	0.3	558	0	119	-335	0	22
Front LHS Filler Cover	0.1	1060	-675	659	166	-675	562
Front RHS Filler Cover	0.1	1060	675	659	166	675	562
Front LHS Wheel Arch Cover	0.15	687	-518	543	-206	-518	446
Front RHS Wheel Arch Cover	0.15	687	518	543	-206	518	446
Front LHS Shell	2.5	676	-368	329	-218	-368	232
Front RHS Shell	2.5	676	368	329	-218	368	232
Lower Floor Covers	5	1921	0	-1	1026	0	-98
Tank	15	1914	0	320	1019	0	222
Electronics							
Fuel Cell	35	3224	0	200	2329	0	103
Battery	75	1760	0	10	865	0	-87
DCDC Board	10	1774	-463	10	879	-463	-87
Suspension							
Rear Swinging Arm	10	2960	0	33	2065	0	-63
Wheel Hub LHS	0.9	3050	-680	97	2156	-680	0.8
Wheel Hub RHS	0.9	3050	-680	97	2156	-680	0.8
Front Lower Wishbone LHS	0.6	966	-393	27	71	-393	-69
Front Lower Wishbone RHS	0.6	966	393	27	71	393	-69
Rear LHS Wheel	10	3051	-653	97	2157	-653	0
Rear RHS Wheel	10	3051	653	97	2157	653	0
Front LHS Wheel	10	894	-653	97	0	-653	0
Front RHS Wheel	10	894	653	97	0	653	0

APPENDICES

APPENDIX B – Model Code

Battery Dymola Code

```
class shepherds_Battery_Model

// import Modelica.Electrical.Analog.Interfaces.OnePort;
  extends Modelica.Electrical.Analog.Interfaces.OnePort;

  parameter Real SOC_start = 1 "Start State of Charge of the battery [%]" annotation(Dialog(group="Battery Start Conditions"));
  parameter Real ns = 24 "Number of cells connected in series in a battery pack" annotation(Dialog(group="Battery Voltage Parameters"));
  parameter Real np = 4 "Number of cells connected in Parallel in a battery pack" annotation(Dialog(group="Battery Voltage Parameters"));
  parameter Modelica.SIunits.Voltage Vmax = 3.65 "Maximum cell voltage at fully charged [V]" annotation(Dialog(group="Battery Voltage Parameters"));
  parameter Modelica.SIunits.Voltage Vexp = 3.3 "Start of constant cell voltage at fully charged [V]"
    annotation(Dialog(group="Battery Voltage Parameters"));
  parameter Modelica.SIunits.Voltage Vcon = 3 "End of const cell voltage at fully charged [V]" annotation(Dialog(group="Battery Voltage Parameters"));
  parameter Modelica.SIunits.Voltage Vmin = 2 "Minimum cell voltage [V]" annotation(Dialog(group="Battery Voltage Parameters"));
  parameter Modelica.SIunits.Current Qcell = 13.2 "Capacity of a Cell [Ah]" annotation(Dialog(group="Battery Voltage Parameters"));
  parameter Modelica.SIunits.Resistance D = 0.0038 "Resistance which creates the Base Drop in Voltage Regardless of the Current, SOC Dependant[Ohm]"
    annotation(Dialog(group="Battery Voltage Parameters"));
  parameter Modelica.SIunits.Resistance Rc = 0.01268 "Cell Normal Charge Resistance [Ohm]" annotation(Dialog(group="Battery Voltage Parameters"));
  parameter Modelica.SIunits.Resistance Rd = 0.00800 "Cell Normal Discharge Resistance [Ohm]" annotation(Dialog(group="Battery Voltage Parameters"));
  parameter Modelica.SIunits.Resistance Bd = 55 "Resistance which creates the speed of the exponential Drop in Voltage at fully charged [Ohm]"
    annotation(Dialog(group="Battery Voltage Parameters"));
  parameter Modelica.SIunits.Resistance Bc = 0.3 "Resistance which creates the speed of the exponential Rise in Voltage at fully charged [Ohm]"
    annotation(Dialog(group="Battery Voltage Parameters"));
  parameter Real Ts = 0.3 "Time response of the battery [s]" annotation(Dialog(group="Battery Voltage Parameters"));

  parameter Real MaxsocEff=0.9998 "Point at which Efficiency reaches its lowest [SOC %]" annotation(Dialog(group="Battery Charge Efficiency Parameters"));
  parameter Real MinsocEff=0.9275 "Point at which Efficiency Started to reduce [SOC %]" annotation(Dialog(group="Battery Charge Efficiency Parameters"));
  parameter Real MaxEff = 1 "Maximum Coulombic Efficiency of the cell [%]" annotation(Dialog(group="Battery Charge Efficiency Parameters"));
  parameter Real MinEff = 0.005 "Minimum Coulombic Efficiency of the cell [%]" annotation(Dialog(group="Battery Charge Efficiency Parameters"));

  Modelica.SIunits.Current ibatt "Current seen at the terminal [A]";
  Modelica.SIunits.Current ifilt "Slow Current Dynamics [A]";
  Modelica.SIunits.Current Qit "Fast Current Count [A]";
  Modelica.SIunits.Current Qil "Slow Current Count [A]";
  Modelica.SIunits.Current Q "Equilvant SOC [A]";
  Modelica.SIunits.Current Qcell_start "Capacity of a Cell [Ah]";
  Real SOC "State of Charge of the battery [0-1]";
  Real SOC_pcmt "State of Charge of the battery [%]";
  Modelica.SIunits.Voltage Ac "Change in Cell Voltage to Full Chare From Const V [V]";
  Modelica.SIunits.Voltage Ad "Change in Cell Voltage to Const V From Full Charge [V]";
  Modelica.SIunits.Voltage E0c "Base Voltage Along Curve [V]";
  Modelica.SIunits.Voltage E1c "Exponential Voltage Representation at Full Charge d [V]";
```

```

Modelica.SIunits.Voltage E2c "Voltage Representation for both Charge and Discharge [V]";
Modelica.SIunits.Voltage E3c "Voltage Representation for both Charge and Discharge [V]";
Modelica.SIunits.Voltage E4c "Voltage Representation for both Charge and Discharge [V]";
Modelica.SIunits.Voltage E0d "Voltage Representation for both Charge and Discharge [V]";
Modelica.SIunits.Voltage E1d "Voltage Representation for Charge Dynamics [V]";
Modelica.SIunits.Voltage E2d "Voltage Representation for Discharge Dynamics [V]";
Modelica.SIunits.Voltage E3d "Voltage Representation for Discharge Dynamics [V]";
Modelica.SIunits.Voltage E4d "Voltage Representation for Discharge Dynamics [V]";
Modelica.SIunits.Voltage vcellc "Cell Voltage During Charge [V]";
Modelica.SIunits.Voltage vcelld "Cell Voltage During Discharge [V]";
Modelica.SIunits.Voltage vcell "Cell Voltage [V]";

Modelica.SIunits.Voltage vbasec "Base Cell Voltage During Charge [V]";
Modelica.SIunits.Voltage vbased "Base Cell Voltage During Discharge [V]";
Modelica.SIunits.Voltage vbase "Base Cell Voltage [V]";

Modelica.SIunits.Voltage vdync "Dynamic Part of the Cell Voltage During Charge [V]";
Modelica.SIunits.Voltage vdynd "Dynamic Part of the Cell Voltage During Discharge [V]";
Modelica.SIunits.Voltage vdyn "Dynamic part of the Cell Voltage [V]";
Real CoolEff "Coloumbic Charge Efficiency";
Real socEffRange = MaxsocEff - MinsocEff "Used to parameterise the Coloumbic Charge Efficiency";
Real CoolEffRange = MinEff - MaxEff "Used to parameterise the Coloumbic Charge Efficiency";
Real Effm = CoolEffRange/socEffRange "Used to parameterise the Coloumbic Charge Efficiency";
Real Effb = MinEff - (Effm*MaxsocEff) "Used to parameterise the Coloumbic Charge Efficiency";
initial equation
  Qil = Qcell*(1-SOC_start);
  ifilt = -i/np;
  Q = (SOC_start*Qcell);

equation
  Ac = ((Vmax - Vexp));
  Ad = ((Vmax - Vcon));
  Qcell_start = Qcell*(1-SOC_start);
  ibatt = (-i)/np;
  der(ifilt) = (-1 / ((Ts*np)/ns) * ifilt) + ibatt / ((Ts * np)/ns);
  der(Qit) = smooth(10,noEvent(if noEvent(ibatt<=0) then (ibatt*CoolEff)/3600 else ibatt/3600));
  der(Qil) = smooth(10,noEvent(if noEvent(ifilt<=0) then (ifilt*CoolEff)/3600 else ifilt/3600));
  Q = Qcell - Qit;
  SOC = smooth(0,noEvent(if noEvent((Q/Qcell) <= 0) then 0 elseif noEvent((Q/Qcell) >= 1) then 1 else (Q/Qcell)));
  SOC_pcmt = SOC*100;
  CoolEff = smooth(0,noEvent(if noEvent(SOC*Effm + Effb>=MaxEff) then MaxEff elseif noEvent(SOC*Effm + Effb<=MinEff) then MinEff else SOC*Effm + Effb));

  E0c = Vexp;
  E1c = (Ac * exp((-Bc)*Qil));
  E2c = ((-D) * ((Qcell)/(Q+Qmod))*Qit);
  E3c = ((-(Rc*0.2)) * ifilt * (Qcell / (Q+Qcell)));
  E4c = ((-(Rc*0.8)) * ibatt * (Qcell / (Q+Qcell)));
  vbasec = E0c + E1c + E2c;
  vdync = E3c + E4c;
  vcellc = vbasec + vdync;

  E0d = Vexp;
  E1d = (Ad * exp((-Bd)*Qil));
  E2d = ((-D) * ((Qcell)/(Q))*Qit);
  E3d = ((-(Rd*0.2)) * ifilt * (Qcell / (Q+Qcell)));

```

APPENDICES

```
E4d      = ((-Rd*0.8)) * ibatt *(Qcell / (Q+Qcell));
vbased   = E0d + E1d + E2d;
vdynd    = E3d + E4d;
vcellld  = vbased + vdynd;

vdyn      = smooth(10000,noEvent(if noEvent(ibatt <=0) then vdynd else vdynd)
);
vbase     = smooth(10000,noEvent(if noEvent(ibatt <=0) then vbasec else vbase
d));

vcell     = vbase + vdyn;
v         = vcell*ns;

end shepherds_Battery_Model;
```

Fuel Cell Dymola Code

```
model FC_Electrical_Model
```

```
Modelica.Blocks.Interfaces.RealOutput Voltage annotation(Placement(transformati
on(extent = {{-96, -60}, {-116, -40}}), iconTransformation(extent = {{-96, -
60}, {-116, -40}})));
Modelica.Blocks.Interfaces.RealOutput Current annotation(Placement(transformati
on(extent = {{-96, -10}, {-116, 10}})));
Modelica.Blocks.Interfaces.RealOutput FCPower annotation(Placement(transformati
on(extent={{100,20},
{120,40}}), iconTransformation(extent={{100,20},{120,40}})));
Modelica.Blocks.Interfaces.RealOutput FC_Temperature_Out annotation(Placement(t
ransformation(extent = {{-96, 40}, {-116, 60}}), iconTransformation(extent = {{-
96, 40}, {-116, 60}})));
Modelica.Blocks.Interfaces.RealInput Fan_Speed annotation (Placement(transforma
tion(extent={{114,-50},{94,-30}})));

inner parameter Modelica.SIunits.Temperature T_START = 299.1 annotation(Dialog(
group="Start Condition"));
parameter Real ns(min = 1) = 70 "Number of Cells in the Fuel Cell" annotation(D
ialog(group="FC Voltage Parameters"));
parameter Modelica.SIunits.ReflectionCoefficient S1 = 1.215822336 "Parametric C
oefficient V"
annotation(Dialog(group="FC Voltage Parameters"
));
parameter Modelica.SIunits.ReflectionCoefficient S2 = 0.043701839 "Parametric C
oefficient V" annotation(Dialog(group="FC Voltage Parameters"));
parameter Modelica.SIunits.ReflectionCoefficient S3 = -
0.003010883 "Parametric Coefficient V" annotation(Dialog(group="FC Voltage Parame
ters"));
parameter Modelica.SIunits.ReflectionCoefficient S4 = 0.012283769 "Parametric C
oefficient V" annotation(Dialog(group="FC Voltage Parameters"));
parameter Real X(min = 0, max = 22, start = 14) = 14 "Water Content in the Memb
rane" annotation(Dialog(group="Chemistry Based Parameters"));
parameter Modelica.SIunits.Pressure Pcath(min=100000,max=300000, start = 149961
) = 294996 "Pressure at Cathode" annotation(Dialog(group="Chemistry Based Paramet
ers"));
parameter Modelica.SIunits.Pressure Panode(min=100000,max=300000, start = 14996
1) = 149961 "Pressure at Anode" annotation(Dialog(group="Chemistry Based Paramete
rs"));
parameter Real Po2(start=-19.4943) = Pcath * (1 - X) / 100000 "Pcath*(1-
X)" annotation(Dialog(group="Chemistry Based Parameters"));
parameter Real Ph2 = Panode * (1 - 0.5 * X) / 100000 "Panode*(1-
0.5*X)" annotation(Dialog(group="Chemistry Based Parameters"));
Electronics_2017.Fuel_Cell.Fuel_Cell_Electrical.Internal.ConcentrationMolarDen
sity
Co2 "Concentration of Oxygen Dissolved in Water";
parameter Modelica.SIunits.Length i = 0.00015 "Thickness of Membrane cm" annota
tion(Dialog(tab = "Membrane Dimensions"));
parameter Modelica.SIunits.Length h = 0.049 "Thickness of Membrane cm" annotati
on(Dialog(tab = "Membrane Dimensions"));
parameter Modelica.SIunits.Length w = 0.042 "Thickness of Membrane cm" annotati
on(Dialog(tab = "Membrane Dimensions"));
parameter Modelica.SIunits.Area A = h * w "Area of the Active Membrane" annotat
ion(Dialog(tab = "Membrane Dimensions"));
```

```

parameter Modelica.SIunits.Resistance Rc = 0.000150367 "Resistance to the Transfer of Protons Through Membrane" annotation(Dialog(group="FC Voltage Parameters"));
parameter Modelica.SIunits.Voltage B = -1.022966863 "Parametric Coefficient V" annotation(Dialog(group="FC Voltage Parameters"));
parameter Modelica.SIunits.Current Imax = 90 "Max Admissable Current from Fuel Cell" annotation(Dialog(group="FC Voltage Parameters"));
parameter Modelica.SIunits.CurrentDensity Jmax = 690 "Max Current Density of Cell" annotation(Dialog(group="FC Voltage Parameters"));
parameter Modelica.SIunits.Power Fan_Power = 800 "Max Power of FC Fan" annotation(Dialog(group="Fan Parameters"));
parameter Real Fan_eff = 0.75 "Efficiency of FC Fan" annotation(Dialog(group="Fan Parameters"));

Real Qcreated "Heat Generated W";
Real J;
Real rm;
Real Rm;
Real Nohm;
Real Ncon;
Real Nact;
Real Ndiff;
Real Enerst;
Real OCV;
Real Vcell;
Real Vfc;
Modelica.SIunits.Current I_FC;
Modelica.SIunits.Current I1;
Modelica.SIunits.Power Fan_Q_Flow "Heat Removed by Fan";
extends Electronics_2017.Fuel_Cell.Fuel_Cell_Electrical.Internals.Components.Element1D(
  useHeatPort=true, T=T_START);
extends Electronics_2017.Fuel_Cell.Fuel_Cell_Electrical.Internals.Components.FCOnePort;
Modelica.SIunits.Temperature T_temp(start = T_START) "Temperature of the FC";
protected
  Modelica.SIunits.Length il;
  Modelica.SIunits.Length hl;
  Modelica.SIunits.Length wl;
  Modelica.SIunits.Area A1;
  Real J1max;
initial equation
  Qcreated = 0;
equation
  Co2 = Po2 / (5080000 * exp(-498 / T_temp));
  T_temp = FC_Temperature_Out;
  i1 = i * 100;
  hl = h * 100;
  wl = w * 100;
  A1 = hl * wl;
  J1max = Jmax / 1000;
  J = if I_FC <= 0 then 0 else if I_FC / Imax * J1max >= J1max then J1max else I_FC / Imax * J1max;
  rm = 181.6 * (1 + 0.03 * (J / J1max) + 0.062 * (T_temp / 303) ^ 2 * ((abs(I_FC) + 0.01) / A1) ^ 2.5) / ((X - 0.634 - 3 * ((abs(I_FC) + 0.01) / A1)) * exp(4.18 * ((T_temp - 303) / T_temp)));
  Rm = rm * i1 / A1;
  Nohm = I_FC * (Rm + Rc);
  Ncon = -B * (1 - J / J1max);
  Nact = if I_FC <= 0.001 then (-S1) + S2 * T_temp + S3 * T_temp * log(abs(Co2)) else (-S1) + S2 * T_temp + S3 * T_temp * log(abs(Co2)) + S4 * T_temp * log(abs(I_FC));
  Ndiff = 2 * (1 - exp(I_FC - Imax)) - abs(1 - exp(I_FC - Imax));
  Enerst = 1.229 - 0.00085 * (T_temp - 298.15) + 0.0000431 * T_temp * (log(abs(Ph2)) + 0.5 * log(abs(Po2)));
  OCV = Enerst * ns;
  Vcell = if I_FC >= Imax then 0 else if (Enerst * ns - Nohm - Ncon - Nact - Ndiff) / ns <= 0 then 0 else (Enerst * ns - Nohm - Ncon - Nact - Ndiff) / ns;
  Vfc = Vcell * ns;
  Vfc = p.v;
  Voltage = p.v;

```

APPENDICES

```
I_FC = if I1 <= 0.001 then 0.001 else I1;
I1 = -I;
der(Qcreated) = ns * (1.253 - Vcell) * I_FC / 3600;
der(Fan_Q_Flow) = (Fan_eff*((-Fan_Power)*Fan_Speed));
LossPowera = Qcreated+Fan_Q_Flow;
FC_Temperature_Out = T_heatPorta;
Current = I1;
FCPower = Voltage * Current;

end FC_Electrical_Model;
```

Motor Model

```
model EMF_Motor_Model

Modelica.Mechanics.Rotational.Interfaces.Flange_b flange
  annotation (Placement(transformation(extent={{80,-10},{100,10}})));
Modelica.Mechanics.Rotational.Interfaces.Support support
  annotation (Placement(transformation(extent={{-10,-100},{10,-80}})));
Modelica.SIunits.AngularVelocity w;
Modelica.SIunits.Angle phi;
Modelica.SIunits.Torque tau;
Modelica.Electrical.Analog.Interfaces.PositivePin p
  annotation (Placement(transformation(extent={{-100,40},{-80,60}})));
Modelica.Electrical.Analog.Interfaces.NegativePin n
  annotation (Placement(transformation(extent={{-100,-60},{-80,-40}})));
Modelica.SIunits.Voltage v;
Modelica.SIunits.Current i;
Real RPM;
Modelica.SIunits.Power MotorOutPower;
Modelica.SIunits.Power MotorInPower;
Modelica.SIunits.Current imotor;
Modelica.SIunits.Current imotort;
Modelica.SIunits.Current imotormax;
Modelica.SIunits.Current imotorbrakemax;
Modelica.SIunits.Voltage vmotor;
Modelica.SIunits.Voltage vshunt;
Real SpeedK;
Modelica.SIunits.Current ifan;
parameter Real Max_RPM = 3955;
parameter Real Rated_Speed = 3600;
parameter Modelica.SIunits.Voltage nominalV = 72;
parameter Modelica.SIunits.Current MaxMotorCurrent = 400;
parameter Modelica.SIunits.Torque MaxMotorTorque = 68;
parameter Modelica.SIunits.Power FanPower=270;
parameter Modelica.SIunits.Current RegenCurrent = 30;

Real RegenDrop;
Real TConst;
Modelica.SIunits.Power Pfan;
Real Efficiency;
Modelica.Blocks.Interfaces.RealInput Throttle
  annotation (Placement(transformation(
    extent={{-20,-20},{20,20}},
    rotation=-90,
    origin={60,80})));
Modelica.Blocks.Interfaces.RealInput Max_I annotation (Placement(transformation
(
  extent={{-20,-20},{20,20}},
  rotation=-90,
  origin={0,80})));
Modelica.Blocks.Interfaces.RealOutput Current annotation (Placement(transformat
ion(
  extent={{20,20},{-20,-20}},
  rotation=-90,
  origin={-60,80})));
Modelica.Blocks.Interfaces.RealInput Brake annotation (Placement(
  transformation(
    extent={{-20,-20},{20,20}},
    rotation=180,
    origin={80,40})));
equation
  phi = flange.phi - support.phi;
```

```

w = der(phi);
RPM = w * 9.5493;
flange.tau = -tau;
support.tau = tau;
0 = p.i+n.i;
v = p.v-n.v;
i = p.i;
TConst = MaxMotorTorque/MaxMotorCurrent;
tau = imotor*TConst;
MotorOutPower = (tau*RPM)/9.5488;
MotorInPower = (imotort)*vmotor;
MotorInPower = v * i;
imotormax = if noEvent(((MaxMotorTorque-(exp((RPM-
Max_RPM)/1000)*MaxMotorTorque))/TConst)*Throttle>=MaxMotorCurrent) then MaxMotorC
urrent else ((MaxMotorTorque-(exp((RPM-
Max_RPM)/1000)*MaxMotorTorque))/TConst)*Throttle;
imotorbrakemax = if noEvent(((MaxMotorTorque-(exp((RPM-
Max_RPM)/1000)*MaxMotorTorque))/TConst)*Brake*RegenDrop>=RegenCurrent) then Regen
Current else ((MaxMotorTorque-(exp((RPM-
Max_RPM)/1000)*MaxMotorTorque))/TConst)*Brake*RegenDrop;
imotor = if noEvent((imotormax-imotorbrakemax)>=Max_I-ifan) then Max_I-
ifan elseif noEvent((imotormax-imotorbrakemax)<=(-RegenCurrent+ifan)) then (-
RegenCurrent+ifan) else imotormax-imotorbrakemax;
imotort = imotor+ifan;
RegenDrop = if noEvent((RPM)>=50) then 1 elseif noEvent(RPM<=0) then 0 else abs
(RPM)/50;
Pfan = ((RPM+1)/Max_RPM)*FanPower;
ifan = Pfan/v;
Current = i;
SpeedK = ((Rated_Speed/nominalV)-2.5)-(exp((RPM-Max_RPM)/1000));
vmotor = RPM/SpeedK;
Efficiency = if noEvent(MotorOutPower<=0) then 100 else ((abs(MotorOutPower)+0.
001)/(abs(MotorInPower)+0.001))*100;
end EMF_Motor_Model;

```

APPENDIX C – Battery Pack Cell Variation

Figure 8-2 shows a snap shot of every battery cell voltage within one of the Coventry University Microcab H2EVs. It shows that at the end of charge there are a few groups of cells which reach the maximum cell voltage, 3.65V, prior to the rest. There is a cell variation of 0.386V across the entire battery pack and from Figure 8-2 it is clear that the BMS has not been programmed correctly to address this. However, where the battery packs, shown in Figure 8-3, are connected in series and then in parallel the nature of the tested 4kW Goodwolfe battery packs is exactly this. Where the BMS is responsible for ensuring that the battery cells are balanced whilst charging but cannot manage the cells during discharging. Therefore, redesigning the battery packs so that the cells are primarily connected in parallel and then in series would prevent large variation in cell voltages as the cells which are connected in parallel would balance themselves. This effectively reduces the number of cells which the BMS should manage from 96 cells to 24 cells for the discussed battery pack.

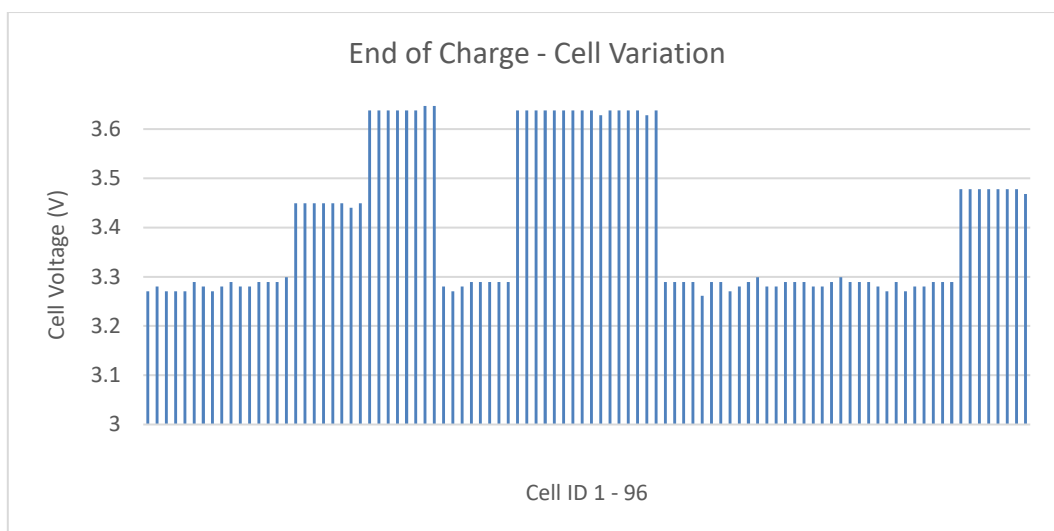


Figure 8-2 - Battery Pack Cell Variation

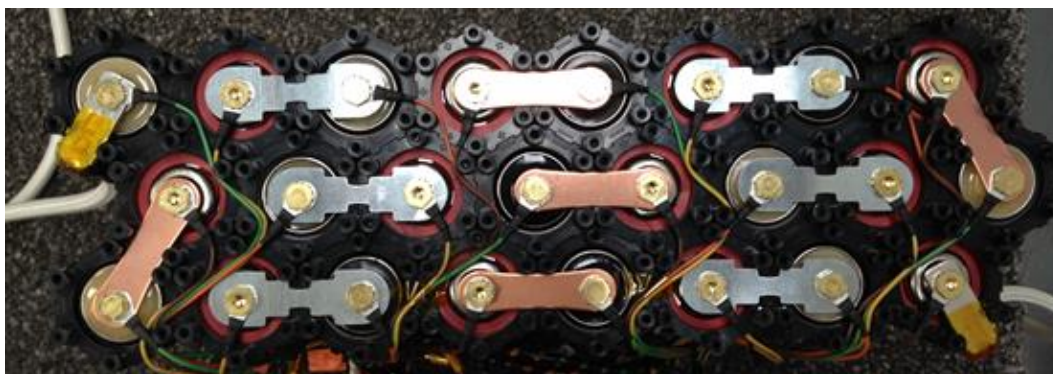


Figure 8-3 - Battery Layout

APPENDIX D – Battery Cell Results

Table 8-5 shows the results of the first battery pack which was disassembled and tested.

Table 8-5 - Battery Cell Capacity and DCIR Results

Cell Test Order ID	Capacity [Ah]	DCIR [mΩ]
1	14.5375	7.238959
2	14.4	7.506071
3	14.6125	7.257266
4	14.1625	7.211362
5	13.8125	8.165067
6	14.4	8.57652
7	14.425	8.445696
8	14.475	7.46241
9	14.375	7.193719
10	14.5875	7.216795
11	14.2375	7.216795
12	14.45	7.143899
13	14.725	7.040712
14	14.5625	7.225223
15	14.35	7.137395
16	14.5125	8.310556
17	14.7	7.098946
18	14.2375	7.214692
19	14.475	7.341335
20	14.425	11.56738
21	13.7375	7.853693
22	14.25	7.460492
24	13.95	7.859489
25	14.35	7.414983
26	14.2125	8.54955
27	14.425	7.302202
28	14.1625	8.499945
29	14.45	7.269141
30	14.3	7.296873
31	13.775	8.121078
32	14.375	7.288042
33	14.1875	7.276583
34	14.2375	7.263039
35	14.4875	7.302752
36	14.35	7.321716
37	14.0375	7.399267
38	13.975	7.282442
40	14.0625	7.354555
41	14.5625	7.095571
42	14.35	7.382231
43	14.725	7.075386
44	14.375	7.163481
49	14.5125	7.481571
50	14.35	7.31743
52	14.4875	7.311812
53	14.4	7.498994
55	14.2125	7.383581
56	14.25	7.195821
57	14.5125	7.207405
58	14.375	7.244256
59	14.425	7.321448
60	14.25	7.301413
61	14.4375	7.294454
62	14.2125	7.317162
63	14.3	7.284041
64	14.375	7.359941
65	14.25	8.440693
66	14.25	7.414713
67	14.5125	7.377378
68	14.5875	7.283774
69	14.5875	7.199503
70	14.2125	8.013172
72	14.1125	7.436715
73	14.325	7.473952
74	14.5375	7.529844
75	14.0875	7.335143
76	14.4875	6.79393
77	14.7	7.168197
78	14.1875	7.422923
79	14.4875	7.464059
80	14.2375	7.245311
81	14.45	7.057368
82	14.2375	7.265956
83	14.2125	8.588775
84	14.2125	8.595139
85	14.725	8.465766

APPENDICES

86	14.5625	8.401495
87	14.375	8.338893
88	14.2125	8.345951
89	14.2125	7.243991
90	14.1625	8.419881
92	14.5625	7.52128
95	14.5625	7.231556
96	14.45	7.25483

Figure 8-4 shows the capacity of each cell which was tested in test order. A total of 4 battery packs were dismantled, 384 cells, and 23 cells were discarded where their open circuit voltage was less than 2.3 V. This was advised by Ashwood Energy. Figure 8-4 shows that over the 361 cells which were tested there is a variation in cell capacity of 3.16 Ah's. Figure 8-5 presents the RMS voltage over each discharge test which was performed on these cells. It shows that there is a variation in RMS voltage of 0.19V over the 361 tested cells.

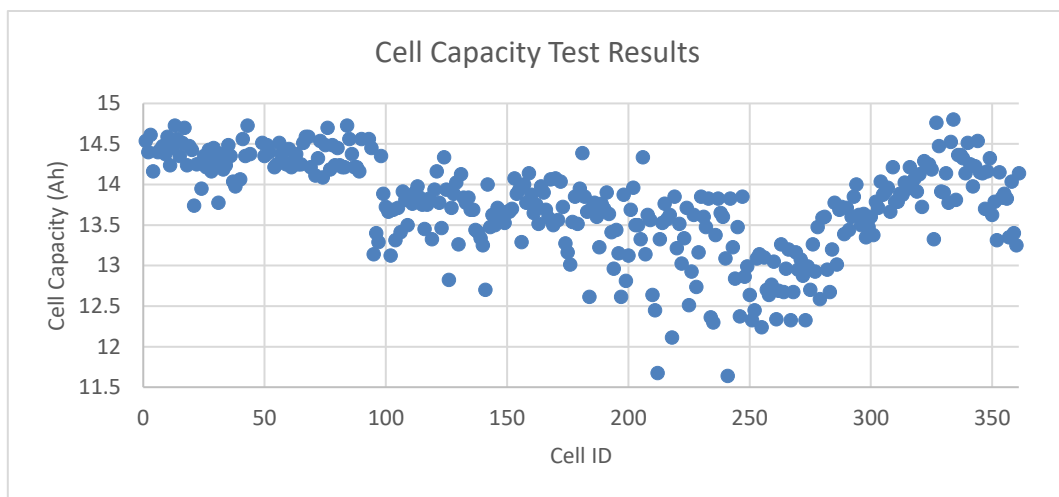


Figure 8-4 - Cell Testing - Capacity Comparison

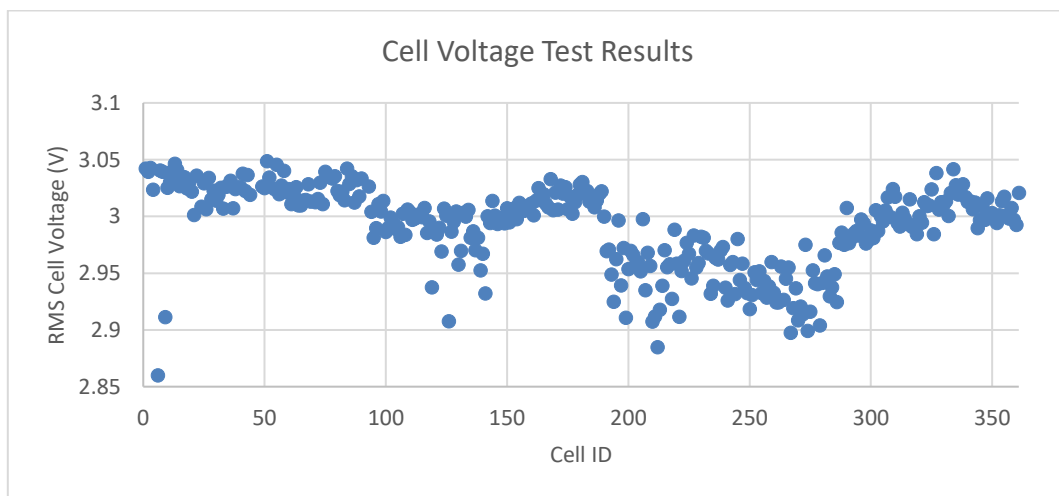


Figure 8-5 - Cell Testing - Voltage Comparison

APPENDIX E – Test Equipment List**Table 8-6 - Test Equipment**

Manufacturer	Model	Measurement
Motohawk	ECM-554-112-0906xD	CAN bus, Analog to Digital Read
Kavasa	HS/HS Professional	CAN bus logger
Race Technology	DL1	Analog Sensors and GPS
Snap-On	EETA308D	Current Clamp
Fluke	117	Multimeter
PicoScope	4424	Voltage and Current
LEM	LAC 300-S	Current Sensor
Dynetek	3-0010-02	Hydrogen Pressure Sensor
Vógtlin	Red-y Smart GSM- CTTCC00	Volume Flow Meter
MTS	4-post Custom Built	Shaker Rig
Analog Devices	ADXL325BCPZ	3-Axis Accelerometer
Analog Devices	ADXL320JCP	2-Axis Accelerometer
Swagelok	PGI-100B-PG100- BBGX-ABJ	Analog Pressure Guage
Burkert	Type 8316 563777	Pressure Transmitter
Longacre	72593	Vehicle Corner Scales
STMicroelectronics	LM235Z	Temperature Sensor
Zentro – Elektrik	EL4500	Electronic Load
Instron	850i	Material Testing System

APPENDIX F – Improper Fuel Cell Control

Figure 8-6 shows test data of the 1080AC 70 cell Ballard stack operating at a fixed power output of 1.5 kW. The Ballard recommended optimum temperature is 43 °C at this power output. Figure 8-6 shows, as the ambient temperature, blue, increases then the fan speed increases to maintain temperature. However, when the ambient temperature reduces below 23 °C the temperature of the fuel cell, red, also reduces and falls below the optimum, with no change in fan speed. Ballard specify that operating below optimum temperature for long periods of time can lead to a decrease in performance, anode flooding, fuel starvation and irreversible degradation (Ballard Power Systems Inc. 2014). Due to the geological location of Coventry University and Microcab Industries, most the year is spent below 23°C and because of this, the result in Figure 8-6 and the statements made within the Ballard user guide, any fuel cell failure of the Ballard fuel cell system currently fitted to the Coventry University Microcab H2EV is may be because of this. To overcome this, a simple modification to the fuel cell controller code could be made, where the minimum fan speed is significantly reduced to prevent overcooling. This incorrect operation of the fuel cell could account for errors between test and simulation results within this thesis.

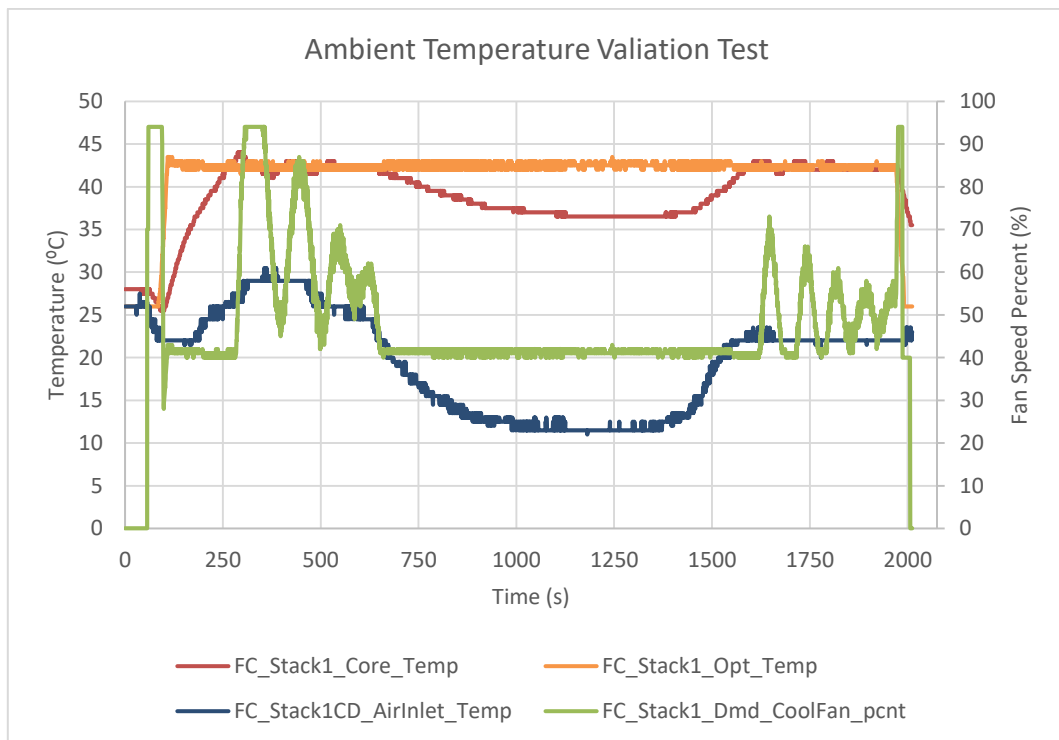


Figure 8-6 - Fuel Cell Ambient Temperature Test

APPENDIX G – Vehicle Attenuation

Fuel Cell Reliability Mounting & Vehicle Attenuation

The Coventry University Microcab H2EV has been placed on the 4-post shaker rig and has been put through a variety of procedures to distinguish whether there is a large amount of torsion at the rear mounting points of vehicle which the fuel cell mounted. To do this, an accelerometer was located on each beam and used to monitor the difference in acceleration. Figure 8-7 shows in red where these accelerometers have been mounted and in yellow where the fuel cell brace bars are mounted.



Figure 8-7 - Chassis Mounted Accelerometers

It can be noted that the tests were carried out with the fuel cell brace bars attached to the vehicle prior to running the tests with them removed. Therefore, the procedures are identified as “#.1” for the procedure with the fuel cell brace bars attached and “#.2” for the procedure with the fuel cell brace bars removed.

Procedure 1

The initial procedure was to shake all four wheels, in phase by 5mm in a sinusoidal motion. The sin wave started at 0.25Hz and increased by 0.25Hz/s until it reached 11.25Hz. Figure 8-8 shows the details of this procedure within 4-Post shaker rig operating software:

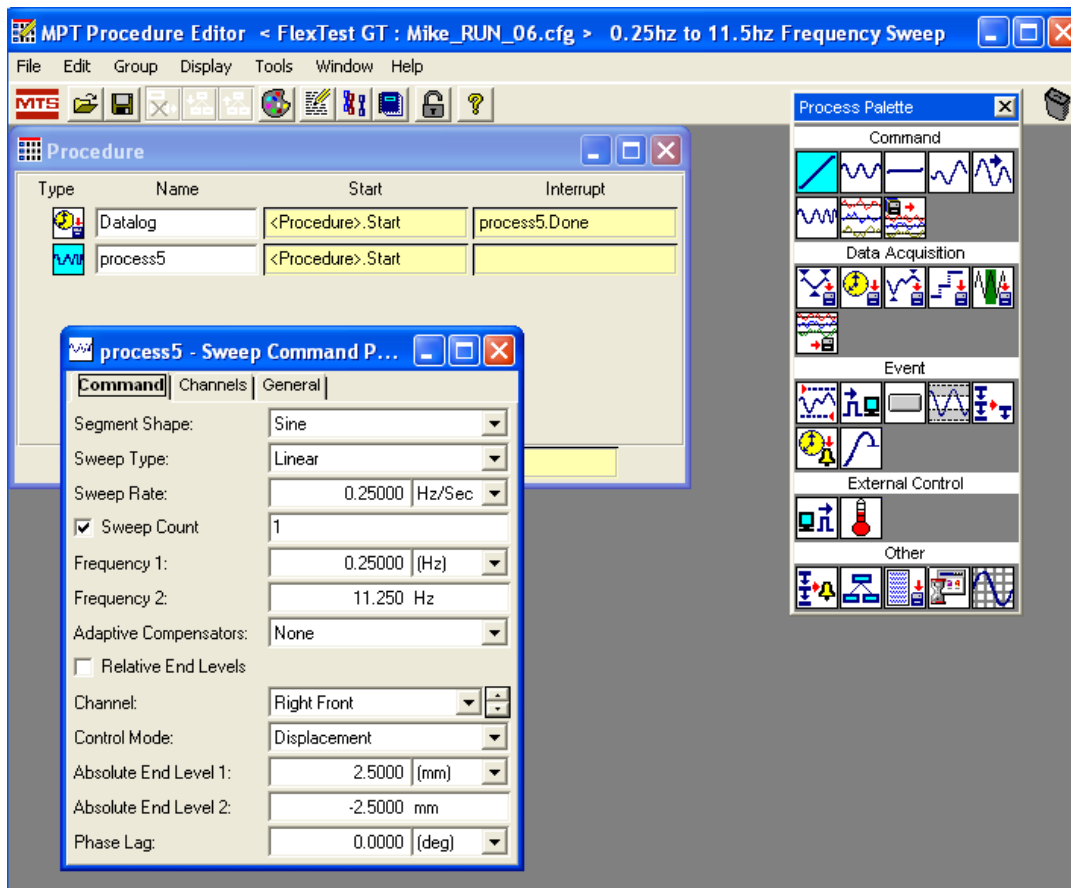


Figure 8-8 - MTS Shaker Rig Procedure 1

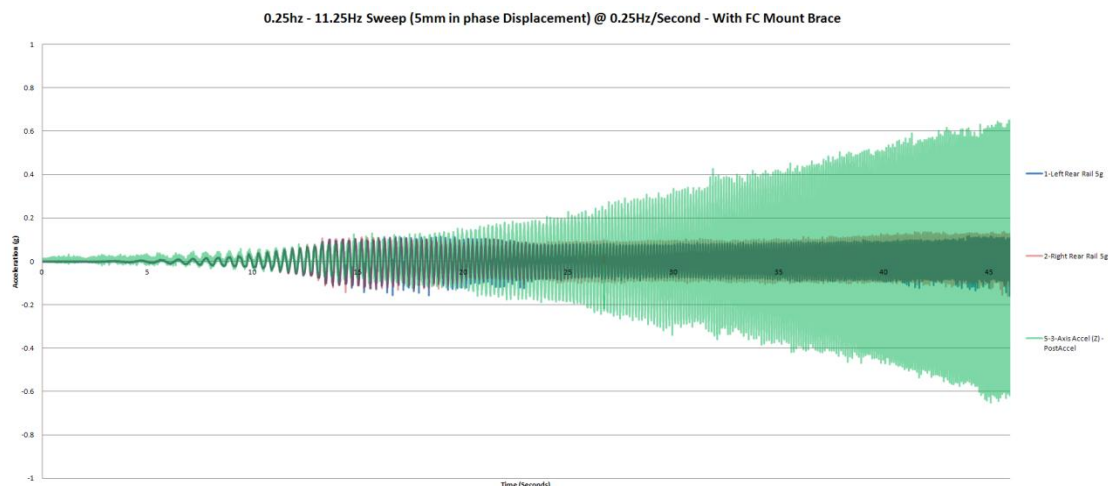


Figure 8-9 - 0.25hz - 11.25hz Frequency Sweep, 5mm In-Phase Displacement, 0.25hz/s, FC Mounts Installed

It can be seen from Figure 8-9 the variation between the rear fuel cell rails is minimal throughout the frequency sweep. There are two supporting brace bars which the fuel cell case mounts on which are still fitted to the vehicle. These can be seen in Figure 8-7 and are highlighted in yellow. The test has been performed again with the brace bars removed to see if there is further difference between the rear beams on the Microcab.

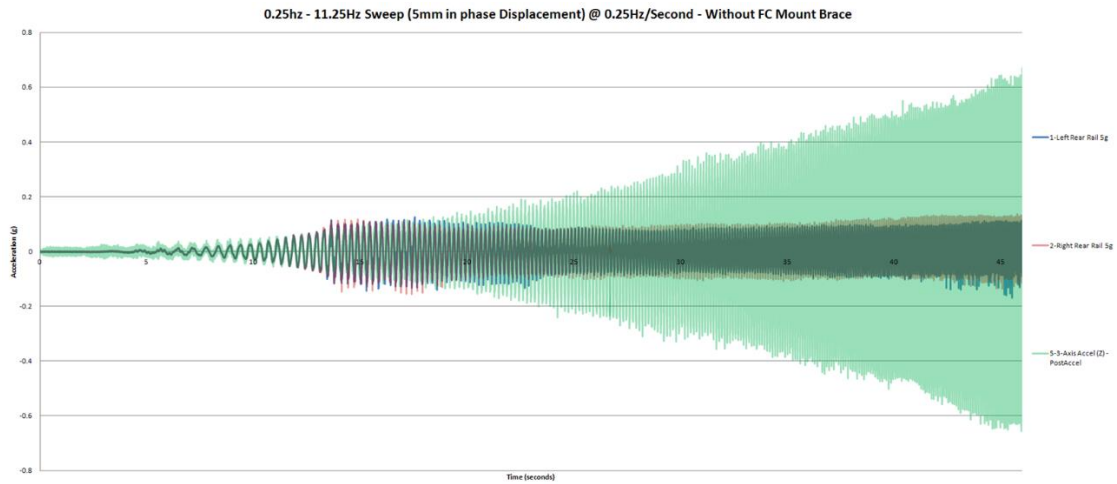


Figure 8-10 - 0.25hz - 11.25hz Frequency Sweep, 5mm In-Phase Displacement, 0.25hz/s – No FC Mounts Installed

By comparing Figure 8-10 to Figure 8-9 it can be seen that there are little to no obvious differences between the two sets of results. However, to make this clearer, Microsoft Excel has been used to create Figure 5 which shows the difference between each test.

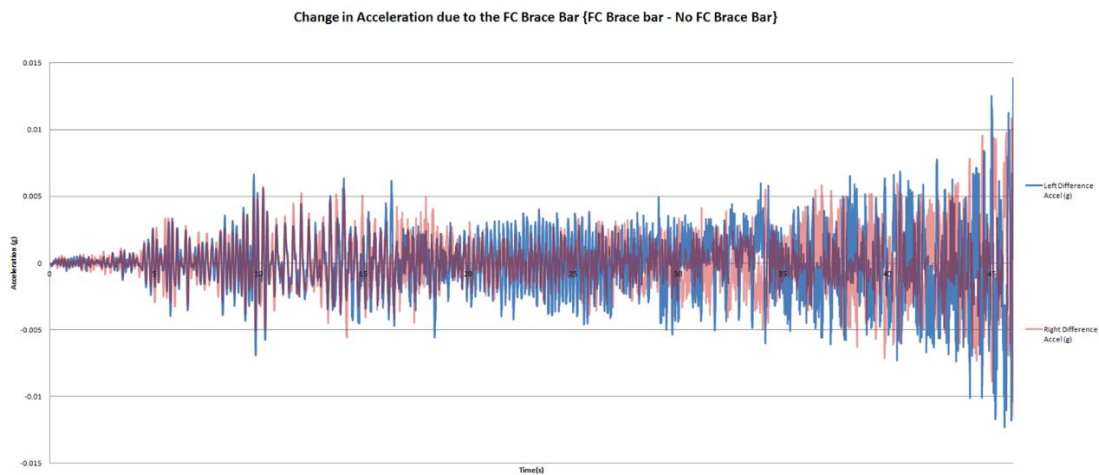


Figure 8-11 - Difference Between Figure 8-9 and Figure 8-10 Results

From the results in Figure 8-11 the average of the LHS & RHS accelerations can be used, then the average of these two results to get the overall average difference in acceleration when having the fuel cell brace bars mounted. Using Microsoft Excel, equation (242) calculates the average difference of acceleration to be 0.0022 g which is equal to 0.02 m/s². Therefore, an average variation of force equal to 0.0022 * 9.81 = 0.02 N, which is possibly due to either, slight tyre pressure variation or slight differences between the dampers in the vehicle.

$$RMS = \sqrt{\frac{\left(\sqrt{\frac{SUMSQ(J4:J19672)}{COUNTA(J4:J19672)}} + \sqrt{\frac{SUMSQ(K4:K19672)}{COUNTA(K4:K19672)}}\right)^2}{2}} \quad (242)$$

APPENDICES

Procedure 2

The second procedure is similar to the previous procedure, however, the two right hand wheels have been actuated out of phase by 180 degrees by using the same 5mm sinusoidal motion. The sin wave started at 0.25 Hz and increased by 0.25 Hz/s until it reached 11.25 Hz. Figure 8-12 shows the details of this procedure:

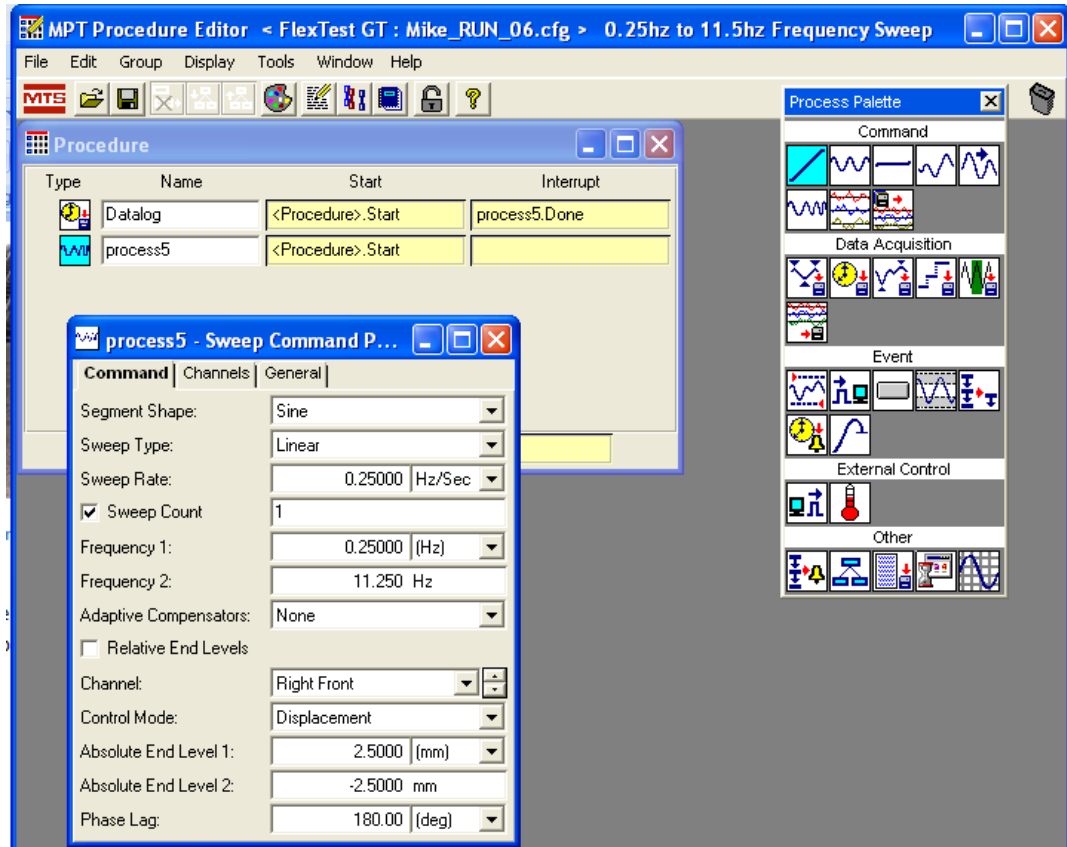


Figure 8-12 - MTS Shaker Rig Procedure 2

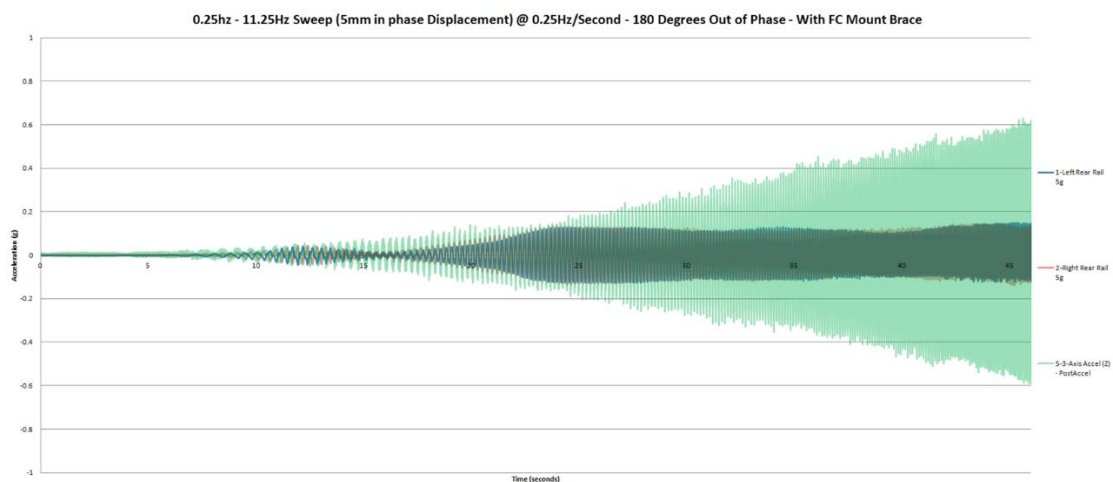


Figure 8-13 - 0.25hz - 11.25hz Frequency Sweep, 5mm, 180 Degrees Out-Of-Phase Displacement, 0.25hz/s, FC Mounts Installed

From Figure 8-13 you can see that the measured accelerations are similar, just opposite, to each other as they are on the opposite sides of the vehicle. However, it

can be difficult to read all this data. Therefore, the graph has been split into 6 graphs each showing 8 seconds of results for ease of analysis.

Within this section the Y-Axis (Acceleration) will vary to enable best analysis of the results and the acceleration of the Post (Green) has been removed for the same purpose.

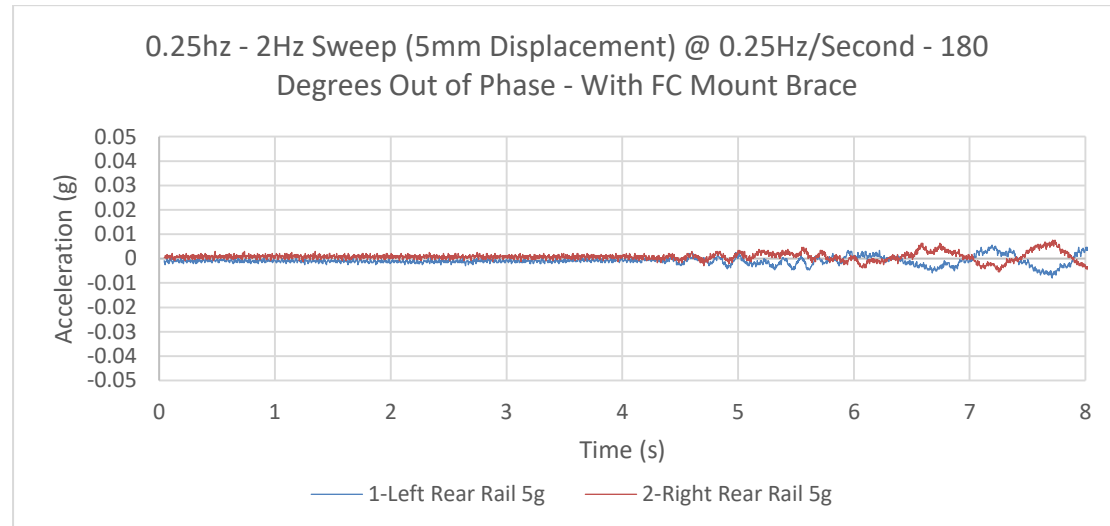


Figure 8-14 - 0.25hz - 2hz Frequency Sweep, 5mm, 180 Degrees Out-Of-Phase Displacement, 0.25hz/s, FC Mounts Installed

From Figure 8-14 we can see that initially the accelerometers show a fair bit of noise and this can be established as a 'dead zone'. Figure 8-14 shows the first 8 seconds of the sweep which is the range of 0.25 Hz to 2 Hz and it can be seen, that at these low frequencies there is no variation between the left and right rear beams.

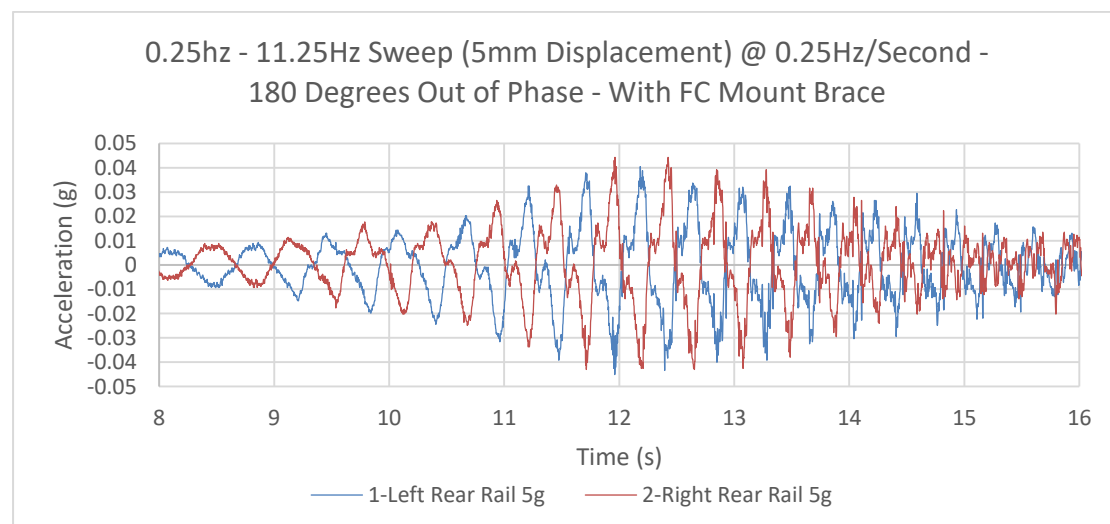


Figure 8-15 - 2hz - 4hz Frequency Sweep, 5mm, 180 Degrees Out-Of-Phase Displacement, 0.25hz/s, FC Mounts Installed

Figure 8-15 shows similar results to that of Figure 8-14, where the acceleration between the left and right rear beams of the vehicle are extremely close to each other,

APPENDICES

showing just the 180 degrees out of phase, due to the procedure that the vehicle is being subjected too. Figure 8-15 shows the frequency range between 2 and 4 Hz. Figure 8-15 also shows, what looks to be a natural frequency of the ride, at 3 Hz ($12s * 0.25 \text{ Hz/s} = 3 \text{ Hz}$), this is due to the shape, in which the accelerations increase and decrease before and after this frequency.

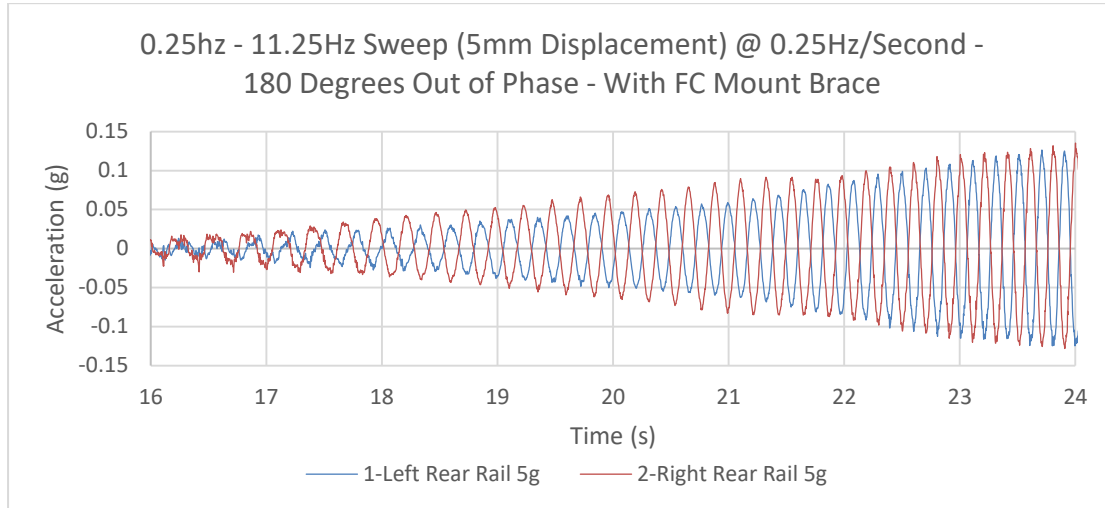


Figure 8-16 - 4hz - 6hz Frequency Sweep, 5mm, 180 Degrees Out-Of-Phase Displacement, 0.25hz/s, FC Mounts Installed

Figure 8-16 shows that between 4.25 Hz and 5.5 Hz that there is a slight variation between the accelerations of the left and right rear beams of the vehicle. The exact variation at 19.35s (4.75 Hz) is 0.016 g which is equal to 0.157 m/s^2 , 0.157 N. From the graph, it could be suggested that the left hand side (LHS) of the vehicle has a lower natural frequency than the right hand side (RHS). This is suggested as you can see how the LHS acceleration increases similar to that of a transmissibility graph between 17 and 22 seconds. The reason which the LHS could have a lower natural frequency than the RHS could be due to weight distribution along the chassis. As the main vehicle wiring harness and Fuel Cell wiring all runs along the LHS of the vehicle, therefore, making it possible to weigh different amounts from left to right, evidence of the weight variation can be seen in 'Table 4-5 - Vehicle Measurements' in section '4.1 Component Mass and Positioning Collection' of this thesis. Figure 8-16 shows the frequency range of 4 to 6 Hz.

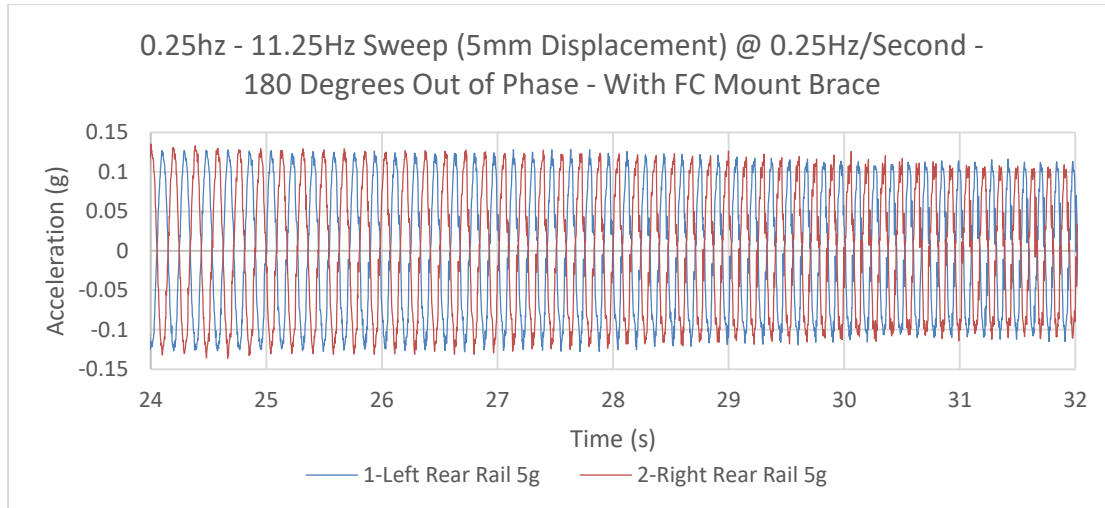


Figure 8-17 - 6hz - 8hz Frequency Sweep, 5mm, 180 Degrees Out-Of-Phase Displacement, 0.25hz/s, FC Mounts Installed

Figure 8-17's results return similar differences as Figure 8-14, where there is little to no variation between the LHS and RHS rear beams of the vehicle. Figure 8-17 shows the frequency range of 6 to 8 Hz.

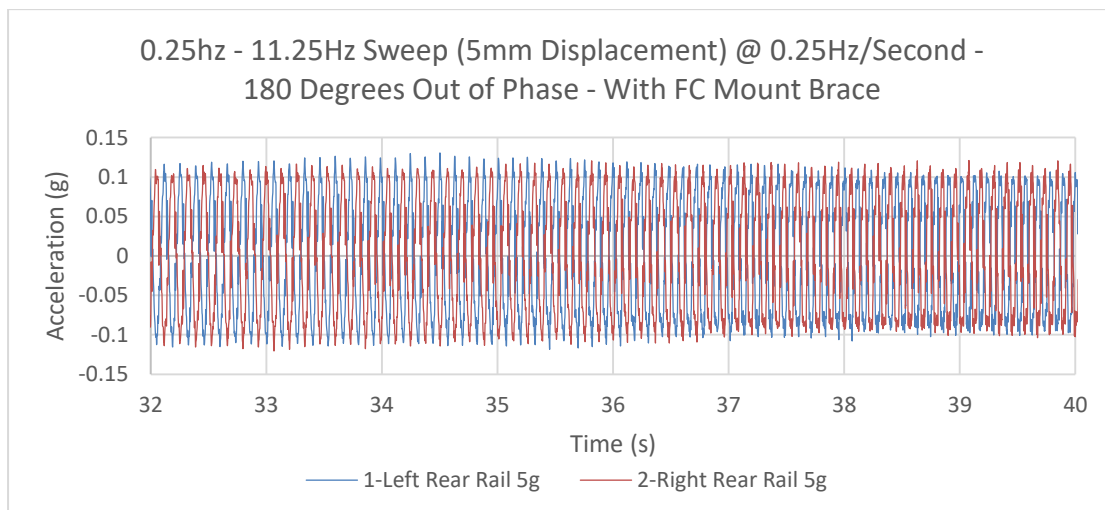


Figure 8-18 - 8hz - 10hz Frequency Sweep, 5mm, 180 Degrees Out-Of-Phase Displacement, 0.25hz/s, FC Mounts Installed

Figure 8-18 shows similar results again where the variation between LHS and RHS is minimal. However, the LHS seems to show slightly more acceleration between 9.5 Hz and 10 Hz. The exact variation at 39.4s (9.75 Hz) is 0.028 g which is equal to 0.275 m/s², 0.275 N. However, this difference is only during the upwards post movement of the sine wave and not during the negative movement of the sine wave.

APPENDICES

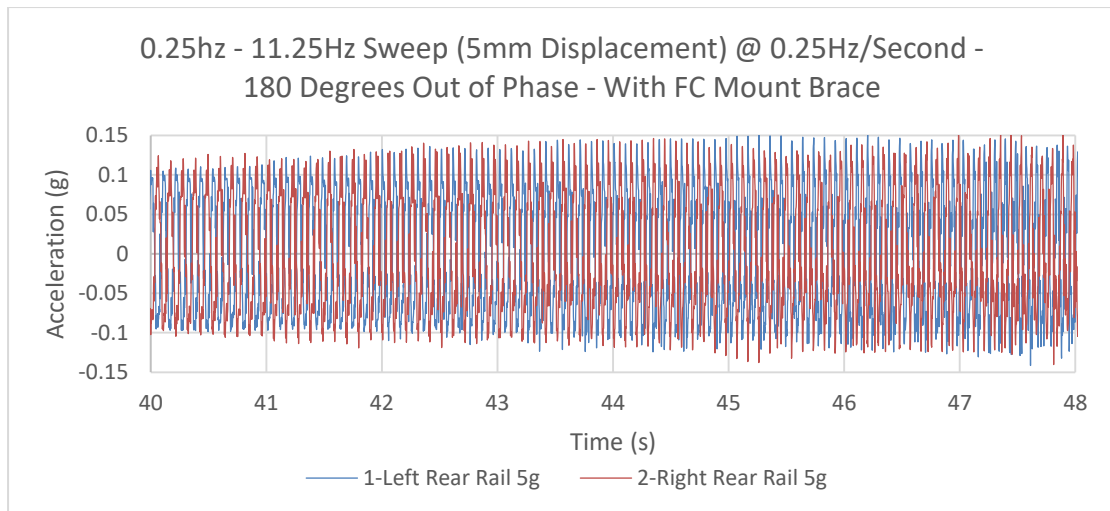


Figure 8-19 - 8hz - 10hz Frequency Sweep, 5mm, 180 Degrees Out-Of-Phase Displacement, 0.25hz/s, FC Mounts Installed

Figure 8-19 continues to show little variation between LHS and RHS accelerations. Except for the lower end of frequencies in the graph where it can be seen that between 10 and 10.25 Hz that the differences stated for Figure 8-18 are continued. It can also be seen in Figure 8-19, that the variation between the LHS and RHS is equal to the differences between positive acceleration and negative acceleration. This shows that when the LHS's positive acceleration is larger than the RHS, then the RHS's Negative acceleration is then larger than the LHS.

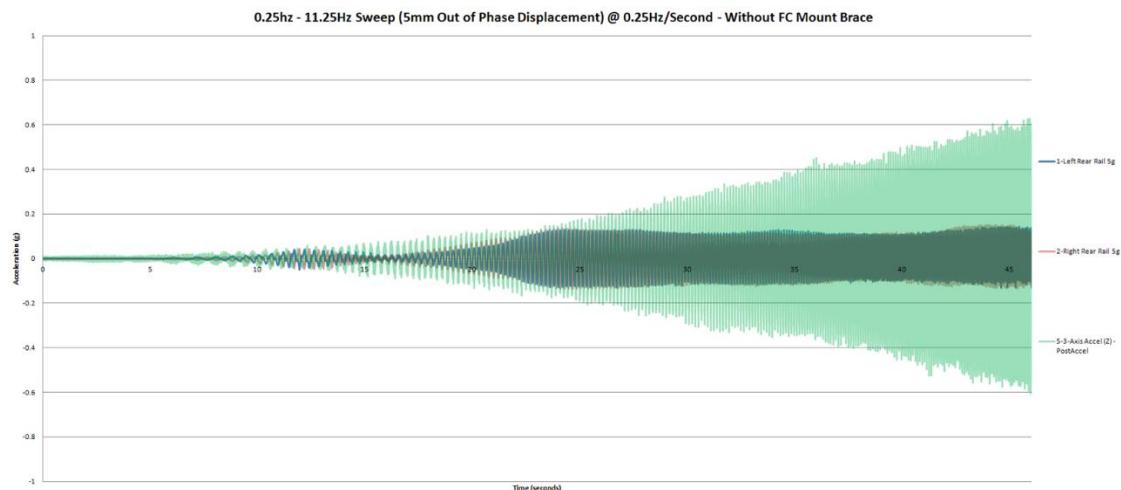


Figure 8-20 - 0.25hz - 11.25hz Frequency Sweep, 5mm, 180 Degrees Out-Of-Phase Displacement, 0.25hz/s, No FC Mounts Installed

The test has been performed again with the brace bars removed to see if there is further difference between the rear beams on the Microcab. If we compare Figure 8-20 to Figure 8-13 we can see little to no obvious differences between the two sets of results. However, to make this clearer, Microsoft Excel has been used to create Figure 14 in which it shows the difference between the fuel cell brace bars being mounted.

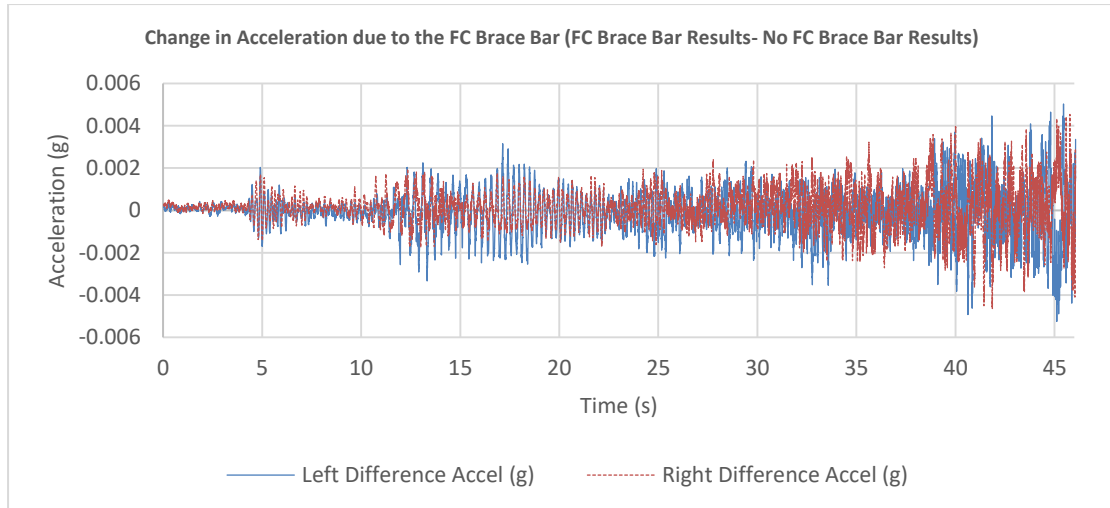


Figure 8-21 - Difference Between Figure 8-13 and Figure 8-20

From the results in Figure 8-21 the average of the LHS and RHS accelerations can be used and then the average of these two can provide the overall average difference of installing the fuel cell brace bars to the chassis. Using Microsoft Excel, equation (243) presents an average difference in acceleration of 0.001 g which is equal to 0.01 m/s² and 0.01 N.

$$RMS = \sqrt{\frac{\left(\sqrt{\frac{SUMSQ(J4:J19672)}{COUNTA(J4:J19672)}} + \sqrt{\frac{SUMSQ(K4:K19672)}{COUNTA(K4:K19672)}} \right)^2}{2}} \quad (243)$$

APPENDIX H – Tabulated Validation Results**Table 8-7 - Model Validation**

Procedure	Measurement	RMS Percentage Error
Battery Pack Steady State Discharge Validation	Battery Voltage	0.88%
Battery Pack Steady State Discharge Validation	Battery SOC	0.77%
Battery Pack Goodwolfe Charge Simulation	Battery Voltage	1.54%
Battery Pack Goodwolfe Charge Simulation	Battery SOC	0.29%
Single Cell Model Validation	2C Charge Cell Voltage	1.1%
Single Cell Model Validation	1C Charge Cell Voltage	1.3%
Single Cell Model Validation	0.5C Charge Cell Voltage	1.5%
Single Cell Model Validation	1C Discharge Cell Voltage	0.8%
Single Cell Model Validation	2C Discharge Cell Voltage	0.6%
Single Cell Model Validation	3C Discharge Cell Voltage	1.9%
Single Cell Model Validation	4C Discharge Cell Voltage	2.5%
Single Cell Model Validation	4C Discharge Cell Voltage	4.1%
Fuel Cell Model Validation	1kW Power Output Voltage	1.2%
Fuel Cell Model Validation	1.25kW Power Output Voltage	2.1%
Fuel Cell Model Validation	1.5kW Power Output Voltage	4.2%
Fuel Cell Model Validation	1.75kW Power Output Voltage	3.1%
Fuel Cell Model Validation	2kW Power Output Voltage	2.7%
Fuel Cell Model Validation	2.25kW Power Output Voltage	2.7%
Fuel Cell Model Validation	2.5kW Power Output Voltage	2.1%

Fuel Cell Model Validation	2.75kW Power Output Voltage	3.4%
Fuel Cell Model Validation	3kW Power Output Voltage	3.4%
Fuel Cell Model Validation	1kW Power Output Tank Pressure	0.5%
Fuel Cell Model Validation	1.25kW Power Output Tank Pressure	0.6%
Fuel Cell Model Validation	1.5kW Power Output Tank Pressure	0.7%
Fuel Cell Model Validation	1.75kW Power Output Tank Pressure	0.6%
Fuel Cell Model Validation	2kW Power Output Tank Pressure	0.5%
Fuel Cell Model Validation	2.25kW Power Output Tank Pressure	0.7 %
Fuel Cell Model Validation	2.5kW Power Output Tank Pressure	0.8 %
Fuel Cell Model Validation	2.75kW Power Output Tank Pressure	0.9%
Fuel Cell Model Validation	3kW Power Output Tank Pressure	0.5%
DCDC System Model Validation	1kW Operation, Power Loss	1.68%
DCDC System Model Validation	1.25kW Operation, Power Loss	6.31%
DCDC System Model Validation	1.5kW Operation, Power Loss	3.37%
DCDC System Model Validation	1.75kW Operation, Power Loss	3.64%
DCDC System Model Validation	2kW Operation, Power Loss	3.27%
DCDC System Model Validation	2.25kW Operation, Power Loss	3.64%
DCDC System Model Validation	2.5kW Operation, Power Loss	2.52%

APPENDICES

DCDC System Model Validation	2.75kW Operation, Power Loss	1.18%
DCDC System Model Validation	3kW Operation, Power Loss	1.31
Motor Model Validation	Back EMF Voltage	0.25%
Motor Model Validation	Motor Current	1.57%
Motor Model Validation	Motor Power In	3%
Motor Model Validation	Motor Speed	0.17%
Motor Model Validation	Motor Power Out	0.42%
Motor Model Validation	Motor Efficiency	1.49%
NEDC Electric Vehicle Simulation	Energy Consumption	1.21%
CUDC 3D Road Electric Vehicle Simulation	Energy Consumption	2.3%
CUDC 3D Road Fuel Cell Vehicle Simulation	1.5kW Fuel Cell Power, Battery Energy Consumption	8%
RMS Error of Validation Results		2.5%
Battery Pack Steady State Discharge Validation	RMS of Section Results	0.83%
Battery Pack Goodwolfe Charge Simulation	RMS of Section Results	1.1%
Single Cell Model Validation	RMS of Section Results	2.03%
Fuel Cell Model Validation	RMS of Section Results	2.1%
DCDC System Model Validation	RMS of Section Results	3.34%
Motor Model Validation	RMS of Section Results	1.52%
Vehicle Validation	RMS of Section Results	4.86%

APPENDIX H – Certificate of Ethical Approval



Certificate of Ethical Approval

Applicant:

Michael Apicella

Project Title:

A Multi-Disciplinary Approach to Fuel Cell Vehicle Modelling and Simulation - A Study to Investigate and Optimise Overall Electric Vehicle and Fuel Cell Electric Vehicle Efficiency

This is to certify that the above named applicant has completed the Coventry University Ethical Approval process and their project has been confirmed and approved as Low Risk

Date of approval:

04 April 2017

Project Reference Number:

P52958

Figure 8-22 - Ethical Approval Certificate